DIN
GMA

Quaderni di ricerca

Decima giornata di studio Ettore Funaioli

15 luglio 2016

A cura di
Umberto Meneghetti e Vincenzo Parenti Castelli

SOCIETÀ EDITRICE ESCULAPIO

AlmaDL
University of Bologna Digital Library

Quaderni del **DIN – GMA**

Atti di giornate di studio – 10

A cura di:
Umberto Meneghetti e Vincenzo Parenti Castelli

Coordinatore di redazione:
Alessandro Zanarini

DIN
Dipartimento di Ingegneria Industriale
http://www.ingegneriaindustriale.unibo.it

GMA
Gruppo di Meccanica Applicata
http://wpage.unina.it/dellaval/GMA/GMA_homeold.htm

Accademia delle Scienze dell’Istituto di Bologna
http://www.accademiascienzebologna.it/AccademiaScienze/default.htm

Decima giornata di studio Ettore Funaioli

15 luglio 2016

A cura di:
Umberto Meneghetti e Vincenzo Parenti Castelli

Decima giornata di studio Ettore Funaioli – 15 luglio 2016 / A cura di Umberto Meneghetti e Vincenzo Parenti Castelli
Bologna: 2017 – pp. 274; 17 cm

ISBN 978-88-9385-037-7

Versione elettronica disponibile alla pagina
http://amsacta.unibo.it/5600/

Stampa a richiesta eseguita da:

SOCIETÀ EDITRICE ESCULAPIO

40131 Bologna – Via U. Terracini 30 – Tel. 051- 6340113 – Fax 051- 6341136
www.editrice-esculapio.com

INDICE

Prefazione

La decima “Giornata di studio Ettore Funaioli" si è svolta il 15 luglio 2016 presso la Scuola di Ingegneria e Architettura dell’Alma Mater Studiorum – Università di Bologna.
Il perdurante successo della manifestazione conferma la stima e l’affetto per il Prof. Ettore Funaioli, che i partecipanti intendono esprimere con la loro presenza.
A tutti gli intervenuti, e in particolare agli autori delle memorie, vanno il vivo apprezzamento e il riconoscente ringraziamento degli organizzatori della Giornata.
L’adesione di tanti valenti studiosi e ricercatori a queste Giornate conferma anche il loro apprezzamento per l’occasione che essa offre di ritrovarsi fra colleghi con affinità di interessi, per scambiarsi idee e opinioni sulle ricerche in corso e sui problemi generali della nostra comunità scientifica.
Sono poi sempre motivo di grande compiacimento l’elevata qualità scientifica dei lavori presentati e il tenace impegno dei Ricercatori di Meccanica che hanno aderito alla manifestazione.
Questo convegno si è svolto con il patrocinio dell’Accademia delle Scienze dell’Istituto di Bologna e del GMA – Gruppo di Meccanica Applicata. Di ciò ringraziamo vivamente il Presidente dell’Accademia delle Scienze, Prof. Emilio Pasquini e il Presidente del GMA, Prof. Federico Cheli.
La Giornata ha potuto svolgersi anche grazie alla collaborazione della Scuola di Ingegneria e Architettura e del DIN – Dipartimento di Ingegneria Industriale dell’Alma Mater Studiorum – Università di Bologna. Ringraziamo il Presidente della Scuola di Ingegneria e Architettura Prof. Ezio Mesini e il Direttore del DIN Prof. Antonio Peretto, che hanno consentito queste collaborazioni.
Infine si ringrazia il continuo supporto dato dall’azienda G.D S.p.A. a questa “Giornata”.

Bologna, 25 giugno 2017

Umberto Meneghetti – Vincenzo Parenti Castelli

L'ORGANIZZAZIONE DELLA DIDATTICA NELLA SCUOLA DI INGEGNERIA DI BOLOGNA AL TEMPO DI FRANCESCO MASI 1891-1927

Umberto Meneghetti
Professore Emerito
Alma Mater Studiorum Università di Bologna
E-mail: umberto.meneghetti@ unibo.it

***Riassunto**. Francesco Masi è stato Professore di Meccanica applicata alle macchine nell'Università di Bologna dal 1891 al 1927. In questo lavoro viene descritta l'organizzazione generale della didattica nella Scuola di applicazione per ingegneri dell'Università di Bologna durante il periodo della sua docenza. Sono presentati gli aspetti più caratteristici di tale organizzazione, evidenziando le differenze rispetto alla situazione attuale. Dal confronto risulta chiaramente che i cambiamenti via via introdotti, forse non tutti singolarmente utili e apprezzati nel momento in cui avvennero, nel loro complesso furono tuttavia indispensabili per la funzionalità e la sopravvivenza stessa della Scuola.*

***Keywords**: Francesco Masi, engineering education, engineering school of Bologna*

1. INTRODUZIONE

Francesco Masi (Guastalla 1852 - Bologna 1944) è stato Professore di Meccanica applicata alle macchine nell'Università di Bologna dal 1891 al 1927. Questo lavoro descrive e commenta l'organizzazione generale della didattica nella Scuola di Ingegneria durante il periodo della sua docenza, con particolare riferimento alla sua materia d'insegnamento. Tracceremo anche per sommi capi l'evoluzione della Scuola d'Ingegneria, dalla sua nascita alla trasformazione in Facoltà universitaria. Non tratteremo invece specificamente dei contenuti del corso di Meccanica applicata alle macchine, né – tantomeno – dell'attività scientifica di Francesco Masi, argomenti che sono stati oggetto di una Conferenza di Facoltà [1] e di altri lavori [2], [3].

Qui ci proponiamo soprattutto di illustrare la distanza fra l'organizzazione della didattica di circa cento anni fa e quella attuale, e come i cambiamenti intercorsi siano stati complessivamente indispensabili. Forse non tutte le innovazioni furono apprezzate nel momento in cui furono realizzate, e certamente molte di esse si dimostrarono in seguito inadeguate rispetto ai risultati attesi; qualcuna potrebbe anzi essere stata controproducente, ma pare in ogni caso indubbio che senza riforme oggi la Scuola di Ingegneria non sarebbe semplicemente obsoleta, ma addirittura scomparsa.

2. NASCITA DELLA SCUOLA DI INGEGNERIA

I precedenti

La Scuola di applicazione per gli ingegneri fu ufficialmente istituita nell'Università di Bologna nel 1877. Prima di allora, dal 1862 fu attivo un *Corso pratico per gl'ingegneri civili e* *architetti*, mentre prima ancora il titolo di “ingegnere civile” poteva essere acquisito dai “laureati in Matematica in un’Università” dello Stato Pontificio tramite un esame presso una commissione di tre “ingegneri riconosciuti”, da sostenere dopo quattro anni di praticantato presso – appunto – un “ingegnere riconosciuto”, cioè abilitato all’esercizio della professione [3], [4].

Osserviamo per inciso che il praticantato presso un professionista abilitato derivava in sostanza dalla prassi in uso nei secoli precedenti, quando gli “ingegneri” erano sostanzialmente degli abili artigiani – dotati spesso d’ingegno ma di regola con scarsa cultura tecnico-scientifica – che acquisivano le loro conoscenze sul campo e sul campo le trasmettevano ai loro allievi [3].

Tra i docenti della Facoltà Matematica di Bologna merita di essere citato Giuseppe Venturoli (Bologna, 1768-1846), che coprì la cattedra di Matematica applicata dal 1802 al 1817, quando fu chiamato a Roma – capitale dello Stato Pontificio – a fondare e dirigere colà la Scuola per ingegneri. *Matematica applicata* era un corso biennale, che trattava i principi di base di tutta quella che poi sarebbe diventata – con i corsi fondamentali di Meccanica razionale, Meccanica applicata alle macchine, Scienza delle costruzioni, Tecnica delle costruzioni, Idraulica, Costruzioni idrauliche – la “Meccanica dell’Ingegneria”. La sua opera più importante, *Elementi di meccanica e d’idraulica*, fu un testo di riferimento in Italia, e non solo, per tutta la prima metà del XIX secolo [3], [5], [6].

Il Corso pratico per gli ingegneri civili e architetti – introdotto, come detto più sopra, nel 1862, quando Bologna entrò a far parte del nuovo Regno d’Italia – non ebbe grande fortuna, soprattutto per mancanza di mezzi. Una relazione del 1875, redatta da L. Cremona, F. Padula e P. Richelmy, rilevava che le "scuole minori o meglio corsi pratici [d’ingegneria] di Padova, Palermo, Pisa e Bologna“ finivano per accentuare in modo insostenibile una "condizione anormale di cose", ossia una "grande disuguaglianza di studii in ingegneri usciti da scuole tutte mantenute dallo stato”: in pratica, la relazione sosteneva che queste scuole non erano in grado di assicurare un’adeguata preparazione. Di conseguenza, il *Corso pratico* di Bologna fu soppresso, attivando però dal 1875 il solo primo anno della nuova *Scuola di applicazione* triennale. Appurato che gli altri due anni non erano previsti per mancanza di fondi, fu creato un Consorzio cittadino che ne assicurò il finanziamento, cosicché nel 1877-78 erano attivi tutti e tre gli anni della Scuola [3], [7], [8].

Fra i docenti del Corso pratico merita comunque una menzione G. Barilli, più noto sotto lo pseudonimo di Quirico Filopanti, che nel suo corso di Meccanica applicata introdusse molti argomenti anche lontani dall’interpretazione usuale di tale corso. Il programma prevedeva, infatti, [3] [9]: “Dei motori in genere, e più specialmente delle forze animali; Delle forze vive; Cenni sull’arte militare: strategia, tattica, balistica, poliorcetica, castrametazione; Delle resistenze passive; Cinematica, e specialmente delle ruote dentate; Delle macchine a vapore con e senza condensazione; Strade ferrate; Strade ordinarie.”

L’istituzione della Scuola di applicazione per gli ingegneri

La Gazzetta Ufficiale del Regno d’Italia del 27 ottobre 1876, n. 251, pubblicava il “Regio Decreto n. 3434, che approva il regolamento generale universitario e gli annessi regolamenti speciali delle Facoltà di giurisprudenza, di medicina e chirurgia, di scienze matematiche, fisiche e naturali, di filosofie e lettere, e delle Scuole di applicazione per gli ingegneri.”

Il successivo Regio Decreto 3648 del 14 gennaio 1877 istituiva la Scuola d'applicazione degli Ingegneri di Bologna. L’art. 1 recita: “È istituita nella regia università di Bologna

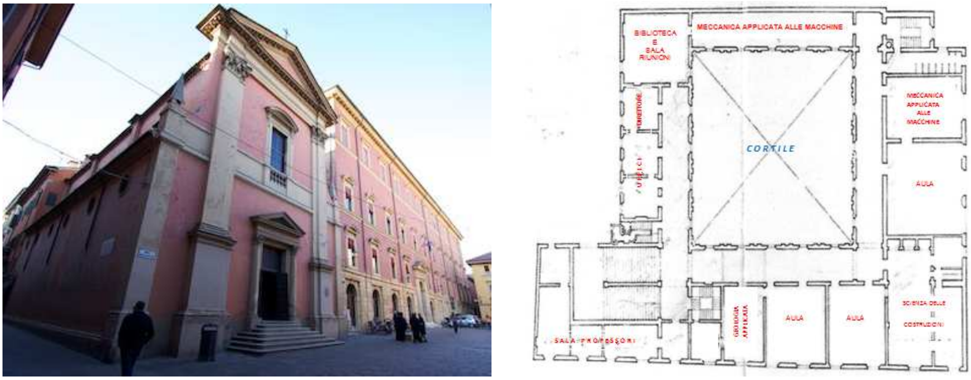

Figura 1. Sede della Scuola in piazza dei Celestini e pianta del II piano.

e annessa alla facoltà di scienze matematiche, fisiche e naturali la scuola completa d'applicazione per gli ingegneri, alla quale è applicato il regolamento comune alle scuole d'applicazione, approvato col nostro [cioè del firmatario Vittorio Emanuele II] decreto 8 ottobre 1876, n. 3434" [7]. Come accennato più sopra, il primo anno della Scuola era a carico dello Stato, mentre il secondo e il terzo erano finanziati da un apposito Consorzio cittadino.

La sede prescelta fu l'ex convento di San Giovanni dei Celestini; alla Meccanica applicata alle macchine era riservato un ampio spazio al II piano dell'edificio, v. Fig. 1.

Il regolamento generale delle Scuole di applicazione

In Fig. 2 sono riportati alcuni punti del regolamento generale delle Scuole di applicazione, che meritano qualche breve commento.

L'art. 1 definisce le Scuole come finalizzate esclusivamente all'istruzione, cioè alla didattica, e non accenna minimamente ad attività di ricerca.

Gli articoli 3 e 4 organizzano la didattica in un biennio fisico-matematico e un triennio di applicazione: schema che rimarrà felicemente in vigore sino alla fine del XX secolo, cioè fino all'emanazione del Decreto MURST 509/1999 ("tre più due"). Per l'immatricolazione, poi, era allora richiesta di regola la licenza liceale (D. R. 842/1862 – Regolamento Matteucci e D. R. 3434/1876 – Regolamento Coppino).

L'art. 5 definisce le cinque materie obbligatorie per il primo anno della Scuola, introducendo fra l'altro la Meccanica razionale e la Statica grafica, la prima delle quali è considerata dunque materia applicativa e non afferente al biennio fisico-matematico, come invece sarà in seguito. La presenza della Statica grafica evidenzia l'importanza che avevano allora per l'Ingegneria i metodi grafici.

L'art. 6 definisce i contenuti dei corsi del secondo e terzo anno, ma l'art. 8 precisa che tali contenuti – tutti obbligatori su piano nazionale – possono essere organizzati da ciascuna Scuola ripartendoli in vario modo fra i vari corsi di insegnamento; anche qui si sottolinea che deve essere esplicitamente prevista attività grafica; inoltre si considerano parte integrante della didattica anche i viaggi d'istruzione. La saggia raccomandazione che i professori s'intendano fra loro "intorno alla disposizione delle varie parti degli insegnamenti e alla coordinazione dei programmi … in modo che nessuna parte sia omessa e nessuna ripetuta" si affida ottimisticamente alla buona volontà dei docenti e alla diligenza del Direttore della Scuola.

1. Le Scuole di Applicazione hanno per fine di dare l'istruzione scientifica e tecnica necessaria a conseguire il Diploma d'Ingegnere civile e quello di Architetto.

2. Il Diploma d'Ingegnere civile **…** abilita **…** a dirigere costruzioni civili, rurali, stradali, idrauliche e meccaniche, **…**

3. Per essere ammesso ad una Scuola di Applicazione si richiede che il giovane, fatti almeno due anni di studio presso una Facoltà Universitaria di Scienze Fisiche, Matematiche e Naturali, abbia ottenuto la licenza Fisico-Matematica, ed i certificati di diligenza ai corsi di Mineralogia, di Geologia e di Disegno o di Ornato e di Architettura. …

4. Gli studi obbligatori pel conseguimento del Diploma d'Ingegnere civile o di Architetto durano tre anni almeno.

5. Nel primo di questi tre anni le materie d'obbligo per gli aspiranti ai due diplomi sono: la Meccanica razionale (con esercizi); la Geodesia teoretica (con esercizi); la Statica grafica (con disegno); le Applicazioni della geometria descrittiva (con disegno); la Chimica docimastica (con manipolazioni). **….**

6. Le materie d'obbligo del secondo e del terzo anno per gli aspiranti al Diploma d'Ingegnere civile sono: la Mineralogia e la Geologia applicate ai materiali da costruzione; la Geometria pratica; la **Meccanica applicata alle macchine**; la Meccanica applicata alle costruzioni; l'Idraulica pratica; le Macchine idrauliche; le Macchine agricole; le Macchine termiche; l'Architettura tecnica; le Costruzioni civili e rurali; le Fondazioni; i Ponti in muratura, in legno ed in ferro; le Strade ordinarie, le Strade ferrate e le Gallerie; le Costruzioni idrauliche ed i Lavori marittimi; l'Idraulica agricola e le bonificazioni; l'Economia rurale e l'Estimo rurale; la Fisica tecnica; le Materie giuridiche.

7. [L'art. 7 si riferisce al diploma di Architetto].

8. Le materie di cui agli articoli 6 e 7 possono essere aggruppate o suddivise variamente da scuola a scuola e da anno in anno, e saranno accompagnate da lavori grafici, da esercitazioni pratiche, da escursioni, da esperimenti e da ripetizioni.

Per cura del Direttore, verso la fine di ogni anno scolastico, i professori s'intenderanno fra loro intorno alla disposizione delle varie parti degli insegnamenti ed alla coordinazione dei programmi … in modo che nessuna parte sia omessa e nessuna ripetuta.

9. 10. [Gli articoli 9 e 10 riguardano dettagli secondari].

11. Alla fine dell'anno scolastico lo studente riceverà un certificato del profitto in ciascuna materia di studio. Col regolamento interno d'ogni singola scuola sarà determinato il modo d'accertare tale profitto ….

12. Lo studente che abbia conseguito il certificato di profitto in tutte le materie prescritte è ammesso ad un esame generale per ottenere il diploma. …

13. Chi non è approvato nell'esame generale non può ripresentarsi prima di un anno.

14. I giudizi sul merito … sono espressi da frazioni con denominatore *cento*. Per la sufficienza il numeratore deve essere almeno 60 nei certificati di profitto e almeno 70 nell'esame generale.

[I successivi articoli da 16 a 20 riguardano dettagli secondari].

Figura 2. Principali articoli del Regolamento generale delle Scuole di applicazione.

Gli articoli da 11 a 14 danno le direttive per la valutazione, lasciando qualche margine di libertà alle singole Scuole. In particolare, l'art. 14 prevede la votazione in centesimi, che a Bologna è stata utilizzata per il voto di laurea fino a tempi relativamente recenti.

3. LA SCUOLA DI INGEGNERIA DI BOLOGNA

Il regolamento interno della Scuola

La Fig. 3 riporta gli articoli più significativi del Regolamento interno della Scuola [10], dove sono precisati quei punti che il Regolamento generale lascia decidere alle singole scuole.

Dall'art. 5 si apprende che l'anno scolastico è diviso in trimestri, per ciascuno dei quali l'allievo riceve in ogni materia una valutazione, espressa in centesimi, che è la media delle valutazioni ottenute "in conferenze, in esercitazioni, e nel disegno": si deduce da qui che in aula i docenti interrogano e assegnano esercizi, attribuendo un voto alle risposte.

L'art. 6 descrive in dettaglio le condizioni per ottenere la promozione, mentre l'art. 7 precisa che "Le prove fallite alla fine dell'anno scolastico potranno essere riparate nel principio del successivo".

Molto indicativo è l'art. 9, con il quale il Direttore s'impegna a informare le famiglie del profitto e della diligenza degli allievi: soprattutto – viene fatto di pensare – dell'eventuale scarso profitto o della negligenza.

L'Annuario dell'Università di Bologna precisa poi che alla fine del terzo anno vi sarà un "Esame generale finale consistente nella completa redazione di un progetto pratico, e in

> 1. L'anno scolastico incomincia col 1° Ottobre di ogni anno, e dura 10 mesi.
>
> [Gli articoli 2, 3 e 4 riguardano argomenti organizzativi secondari].
>
> 5. Entro ogni trimestre, il merito ottenuto dagli allievi in conferenze, in esercitazioni, e nel disegno sarà a cura di ogni insegnante registrato in apposita tabella, la quale al termine del trimestre sarà consegnata alla Segreteria della Scuola.
>
> 6. Al termine dell'anno scolastico il Direttore della Scuola farà la media aritmetica delle medie trimestrali di ogni materia dell'anno, e l'allievo si riterrà promosso in tutte quelle materie nelle quali avrà conseguita una media non minore di 80/100. Gli allievi dovranno sostenere una conferenza finale in quelle materie per le quali la media annuale risulterà compresa fra 50/100 e 80/100 e per essere promossi dovranno riportare almeno 60/100. Nei casi in cui la media annua risulti minore di 50/100 si deciderà dal Direttore della Scuola in concorso dei Professori dell'anno di studio in cui è iscritto l'allievo se questi deve o no essere ammesso alla conferenza finale.
>
> 7. Le prove fallite alla fine dell'anno scolastico potranno essere riparate nel principio del successivo.
>
> 8. Nel corso dell'anno gli insegnanti della Scuola potranno accertare con appelli nominali la presenza degli allievi alle lezioni, al disegno, alle esercitazioni, ed agli esperimenti, ed informeranno il Direttore delle mancanze avvenute.
>
> 9. Il Direttore della Scuola informerà le famiglie degli allievi del loro profitto e della loro diligenza.
>
> [I successivi articoli 10 e 11 riguardano argomenti secondari].

Figura 3. Principali articoli del Regolamento interno della Scuola di applicazione di Bologna.

I ANNO	II ANNO	III ANNO
Applicazioni della geometria descrittiva Architettura tecnica Chimica docimastica Geodesia teoretica Geologia applicata Meccanica razionale Statica grafica	Economia ed estimo rurale Fisica tecnica Geometria pratica e celerimensura Materie giuridiche Meccanica applicata alle costruzioni **Meccanica applicata alle macchine**	Architettura tecnica Costruzioni stradali e ferroviarie Ferrovie Idraulica pratica Macchine termiche ed idrauliche Materiali da costruzione ed elementi delle fabbriche Ponti e costruzioni idrauliche

Figura 4. Ordine degli studi della Scuola di applicazione di Bologna per l'anno scolastico 1894-95.

una conferenza sul tema del progetto e sulle materie affini": qualcosa, quindi, di molto simile a una tesi di laurea.

Gli articoli da 5 a 9 configurano una scuola molto rigida, che per il nostro metro di valutazione è più simile a una scuola media – o, forse, a un'accademia militare – che a un'Università come la concepiamo ora. Questo giudizio è confermato anche dall'ordine degli studi, che sarà illustrato nel prossimo paragrafo.

L'ordine degli studi

La Fig. 4 riporta l'ordine degli studi per l'anno scolastico 1894-95. Sono presenti venti materie – forse sarebbe meglio dire venti esami – nelle quali sono trattati i contenuti previsti dagli articoli 5 e 6 del Regolamento generale delle Scuole di applicazione (Fig. 2).

L'ordine degli studi è rigido, non sono presenti né indirizzi né – tanto meno – corsi a scelta. Le materie presenti dovrebbero coprire l'intero campo dell'Ingegneria "civile", escludendo quindi solo l'Ingegneria militare e le Ingegnerie specialistiche, come la navale. In realtà, tutta quella che poi sarebbe stata chiamata "Ingegneria industriale" è assai poco presente, giacché l'unico settore rappresentato, e per la verità molto limitatamente, è quello meccanico, con i corsi di Meccanica applicata alle macchine e di Macchine termiche e idrauliche e – in parte – di Fisica tecnica (che introduce alcuni argomenti di Elettrotecnica) e di Ferrovie (che tratta principalmente del materiale rotabile e dell'esercizio delle ferrovie).

È lecito quindi affermare che l'ordine degli studi non appare adeguato ai tempi, in un periodo nel quale anche in Italia era in corso – in ritardo rispetto ai Paesi più avanzati, ma contemporaneamente o addirittura in anticipo rispetto a molti altri Paesi europei – un importante processo d'industrializzazione.

A questo proposito, appare indicativo che un decreto del 3 luglio 1879 istituisse nella Regia Scuola d'applicazione per gli ingegneri di Torino – e solo là – una nuova categoria di ingegneri, detti "industriali", precisando che il Diploma di Ingegnere Industriale "abilita chi l'ha ottenuto a dirigere l'impianto e l'esercizio di opifici industriali, strade ferrate, coltivazioni minerarie, costruzioni metalliche, idrauliche e meccaniche e a sostenere l'ufficio di Perito giudiziale sulle questioni relative." Un'esclusiva per Torino che forse non era del tutto giustificata. L'Ingegneria industriale fu poi introdotta a livello nazionale nel 1913, ma, come vedremo, arrivò a Bologna solo nel 1926-27.

L’orario di lezioni ed esercitazioni

La Fig. 5 riporta l’orario delle lezioni ed esercitazioni del II anno per l’anno scolastico 1894-95. L’orario prevede sette ore il giorno, per sei giorni la settimana, dalla mattina del lunedì alla sera del sabato. Il mattino ci sono tre ore di lezione, dalle 9 alle 12, e il pomeriggio quattro ore di esercitazioni e disegno, dalle 13 alle 17; in seguito l’orario del pomeriggio fu posticipato di un’ora, con due ore d’intervallo – dalle 12 alle 14 – fra lezioni ed esercitazioni.

Per gli altri anni di corso la distribuzione delle ore era analoga.

L’impegno di quarantadue ore settimanali può sembrare gravoso, ma riportato alla situazione generale del tempo non doveva sembrare tale a nessuno, nemmeno agli studenti. In quegli anni, infatti, l’orario di lavoro di un lavoratore dipendente era normalmente di “quattordici ore il giorno, compreso quel poco tempo di riposo pei pasti.” [11]. Anche i sei giorni la settimana dovevano apparire naturali: si tenga infatti presente che solo nel 1907 il governo Giolitti promulgò una legge (Legge 489/1907) che introduceva il riposo settimanale obbligatorio. Più precisamente, l’art. 1 stabiliva che “Gli imprenditori ed i direttori di aziende industriali e commerciali di qualunque genere debbono dare alle persone non appartenenti alla loro famiglia, comunque occupate nelle aziende stesse, un periodo di riposo non inferiore ad ore 24 consecutive per ogni settimana“, mentre l’art. 3 precisava che “Il riposo settimanale dovrà cadere normalmente di domenica, salvo le eccezioni stabilite negli articoli seguenti.”

	9 10	**10** 11	**11** 12		**13** 17
LUNEDÌ	Economia ed Estimo rurale	Fisica tecnica	**Meccanica applicata alle macchine**		**Meccanica applicata alle macchine Disegno ed esercizi**
MARTEDÌ	Meccanica applicata alle costruzioni	Materie giuridiche	Geometria pratica e celerimensura		Meccanica applicata alle costruzioni Disegno ed esercizi
MERCOLEDÌ	Meccanica applicata alle costruzioni	Fisica tecnica	**Meccanica applicata alle macchine**		Meccanica applicata alle costruzioni Disegno ed esercizi
GIOVEDÌ	Economia ed Estimo rurale	Materie giuridiche	**Meccanica applicata alle macchine**		**Meccanica applicata alle macchine Disegno ed esercizi**
VENERDÌ	Meccanica applicata alle costruzioni	Fisica tecnica	Geometria pratica e celerimensura		Meccanica applicata alle costruzioni Disegno ed esercizi
SABATO	Geometria pratica e celerimensura	Fisica tecnica	Geometria pratica e celerimensura		Disegno topografico

Figura 5. Orario del II anno della Scuola di applicazione di Bologna per l’a. s. 1894-95.

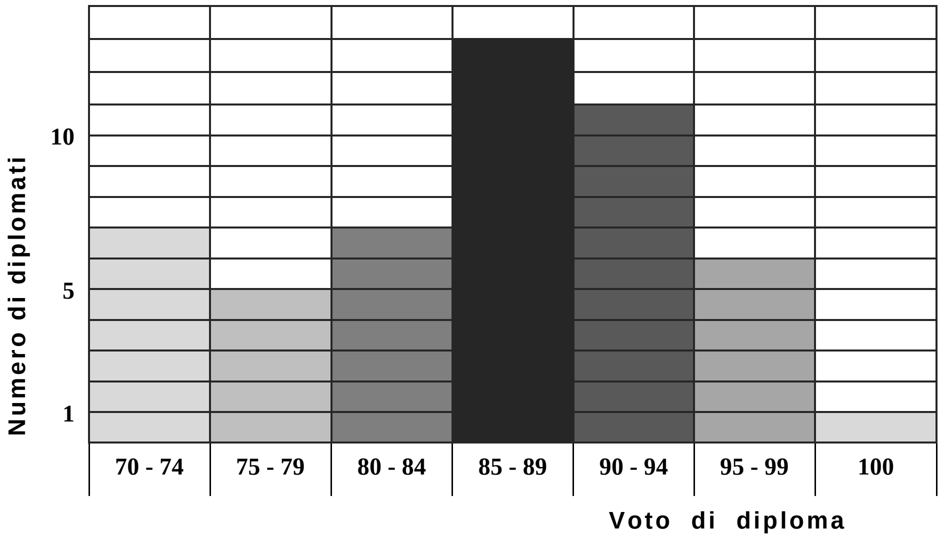

Figura 6. Votazioni riportate dai diplomati dell'anno scolastico 1894-95.

Gli studenti

Il numero di studenti variava sensibilmente da anno ad anno; nell'anno scolastico 1994-95 in numero complessivo degli iscritti ai tre anni era centotrentadue, tutti di sesso maschile.

I luoghi di nascita dei trentatré studenti che s'iscrissero nell'a. s. 1894-95 erano: Bologna 5, altre località dell'Emilia Romagna 15, altre regioni dell'Italia settentrionale 5, Italia centrale 4, Italia meridionale 4.

Le Università di provenienza erano: Bologna 17, Ferrara 5, Genova 3, Modena e Pisa 2, Milano, Parma e Roma 1, Accademia militare 1.

Dei cinquanta diplomati dell'anno scolastico 1894-95, due si diplomarono con 70/100, dieci con voti tra 72 e 76, quattro con 80, sedici fra 82 e 88, sei con 90, undici fra 92 e 97 e uno solo con 100/100, v. Fig. 6. La selezione era dunque piuttosto severa anche in termini di votazioni, coerentemente con l'organizzazione e gli scopi della Scuola.

Il corpo docente

Per l'anno scolastico 1894-95 il corpo docente del triennio di applicazione è composto di otto Ordinari – dei quali due appartenenti alla Facoltà di Scienze – tre Straordinari e dieci Assistenti. Vi sono poi nove incaricati, dei quali quattro sono ordinari o straordinari della Scuola o della Facoltà di Scienze, quattro sono assistenti della Scuola e uno è ordinario della Facoltà di Giurisprudenza.

Si osserva che è in sostanza rispettato il rapporto 1:1 fra Professori di ruolo e Assistenti, mentre non vi sono ruoli intermedi, giacché non possono considerarsi tali neppure gli assistenti con incarico d'insegnamento. Questa situazione – assenza di ruoli intermedi – rimase sostanzialmente invariata fino alla riforma introdotta con il DPR 382/1980.

4. ALTRI ASPETTI DELL'ORGANIZZAZIONE DELLA DIDATTICA

Lezioni ed esercitazioni

Le lezioni erano di regola impartite in tre ore settimanali, disposte in tre giorni distinti. Per alcuni corsi – come per es. per Materie giuridiche al II anno – le ore erano solo due, mentre per altri – come per Fisica tecnica, corso per il quale non erano peraltro previste esercitazioni – erano quattro.

Le ore pomeridiane prevedevano principalmente esercitazioni e disegno al I e al II anno, progetti (di Costruzioni stradali e ferroviarie, di Ponti e costruzioni idrauliche, di Architettura tecnica) al III anno. Per Chimica docimastica, al I anno, era prevista anche Analisi; infine a Macchine termiche e idrauliche, collocato al III anno, erano assegnate tre ore di lezione il mattino e quattro di esercitazioni in un pomeriggio.

Le lezioni in aula erano verosimilmente svolte con le usuali modalità "ex-cathedra", mentre si può presumere che le esercitazioni costituissero la vera ossatura portante della didattica. Venivano infatti svolti in aula – con la presenza di docenti – esercizi, applicazioni, disegni e progetti. Questo tipo di attività doveva favorire sia lo scambio di idee fra docenti e discenti, sia la collaborazione fra gli studenti, aprendoli all'attività di gruppo, fondamentale per laureati destinati per la maggior parte a coordinare e dirigere il lavoro di collaboratori e dipendenti.

Grande peso, come abbiamo visto, aveva il disegno, essenziale per ogni attività di progettazione, ma molto utile anche per familiarizzarsi con gli oggetti – componenti, utensili, strumenti, e quant'altro – di uso quotidiano nella futura attività professionale.

L'attività sperimentale appare invece molto limitata, sia per carenza di attrezzature adeguate, sia per l'impostazione generale degli studi. A questa mancanza si cercava di supplire, almeno in parte, con il disegno e con visite e viaggi di istruzione.

Escursioni e viaggi di istruzione

Escursioni e viaggi d'istruzione erano parte integrante della didattica della Scuola di applicazione per ingegneri.

L'annuario di ogni anno scolastico riporta la descrizione dettagliata delle escursioni, esercitazioni e viaggi d'istruzione dell'anno precedente. In Fig. 7 sono riportati in modo sommario i viaggi e le escursioni dei singoli corsi per l'a. s. 1894-95. È evidente la finalità didattica di queste iniziative, che vogliono portare gli allievi ad avere qualche contatto con il mondo reale riguardo agli argomenti che stanno studiando nelle aule e sui libri. Sicuramente l'efficacia di queste attività era legata anche al numero relativamente esiguo di studenti che vi partecipavano: gli iscritti a ciascun anno erano, infatti, solo poche decine.

Molto importante era anche il viaggio annuale d'istruzione, che in seguito sarà esplicitamente riservato ai laureandi. Il viaggio dell'a. s. 1894-95 durò undici giorni, dal 2 al 12 luglio 1895, ed è dettagliatamente descritto nell'Annuario della Scuola; ne riportiamo di seguito le tappe fondamentali. Giorno 1: Bologna – Brescia – Lovere. Giorno 2: Visita allo stabilimento siderurgico Gregorini e allo stabilimento Bonara per la fabbricazione della latta stagnata. Giorno 3: Visita al Museo Tadini o, in alternativa, ai lavori della costruenda centrale idroelettrica; nel pomeriggio, visita al cementificio di Palazzolo sull'Oglio e trasferimento a Bergamo. Giorno 4: Visita al ponte in ferro di Paderno d'Adda e trasferimento a Lecco. Giorno 5: Visita di Bellagio, trasferimento a Lugano e visita della funicolare a peso d'acqua. Giorno 6: Visita di una centrale idroelettrica in costruzione e di una ferrovia a cremagliera. Giorno 7: Viaggio sulla ferrovia del San Gottardo fino a Lucerna e a Berna.

Materia	Escursioni e Viaggi di istruzione a. s. 1894-95
Chimica docimastica	Tre escursioni: Officine Meccaniche Calzoni, Stazione ferroviaria, Officina del gas.
Costruzioni stradali	Studi di campagna e di tavolino per determinare il tracciato di due tronchi di strada ordinaria nei dintorni di Bologna.
Ferrovie e Macchine	Visite alla Stazione ferroviaria e annesse officine, ad un Mulino e alle Officine Meccaniche Calzoni.
Geologia applicata	Una escursione: Giacimento di cera minerale a Monte Falò e frana di Ciano nel Comune di Zocca.
Geometria pratica	Esercitazioni pratiche sull'uso degli strumenti e rilievi topografici nella città di Bologna e nei dintorni.
Meccanica applicata alle costruzioni	Diverse visite ai lavori per la ricostruzione del ponte sul Reno.

Figura 7. Escursioni e viaggi di istruzioni dell'anno scolastico 1894-95.

Giorno 8: A Berna, visita a diversi ponti, a impianti idroelettrici e di aria compressa, al Museo Nazionale, alla Cattedrale, a diversi palazzi, alla stazione ferroviaria, e trasferimento a Interlaken. Giorno 9: Visita ad alcune ferrovie di diverse tipologie. Giorno 10: Trasferimento a Lucerna e visita della ferrovia funicolare, quindi viaggio di ritorno per ferrovia, conclusosi il Giorno 11 alla stazione di Bologna. Presero parte al viaggio tre professori, un assistente effettivo, un assistente volontario, il tecnico della Scuola, undici allievi dell'ultimo anno e, solo per i primi sei giorni, tredici allievi del secondo anno, rientrati questi ultimi con un professore, due assistenti e il tecnico prima dell'ingresso della comitiva in Svizzera.

La durata e la complessità del viaggio ne illustra chiaramente l'intento, che non era solo quello di far conoscere alcune delle più recenti realizzazioni ingegneristiche di livello mondiale, ma anche quello di favorire – in un'epoca in cui i viaggi non erano così facili e comuni come ora – la maturazione culturale di giovani destinati in futuro a far parte della classe dirigente del Paese.

5. LE RIFORME DEL 1913 E 1926

La riforma del 1913

Il D. R. 6 settembre 1913 n. 1242 introdusse nelle Scuole d'applicazione alcune novità importanti. Innanzi tutto, stabiliva che esse hanno per fine di dare l'istruzione necessaria a conseguire il diploma di ingegnere civile e di ingegnere industriale; in secondo luogo, le materie sono distinte in fondamentali, che sono obbligatorie su piano nazionale, e facoltative, che sono invece determinate dai regolamenti delle singole scuole. Per passare da un anno a quello successivo l'allievo deve avere superato tutte le materie fondamentali, mentre il mancato superamento delle materie complementari non impedisce l'iscrizione all'anno successivo.

A Bologna continuano a essere attivate solo Ingegneria civile e Architettura. Le materie fondamentali previste per l'ingegneria industriale dal Decreto 1242 sono: Fisica tecnica (compresa la termodinamica), Meccanica applicata alle costruzioni, Meccanica applicata alle macchine (cinematica e dinamica applicate); Topografia e geodesia, Idraulica, Macchine termiche e idrauliche, Elettrotecnica generale (principi); Strade e ferrovie. L'ordinamento degli studi della Scuola di applicazione di Bologna era il seguente. Primo anno: Fisica tecnica, Meccanica applicata alle costruzioni, Meccanica applicata alle macchine, Chimica docimastica con esercizi, Statica grafica ed applicazioni di Geometria descrittiva, Geologia applicata ai materiali da costruzione. Secondo anno: Geometria pratica e Geodesia, Idraulica, Macchine termiche e idrauliche, Elettrotecnica generale, Architettura tecnica (biennale), Costruzioni civili, rurali e fondazioni. Terzo anno: Strade e ferrovie (costruzione ed esercizio), Architettura tecnica (biennale), Ingegneria legale; Ponti e Costruzioni idrauliche; Economia ed estimo rurale; Ingegneria sanitaria.

Come si vede, la Scuola di Bologna rimane ancora limitata all'Ingegneria civile, senza alcuna considerazione per i mutamenti intervenuti nel campo delle attività produttive: tutto considerato, un relativo regresso rispetto all'ordinamento del 1876.

INGEGNERIA CIVILE

I ANNO	II ANNO	III ANNO
Scienza delle costruzioni **Meccanica applicata alle macchine** Fisica tecnica Chimica applicata Materiali da costruzione, costruzioni civili ed industriali Mineralogia e geologia applicate Lingue straniere (corsi facoltativi)	Architettura tecnica (biennale) Geodesia e Topografia Idraulica Elettrotecnica Macchine termiche e idrauliche Materie giuridiche Lingue straniere (corsi facoltativi)	Ponti Costruzioni stradali e ferroviarie Architettura tecnica (biennale) Impianti elettrici e misure elettriche Ingegneria sanitaria Costruzioni idrauliche Esercizio e materiale ferroviario Elementi di agronomia – attuaria – estimo Lingue straniere (corsi facoltativi)

INGEGNERIA INDUSTRIALE

I ANNO	II ANNO	III ANNO
Scienza delle costruzioni **Meccanica applicata alle macchine** Fisica tecnica *Chimica analitica* *Chimica applicata* Materiali da costruzione, costruzioni civili ed industriali Mineralogia e geologia applicate *Lingue straniere (corsi facoltativi)*	Topografia Idraulica *Elettrotecnica generale* Macchine termiche e idrauliche *Tecnologia meccanica* *Costruzione di macchine* *Chimica industriale (biennale)* *Lingue straniere (corsi facoltativi)*	*Impianti industriali* Materie giuridiche (semestrale) *Economia e legislazione industriale (semestrale)* *Impianti elettrici e misure elettriche* Costruzioni idrauliche Esercizio e materiale ferroviario *Chimica industriale (biennale)* Ingegneria sanitaria *Lingue straniere (corsi facoltativi)*

Figura 8. Ordinamenti degli studi per ingegneria civile e per ingegneria industriale nell'a. s. 1926-27. In *corsivo* le discipline di nuova istituzione.

La riforma del 1926

Sulla base del Regolamento generale universitario approvato con R. D. 674/1924 e del decreto legge 25 settembre 1924, lo Statuto della Scuola d'ingegneria di Bologna fu modificato con D. M. 25 ottobre 1924 e in seguito aggiornato con D. M. 14 ottobre 1926. I nuovi statuti stabilivano che "La Regia Scuola d'Ingegneria di Bologna ha per fine di impartire l'istruzione scientifica e tecnica necessaria per conseguire la laurea in ingegneria civile, in ingegneria industriale e in architettura, nonché di contribuire al progresso degli studi nel campo della ingegneria."

Le novità, come si vede, sono importanti: viene introdotta la laurea in Ingegneria industriale e si menziona esplicitamente la ricerca scientifica come compito istituzionale della Scuola. Con la laurea in ingegneria industriale fanno la loro comparsa molte nuove discipline. In particolare, accanto alle confermate Meccanica applicata alle macchine e Macchine termiche e idrauliche, entrano nell'ordinamento anche le altre principali materie caratterizzanti dell'ingegneria meccanica: Tecnologia meccanica, Costruzione di macchine, Impianti industriali. Da notare pure il rilievo dato all'Elettrotecnica, presente con due corsi sia nell'ingegneria industriale sia nell'ingegneria civile, e la timida comparsa delle lingue straniere.

Lo schema generale dell'orario delle lezioni ed esercitazioni rimane invece molto simile a quello del 1894-95 (Fig. 9), con tre ore il mattino e quattro il pomeriggio, sempre per sei giorni la settimana.

La riforma del 1926 arriva praticamente in coincidenza con l'uscita del prof. Masi dall'Università: un'epoca è definitivamente tramontata e tutto il Paese è coinvolto in profondi sconvolgimenti. Il caso ha voluto che con il commiato di Francesco Masi incominciasse un'altra storia, che altri vorranno narrare.

	9 10	**10** 11	**11** 12		**14**	18
LUNEDÌ	Scienza delle costruzioni	Fisica tecnica	Chimica applicata		Geologia e mineralogia	Disegno di scienza delle costruzioni
MARTEDÌ	Meccanica applicata alle macchine	Scienza delle costruzioni	Esercizi di meccanica delle macchine		Disegno di meccanica applicata alle macchine	Esercizi di chimica applicata
MERCOLEDÌ	Scienza delle costruzioni	Fisica tecnica	Chimica applicata		Disegno di scienza delle costruzioni	Esercizi di fisica tecnica
GIOVEDÌ	Meccanica applicata alle macchine	Materiali da costruzione e costruzioni civili	Esercizi di meccanica delle macchine		Geologia e mineralogia	Disegno di meccanica applicata alle macchine
VENERDÌ	Materiali da costruzione e costruzioni civili	Geologia e mineralogia	Chimica applicata		Esercizi di fisica tecnica	Disegno di costruzioni civili
SABATO	Meccanica applicata alle macchine	Materiali da costruzione e costruzioni civili	Fisica tecnica		Materiali da costruzione e costruzioni civili	Esercizi di chimica applicata

Figura 9. Orario del I anno del corso di ingegneria industriale della Scuola di applicazione di Bologna per l'a. s. 1926-27.

6. CONCLUSIONI

Si è esaminata l'organizzazione generale della didattica nella Scuola di applicazione per ingegneri di Bologna durante il periodo della docenza del Prof. Masi (1891-1927), seguendo per sommi capi l'evoluzione della Scuola, dalla nascita alla trasformazione in Facoltà universitaria.

L'esame svolto ha permesso di rilevare alcune caratteristiche positive di tale organizzazione, quali l'alto rapporto numerico docenti/studenti e le molte ore di didattica assistita, costituita, quest'ultima, dalle ventiquattro ore settimanali di esercitazioni e disegno in aula con la presenza di docenti. Alla cronica carenza di attività sperimentale, legata all'assenza di laboratori ma attribuibile anche a un generale atteggiamento culturale, si cercava di rimediare con le molte ore dedicate al disegno e con visite e viaggi d'istruzione, mentre alcuni professori – tra i quali lo stesso Masi – s'impegnavano per introdurre qualche attività sperimentale almeno nelle esercitazioni [2].

Il giudizio più negativo sull'Università ai tempi di Masi non riguarda tanto la didattica in sé, quanto il fatto che l'Università fosse in pratica riservata alle classi abbienti, ciò che va però imputato alla situazione sociale di allora; si deve peraltro riconoscere che l'Università aveva se non altro il merito di consentire, ai pochi che vi accedevano da famiglie economicamente disagiate, di trovare nel titolo di studio l'ascensore sociale che gli permetteva di uscire dal loro stato. Analogo discorso si può fare a proposito della mancanza di studenti di sesso femminile: coerente, anche in questo caso, con la situazione generale della società.

Per quanto riguarda l'organizzazione didattica in senso stretto, è interessante seguirne l'evoluzione: da un ordine degli studi assolutamente rigido e indirizzato esclusivamente alla formazione dell'ingegnere civile, si passa progressivamente – nel corso della quasi quarantennale militanza professorale di Francesco Masi – a un ordinamento ancora piuttosto rigido, ma molto più aperto e adeguato alle nuove necessità e prospettive del Paese.

Guardando in prospettiva i cambiamenti e le riforme, pare di dover riconoscere che nel complesso questi si sono mossi nella giusta direzione, come imponeva peraltro quanto avveniva nel mondo esterno; non però con l'ambizione e la capacità di produrre o almeno anticipare la trasformazione del mondo stesso: ambizione coltivata da pochi [9] [12], ma sempre frustrata dalla realtà dei fatti.

È facile immaginare che non tutte le innovazioni siano state apprezzate nel momento in cui furono introdotte – chi, avendo vissuto nell'Università gli ultimi decenni, non ha sentito sentenziare a ogni riforma che la riforma stessa aveva decretato "la fine dell'Università"? – e certamente molte di esse si dimostrarono in seguito poco adeguate o addirittura controproducenti; ma dall'esame della situazione del 1894 appare certo che senza riforme, oggi la Scuola di Ingegneria sarebbe davvero scomparsa, perdendo ogni ragione di essere. Se è vero che ogni riforma porta a perdere qualcosa di buono, è dunque opportuno tenere sempre presente la saggia osservazione che "… la cagione della trista e della buona fortuna degli uomini è riscontrare il modo del procedere suo con i tempi." [13]. Questo è forse l'insegnamento più importante che si possa trarre dall'analisi svolta in questo lavoro: è doveroso accogliere sempre con atteggiamento critico ogni innovazione, ma è altrettanto necessario avere presente che il rinnovamento è indispensabile; chi, infatti, può ritenere che l'organizzazione della didattica vigente nel 1894 sarebbe oggi ancora accettabile?

In questo lavoro non si è toccato l'argomento più importante riguardo la didattica, cioè i contenuti della didattica stessa. L'argomento esula, infatti, dai limiti che ci siamo qui proposti; una breve trattazione – con riferimento alla Meccanica applicata alle macchine – si può trovare in [1], [3], [14].

RIFERIMENTI

[1] Ceccarelli, M., 2012. “Attività e influenza di Francesco Masi in Italia alla fine del XIX secolo”. In: *Scienza e Tecnica nel Settecento e nell’Ottocento,* a cura di E. Mesini e D. Mirri , 467–492.

[2] Ceccarelli, M., Molari, P. G., 2016. “Come insegnare la meccanica. Il metodo di Francesco Masi all’Università di Bologna e all’Istituto Aldini Valeriani”. *Rivista Scuola Officina,* n. 2/2016. Bologna, Museo del Patrimonio Industrale.

[3] Meneghetti, U., 2016. “L’insegnamento della Meccanica applicata alle macchine nell’Università di Bologna”. Conferenza tenuta presso la Scuola di Ingegneria e Architettura dell’Alma Mater Studiorum - Università di Bologna, http//www.biblioteche.unibo.it/ingegneria/risorse-disciplinari/relazioni-delle-conferenze-della-scuola-di-ingegneria-e-architettura

[4] “Regolamento per l’abilitazione alle professioni di Perito, Architetto, ed Ingegnere Civile”, 1882. In: *Collezione di pubbliche disposizioni emanate in seguito al moto proprio di N. S. Papa Pio Settimo sulla organizzazione dell’amministrazione pubblica,* Tomo V. Roma, presso Vincenzo Poggioli.

[5] Venturoli, G., 1806-1807. *Elementi di Meccanica e d’Idraulica*. A questa prima edizione ne seguirono altre, anche dopo la morte dell’Autore. La quinta edizione del I volume “Meccanica” è reperibile in https://books.google.it/

[6] Di Fidio, M., Gandolfi, C., 2014. “Giuseppe Venturoli”. In: *Idraulici italiani*. Milano, Fondazione Biblioteca Europea di Informazione e Cultura.

[7] Diotallevi, P.P., 2012. “Una Facoltà tra due Scuole. La Facoltà di Ingegneria dell’Università di Bologna (1935-2012)”. In: *Scienza e Tecnica nel Settecento e nell’Ottocento,* a cura di E. Mesini e D. Mirri , 573–596.

[8] Calcagno, G.C., 1997. “La Scuola per gli ingegneri dell'Università di Bologna tra Otto e Novecento”**.** In: *Annali di Storia delle Università italiane*, Volume 1.

[9] Molari, G., 2012. “Quirico Filopanti professore di meccanica applicata”. In: *Scienza e Tecnica nel Settecento e nell’Ottocento,* a cura di E. Mesini e D. Mirri , 493–518.

[10] www.biblioteche.unibo.it/ingegneria/informazioni/storia-e-collezioni/fonti-per-la-storia-della-facolta/pdf-annuari/Annuario1894-95

[11] Masi, F., 1880. “Il canepificio della Canonica presso Bologna”. *Il politecnico. Giornale del l’ingegnere architetto civile ed industriale,* 644-657.

[12] Filopanti, Q., 1866. *Intorno alla necessità ed ai mezzi di promuovere l’industria meccanica in Italia*. Bologna, Tipografia del Giornale d’Agricoltura del Regno d’Italia.

[13] Machiavelli N., 1531. *Discorsi sopra la prima deca di Tito Livio,* III, 9.

[14] Ceccarelli, M., 2014. “Breve storia della Meccanica applicata alle macchine in Italia”. Atti del V Congresso Italiano di Storia dell’Ingegneria, 87-102. ISBN 978-88-87479-80-5.

START-UP AND CESSATION OF AXISYMMETRIC FLOW OF A BINGHAM FLUID

Irene Daprà
Department of Civil, Chemical, Environmental and Materials Engineering
University of Bologna, Italy
E-mail: irene.dapra@unibo.it

Gianbattista Scarpi
Department of Civil, Chemical, Environmental and Materials Engineering
University of Bologna, Italy
E-mail: giambattista.scarpi@unibo.it

***Abstract**. This paper investigates numerically the start-up and the cessation of the flow of a viscoplastic fluid in a circular pipe. The rheological behaviour of the fluid has been regularised using two different relations: that of Papanastasiou and a new model proposed by the authors, based on the error function erf. The results obtained using the two different models are compared.*

***Keywords**: Bingham fluid, unsteady Poiseuille flow, start-up and cessation of flow*

1. INTRODUCTION

Viscoplastic fluids, such as Bingham fluids, require the application of a greater shear stress than a critical value, the yield stress, to begin to move. After yielding, the rheological behaviour is that of a Newtonian fluid, while in the core region the material moves as a solid body. The beginning and the cessation of motion are classical problems in fluid dynamics, whose analytical solution is well known for Newtonian fluids. The most relevant characteristic of the unsteady flow for a Bingham fluid is the fact that its stopping time is finite, whereas Newtonian fluids and generally any fluid without yield stress need an infinite time to reduce to zero the velocity. Glowinski [1-2] and Huilgol et al. [3] gave a theoretical upper bound for the stopping time. Chatzimina et al. [4] study numerically the cessation of the Couette and Poiseuille flow for a Bingham fluid using the Papanastasiou regularised model comparing the numerical results with the theoretical predictions.

The discontinuity in the constitutive equation at zero shear rate introduces severe difficulties for analytical and even for numerical solution. To overcome that, Glowinski et al. [5] suggested to regularise the constitutive equation, substituting the discontinuous function with a continuous one, which, as a given parameter tends to a proper limit, usually zero or infinity, tends (at least in the sense of distributions theory) to the true Bingham law. Proposals to regularise have been made in the past either using bi-viscous or multi-viscous models (i.e. using function with piecewise continuous derivative), or smooth functions with at least a continuous first derivative. Among these, the most used in literature are that of Bercovier and Engleman [6] and, very frequently, that proposed by Papanastasiou [7]. A complete analysis of advantages and disadvantages of regularised models with exhaustive references is given by Frigaard & Nouar [8].

In this paper we employ a regularizing law (Erf) based on the error function and compare the numerical results obtained using Papanastasiou and Erf models for the simulation of the Poiseuille axisymmetric flow of a Bingham fluid.

2. CONSTITUTIVE EQUATIONS

The constitutive equation of a Bingham fluid is

$$\begin{cases} \dot{\boldsymbol{\gamma}} = 0 & \tau \le \tau_0 \\ \mathbf{T} = \left(\dfrac{\tau_0}{\dot{\gamma}} + \mu \right) \dot{\boldsymbol{\gamma}} & \tau \ge \tau_0 \end{cases} \tag{1}$$

where $\mathbf{v}$, $\mathbf{T}$ and $\dot{\boldsymbol{\gamma}}$ are the velocity vector, the stress tensor and the rate of strain tensor, τ_0 is the yield stress, μ the fluid viscosity, $\dot{\gamma}$ the magnitude of $\dot{\boldsymbol{\gamma}}$, $\dot{\gamma} = \sqrt{\frac{1}{2} \dot{\boldsymbol{\gamma}} : \dot{\boldsymbol{\gamma}}}$. The discontinuity in Eqn. (1) complicates the analytical and the numerical solution of any problem, even in simple cases. In the past many models have been proposed, which substitute Eqn. (1) with a continuous function; there are several possible choices to approximate it, which corresponds to suitable approximations of the unit step function (or of its derivative, the Dirac δ-function). Quite simple algebraic models have been proposed (e.g. Allouche et al. [9], Frigaard & Scherzer [10]), or more complicated ones, involving exponential functions: in 1987 Papanastasiou proposed the following equation

$$\mathbf{T} = \left[\frac{\tau_0 \left[1 - \exp\left(-m\dot{\gamma} \right) \right]}{\dot{\gamma}} + \mu \right] \dot{\boldsymbol{\gamma}} \tag{2}$$

which as the parameter $m \to \infty$, tends (in the sense of distributions) to the Bingham law.

We propose the following model (Erf) which is continuous and infinitely derivable everywhere:

$$\mathbf{T} = \left[\frac{\tau_0}{\dot{\gamma}} \operatorname{erf}\left(k\dot{\gamma} \right) + \mu \right] \dot{\boldsymbol{\gamma}} \tag{3}$$

where, as usual,

$$\operatorname{erf}\left(x \right) = \frac{2}{\sqrt{\pi}} \int_0^x e^{-t^2} dt \tag{4}$$

is the error function.

Many analytical solutions of steady motion of Bingham fluids in different geometries are known, whereas, for unsteady motion, the only one is probably that given by Sekimoto [11] for a simple shear flow with velocity field $v = v\left(y,t \right)$, in the semi-infinite region $y \ge 0$. The availability of this closed solution is very important to test the numerical results obtained using regularizing constitutive equations. In a previous paper Daprà & Scarpi [12] solved numerically the same problem of Sekimoto using the Papanastasiou and the Erf models and compared the numerical results with the closed analytical solution. The obtained results show that the difference between analytical and numerical solution in the yielded region are of an order of magnitude smaller than in the unyielded region. The analysis in the unyielded zone emphasizes that the errors decrease increasing the value of the regularization parameters. The Erf model approximates both velocity and shear stress better than the Papanastasiou model; the difference between the results of the two models tends obviously to vanish increasing the value of the regularization parameters.

3. AXISYMMETRIC POISEUILLE FLOW

The momentum equation in axial direction can be written as

$$-\frac{\partial p}{\partial x}+\frac{1}{r}\frac{\partial(r\tau)}{\partial r}=\rho\frac{\partial u}{\partial t} \tag{5}$$

where x is the direction of the motion, r the radial coordinate, p the pressure, $\tau=\tau_{xr}$ the shear stress, u the velocity, ρ the fluid density and t the time.

Introducing the following dimensionless quantities $\eta=r/R$, $v=u/V$, $P=-\frac{\partial p}{\partial x}\frac{R^2}{\mu V}$, $\theta=\tau R/\mu V$, $T=t\mu/\rho R^2$, where V is the mean velocity, Eqn. (5) becomes

$$P+\frac{1}{\eta}\frac{\partial(\eta\theta)}{\partial\eta}=\frac{\partial v}{\partial T} \tag{6}$$

If $P=const$ we obtain the steady-state velocity

$$v(\eta,0)=\begin{cases}\frac{P}{4}(1-\eta_0)^2 & 0\le\eta\le\eta_0\\ \frac{P}{4}(1-\eta^2)-Bn(1-\eta) & \eta_0\le\eta\le 1\end{cases} \tag{7}$$

where $Bn=\tau_0 R/\mu V$ is the Bingham number, which corresponds to the dimensionless yield stress, and $\eta_0=\frac{R_0}{R}$ is the dimensionless radius of the unyielded core, which is related to the Bingham number by the relation (plotted in Fig. 1)

$$Bn=\frac{12\eta_0}{\eta_0^4-4\eta_0+3} \tag{8}$$

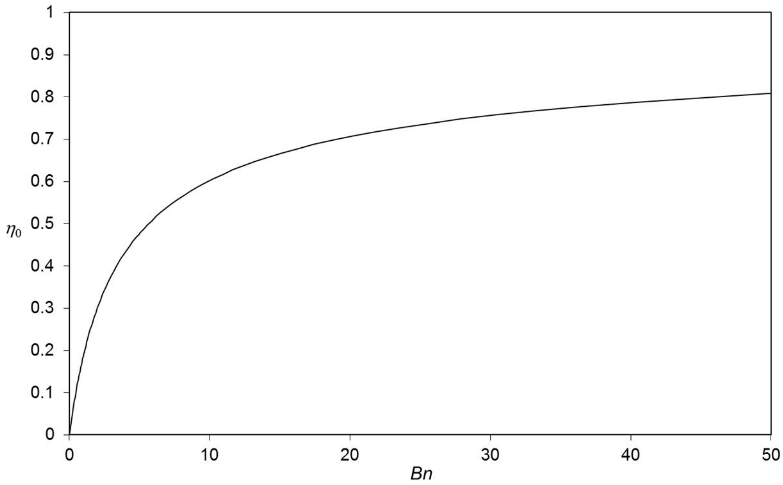

Figure 1. Plug radius versus Bingham number for a steady pipe flow.

The dimensionless regularizing equations for axial flow become respectively, being $\dot{\gamma} = \dfrac{\partial v}{\partial \eta}$

$$\theta = Bn\left[1 - \exp\left(-M\left|\dot{\gamma}\right|\right)\right]\frac{\dot{\gamma}}{\left|\dot{\gamma}\right|} + \dot{\gamma} \tag{9}$$

$$\theta = Bn\,\mathrm{erf}\left(K\dot{\gamma}\right) + \dot{\gamma} \tag{10}$$

where, $M = mV / R$, and $K = kV / R$.

To compare the two models, the values of the regularization parameters M and K are assigned in such a way that the tangent viscosity at zero shear stress, i.e. $\left.\dfrac{d\theta}{d\dot{\gamma}}\right|_{\dot{\gamma}=0}$, is the same; as a consequence

$$M = \frac{2K}{\sqrt{\pi}} \tag{11}$$

Figure 2 illustrates Eqns. (9) and (10), whereas in Fig. 3 the tangent viscosity $d\theta / d\dot{\gamma}$ is shown.

Substituting Eqns. (9) and (10) in (6) we obtain the following equations:

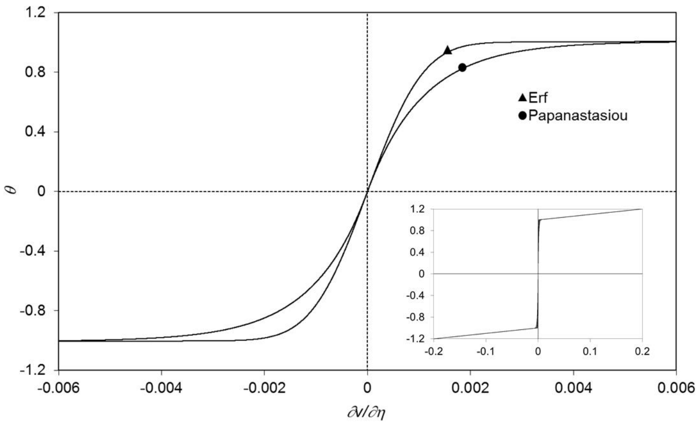

Figure 2. Regularized shear stress versus shear rate ($Bn = 1$, $K = 800$, $M = 903$). The figure is a distorted enlargement near (0,0) of the smaller diagram.

Papanastasiou:

$$P + \left[1 + MBn\exp\left(-M\left|\frac{\partial v}{\partial \eta}\right|\right)\right]\frac{\partial^2 v}{\partial \eta^2} + \frac{1}{\eta}\left[Bn\left(1 - \exp\left(-M\left|\frac{\partial v}{\partial \eta}\right|\right)\right)\mathrm{sgn}\left(\frac{\partial v}{\partial \eta}\right) + \frac{\partial v}{\partial \eta}\right] = \frac{\partial v}{\partial T} \quad (12)$$

Erf:

$$P + \left[\frac{2KBn}{\sqrt{\pi}}\exp\left(-\left(K\frac{\partial v}{\partial \eta}\right)^2\right) + 1\right]\frac{\partial^2 v}{\partial \eta^2} + \frac{1}{\eta}\left[\frac{\partial v}{\partial \eta} + Bn\,\mathrm{erf}\left(K\frac{\partial v}{\partial \eta}\right)\right] = \frac{\partial v}{\partial T} \quad (13)$$

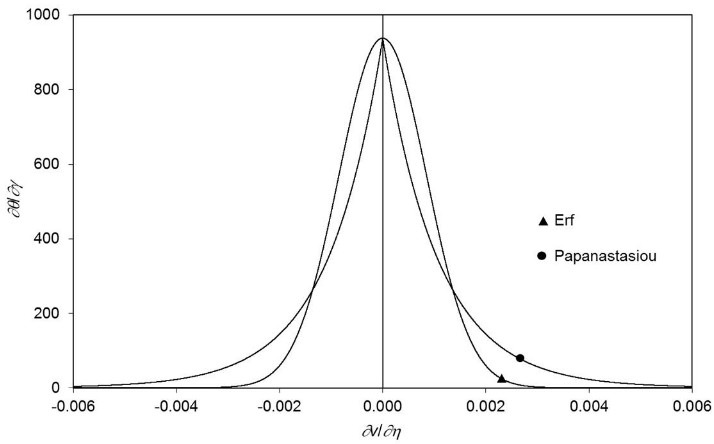

Figure 3. Tangent viscosity versus shear rate for regularized models.

4. START UP: NUMERICAL SOLUTIONS

We analyse numerically the start-up of the axisymmetric Poiseuille flow as a constant pressure gradient P is suddenly applied to the fluid at rest.

Initial and boundary conditions are respectively:

$$v(\eta, T \leq 0) = 0 \qquad 0 \leq \eta \leq 1 \tag{14}$$

$$v(1, T) = 0 \qquad \forall\, T \tag{15}$$

Numerical results

The numerical solution of Eqn. (12) and (13) is calculated via an implicit finite-difference method: being $\theta = f(\dot{\gamma})$ and $v_j^n = v(\eta_j, T_n)$, the discretized equation becomes

$$P^n + \frac{df}{d\dot{\gamma}} \frac{v_{j+1}^{n+1} + v_{j+1}^n - 2v_j^{n+1} - 2v_j^n + v_{j-1}^{n+1} + v_{j-1}^n}{2\Delta\eta^2} + \frac{f(\dot{\gamma})}{\eta_j} = \frac{v_j^{n+1} - v_j^n}{\Delta T} \tag{16}$$

where $\dot{\gamma} = \dfrac{v_{j+1}^n - v_{j-1}^n}{2\Delta\eta}$.

The numerical procedure has been first validated for a Newtonian fluid, for which the analytical results are well known. Numerical experiments indicated that the maximum value for parameter M in order to obtain valid results can be evaluated as

$$M \approx 5000 \frac{\eta_0}{Bn} \tag{17}$$

If M exceeds this value, the numerical procedure can exhibit instabilities. The corresponding value of the parameter, K is evaluated using (11); Figure 4 shows the parameters as a function of Bn as given by eq. (11).

We adopted a uniform spatial grid of 2000 points, i.e. $\Delta\eta = 0.5 \cdot 10^{-3}$ and a time step $\Delta T = 10^{-7}$.

A smaller value of $\Delta\eta$ or ΔT gives the same results, whereas greater ΔT generates instabilities. The difference between the steady-state velocity profiles obtained with the two models and the theoretical one for a true Bingham fluid are always less than 1%. The results show that the tested models are equally suitable: they practically give the same diagram of the solid plug velocity as function of time. The percent difference between the values given by the two models is less than 1%. Figure 5 shows the results for $Bn = 5$. Figure 6 illustrates the theoretical steady velocity profile for the used models and for a Bingham fluid, when $Bn = 10$: the greatest difference, 0.76%, is obtained using the Papanastasiou model.

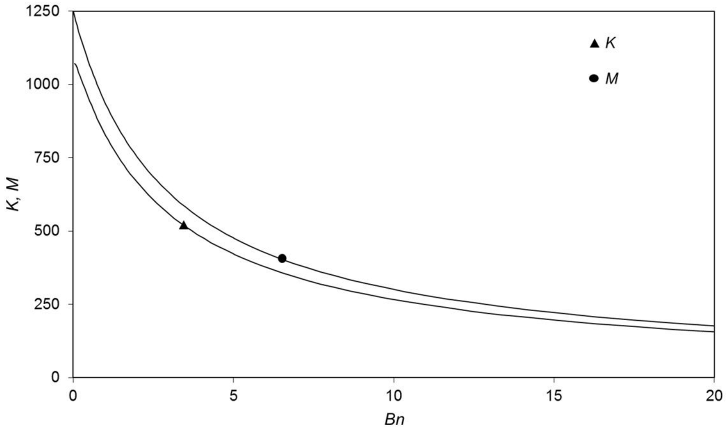

Figure 4. Regularization parameters versus Bingham number for numerical calculation.

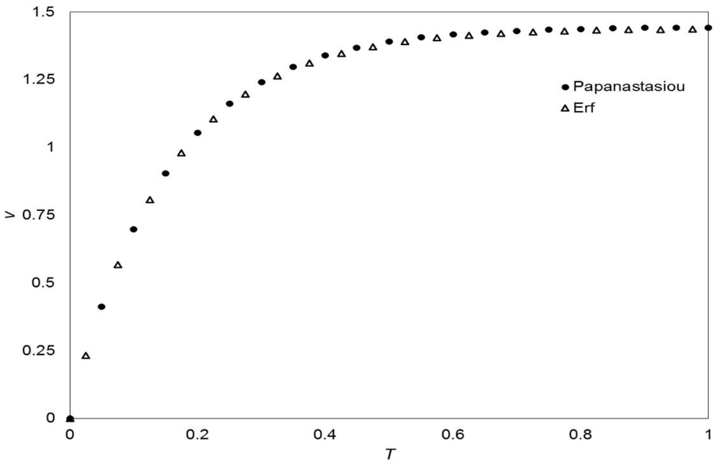

Figure 5. Start-up: plug velocity versus time. The results obtained with the different models are almost indistinguishable $(Bn = 5,\ K = 400)$.

5. CESSATION OF FLOW

Starting from a steady state condition, the constant pressure gradient P applied to the fluid is suddenly cancelled at $T = 0$.

The boundary condition at the wall is the same as for start-up

$$v(1,T) = 0 \qquad \forall\, T \tag{18}$$

whereas the conditions at $T = 0$ are now given by Eqn. (7).

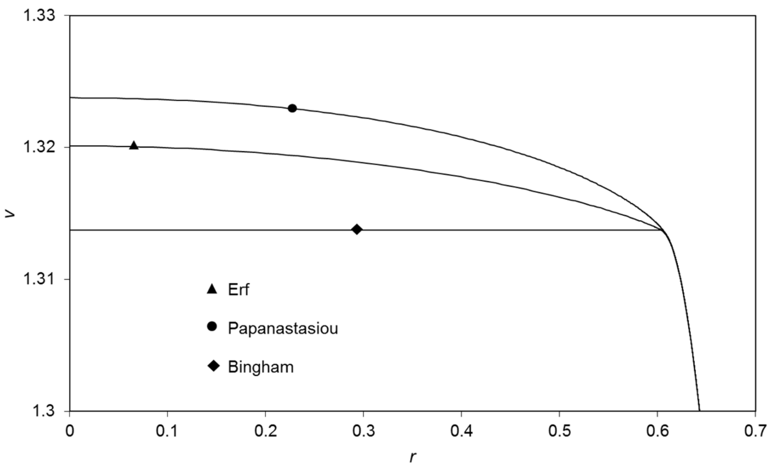

Figure 6. Detail of the steady velocity profiles for $Bn = 10$ and $K = 250$.

Numerical solution

As for the start-up the numerical solution is calculated via an implicit finite-difference method: being $\theta = f\left(\dot{\gamma}\right)$ and $v_j^n = v\left(\eta_j, T_n\right)$ the discretized equation becomes

$$\frac{df}{d\dot{\gamma}} \frac{v_{j+1}^{n+1} + v_{j+1}^{n} - 2v_j^{n+1} - 2v_j^n + v_{j-1}^{n+1} + v_{j-1}^{n}}{2\Delta\eta^2} + \frac{f\left(\dot{\gamma}\right)}{\eta_j} = \frac{v_j^{n+1} - v_j^n}{\Delta T} \tag{19}$$

where again $\dot{\gamma} = \dfrac{v_{j+1}^n - v_{j-1}^n}{2\Delta\eta}$.

The solution has been carried out with a spatial uniform grid of 400 points i.e. $\Delta\eta = 2.5 \cdot 10^{-3}$: using a finer grid does not produce appreciable effects on the results. The time step ΔT has been fixed at $5 \cdot 10^{-8}$, for both models and for all values of Bn. Such a value allows to have a good description of the evolution of velocity even for great Bingham numbers, as the stopping time becomes very small.

Unlike what happens for start-up, the behaviour of the two models is quite different. Figures 7 and 8 show the velocity profiles at different times, each for a given Bingham number. The initial steady state profile is that of a true Bingham fluid. For both models the velocity profiles show a small unyielded region near the wall (where the stress should be greater) which (as already observed in Chatzimina et al. [4]) has no physical explanation. This region is better shown in Fig. 9 which is an enlargement of Fig. 8, and becomes more evident for increasing Bingham numbers; it seems not to appear in plane motion, and to arise both from geometrical and numerical reasons.

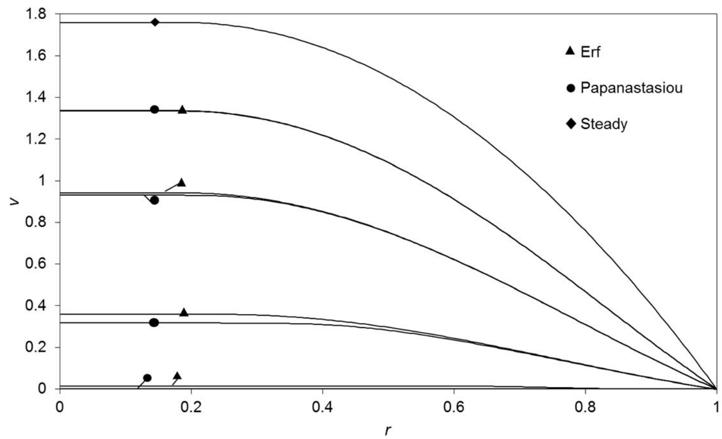

Figure 7. Cessation of flow: velocity profiles for $Bn = 1$, $K = 800$ at T=0.04, 0.08, 0.16, 0.24.

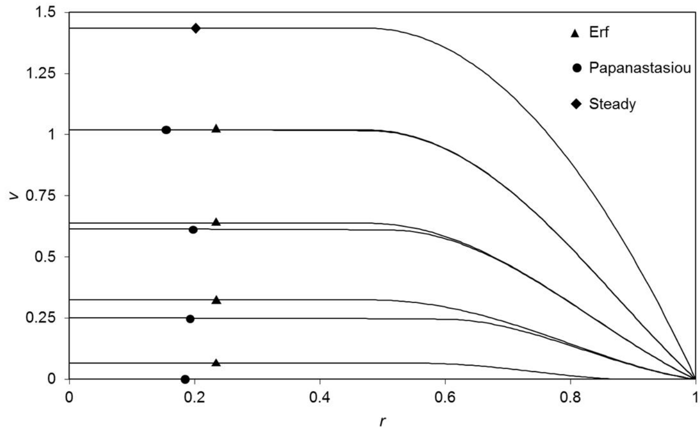

Figure 8. Velocity profiles for $Bn = 5$, $K = 400$ at T=0.02, 0.04, 0.06, 0.08.

Figures 10 and 11 show the flow rate as function of time for the tested models when $Bn = 1$ and $Bn = 5$ respectively. The Papanastasiou model, which for small Bingham numbers behaves like Erf, becomes quite different for increasing Bn and needs a smaller time to stop.

Figure 12 shows the rate of flow as function of time at different Bingham numbers. As expected, the rate of flow decreases the more rapidly the greater Bn is.

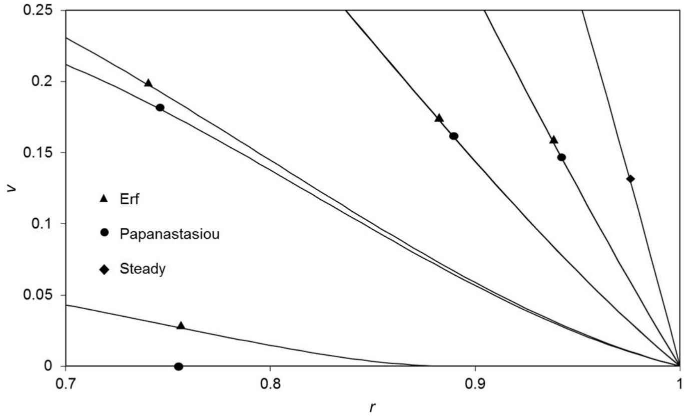

Figure 9. Enlargement of Fig. 8, which emphasizes the anomalous unyielded region near the wall.

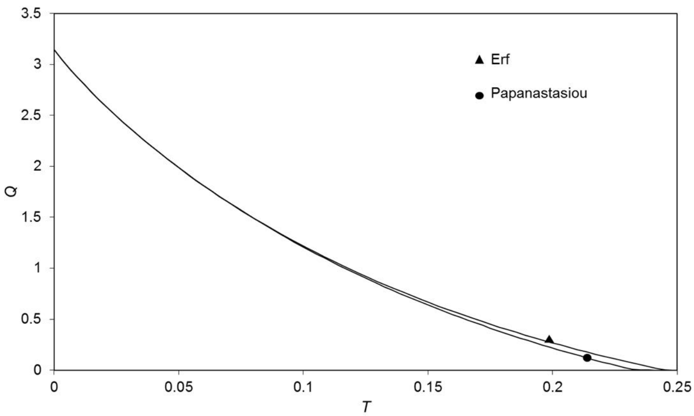

Figure 10. Rate of flow versus time, for $Bn = 1$, $K = 800$.

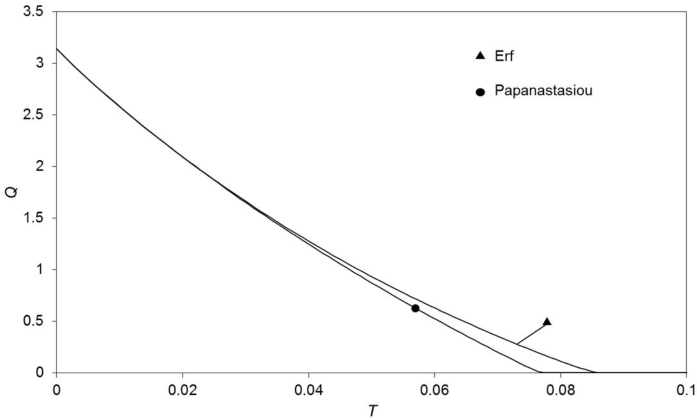

Figure 11. Rate of flow versus time, for $Bn = 5$, $K = 400$.

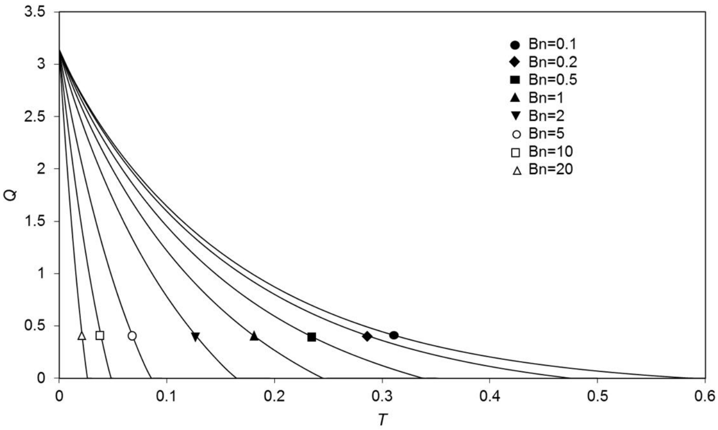

Figure 12. Erf model: cessation of flow. Rate of flow versus time for several *Bn*.

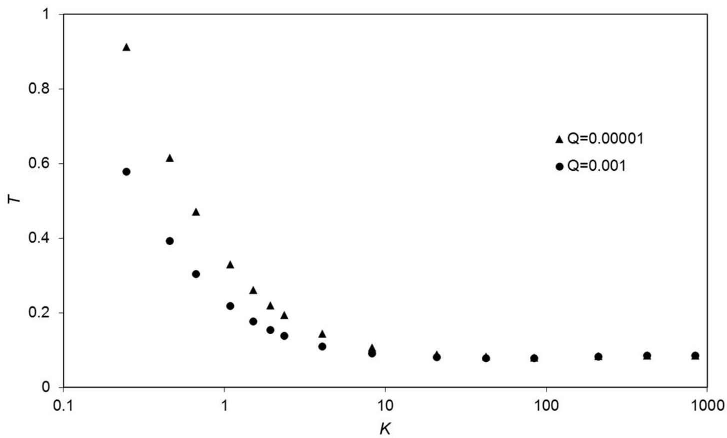

Figure 13. Erf model: cessation of flow. Stopping time versus parameter *K* for $Bn = 5$.

Figure 13 points out the influence of the parameter *K* on the cessation time T_f : if $Bn = 5$ and $K > 50$, T_f does not depend on *K*. The stopping times are evaluated when the discharge is reduced to 10^{-3} and 10^{-5} respectively. Fig. 14 shows the time needed to reduce the rate of flow to 10^{-2} and 10^{-3} respectively, as function of Bn . The difference between the two values of time becomes appreciable only if $Bn < 0.1$. Finally, Fig. 15 emphasizes (for the Erf model) the strong agreement between the calculated stopping time and the theoretical upper bound given by Glowinski [2] for a large range of Bn .

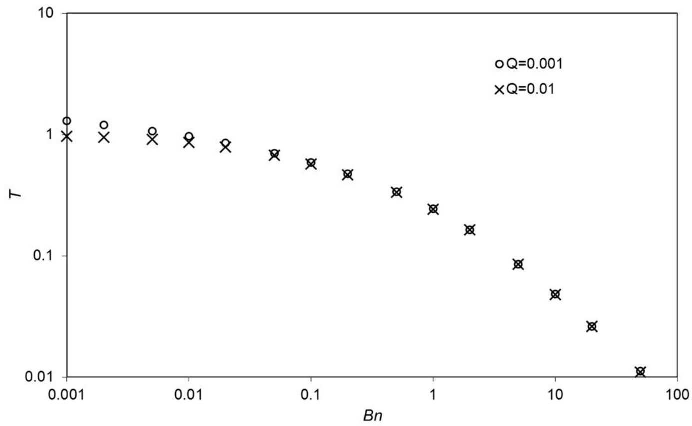

Figure 14. Erf model: stopping time versus *Bn*.

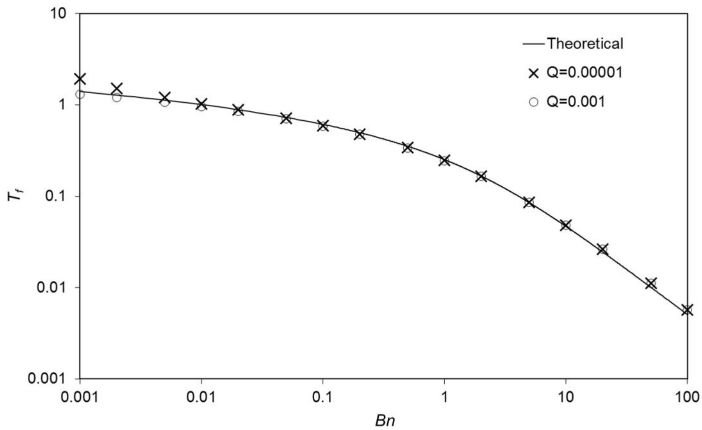

Figure 15. Erf model: theoretical upper bound and numerical stopping time versus *Bn*.

6. CONCLUSIONS

The start-up and the cessation of flow for a viscoplastic fluid have been examined numerically using two different regularizing models: Papanastasiou and Erf. The results have been obtained with an implicit finite difference method and show that the models are practically equivalent for the start-up problem. For the cessation of motion however, there are appreciable differences, particularly for the determination of the stopping time.

The stopping time given by the Papanastasiou model is smaller as that of the Erf model. The optimal value of the regularisation parameter has been determined evaluating its influence on the stopping time.

The stopping time for the Erf model has been evaluated as function of the Bingham number, emphasizing the very strong agreement between the numerical results and the theoretical upper limit given by Glowinski.

REFERENCES

[1] Glowinski, R., 1984. *Numerical methods for nonlinear variational problems*. Springer-Verlag.

[2] Glowinski, R., 1974. "Sur l'écoulement d'un fluide de Bingham dans une conduite cylindrique". *J. de Méc.*, **13** (4), pp. 601-621.

[3] Huilgol, R.R., Mena, B., Piau, J.M., 2002. "Finite stopping time problems and rheometry of Bingham fluids". *J. Non-Newtonian Fluid Mech*., **102** (1), pp. 97-107.

[4] Chatzimina, M., Georgiou, J.C., Argyropaidas, I., Mitsoulis, E., Huilgol, R.R., 2005. "Cessation of Couette and Poiseuille flows of a Bingham plastic and finite stopping times". *J. Non-Newtonian Fluid Mech*., **129** (3), pp. 117-127.

[5] Glowinski, R., Lions, JL., Trémolières, R., 1981. *Numerical analysis of variational inequalities*. North-Holland.

[6] Bercovier, M., Engleman, M., 1980. "A finite-element method for incompressible non-Newtonian flows". *J. Comp. Phys,* **36** (3), pp. 313-326.

[7] Papanastasiou, T.C., 1987. "Flows of materials with yield", *J. Rheol*., **31** (5), pp. 385-404.

[8] Frigaard, I.A., Nouar, C., "On the usage of viscosity regularisation methods for visco-plastic fluid flow computation". *J. Non-Newtonian Fluid Mech.*, **127** (1), pp. 1-26.

[9] Allouche, M., Frigaard, I.A., Sona, G., 2000. "Static wall layers in the displacement of two visco-plastic fluids in a plane channel". *J. Fluid Mech.*, **424**, pp. 243-277.

[10] Frigaard, I.A., Scherzer, O., 2000. "The effect of yield stress variation on uniaxial exchange flows of two Bingham fluids in a pipe". *SIAM J. Appl. Math*., **60** (6), pp. 1950-1976.

[11] Sekimoto, K, 1991. "An exact non-stationary solution of simple shear flow in a Bingham fluid". *J. Non-Newtonian Fluid Mech.*, **39** (1), pp. 107-113.

[12] Daprà, I., Scarpi, G., 2010. "Unsteady simple shear flow in a viscoplastic fluid: comparison between analytical and numerical solutions". *Rheol. Acta*, **49** (1), pp. 15-22.

MULTIPHYSIC MODELING OF A MEMS GYROSCOPE

D. Marano, F. Pellicano, A. O. Andrisano
Department of Engineering ”Enzo Ferrari”,
University of Modena and Reggio Emilia, Italy
E-mail: davide.marano@unimore.it; francesco.pellicano@unimore.it

Abstract. *The present paper is focused on the modeling and experimental analysis of a three-axes MEMS gyroscope, implementing an electrostatic quadrature compensation architecture. The gyroscope structure is explained and equations of motion are written; modal shapes and frequencies are obtained by finite element simulations. Electrostatic softening effect is explained and natural frequencies of the device derived as a function of the applied tuning voltage.*

Keywords: *MEMS, Gyroscope, Quadrature error, Multiphysic Analysis, FEM modeling, Electrostatic quadrature compensation*

1. INTRODUCTION

The term ”Micro Electro-Mechanical Systems” (MEMS) was first introduced in a proposal submitted to DARPA in 1986 referring to miniaturized devices made using the techniques of microfabrication. The potential of very small machines was appreciated before the technology that could make them existed; as noted by Richard Feynman in his talk at an American Physical Society meeting on 1959, ”There’s plenty of room at the Bottom”: miniaturization opens new perspectives and possibilities for the development of completely new class of sensors, where micro-scale phenomena are effectively pursued to achieve results that would be unfeasible at macro-scale. The physical dimensions of MEMS can vary from well below one micron, for very simple structures having no moving parts, up to several millimeters for complex systems with multiple moving elements under the control of integrated microelectronics. Benefits of reduced size in electromechanical systems include greater efficiencies, decreased power consumption and lower manufacturing costs due to batch fabrication. The characteristic elements of MEMS are miniaturized structures, sensors, actuators, and onboard microelectronics. Microsensors and microactuators are defined as transducers: devices that convert energy from one form to another. In the case of microsensors (microactuators), the device typically converts a measured mechanical (electrical) signal into an electrical (mechanical) signal.

Inertial sensors convert the inertial forces caused by the input acceleration or rate signal into some physical changes such as deflection of masses or deviations of stresses, which then are captured by a corresponding transducer and transformed into an electrical signal.

The electrical signal is subjected to some estimation procedures such as linear or nonlinear filtering in order to derive an estimate of the input signal. Accelerations and angular velocities are vectorial signals possessing absolute values and orientations; if only one component of the vector is measured the sensor is denoted 1D or one-axis, whereas if two or all three components of the acceleration or the rate signal are captured, the sensor is called a 2D or 3D. A comprehensive review of theory, conventional designs and technology for inertial MEMS can be found in [1].

MEMS Fabrication Technologies

Two alternative technologies are available for the manufacturing of micromechanical devices: the *bulk micro-machining* and the *surface micro-machining* techniques.

- In *Bulk micro-machining* [2] the micro-structures are formed by selectively removing (etching) parts from a bulk material, typically a silicon wafer. Although various different materials can be used as the substrate for micro-machined structures, silicon is being used for that purpose in most cases because of the great level of experience achieved through the production of semiconductor devices. Additionally, silicon offers the best characteristics with respect to cost, metallization and machinability. Alternatives to Si include ceramic, plastic or glass materials.
- *Surface micro-machining* builds microstructures by deposition and etching of different structural layers on top of the substrate [3]. Polysilicon is commonly used as one of the layers and silicon dioxide is used as a sacrificial layer which is removed or etched out to create the necessary void in the thickness direction. Size of added layers generally ranges from 2 μm over to 5 μm; surface planarization is often required before the deposition of every structural layer, to prevent critical issues during photolitography [4]. The main advantage of this machining process is the possibility of realizing monolithic microsystems in which the electronic and the mechanical components are built on the same substrate. As the structures are built on top of the substrate and not inside it, the substrate's properties are not as important as in bulk micromachining, and the expensive silicon wafers can be replaced by cheaper substrates, such as glass, plastic, quartz, ceramic of other piezoelectric materials.

MEMS Gyroscopes

Gyroscopes are sensors designed to measure angular rotations about some specific axes with respect to inertial space. *Rate gyroscopes* measure a rotation rate (angular velocity), while *displacement gyroscopes* measure a rotation-angle. They have been traditionally designed as either mechanical devices exploting the conservation on angular momentum or as optical systems exploiting the Sagnac effect experienced by counter-propagating laser beams in a ring cavity or a fiber optic coil. MEMS gyroscopes are mainly vibratory gyroscopes based on the energy transfer between two orthogonal vibration modes, the drive-mode and the sense-mode [5]. Generally, a Coriolis mass is actuated into resonant vibration with constant amplitude in the drive direction; when an angular rate is applied, a Coriolis-effect-induced force couples the vibration modes and the drive mode excites the sense mode, as shown in Fig. 1. Thus, detecting the sense mode position, the value of input angular rate can be obtained. However, due to non-ideal factors such as fabrication imperfections, other coupling mechanisms also exist between these two vibration modes, introducing bias into the gyroscope

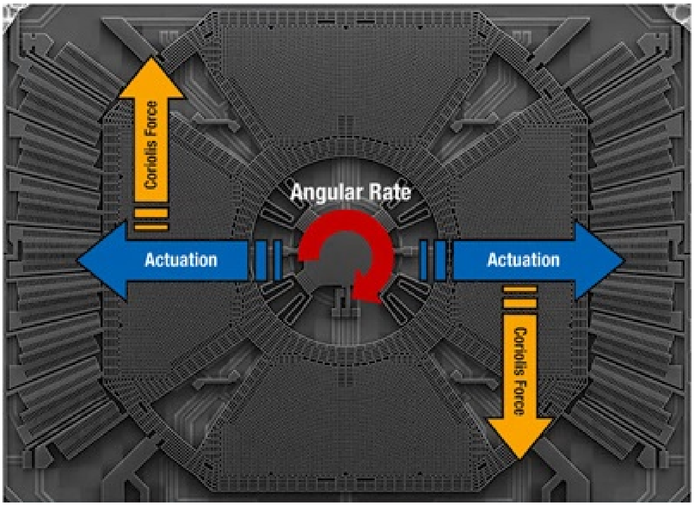

Figure 1. Coriolis Vibratory Gyroscope

output. Most common coupling mechanisms are elastic coupling, viscous coupling, and electrostatic coupling; among all, elastic coupling is the largest in magnitude. Elastic coupling is mainly caused by the anisoelasticity existing in the suspension elements or introduced by fabrication imperfections, that is, an off-diagonal coupling term often exists in the mechanical stiffness matrix of the micro-gyroscope structure.

Because of this mechanical coupling stiffness, a quadrature force will appear in the sense direction, which is proportional to the drive-mode position. Therefore, quadrature vibration response also exists in the sense direction and will mix into the gyroscope output if it is not thoroughly distinguished from the Coriolis vibration response. In comparison with the amplitude of the Coriolis response, that of the quadrature response is often considerably large. Hence, quadrature reduction has become one of the primary issues in the design of high-performance silicon micro-gyroscopes. Several quadrature compensation methods, based either on mechanical [6] or electronic principles [7, 8] have been proposed in literature; among all an effectual approach capable to provide a complete quadrature error cancellation is the electrostatic quadrature compensation. This approach is based on the electromechanical interaction between properly designed mechanical electrodes and the movable mass of the gyroscope: electrostatic forces, mechanically balancing quadrature forces, are generated biasing electrodes with differential dc voltages [9, 10].

However, the interaction between forces generated by quadrature compensation electrodes and the mechanical structure varies the natural frequencies of the device. In the present paper, the dynamics of a three-axes MEMS gyroscope manufactured by ST Microelectronics, is derived; natural frequencies of the device are determined in biased conditions by an Electromechanical FEM simulation.

2. CASE STUDY GYROSCOPE STRUCTURE AND DYNAMICS

Structure

The three-axes Coriolis Vibrating Gyroscope presented in the following is a compact device, conceived for consumer applications, manufactured by ST Microelectronics. The device is manufactured by a surface micro-machining process, ThELMA-ISOX *(Thick Epipoly Layer for Microactuators and Accelerometers)* technology platform, proprietary of ST Microelectronics. The structure (Fig.2) is composed of 4 suspended plates ($M_{1,2,3,4}$) coupled by 4 folded springs, elastically connected to a central anchor by a further set of coupling springs. The fundamental vibration mode (driving mode) consists of a planar oscillatory radial motion of the plates: globally, the structure periodically expands and contracts. Plates $M_{1,2}$ are actuated by a set of comb-finger electrodes and the motion is transmitted to the secondary plates $M_{3,4}$ by the folded springs at the corners. The sensing modes of the device consist of two out-of-plane modes (Roll and Pitch) characterized by counter-phase oscillation of plates $M_{1,2}$ ($M_{3,4}$) and one in-plane counter-phase motion of the yaw plates ($M_{3,4}$) (Yaw mode). Rotation of yaw plates ($M_{3,4}$) is measured by a set of parallel-plate electrodes, $PP_{1,2}$, located on the yaw plates; pitch and roll angular rotations are measured sensing the capacitive variations between each plate and an electrode placed below (respectively $R_{1,2}$ and $P_{1,2}$ for roll and pitch masses); the driving mode vibration is measured by additional comb-finger electrodes $SD_{1,2}$. Electrostatic quadrature compensation is implemented on Roll (Quadrature Compensation Roll, QCR) and Pitch axis (QCP) by means of electrodes placed under each moving mass. Yaw axis quadrature compensation electrodes (QCY) are slightly different from the ones of other axis since they are not placed underneath the moving mass and have height equal to the gyroscope's rotor mass.

Dynamics

A general derivation of equations of motion for a vibratory MEMS gyroscope can be found in [1, 11]. The coordinate-system model shown in Fig. 3 consists of three coordinate frames respectively defined by their versors $\Sigma_{inertial} = [X, Y, Z]$; $\Sigma_{platform} = [x, y, z]$; $\Sigma = [\hat{x}, \hat{y}, \hat{z}]$. The frame Σ coordinate system is integral with a point P of a body moving respect to the platform (for a 3-axes gyroscope the considered body is one of the four moving suspended plates and the platform frame is usually assigned to the fixed silicon substrate). Simplifying assumptions (constant angular rate inputs, operating frequency of the gyroscope much higher than angular rate frequencies) can be done for a decoupled three axes gyroscope [11, 12]; EoM become:

$$m\ddot{r}_x + c_x\dot{r}_x + k_x r_x = -2m\Omega_y\dot{r}_z + 2m\Omega_z\dot{r}_y + F_{D_x} \tag{1}$$

$$m\ddot{r}_y + c_y\dot{r}_y + k_y r_y = 2m\Omega_x\dot{r}_z - 2m\Omega_z\dot{r}_x + F_{D_y} \tag{2}$$

$$m\ddot{r}_z + c_z\dot{r}_z + k_z r_z = -2m\Omega_x\dot{r}_y + 2m\Omega_y\dot{r}_x + F_{D_z} \tag{3}$$

Drive system The mechanical subsystem generating momentum (drive system), is constituted by comb fingers driving the *x*-axis masses of the gyro into a harmonic oscillation; since the drive motion is significantly greater than the Coriolis response, the terms $(-2m\Omega_y\dot{r}_z +$

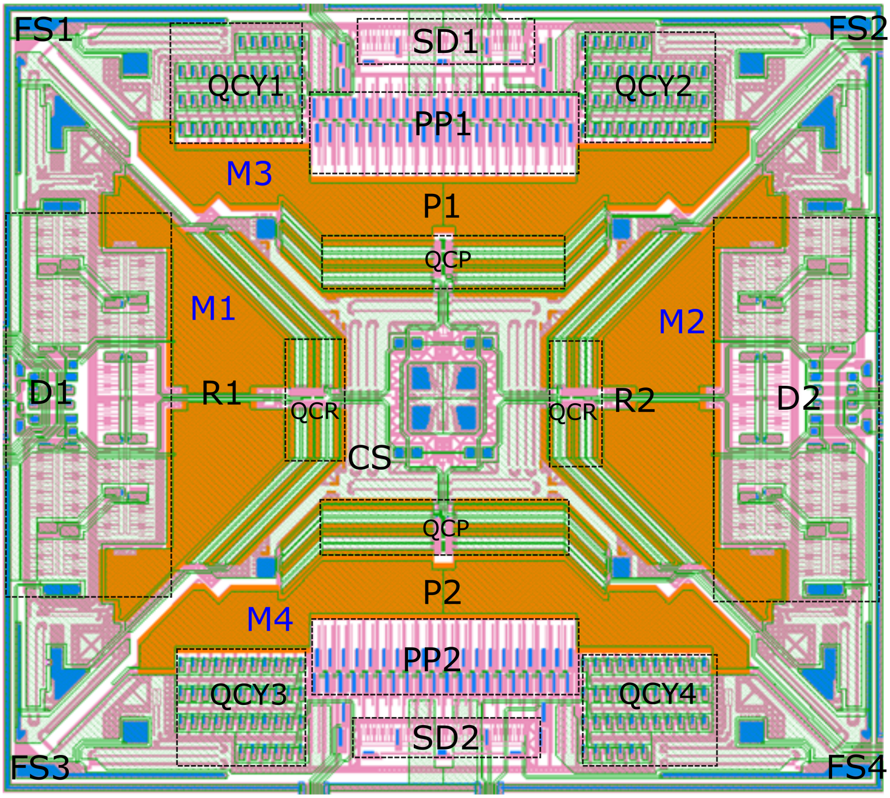

M1,M2: Roll sensing masses
M3,M4: Pitch & Yaw sensing masses

D1-2: *Drive-forcing* comb fingers
SD 1-2: *Drive-readout* comb fingers
P1-2: *Pitch*-mode sensing electrodes
R1-2: *Roll*-mode sensing electrodes
PP1-2: *Yaw*-mode parallel plates
QCR: *Roll* quadrature compensation electrodes
QCP: *Pitch* quadrature compensation electrodes
QCY1-4: *Yaw* quadrature compensation electrodes

FS1-4: coupling folded springs
CS: central coupling springs

Figure 2. Case-study gyroscope layout

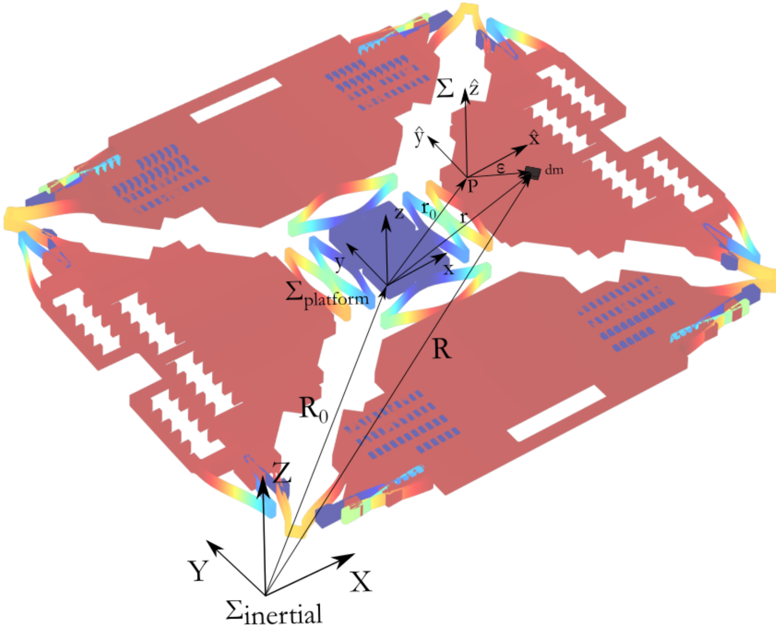

Figure 3. Coordinate system model for the derivation of kinematic equations

$2m\Omega_z\dot{r}_y$) in Eq.(1) are practically negligible. The drive oscillator is therefore modeled by a 1-DOF system, considering as proof-mass one of the moving masses m_d, as damping c_d the equivalent damping given by viscous and thermoelastic effects and a stiffness k_d. Planar equation can be written as:

$$m_d\ddot{x} + c_d\dot{x} + k_d x = F_{D_x}(t) = F_0 \sin(\omega t) \tag{4}$$

The response function of such system is

$$x(s) = \frac{1/m}{s^2 + s\omega_0/Q + \omega_0^2} F(s) = H(s)F(s) \tag{5}$$

where $\omega_0 = \sqrt{k_d/m_d}$ is the natural or resonance frequency and $Q = \omega_0 m_d/c_d$ is the quality factor; the amplitude of drive motion is shown in fig 4.

It is fundamental to keep stable the amplitude, phase and frequency of the drive-mode oscillation, since they directly determine phase and amplitude of the Coriolis force. The device is thus operated at drive-mode resonant frequency, usually determined by FEM analysis. The Automatic Gain Control (AGC), determines the oscillation amplitude of the drive motion and compares it with a reference signal; an amplitude controller modulates the force amplitude F_0 until the desired amplitude is set. Examples of AGC can be found in [13, 14].

Coriolis response Mechanical response to the Coriolis force is amplified exploiting resonance imposed by the drive motion; the validity of modes decoupling condition is verified by FEM simulation. The out-of-plane dynamics of the Pitch mass is given by Eq. (3); due to

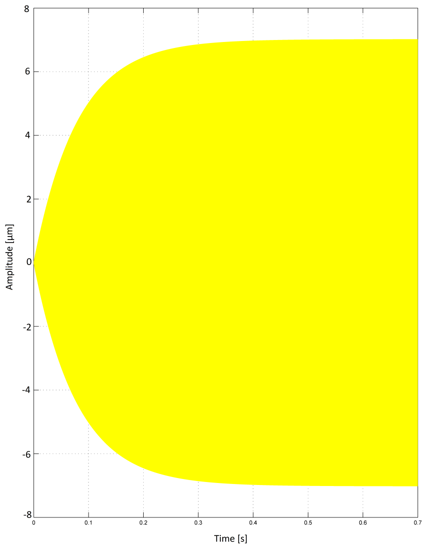

Figure 4. Drive motion amplitude

modes decoupling, the effect of Ω_y on pitch mode in negligible and since $F_{D_z} = 0$ Eq. (3) reduces to

$$m_p\ddot{z} + d_p\dot{z} + k_p z = -2\Omega_x(t)m_p\dot{y} \tag{6}$$

where m_p is the pitch mass responding to the Coriolis force, d_p is the equivalent damping, and k_p is the stiffness given by the suspensions. By defining the pitch-mode natural frequency $\omega_{0p} = \sqrt{\frac{k_p}{m_p}}$ and quality factor $Q_p = \frac{\omega_{0p}m_p}{d_p}$, previous equation becomes

$$\ddot{z} + \dot{z}\frac{\omega_{0p}}{Q_p} + \omega_{0p}^2 z = -2\Omega_x(t)\dot{y} \tag{7}$$

Equation (7) is implemented as a 1 DoF mechanical harmonic resonator, whose response function is:

$$z(s) = \frac{1/m_p}{s^2 + s\omega_{0p}/Q_p + \omega_{0p}^2}F(s) = H(s)F(s) \tag{8}$$

The out-of-plane dynamics of the Roll mass for a decoupled structure, due to an angular velocity $\Omega_y(t)$, is obtained posing $\Omega_x(t) = 0$ (mode decoupling condition) and $F_{D_z} = 0$ in Eq. (3), leading to

$$m_r\ddot{z} + d_r\dot{z} + k_r z = 2\Omega_y(t)m_r\dot{x} \tag{9}$$

The in-plane equations of motion of the Yaw mass in response to an angular velocity $\Omega_z(t)$ are:

$$\begin{bmatrix} m_p & 0 \\ 0 & m_r \end{bmatrix}\begin{bmatrix} \ddot{x} \\ \ddot{y} \end{bmatrix} + \begin{bmatrix} d_p & 0 \\ 0 & d_r \end{bmatrix}\begin{bmatrix} \dot{x} \\ \dot{y} \end{bmatrix} + \begin{bmatrix} k_p & 0 \\ 0 & k_r \end{bmatrix}\begin{bmatrix} x \\ y \end{bmatrix} = \tag{10}$$
$$= 2\Omega_z(t)\begin{bmatrix} m_p & 0 \\ 0 & m_r \end{bmatrix}\begin{bmatrix} 0 & 1 \\ -1 & 0 \end{bmatrix}\begin{bmatrix} \dot{x} \\ \dot{y} \end{bmatrix}$$

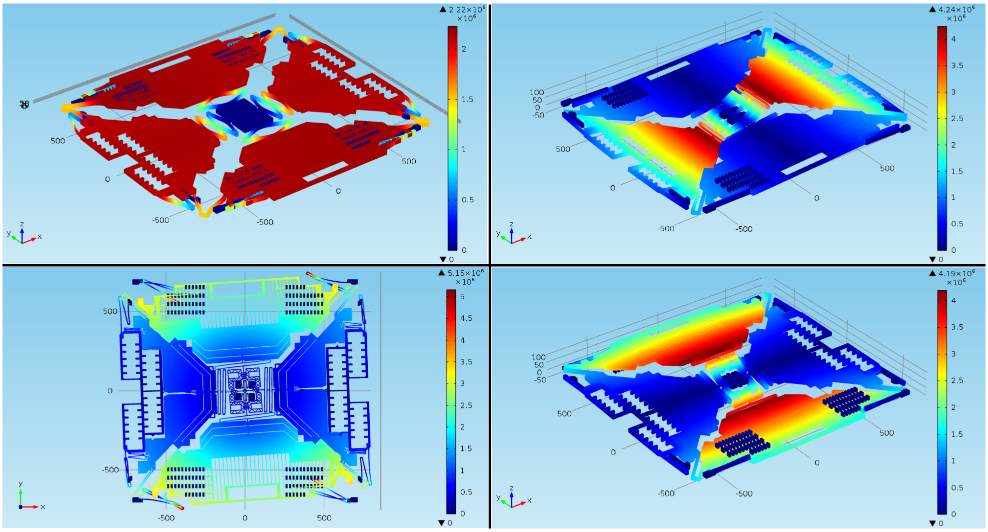

Figure 5. Fundamental vibration modes (drive, pitch, yaw, roll)

By the small-angle approximation one, if L denotes the length of the fixed sensing electrode and θ denotes the angular rotation, $x = L\theta$; the angular rotation is thus obtained measuring the displacement x. The equation of motion relative to the Yaw mode is

$$m_p\ddot{x} + d_p\dot{x} + k_p x = 2\Omega_z(t)m_p\dot{x} \tag{11}$$

Modal analysis

The device eigenfrequencies are determined by FEM simulation (Fig. 5); as imposed by mechanical design the fundamental mode of vibration consists of an in-plane inward/outward radial motion of the plates, and the structure cyclically expands and contracts, the fundamental sensing modes (pitch, yaw, roll) are identified. Several spurious modes at higher frequencies, not reported here, are found.

3. ELECTROSTATIC QUADRATURE CANCELLATION

Quadrature force

The dynamics equations of a real linear yaw vibrating gyroscope can be expressed, considering the off-diagonal entries of the mechanical stiffness matrix, as

$$\begin{bmatrix} m & 0 \\ 0 & m \end{bmatrix} \ddot{\mathbf{p}}(t) + \begin{bmatrix} d_x & 0 \\ 0 & d_y \end{bmatrix} \dot{\mathbf{p}}(t) + \begin{bmatrix} k_x & k_{xy} \\ k_{yx} & k_y \end{bmatrix} \mathbf{p}(t) = \begin{bmatrix} F_d \\ F_C \end{bmatrix}$$

where $\mathbf{p}(t) = [x(t), y(t)]^T$ is the position vector of the mass in drive and sense direction, m represents the Coriolis mass, d_x (d_y) and k_x (k_y) represent the damping and stiffness along the X-axis (Y-axis); k_{xy} (k_{yx}) are the cross coupling stiffness terms bringing the quadrature vibration response; F_d is the driving force and F_C is the Coriolis force. The dynamic equation in sense direction can be expressed as

$$m\ddot{y} + d_y\dot{y} + k_y y = F_C + F_q$$

Applied Voltage [V]	Roll [Hz]	Pitch [Hz]	Yaw [Hz]
0	21318.74	21561.57	21021.3
5	21310.68	21554.20	21001.42
10	21097.24	21359.44	20475.74
15	20655.21	20956.36	19388.26

Table 1. Electromechanical simulation results

where $F_C = -2m\Omega_z\dot{x}$ is the Coriolis force and $F_q = -k_{yx}x$ is the quadrature force. The Coriolis mass is usually actuated into resonant vibration with constant amplitude in drive direction, thus the drive-mode position can be expressed by $x(t) = A_x \sin(\omega_x t)$. Introducing the sinusoidal drive movement, Coriolis and quadrature force can be expressed as

$$F_C = 2m\Omega_z\omega_x A_x \cos(\omega_x t) \quad , \quad F_q = -k_{yx}A_x sin(\omega_x t) \tag{12}$$

Electrostatic softening

Electrostatic quadrature compensation is performed applying a different potential among quadrature compensation electrodes and rotor mass. The interaction between forces generated by quadrature compensation electrodes and the mechanical structure causes a variation of the natural modes of the gyroscope; an electromechanical analysis is performed to determine the eigenfrequencies variation due to voltage tuning of quadrature compensation electrodes. Results show that increasing the voltage of quadrature compensation of either roll, pitch, or yaw electrodes, the eigenfrequency of motion decreases in magnitude following a quadratic rule (Tab.2); in Fig. 6, results of electromechanical simulation for roll axis are shown. The mechanical effect of increasing the quadrature compensation electrodes voltage is thus an "added mass" lowering the vibration modes frequencies; this effect is called electrostatic softening. Experimental analysis of electrostatic softening is performed and results confirm a quadratic decrease of the resonance frequency increasing the differential voltage (Fig. 6).

Mode	Interpolating polynomial	Regression coefficient (r)
Roll	$y = -4.3397x^2 + 21.016x + 21318$	0.99
Pitch	$y = -3.9571x^2 + 19.149x + 21561$	0.99
Yaw	$y = -10.676x^2 + 51.644x + 21019$	0.99

Table 2. Interpolating laws of electromechanical simulation results

4. CONCLUSIONS

In this paper a theoretical and experimental analysis of a three-axes MEMS gyroscope, developed by ST Microelectronics, is presented. An innovative feedforward PI quadrature compensation architecture is developed. Exploiting the equations of motions for a 3-DoF gyroscope structure has provided us an estimation of the drive and sense motion amplitude. Natural mode shapes and frequencies of the device have been obtained by finite element simulations to characterize the device. Electrostatic softening effect has been explained and

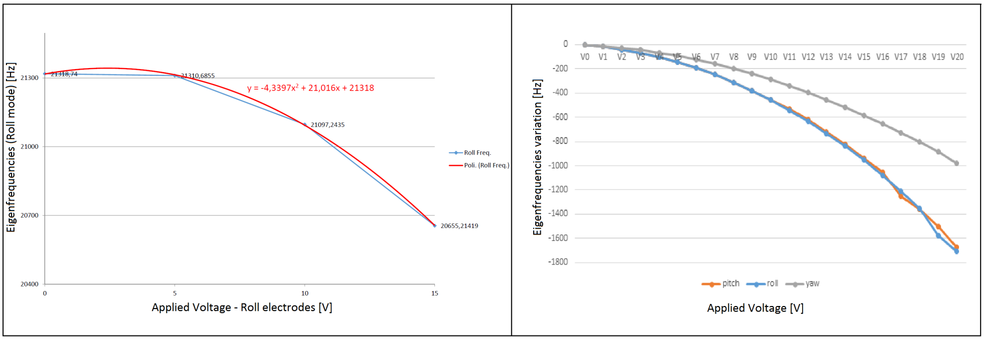

Figure 6. Simulation of electrostatic softening for Roll axis: increasing voltage applied to quadrature electrodes, natural frequencies lower following a quadratic rule; Experimental electrostatic softening for Roll, Pitch and Yaw axis

natural frequencies of the device derived as a function of the applied tuning voltage. Finally, fabrication details and measurement results of test devices have been reported.

REFERENCES

[1] Kempe, V., 2011. *Inertial MEMS: principles and practice*. Cambridge University Press.

[2] Kovacs, G. T., Maluf, N. I., and Petersen, K. E., 1998. "Bulk micromachining of silicon". *Proceedings of the IEEE,* **86**(8), pp. 1536–1551.

[3] Bustillo, J. M., Howe, R. T., and Muller, R. S., 1998. "Surface micromachining for microelectromechanical systems". *Proceedings of the IEEE,* **86**(8), pp. 1552–1574.

[4] Antonello, R., and Oboe, R., 2011. *MEMS Gyroscopes for Consumers and Industrial Applications*. INTECH Open Access Publisher.

[5] Kaajakari, V., 2009. Practical mems: Analysis and design of microsystems.

[6] Geen, J. A., 2006. Micromachined sensor with quadrature suppression, Apr. 25. US Patent 7,032,451.

[7] Clark, W. A., Howe, R. T., and Horowitz, R., 1996. "Surface micromachined z-axis vibratory rate gyroscope". In Tech. Dig. Solid-State Sensor and Actuator Workshop, pp. 283–287.

[8] Marano, D., Cammarata, A., Fichera, G., Sinatra, R., and Prati, D., 2017. "Modeling of a three-axes mems gyroscope with feedforward pi quadrature compensation". In *Advances on Mechanics, Design Engineering and Manufacturing*. Springer, pp. 71–80.

[9] Ni, Y., Li, H., and Huang, L., 2014. "Design and application of quadrature compensation patterns in bulk silicon micro-gyroscopes". *Sensors,* **14**(11), pp. 20419–20438.

[10] Weinberg, M. S., and Kourepenis, A., 2006. "Error sources in in-plane silicon tuning-fork mems gyroscopes". *Journal of Microelectromechanical systems,* **15**(3), pp. 479–491.

[11] Acar, C., and Shkel, A., 2008. *MEMS vibratory gyroscopes: structural approaches to improve robustness*. Springer Science & Business Media.

[12] Acar, C., and Shkel, A. M., 2003. "Nonresonant micromachined gyroscopes with structural mode-decoupling". *IEEE Sensors Journal,* **3**(4), pp. 497–506.

[13] Grayver, E., and M'Closkey, R. T., 2001. "Automatic gain control asic for mems gyro applications". In American Control Conference, 2001. Proceedings of the 2001, Vol. 2, IEEE, pp. 1219–1222.

[14] Park, S., Tan, C.-W., Kim, H., and Hong, S. K., 2009. "Oscillation control algorithms for resonant sensors with applications to vibratory gyroscopes". *Sensors,* **9**(8), pp. 5952–5967.

NATURAL FREQUENCIES OF TRIPLE-WALLED CARBON NANOTUBES

Angelo Oreste Andrisano
Department of Engineering "Enzo Ferrari",
University of Modena and Reggio Emilia, Italy
E-mail: angelooreste.andrisano@unimore.it

Francesco Pellicano
Department of Engineering "Enzo Ferrari",
University of Modena and Reggio Emilia, Italy
E-mail: francesco.pellicano@unimore.it

Matteo Strozzi
Department of Engineering,
University of Ferrara, Italy
E-mail: strmtt@unife.it

***Abstract**. In this paper, the linear vibrations of Triple-Walled Carbon Nanotubes (TWNTs) are analysed. A multiple elastic shell model is considered. The shell dynamics is studied in the framework of the Sanders-Koiter shell theory. The van der Waals (vdW) interaction between two layers of the TWNT is modelled by a radius-dependent function. The circular cylindrical shell deformation is described in terms of longitudinal, circumferential and radial displacements. Simply supported, clamped and free boundary conditions are considered. The three displacement fields are expanded by means of a double mixed series based on Chebyshev orthogonal polynomials for the longitudinal variable and harmonic functions for the circumferential variable. The Rayleigh-Ritz method is applied to obtain approximate natural frequencies and mode shapes. The present model is validated in linear field by means of data derived from the literature. This study is focused on determining the effect of the geometry and boundary conditions on the natural frequencies of TWNTs.*

***Keywords**: carbon nanotubes, multiple elastic shell model, van der Waals interaction*

1. INTRODUCTION

Single-Walled Carbon Nanotubes (SWNTs) were discovered in 1991 by Iijima [1], who first analysed molecular carbon structures in the form of fullerenes and then reported the preparation of the carbon nanotubes, as helical microtubules of graphitic carbon.

The analogies between the continuous shells and the discrete SWNTs led to a very large application of the elastic shell theories for the SWNT structural analysis [2-7].

Triple-Walled Carbon Nanotubes (TWNTs) can be described as systems composed by three concentric SWNTs, whereby each SWNT is treated as a cylindrical shell continuum; an elastic multiple shell model is used for the vibration analysis of the TWNT and the van der Waals interaction between any two layers of the system can be modelled by means of a radius-dependent function [8-10].

In this paper, the linear vibrations of TWNTs are investigated. The shell dynamics is studied in the framework of the Sanders-Koiter shell theory and a multiple elastic shell model is considered. The van der Waals (vdW) interaction between any two layers of the TWNT is modelled by a radius-dependent function.

The shell deformation is described in terms of longitudinal, circumferential and radial displacements. Simply supported, clamped and free boundary conditions are considered. The three displacement fields are expanded by means of a double mixed series based on Chebyshev polynomials and harmonic functions. The Rayleigh-Ritz method is applied to obtain approximate natural frequencies and mode shapes.

The model proposed in the present paper is validated in linear field by means of data derived from the literature. This study is focused on determining the effect of the geometry and boundary conditions on the natural frequencies of TWNTs.

2. SANDERS-KOITER LINEAR SHELL THEORY EXTENDED TO TWNTS

In Figure 1, a circular cylindrical shell having radius R_i, length L_i and thickness h_i is shown; a cylindrical coordinate system (O; x, θ, z) is considered where the origin O of the reference system is located at the centre of one end of the circular shell. Three displacement fields are represented: longitudinal u_i (x, θ, t), circumferential v_i (x, θ, t) and radial w_i (x, θ, t), where (x, θ) are the longitudinal and angular coordinates of the circular cylindrical shell, z is the radial coordinate along the thickness h_i and t is the time.

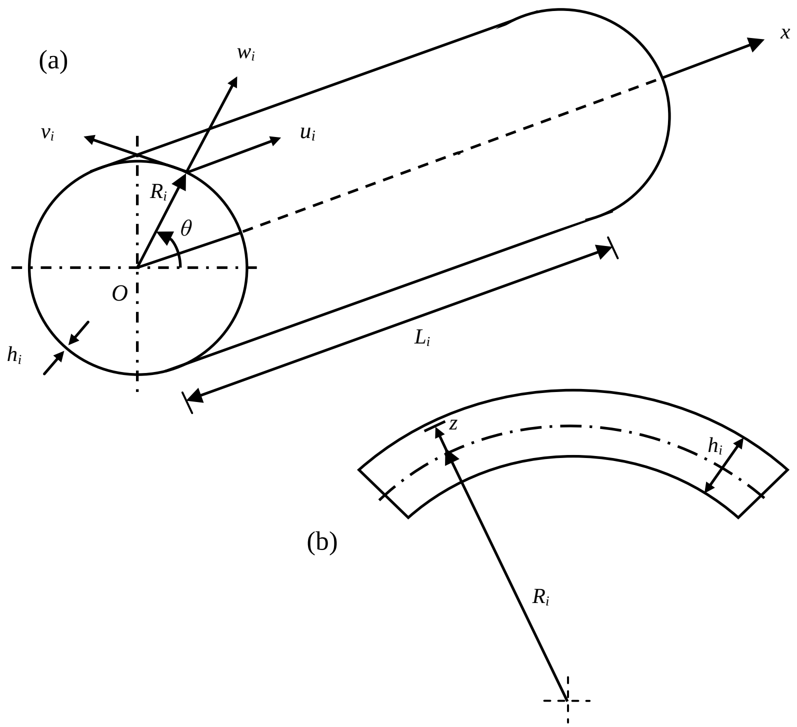

Figure 1. Geometry of the i-th shell. (a) Complete shell; (b) cross-section of the shell.

Strain-Displacement Relationships

The three nondimensional displacement fields ($\tilde{u}_i$,$\tilde{v}_i$,$\tilde{w}_i$) of the *i*-th cylindrical shell can be written in the following form [2]

$$\tilde{u}_i = \frac{u_i}{R_i} \qquad \tilde{v}_i = \frac{v_i}{R_i} \qquad \tilde{w}_i = \frac{w_i}{R_i} \qquad i = (1,3) \tag{1}$$

where (u_i,v_i,w_i) are the three dimensional displacement fields and R_i is the radius of the *i*-th shell.

The nondimensional middle surface strains of the *i*-th cylindrical thin shell are given as [2]

$$\tilde{\varepsilon}_{x,0,i} = \alpha_i \frac{\partial \tilde{u}_i}{\partial \eta} \qquad \tilde{\varepsilon}_{\theta,0,i} = \frac{\partial \tilde{v}_i}{\partial \theta} + \tilde{w}_i \qquad \tilde{\gamma}_{x\theta,0,i} = \frac{\partial \tilde{u}_i}{\partial \theta} + \alpha_i \frac{\partial \tilde{v}_i}{\partial \eta} \qquad i = (1,3) \tag{2}$$

where $\eta = x/L$ is the nondimensional longitudinal coordinate of the shell and $\alpha_i = R_i/L$.

The nondimensional middle surface changes in curvature and torsion of the *i*-th cylindrical shell are expressed as [2]

$$\begin{aligned} &\tilde{k}_{x,i} = -\alpha_i^2 \frac{\partial^2 \tilde{w}_i}{\partial \eta^2} \qquad \tilde{k}_{\theta,i} = \frac{\partial \tilde{v}_i}{\partial \theta} - \frac{\partial^2 \tilde{w}_i}{\partial \theta^2} \\ &\tilde{k}_{x\theta,i} = -2\alpha_i \frac{\partial^2 \tilde{w}_i}{\partial \eta \partial \theta} + \frac{3\alpha_i}{2} \frac{\partial \tilde{v}_i}{\partial \eta} - \frac{1}{2} \frac{\partial \tilde{u}_i}{\partial \theta} \end{aligned} \qquad i = (1,3) \tag{3}$$

Elastic Strain and Kinetic Energy

The nondimensional elastic strain energy of the *i*-th cylindrical shell is written in the following form [7]

$$\begin{aligned} \tilde{U}_i = {} & \frac{1}{2}\frac{1}{(1-\nu^2)} \int_0^1 \int_0^{2\pi} \left[\tilde{\varepsilon}_{x,0,i}^2 + \tilde{\varepsilon}_{\theta,0,i}^2 + 2\nu \tilde{\varepsilon}_{x,0,i} \tilde{\varepsilon}_{\theta,0,i} + \frac{(1-\nu)}{2} \tilde{\gamma}_{x\theta,0,i}^2 \right] d\eta d\theta + \\ & \frac{1}{2}\frac{\beta_i^2}{12(1-\nu^2)} \int_0^1 \int_0^{2\pi} \left[\tilde{k}_{x,i}^2 + \tilde{k}_{\theta,i}^2 + 2\nu \tilde{k}_{x,i} \tilde{k}_{\theta,i} + \frac{(1-\nu)}{2} \tilde{k}_{x\theta,i}^2 \right] d\eta d\theta \end{aligned} \qquad i = (1,3) \tag{4}$$

where $\beta_i = h/R_i$.

The nondimensional kinetic energy of the *i*-th cylindrical shell is given by [4]

$$\tilde{T}_i = \frac{1}{2}\gamma_i \int_0^1 \int_0^{2\pi} (\tilde{u}_i'^2 + \tilde{v}_i'^2 + \tilde{w}_i'^2) d\eta d\theta \qquad i = (1,3) \tag{5}$$

where $\gamma_i = \rho R_i^2 \omega_0^2 / E$.

Van der Waals Interaction Energy

The nondimensional pressure $\tilde{p}_i$ exerted on the i-th shell due to vdW interaction between two different layers can be written as a function of the nondimensional radial displacements ($\tilde{w}_i$,$\tilde{w}_j$) of the shells in the following form [8,9]

$$\tilde{p}_i(\eta,\theta) = \sum_{j=1}^{3} \tilde{c}_{ij} \left(\delta_i \tilde{w}_i - \delta_j \tilde{w}_j \right) \qquad i = (1,3) \qquad (6)$$

where $\delta_i = R_i/\hat{R}$, $\delta_j = R_j/\hat{R}$, $\hat{R} = R_1$.

The nondimensional vdW interaction coefficient $\tilde{c}_{ij}$ is expressed as [10]

$$\tilde{c}_{ij} = -\left(\frac{1001\pi\tilde{\varepsilon}\tilde{\sigma}^{12}}{3\tilde{a}^4} \tilde{E}_{ij}^{13} - \frac{1120\pi\tilde{\varepsilon}\tilde{\sigma}^{6}}{9\tilde{a}^4} \tilde{E}_{ij}^{7} \right) \delta_j \qquad (i,j) = (1,3) \qquad (7)$$

The nondimensional elliptical integral $\tilde{E}_{ij}^{m}$ is given by [10]

$$\tilde{E}_{ij}^{m} = (\delta_j + \delta_i)^{-m} \int_0^{\pi/2} \frac{d\theta}{(1 - \tilde{k}_{ij} \cos^2\theta)^{m/2}} \qquad (i,j) = (1,3) \qquad (8)$$

The nondimensional coefficient $\tilde{k}_{ij}$ is expressed in the form [10]

$$\tilde{k}_{ij} = \frac{4\delta_j \delta_i}{(\delta_j + \delta_i)^2} \qquad (i,j) = (1,3) \qquad (9)$$

3. LINEAR VIBRATION ANALYSIS

A modal vibration, i.e., a synchronous motion, can be formally written in the form [6]

$$\tilde{u}_i(\eta,\theta,\tau) = \tilde{U}_i(\eta,\theta) f_i(\tau) \qquad \tilde{v}_i(\eta,\theta,\tau) = \tilde{V}_i(\eta,\theta) f_i(\tau) \qquad \tilde{w}_i(\eta,\theta,\tau) = \tilde{W}_i(\eta,\theta) f_i(\tau) \qquad i = (1,3) \qquad (10)$$

where $\tilde{U}_i(\eta,\theta)$, $\tilde{V}_i(\eta,\theta)$, $\tilde{W}_i(\eta,\theta)$ are the mode shape of the i-th shell, $f_i(\tau)$ is the time law, which is supposed to be the same for each displacement field in the modal analysis.

The mode shape ($\tilde{U}_i$, $\tilde{V}_i$, $\tilde{W}_i$) is expanded by means of a double series in terms of m-th order Chebyshev polynomials $T_m^*(\eta)$ in the longitudinal direction and harmonic functions ($\cos n\theta$, $\sin n\theta$) in the circumferential direction, in the following form [6]

$$\tilde{U}_i(\eta,\theta) = \sum_{m=0}^{M_u} \sum_{n=0}^{N} \tilde{U}_{i,m,n} T_m^*(\eta) \cos n\theta \qquad \tilde{V}_i(\eta,\theta) = \sum_{m=0}^{M_v} \sum_{n=0}^{N} \tilde{V}_{i,m,n} T_m^*(\eta) \sin n\theta$$
$$\tilde{W}_i(\eta,\theta) = \sum_{m=0}^{M_w} \sum_{n=0}^{N} \tilde{W}_{i,m,n} T_m^*(\eta) \cos n\theta \qquad i = (1,3) \qquad (11)$$

where $T_m^* = T_m(2\eta - 1)$, m is the polynomials degree, n is the number of nodal diameters and ($\tilde{U}_{i,m,n}$, $\tilde{V}_{i,m,n}$, $\tilde{W}_{i,m,n}$) are unknown coefficients of the boundary conditions.

Rayleigh-Ritz Method

The maximum number of variables needed for describing a general vibration mode with n nodal diameters is obtained by the relation ($N_p = 3\times(M_u + M_v + M_w + 3 - p)$), where ($M_u = M_v = M_w$) are the degree of the Chebyshev polynomials and p is the number of equations which are needed to satisfy the boundary conditions.

For a multi-mode analysis including different values of nodal diameters n, the number of degrees of freedom of the system is computed by the relation ($N_{max} = N_p \times (N + 1)$), where N represents the maximum value of the nodal diameters n considered.

Equations (10) are inserted in the expressions of the elastic strain energy (4) and kinetic energy (5) in order to compute the Rayleigh quotient; after imposing the stationarity to the Rayleigh quotient, one obtains the eigenvalue problem [6]

$$(-\omega_i^2 \tilde{\mathrm{M}}_i + \tilde{\mathrm{K}}_i)\tilde{\mathrm{q}}_i = \tilde{0} \qquad i = (1,3) \qquad (12)$$

which furnishes the approximate natural frequencies and mode shapes, where $\tilde{\mathrm{q}}_i$ denotes a vector containing all the unknown variables in the form [6]

$$\tilde{\mathrm{q}}_i = \begin{bmatrix} \ldots \\ \tilde{U}_{i,m,m} \\ \tilde{V}_{i,m,n} \\ \tilde{W}_{i,m,n} \\ \ldots \end{bmatrix} \qquad i = (1,3) \qquad (13)$$

4. NUMERICAL RESULTS

The mechanical parameters of the TWNT analysed in this paper are shown in Table 1.

Table 1. Mechanical parameters of the TWNT [10].

Young's modulus *E*	5.5 TPa
Poisson's ratio *ν*	0.19
Mass density *ρ*	11700 kg/m^3
Thickness *h*	0.066 nm
Innermost radius R_1	5.00 nm
Intermediate radius R_2	5.34 nm
Outermost radius R_3	5.68 nm
Length *L*	56.8 nm

Table 2. Natural frequencies (THz) of a simply-simply TWNT with R_1 = 5.00 nm, R_3 = 5.68 nm and L/R_3 = 10 with vdW interaction. Circumferential flexural modes. Comparisons between Sanders-Koiter (present model) and Donnell-Mushtari (Ref. [10]) shell theories.

Mode	**Displacement**	**Radius**	**Natural frequency (THz)**		**Difference %**
(*j*,*n*)	**(*u*,*v*,*w*)**	***R***	**Present model**	**Ref. [10]**	
1,2	*w*	R_3	0.0149	0.0150	0.67
	w	R_1	2.0557	2.0550	0.03
	w	R_2	3.3479	3.3480	0.00
2,2	*w*	R_3	0.0466	0.0469	0.64
	w	R_1	2.0586	2.0580	0.03
	w	R_2	3.3481	3.3490	0.03
3,2	*w*	R_3	0.0944	0.0942	0.21
	w	R_1	2.0638	2.0630	0.04
	w	R_2	3.3483	3.3490	0.02

Validation of the Present Method in Linear Field

In Table 2, comparisons between the natural frequencies of a simply supported TWNT obtained by considering the Sanders-Koiter shell theory (present model) and the Donnell-Mushtari shell theory (Ref. [10]) are reported.

The mechanical parameters of Table 1 are used. The vdW interaction is taken into account. The circumferential flexural modes (n=2) are studied. The radial displacement w is considered. The three concentric SWNTs which give the TWNT are denoted by innermost radius R_1, intermediate radius R_2 and outermost radius R_3, respectively.

From these comparisons, it can be noted that the present model is in good accordance with the results from the pertinent literature, the differences between the natural frequencies being less than 1%.

Effect of the Boundary Conditions

In Figure 2, comparisons between the natural frequencies of a TWNT obtained considering the Sanders-Koiter shell theory are reported. The mechanical parameters of Table 1 are used. The vdW interaction is taken into account. The circumferential flexural modes (n=2) are studied. The radial displacement w is considered. The SWNT with outermost radius R_3 is analysed.

Free-free, simply supported-free, clamped-free, simply supported-simply supported, clamped-simply supported and clamped-clamped boundary conditions are considered.

From these comparisons, it can be noted that, for the value of the radius R_3, the natural frequency for the clamped-clamped TWNT is the highest, followed by the clamped-simply supported, simply supported-simply supported, clamped-free, simply supported-free and free-free natural frequencies.

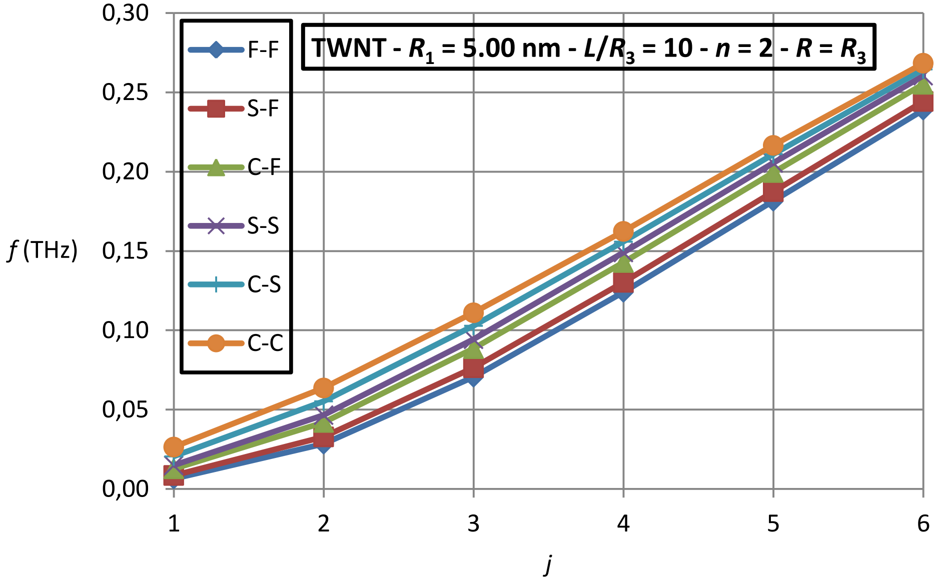

Figure 2. Natural frequencies (THz) of a TWNT with vdW interaction. Mode (n=2). Radial displacement w. Radius R_3. Sanders-Koiter shell theory. Mechanical parameters of Table 1.

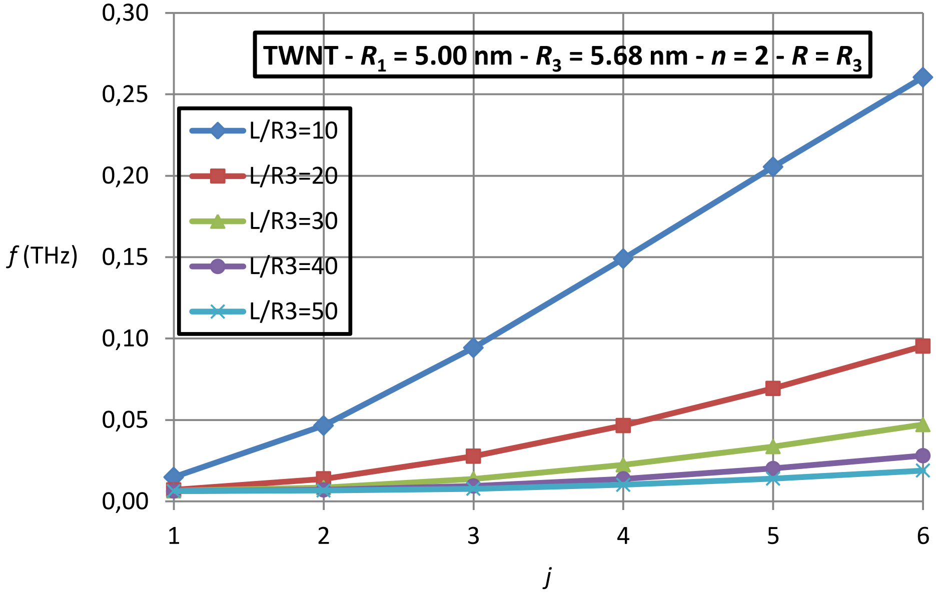

Figure 3. Natural frequencies (THz) of a simply supported TWNT with vdW interaction. Mode (n=2). Radial displacement w. Radius R_3. Sanders-Koiter shell theory. Mechanical parameters of Table 1.

Effect of the Aspect Ratio

In Figure 3, comparisons between the natural frequencies of a simply supported TWNT obtained considering the Sanders-Koiter shell theory are given. The mechanical parameters of Table 1 are used. The vdW interaction is taken into account. The circumferential flexural modes (n=2) are investigated. The radial displacement w is considered. The SWNT with outermost radius R_3 is analysed. Five different aspect ratios L/R_3 = (10,20,30,40,50) are compared.

From this Figure, it is confirmed that the natural frequency of a vibrational mode (j, n) increases with the number of longitudinal half-waves j and decreases with increasing length L. In particular, it can be seen that the natural frequencies for the lower aspect ratio L/R_3=10 increase almost linearly with j, while the natural frequencies for the higher aspect ratio L/R_3=50 tend to an horizontal asymptote.

5. CONCLUSIONS

In this paper, the linear vibrations of TWNTs are analysed considering a multiple elastic shell model. The shell dynamics is studied in the framework of the Sanders-Koiter theory, where the vdW interaction between any two layers of the TWNT is modelled by a radius-dependent function. Simply supported, clamped and free boundary conditions are applied. The circumferential flexural modes are studied. The radial displacement is considered. The Rayleigh-Ritz method is used in order to obtain approximate natural frequencies and mode shapes.

The present model is validated in linear field by means of data derived from the literature. From comparisons between the natural frequencies of a simply supported TWNT obtained by considering the Sanders-Koiter and Donnell-Mushtari shell theories, it can be noted that the present model is in good accordance with the results retrieved from the literature.

The effect of the boundary conditions on the natural frequencies of a TWNT obtained by considering the Sanders-Koiter shell theory is investigated. The outermost radius is analysed. From these comparisons, it can be noted that the natural frequency of the clamped-clamped TWNT is the highest, followed by the clamped-simply supported, simply supported-simply supported, clamped-free, simply supported-free and free-free natural frequencies, respectively.

The influence of the aspect ratio on the natural frequencies of a TWNT obtained by considering the Sanders-Koiter shell theory is studied. The outermost radius is investigated. From these comparisons, it is confirmed that the natural frequency of a vibrational mode increases with the number of the longitudinal half-waves and decreases with increasing the length. Moreover, it can be noted that the natural frequencies for the lower aspect ratio increase almost linearly with the longitudinal half-waves, while the natural frequencies for the higher aspect ratio tend to an horizontal asymptote.

REFERENCES

[1] Iijima S, 1991. “Helical microtubules of graphitic carbon”, *Nature*, **354**, pp. 56-58.

[2] Strozzi M, Manevitch LI, Pellicano F, Smirnov VV, and Shepelev DS, 2014. “Low-frequency linear vibrations of single-walled carbon nanotubes: Analytical and numerical models”, *Journal of Sound and Vibration*, **333**, pp. 2936-2957.

[3] Silvestre N, Wang CM, Zhang YY, and Xiang Y, 2011. “Sanders shell model for buckling of single walled carbon nanotubes with small aspect ratio”, *Composite Structures*, **93**, pp. 1683-1691.

[4] Smirnov VV, Manevitch LI, Strozzi M, and Pellicano F, 2016. “Nonlinear optical vibrations of single-walled carbon nanotubes. 1. Energy exchange and localization of low-frequency oscillations”, *Physica D: Nonlinear Phenomena*, **315**, pp. 113-125.

[5] Silvestre N, 2012. “On the accuracy of shell models for torsional buckling of carbon nanotubes”, *European Journal of Mechanics A/Solids*, **32**, pp. 103-108.

[6] Strozzi M, Smirnov VV, Manevitch LI, Milani M, and Pellicano F, 2016. “Nonlinear vibrations and energy exchange of single-walled carbon nanotubes. Circumferential flexural modes”, *Journal of Sound and Vibration*, **381**, pp. 156-178.

[7] Ghavanloo E, Fazelzadeh S, 2012. “Vibration characteristics of single-walled carbon nanotubes based on an anisotropic elastic shell model including chirality effect”, *Applied Mathematical Modelling*, **36**, pp. 4988-5000.

[8] He XQ, Kitipornchai S, and Liew KM, 2005. “Buckling analysis of multi-walled carbon nanotubes: a continuum model accounting for van der Waals interaction”, *Journal of Mechanics and Physics of solids*, **53**, pp. 303-326.

[9] He XQ, Kitipornchai S, Wang CM, and Liew KM, 2005. “Modeling of van der Waals force for infinitesimal deformation of multi-walled carbon nanotubes treated as cylindrical shells”, *International Journal of Solids and Structures*, **42**, pp. 6032-6047.

[10] He XQ, Eisenberger M, and Liew KM, 2006. “The effect of van der Waals interaction modeling on the vibration characteristics of multiwalled carbon nanotubes”, *Journal of Applied Physics*, **100**, 124317, pp. 1-12.

MODELLING AND TESTING TECHNIQUES FOR GEARBOX ANALYSIS AND OPTIMIZATION

Angelo Oreste Andrisano
Department of Engineering "Enzo Ferrari",
University of Modena and Reggio Emilia, Italy
E-mail: angelooreste.andrisano@unimore.it

Francesco Pellicano
Department of Engineering "Enzo Ferrari",
University of Modena and Reggio Emilia, Italy
E-mail: francesco.pellicano@unimore.it

Marco Barbieri
Department of Engineering "Enzo Ferrari",
University of Modena and Reggio Emilia, Italy
E-mail: mark@unimore.it

Antonio Zippo
Department of Engineering "Enzo Ferrari",
University of Modena and Reggio Emilia, Italy
E-mail: antonio.zippo@unimore.it

Matteo Strozzi
Department of Engineering,
University of Ferrara, Italy
E-mail: strmtt@unife.it

***Abstract**. In this paper pitting phenomenon and stress distribution of gears are investigated by means of experimental activities and numerical finite element analyses. In the first part, results of experimental accelerated endurance tests for the investigation of the pitting phenomenon of gears are reported. These durability tests are made at a specific nominal load and far from the resonance. After a short time, a visible pitting phenomenon arises. In the second part, finite element numerical analyses for the evaluation of gear stresses are given. The numerical analyses start from stress-vibration correlations and dynamic factors obtained by means of a 2-dof dynamic model previously developed; these results are used in the dynamic FEM simulations to calculate maximum normal stress and contact pressure on the contact tooth of the pinion vs. vibration amplitude for different dynamic factors.*

***Keywords**: industrial gearboxes, pitting phenomenon, stress distribution*

1. INTRODUCTION

Pitting and stress analyses deeply improve the mechanical resistance of gear teeth, which are subjected to very high contact pressures and fatigue loads in operating conditions [1-5];

gear dynamic optimization and profile modification can increase gearbox reliability [6-8].

Moreover, the analysis of the effects of surface pitting and wear on the vibration of a gear transmission together with the investigation of pressure and normal stress distributions in gears can improve the mechanical properties of the mechanical system [9-10].

In the present paper, results of experimental and FEM analyses of pitting and stress distribution of gears are reported.

In the experimental measurements, an overload in terms of applied torque is used, in order to exert excessive stresses of gear and to produce pitting within a short time. In these accelerated endurance tests, the goal is to get a pitting of order of 4-8% in terms of relative size in undamaged gears under non-stationary conditions.

A FEM model is developed in order to simulate the same test rig considered in the pitting tests, including gear crowning. Numerical analyses estimate contact pressure and normal stress distribution on the gear teeth, which are the bases for diagnosis, root cause analysis and prognosis technologies based on vibration measurements of gear damage.

2. EXPERIMENTAL ANALYSIS OF GEAR PITTING

In this section, experimental activities performed by means of accelerated endurance tests in order to investigate the pitting phenomenon of gears are reported. The test rig used in the experimental activities is an open-loop configuration experiment designed for testing single gear pairs, with maximum torque of 200Nm and rotational frequency of 3000RPM. Two DC motors are present, one of them acts as a motor and the second has the role of electric brake (generator); the controller allows an internal electric energy recirculation.

The test rig considered allows single spur gear pairs with arbitrary centre distance and two angular misalignments to be tested. Two torque-meters measure the applied input and output torque, while four tangential rotating accelerometers measure the rotational vibration of the wheels and consequently the dynamic transmission error (DTE).

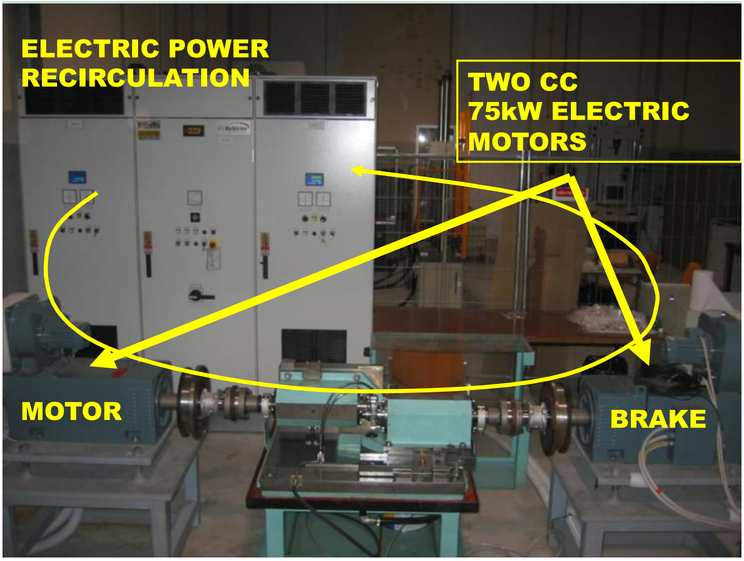

Figure 1. Test rig for the lab experiments.

Experimental Setup

The test bench considered is shown in Figure 1, two gears are mounted on shafts connected to two DC motors (engine + brake), these are highly balanced motors characterized by very low torque ripple.

Starting from the motor on the left of Figure 1, and moving to the right, one finds: i) a flywheel; ii) an elastic joint (Falk Steelflex T10" model 1050T); iii) a torque-meter; iv) an hollow super-stiff shaft mounted on two roller bearings, where the bearings are connected on a very stiff foundation.

The experimental setup consists mainly of three parts, as shown in Figure 2: i) control panel; ii) test bench gear; iii) data acquisition system.

The main features of the engine test stands are the following: maximum power 75KW, maximum speed 2880RPM. The motor M2 is used to rotate the pinion, while the motor M1 is used to provide the load torque to the wheel and therefore works as a brake. The control and regulation of the two motors can be done by acting on two parameters: revolutions per minute (RPM), current (A). The gear vibration is measured by tangential accelerometers.

The test bench is a gear system that can simulate and monitor the dynamic behaviour of gear pairs. The structure is constituted by two hollow shafts supported by two casings on which flanges are connected through screws. The possibility to mount the wheels on the shafts individually simulating the operation of a reduction gear represents a great advantage compared to the case in which it has to handle gearbox. In this way, it can be continuously monitored by mounted accelerometers. The test bench has a system of self-lubricating drop and the distance between the two gears can be adjusted via a micrometric screw.

A specific activity was carried out in order to design a special gear pair undergoing to a fast pitting phenomena with maximum available torque (DC engines) of 200Nm, where at the same time the bending failures must be avoided. This was reached by introducing a large amount of crowning along the face width. The goal was to obtain a gear pair so that the pitting arises within 60 hours. Accurate data on the gear material and surface finishing are needed for a proper estimate of the pitting phenomenon.

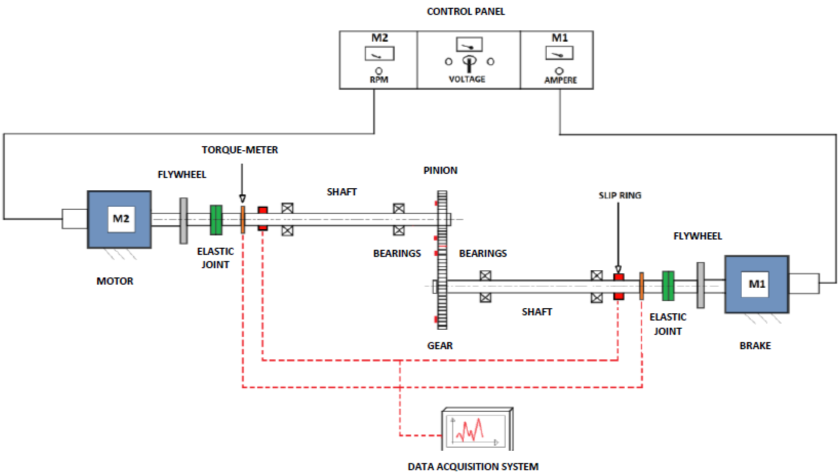

Figure 2. Scheme of the test rig.

Amplitude-Frequency Curves

In the present section, the first experiments performed on the test rig are described. The goal is to obtain amplitude-frequency diagrams in order to find out the main resonances of the gear transmission system by varying the excitation frequency, i.e., the mesh frequency.

Considering the reference load of the pinion equal to 130Nm, four tests were carried out at different vibration levels, i.e., percentual nominal loads.

For each load value, the interval of acquisition was 5s, from 100RPM to 1500RPM, with frequency step between two acquisitions equal to 20RPM. Filters were set as follows: i) moving average filter; ii) automatic cut-off frequency (accordingly to mesh frequency); iii) high pass filter at 50Hz.

Figure 3 shows the values of the RMS amplitude [g] obtained by varying the rotational frequency n [RPM] at the pinion for the four different external loads. In all the cases, the highest peak is found at 1200RPM, corresponding to 640Hz, which is the natural frequency of resonance of the system. Moreover, the resonance peak has an amplitude equal to 1.7g (100% of nominal load).

Durability and Pitting Tests

After performing tests for measuring the transmission error, pitting tests are carried out. These durability tests are made at the nominal load (130Nm), far from the resonance: the chosen frequency is 840RPM, which corresponds to the minimum value of RMS amplitude of 0.2g. The signals were collected by two tri-axial accelerometers on pinion and gear shaft supports respectively, and by two uni-axial accelerometers on motor side and on brake side.

After a 4 hours test performed at external torque 130Nm, speed 840RPM and external temperature 20°C, a visible pitting phenomenon arises, with the presence of two craters on the side of two adjacent teeth of the pinion, together with several smaller pits.

In particular, the pitting phenomenon is present in four different teeth (4,8,9,12), where for each pitted tooth the pitting size is estimated as a percentual of the total flank area $1.42 cm^2$ (the pitting sizes are 3.3%, 4.4%, 2%, 1.1%, respectively), see Figures 4-8.

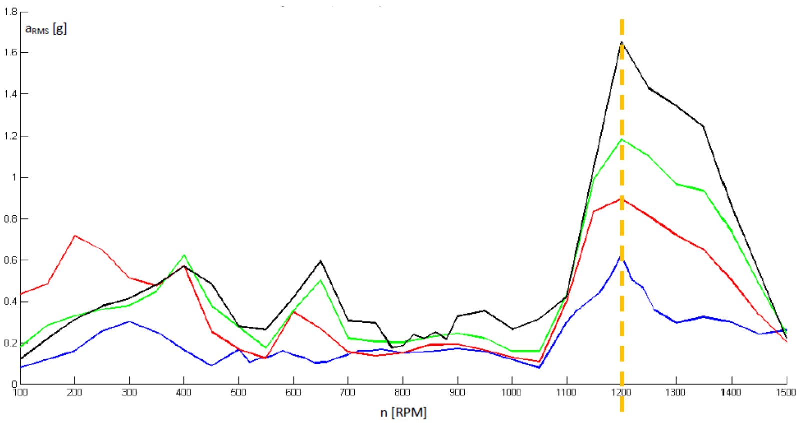

Figure 3. Amplitude-frequency curves for different external loads. 100-1500RPM.
▬ 15% of the nominal load (20Nm); ▬ 50% of the nominal load (65Nm);
▬ 80% of the nominal load (105Nm); ▬ 100% of the nominal load (130Nm).

Figure 4. Numbering of the pitted teeth (4,8,9,12) of the pinion. Tooth 1 as reference.

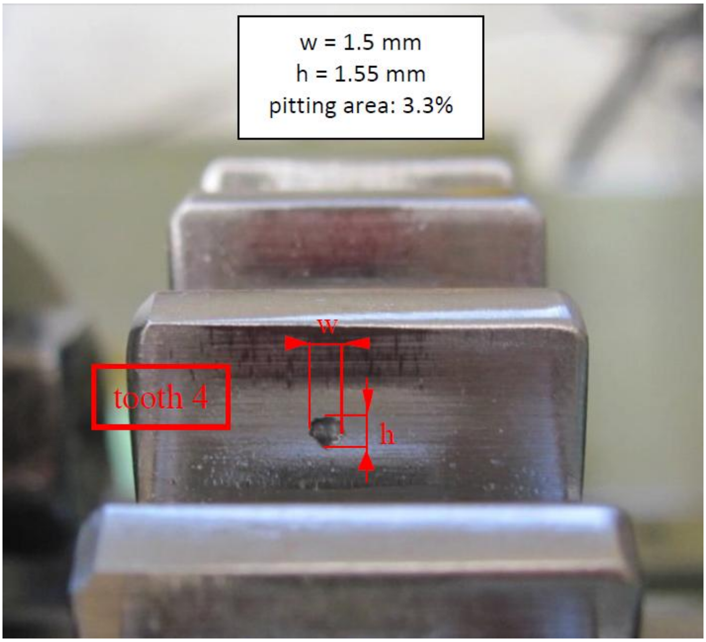

Figure 5. Pitting on tooth 4 of the pinion.

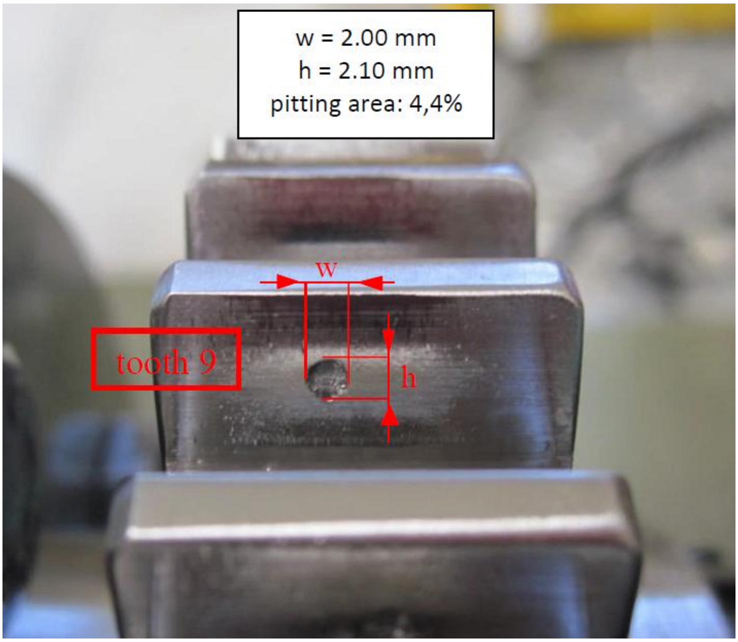

Figure 6. Pitting on tooth 9 of the pinion.

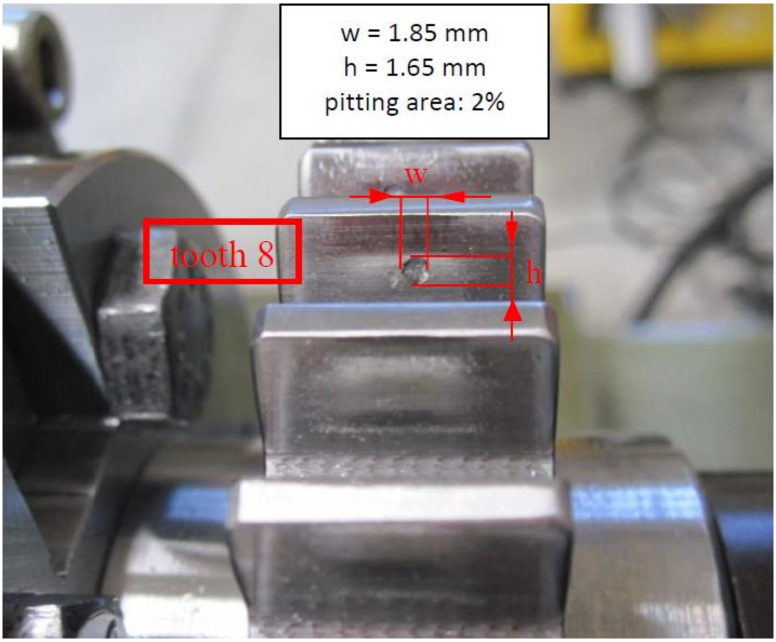

Figure 7. Pitting on tooth 8 of the pinion.

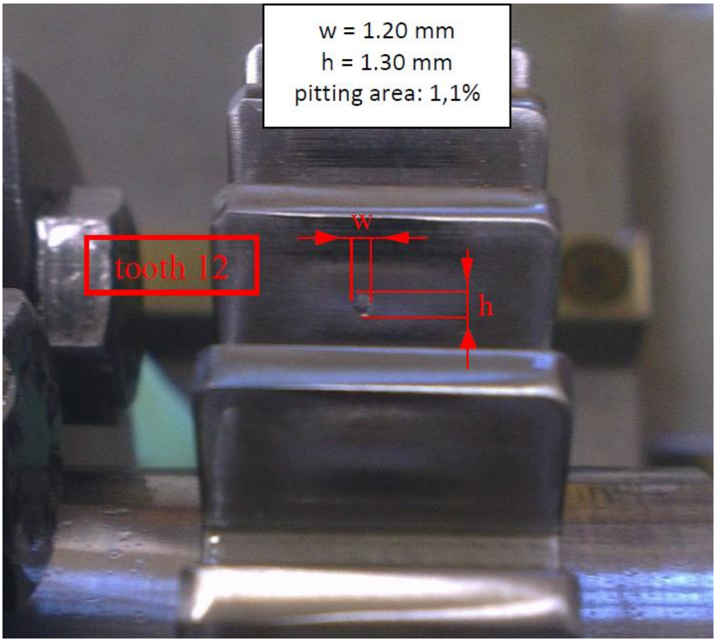

Figure 8. Pitting on tooth 12 of the pinion.

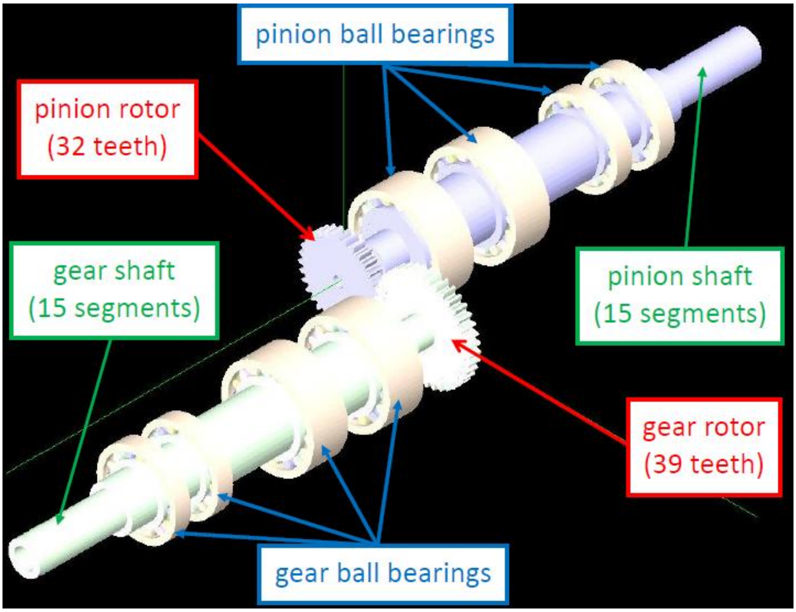

Figure 9. FEM modelling of the mechanical system (pinion, gear, shafts, bearings).

3. NUMERICAL ANALYSIS OF GEAR STRESS

In this section, results of finite element analyses performed in order to obtain the gear stress distribution and to validate the experimental stress-vibration correlations are reported.

The FEM modelling of the test rig is carried out using the numerical software Calyx® (Transmission3D): the multi-body finite element model is build up, the stresses and strains of the different elements of the mechanical system are investigated.

The FEM modelling of the overall mechanical system (pinion, gear, shafts, bearings) is shown in Figure 9.

The mechanical system is composed by:

- pinion rotor (sun: 32 teeth, shaft: 15 segments, bearing inner race: 6 sectors);
- gear rotor (sun: 39 teeth, shaft: 15 segments, bearing inner race: 6 sectors);
- ground (bearing outer race: 12 sectors);
- bearings (pinion: 2 sectors × 15 rollers + 4 sectors × 17 rollers, gear: 4 sectors × 17 rollers + 2 sectors × 15 rollers).

In the present dynamic analyses, the external torque is applied to the pinion, while the rotational frequency is applied to the gear; the displacement constrains (u,v,w) = 0 are imposed to the pinion; the displacement constrains (u,v,w) = 0 and the rotational constraints $(\theta x,\theta y,\theta z) = 0$ are imposed to the gear.

The dynamic factors and RMS accelerations obtained by means of a 2-dof dynamic model previously developed are given in Table 1; these last results are used in the dynamic FEM simulations in order to obtain numerical stress-vibration correlations.

In particular it must be underlined that test A (with n_1=0RPM) denotes a static analysis, tests B-E (with n_1=800-1325RPM) represent dynamic analyses.

In the following, the maximum normal stress and contact pressure on the contact tooth of the pinion vs. vibration amplitude for the different cases of Table 1 are investigated.

Maximum Normal Stress vs. Vibration Amplitude

In Figure 10, the behaviour of the maximum normal stress σ_{max} at the base of the contact tooth of the pinion rotor vs. the vibration amplitude a_{RMS} at the initial contact time obtained by FEM analyses is reported.

The input rotor is the pinion (contact tooth 25), the output rotor is the gear (contact tooth 9).

The external torques T[Nm] of Table 1 are imposed to the pinion. The corresponding values of maximum normal stress are reported in Table 2.

From Figure 10, it can be observed a linear behaviour of the maximum normal stress for all the vibration amplitudes considered.

Table 1. Dynamic factors and RMS accelerations.

Test	**n_1[RPM]**	**a_{RMS}[g]**	**T[Nm]**	**f_d=T/T_n**
A	0	0	130.0	1.00
B	800	0.15	161.2	1.24
C	985	0.33	194.0	1.49
D	1200	1.73	455.5	3.50
E	1325	0.73	256.8	1.97

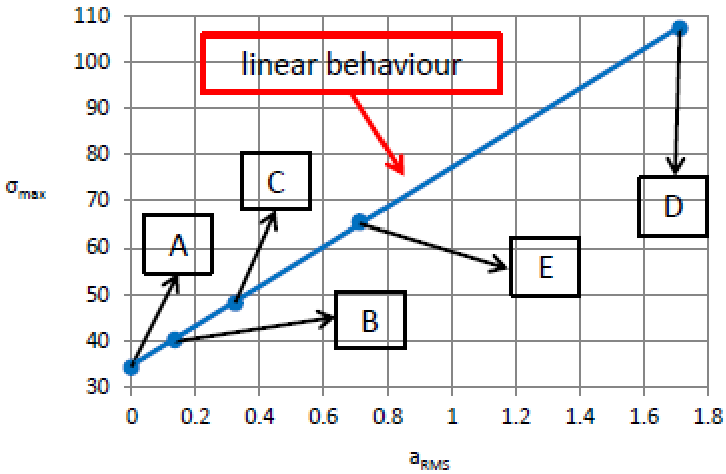

Figure 10. Maximum normal stress σ_{max} at the base of the contact tooth of the pinion rotor vs. vibration amplitude a_{RMS}. FEM analyses.

Maximum Contact Pressure vs. Vibration Amplitude

In Figure 11, the maximum contact pressure p_{max} on the contact tooth of the pinion rotor vs. the vibration amplitude a_{RMS} at the initial contact time obtained by FEM analyses is reported.

The input rotor is the pinion (contact tooth 25), the output rotor is the gear (contact tooth 9).

The imposed lead crown surface modification along the face width of the teeth gives a semi-elliptical Hertzian distribution of the contact normal pressure.

The different external torques T reported in Table 1 are imposed to the pinion. The values of maximum contact pressure are reported in Table 3.

From Figure 11, it can be observed an initial nonlinear behaviour of the maximum contact pressure (for a_{RMS}=0-0.5g, tests A-B-C), which becomes quasi-linear by increasing the vibration amplitude (for a_{RMS}=0.5-1.8g, tests E-D).

Table 2. Maximum normal stress vs. Vibration amplitude.

Test	$\mathbf{a_{RMS}}$**[g]**	$\boldsymbol{\sigma_{max}}$**[N/mm^2]**
A	0	33.2
B	0.15	40.5
C	0.33	48.2
D	1.73	106.4
E	0.73	62.6

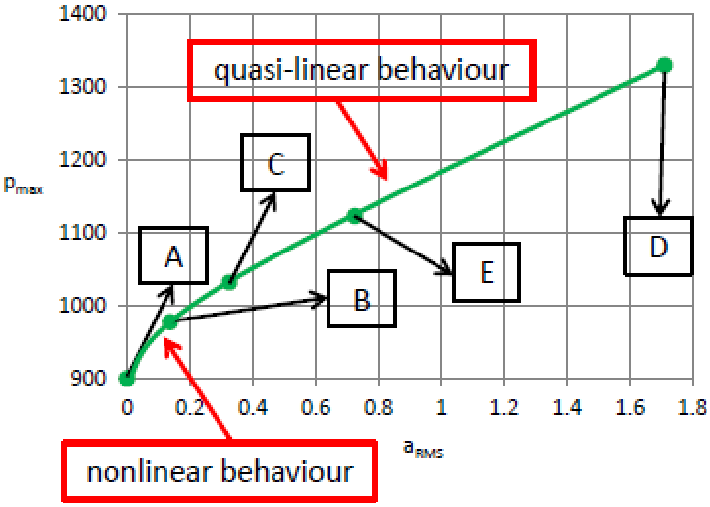

Figure 11. Maximum contact pressure p_{max} on the contact tooth of the pinion rotor vs. vibration amplitude a_{RMS}. FEM analyses.

4. CONCLUSIONS

In this paper, the pitting phenomenon and stress distribution of gears are considered.

Pitting durability experimental tests are made at 130Nm of nominal load, 840RPM of rotational frequency and 0.2g of RMS amplitude.

After a 4 hour test at an external temperature of 20°C, a visible pitting phenomenon is present in four different teeth (4,8,9,12) of the pinion, where for each pitted tooth the pitting size is estimated as a percentual of the total flank area 1.42cm^2, with pitting sizes 3.3%, 4.4%, 2%, 1.1%, respectively.

Numerical FEM analyses are performed in order to investigate gear contact pressure and normal stress distribution.

The maximum normal stress at the base of the contact tooth of the pinion at the initial time presents a linear behaviour for all the vibration amplitude values.

The maximum contact pressure on the contact tooth of the pinion at the initial time gives an initial nonlinear behaviour, which becomes quasi-linear by increasing the vibration amplitude.

Table 3. Maximum contact pressure vs. vibration amplitude.

Test	a_{RMS}[g]	p_{max}[N/mm^2]
A	0	904.7
B	0.15	972.4
C	0.33	1023.2
D	1.73	1329.7
E	0.73	1108.6

REFERENCES

[1] Fukumasu NK, Machado GAA, Souza RM, and Machado IF, 2016. "Stress Analysis to Improve Pitting Resistance in Gear Teeth", *Proceedings of the 3rd CIRP Conference on Surface Integrity*, **45**, pp. 255-258.

[2] Faggioni M, Samani FS, Bertacchi G, and Pellicano F, 2011. "Dynamic optimization of spur gears", *Mechanism and Machine Theory*, **46**, pp. 544-557.

[3] Bonori G, Barbieri M, and Pellicano F, 2008. "Optimum profile modifications of spur gears by means of genetic algorithms", *Journal of Sound and Vibration*, **313**, pp. 603-616.

[4] Barbieri M, Bonori G, and Pellicano F, 2012. "Corrigendum to: Optimum profile modifications of spur gears by means of genetic algorithms", *Journal of Sound and Vibration*, **331**, pp. 4825-4829.

[5] Choy FK, Polyshchuk V, Zakrajsek JJ, Handschuh RF, and Townsend DP, 1996. "Analysis of the effects of surface pitting and wear on the vibration of a gear transmission system", *Tribology International*, **29**, pp. 71-83.

[6] Barbieri M, Zippo A, and Pellicano F, 2014. "Adaptive grid-size finite element modelling of helical gear pairs", *Mechanism and Machine Theory*, **82**, pp. 17-32.

[7] Masoumi A, Pellicano F, Samani FS, and Barbieri M, 2015. "Symmetry breaking and chaos-induced imbalance in planetary gears", *Nonlinear Dynamics*, **80**, pp. 561-582.

[8] Del Rincon F, Viadero F, Iglesias M, De-Juan A, Garcia P, and Sancibrian R, 2012. "Effect of cracks and pitting defects on gear meshing", *Proceedings of the IMechE Part C: Journal of Mechanical Engineering Science*, **226**, pp. 2805-2815.

[9] Gelman L, Chandra NH, Kurosz R, Pellicano F, Barbieri M, and Zippo A, 2016. "Novel spectral kurtosis technology for adaptive vibration condition monitoring of multi-stage gearboxes", *Non-Destructive Testing and Condition Monitoring*, **58**, pp. 409-416.

[10] Barbieri M, Lubrecht AA, and Pellicano F, 2013. "Behavior of lubricant fluid film in gears under dynamic conditions", *Tribology International*, **62**, pp. 37-48.

METRICHE VIBRAZIONALI PER IL MONITORAGGIO DELL'USURA DISTRIBUITA IN RIDUTTORI EPICICLOIDALI

Francesco Berlato
Department of Engineering,
University of Ferrara, Italy
E-mail: francesco.berlato@unife.it

Gianluca D'Elia
Department of Engineering,
University of Ferrara, Italy
E-mail: gianluca.delia@unife.it

Emiliano Mucchi
Department of Engineering,
University of Ferrara, Italy
E-mail: emiliano.mucchi@unife.it

Giorgio Dalpiaz
Department of Engineering,
University of Ferrara, Italy
E-mail: giorgio.dalpiaz@unife.it

Abstract.
Oggigiorno il monitoraggio dei riduttori è un'esigenza sempre più sentita ed importante nell'industria. In particolare, questo lavoro riguarda il monitoraggio dell'usura distribuita (pitting) nei riduttori epicicloidali, mediante l'impiego di alcune metriche della media sincrona del segnale vibratorio, basate sul momento statistico del quart'ordine: si tratta di FM4, NA4 e NA4; si propone inoltre un nuovo indicatore di condizione chiamato NA4mod. L'efficacia di queste metriche nell'individuare l'insorgere di difetti distribuiti è stata valutata e confrontata conducendo una prova di usura accelerata su banco prova in configurazione back-to-back della durata di circa 700 ore, in cui uno dei due riduttori è stato portato a fine vita. L'articolo introduce le metriche impiegate, descrive la prova condotta e ne presenta e discute i risultati. La nuova metrica proposta, NA4mod, ha evidenziato una soddisfacente capacità di rilevamento dell'insorgere del pitting, con maggiore affidabilità rispetto ad altre metriche presenti in letteratura; NA4mod risulta inoltre sensibile sia all'innesco sia all'evoluzione del pitting.*

Keywords: *Monitoraggio, Vibrazioni, Metriche, Riduttori epicicloidali, Usura distribuita*

1. INTRODUZIONE

I rotismi epicicloidali permettono di ottenere rapporti di trasmissione spinti, mantenendo peso e dimensioni contenuti [1] e un buon rendimento. Offrono quindi interessanti vantaggi applicativi, tali da proporsi come una valida alternativa ai riduttori ordinari in diverse applicazioni industriali: i vantaggi sono tanto più sensibili quanto più le applicazioni richiedono riduttori con elevati rapporti di riduzione, elevate coppie da trasmettere ed elevati carichi da sopportare sull'albero in uscita. Per un riduttore epicicloidale ciò comporta, a parità di rapporto di trasmissione un miglior dimensionamento degli ingranaggi, ingombri contenuti e costi minori.

Ogni macchinario in cui vi siano componenti in movimento dà luogo a vibrazioni e quindi a rumore. In funzione del proprio stato di funzionamento, ogni macchinario è caratterizzato da una specifica "firma vibratoria". E' quindi possibile utilizzare i cambiamenti di questa firma, come indicatori dell'imminente presentarsi di un difetto. Molteplici procedure di analisi dei segnali sono state sviluppate per il monitoraggio e la diagnostica a partire da circa una trentina di anni fa [2, 3], quando si cominciò ad applicare un gran numero di tecniche di analisi del segnale con lo scopo di estrarre interessanti informazioni dalla firma vibratoria: si citano, a titolo di esempio, le applicazioni a riduttori epicicloidali utilizzati negli impianti di sollevamento [4], nelle turbine eoliche [5] o nella trasmissione degli elicotteri [6].

Le tecniche di analisi dei segnali possono essere suddivise in base al loro dominio di appartenenza: si può quindi distinguere tecniche di analisi in base tempo, frequenza e tempo-frequenza. Nell'ambito delle tecniche in base tempo, un efficace strumento d'indagine per molte tipologie di difetto è lo studio della media sincrona del segnale [7–9]. Il risultato della media sincrona è un segnale mediato, sincronizzato con la rotazione di un organo rotante di riferimento, in cui le componenti aleatorie e non sincronizzate con il riferimento vengono attenuate dall'operazione di media. Inoltre si possono applicare alla media sincrona dei filtri passa-banda per filtrare le principali componenti dell'ingranamento e le relative armoniche; l'applicazione della trasformata di Hilbert permette poi di determinare le modulazioni di ampiezza e fase [10–12], che possono indicare la presenza di difetti locali. Per ottenere indici della presenza di malfunzionamenti e della loro severità si caratterizza il segnale nel dominio del tempo o la media sincrona tramite parametri statistici o metriche di vario tipo [13–18]. Nell'articolo di D'Elia et al. [17] vengono confrontati alcuni indici di condizione presenti in letteratura [13, 18] mediante un test accelerato a fine vita. I risultati ottenuti mostrano i limiti delle tecniche presenti in letteratura se applicate ad un riduttore epicicloidale soggetto a pitting e pertanto vengono definite due nuove metriche che risultano essere più promettenti per l'individuazione del pitting in uno stadio di riduzione epicicloidale.

Potenziali difetti possono essere individuati anche mediante lo studio dello spettro in frequenza del segnale come descritto da Randall [19]. E' importante ricordare che tutti i metodi di calcolo della trasformata di Fourier discreta si applicano a segnali stazionari periodici nel dominio di riferimento o a singoli transitori. Tuttavia, i difetti localizzati di un ingranaggio in genere introducono componenti non-stazionarie nel segnale [12, 20], che non possono essere studiate mediante le tecniche di analisi convenzionali. Da qui emerge l'importanza di utilizzare tecniche di analisi tempo-frequenza come la Trasformata Wavelet Continua (CWT) [7, 21–23] e la Distribuzione di Wigner-Ville (WVD) [15, 20, 24, 25]. Come descritto in [12, 20], l'ingranamento di un dente difettoso può essere efficacemente individuato sia dalla distribuzione delle ampiezze che dalla distribuzione delle fasi della CWT. La WVD fornisce una rappresentazione in alta risoluzione nel dominio tempo-frequenza per un segnale non stazionario e possiede molte altre interessanti caratteristiche enunciate in [24, 25]. Purtroppo questa distribuzione di energia contiene anche fuorvianti termini incrociati, relativi a componenti in diverse regioni tempo-frequenza [20].

In questo articolo viene valutata e confrontata l'efficacia di alcune metriche del segnale vibratorio, basate sul momento statistico del quart'ordine, ai fini del monitoraggio dell'usura distribuita in riduttori epicicloidali [13, 18, 26, 27]; si proporrà a tal riguardo una nuova metrica, NA4mod, derivata dal parametro NA4 introdotto da Zakrajsek [14].

La struttura dell'articolo è la seguente. In questo paragrafo si è introdotto lo stato dell'arte per il monitoraggio di difetti distribuiti nei riduttori epicicloidali. Nel prossimo paragrafo sarà descritta più nel dettaglio la metodologia utilizzata in questo articolo con la definizione delle metriche discusse in questo lavoro. Infine si presentano l'apparato sperimentale utilizzato e i risultati con la loro discussione, chiudendo quindi con le conclusioni sul lavoro svolto.

2. METRICHE IMPIEGATE NELL'ANALISI DEL SEGNALE

In letteratura il metodo di McFadden [8, 9] è uno degli algoritmi più utilizzati per estrarre la media sincrona (TSA) con le ruote dentate di un rotismo epicicloidale partendo dal segnale di un accelerometro montato sulla cassa. Innanzitutto, mediante un segnale tachimetrico, il segnale vibratorio va ricampionato in base angolo sulla rotazione del portasatelliti.

Partendo da un segnale in base angolo riferito al portasatelliti dello stadio epicicloidale di interesse, si deve quindi estrarre uno alla volta il segnale del dente del satellite che ingrana con il dente della corona sotto l'accelerometro. Per farlo si utilizza una finestra temporale di lunghezza opportuna e si ripete l'operazione una volta al giro del portasatelliti, finché non sono stati estratti i segnali relativi a tutti i denti della ruota di interesse, satellite o solare. Si ripete poi l'operazione, ottenendo il segnale corrispondente a più giri della ruota di interesse, e si mediano i segnali dei diversi giri in modo sincrono. Va impiegato un numero di medie opportuno per ottenere un elevato rapporto tra segnale e rumore. Con questa serie di operazioni si ottiene il segnale sincrono della ruota dentata di interesse.

Oltre a trattare la media sincrona del segnale, ottenuta attraverso il metodo di McFadden [9], come un qualsiasi segnale di vibrazione (cioè l'analisi nel dominio del tempo e l'analisi spettrale possono ancora essere applicati), la sua natura periodica consente di dare maggiore spazio alla manipolazione del segnale rispetto ad un segnale di vibrazione convenzionale. Infatti la trasformata di Fourier di un segnale periodico è costituito da linee spettrali discrete pure e senza leakage, alla quale si può applicare un filtraggio ideale; cioè, una o più linee di frequenza (che qui rappresentano ordini di rotazione della ruota) possono essere completamente rimosse dallo spettro senza causare discontinuità quando il segnale è tradotto nuovamente al dominio dell'angolo. Questo permette l'applicazione di varie tecniche di analisi del segnale, specificamente progettate per il trattamento delle medie dei segnali sincroni, e di una serie di relative metriche del segnale da utilizzare come ausilio al rilevamento dei guasti e per la diagnosi.

Nel proseguo di questo paragrafo si definiscono le metriche impiegate nel presente lavoro. Si premette la definizione dei segnali regolare, differenza e residuo, ottenuti dalla media sincrona [28] e impiegati nelle metriche descritte in seguito, come illustrato anche dallo schema di Fig. 1.

Segnale regolare: segnale contenente soltanto la frequenza di ingranamento e le sue armoniche.

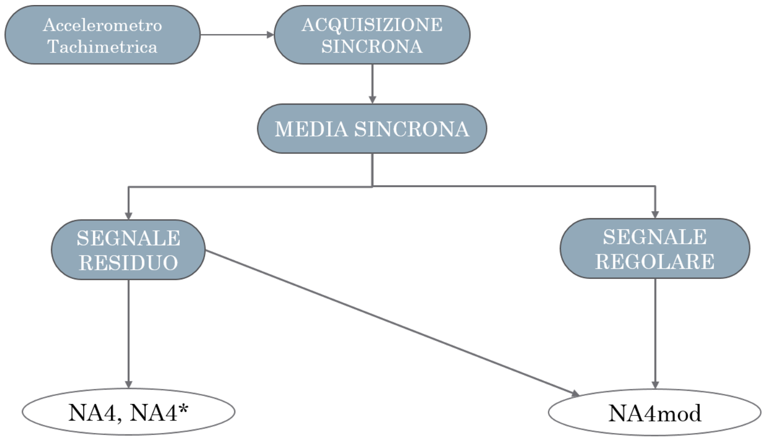

Figura 1. Schema della metodologia di analisi delle vibrazioni per il calcolo di NA4, NA4*, NA4mod.

Segnale differenza: segnale ottenuto dalla media sincrona eliminando le componenti dell'ingranamento (fondamentale ed armoniche), la prima banda laterale associata alle componenti dell'ingranamento e la $1x$ e la $2x$ della frequenza di rotazione.

Segnale residuo: segnale ottenuto dalla media sincrona eliminando le componenti dell'ingranamento (fondamentale ed armoniche) e la $1x$ e la $2x$ della frequenza di rotazione.

FM4

Stewart [13] ha sviluppato un certo numero di parametri adimensionali basati sulla media sincrona del segnale, che ha definito 'figure di merito'. Queste sono state originariamente definite come un gruppo gerarchico con cui Stewart descriveva una procedura per l'individuazione e la diagnosi parziale dei guasti. Il parametro FM4 fu proposto da Stewart nel 1977 [13], come complemento al parametro FM0 per l'individuazione di difetti localizzati su un numero limitato di denti [17]. Se la variazione della media del segnale non poteva essere attribuita ad uno qualsiasi degli errori specifici di ingranamento predefiniti, FM4 fu definito per rilevare difetti legati all'ingranamento. Stewart ha argomentato che, se si potesse definire il contenuto in frequenza previsto per la vibrazione di un albero particolare (il segnale normale), allora tutte le altre vibrazioni rappresenterebbero la deviazione (il segnale residuo) dal segnale atteso. Egli ha proposto che il segnale regolare normalmente include tutte le frequenze di ingranamento e le loro armoniche, più le loro bande laterali immediatamente adiacenti. Il segnale differenza viene semplicemente calcolato trasformando nel dominio delle frequenze, eliminando tutte le componenti definite per il segnale regolare e ritrasformando nel dominio angolare. L'indagine sperimentale di Stewart [13] ha mostrato che FM0 non era un rilevatore molto sensibile di guasti localizzati sul dente, come le fratture dei denti, e ha suggerito che FM4 poteva essere usato come rilevatore generale più sensibile.

In virtù della sensibilità di FM4 in qualità di rilevatore del guasto generale, e della sua facilità di implementazione rispetto ai rilevatori di guasto più specifici (FM1, FM2 e FM3), una serie di indagini sperimentali basate sul lavoro di Stewart si è concentrata su tecniche di miglioramento collegate alla metrica FM4 (ad esempio Zakrajšek [14]).

La metrica di diagnostica vibrazionale FM4 è una delle più utilizzate; essa individua le variazioni nelle vibrazioni risultanti dai difetti localizzati su pochi denti. L'indice FM4 è adimensionale ed è ottenuto dividendo il quarto momento statistico centrale del segnale differenza (d_i) per il quadrato della varianza del segnale differenza stesso. In generale il risultato è che, fintanto che il difetto si propaga localmente, la metrica FM4 aumenta, mentre quando il difetto inizia a diventare distribuito, il valore cala.

$$FM4 = \frac{\frac{1}{N}\sum_{i=1}^{N}(d_i - \overline{d})^4}{[\frac{1}{N}\sum_{i=1}^{N}(d_i - \overline{d})^2]^2} \tag{1}$$

NA4

Il parametro NA4 fu ideato nel 1993 da Zakrajsek et al. al Centro di Ricerca Lewis della NASA come un indicatore generale di guasto sensibile non solo all'inizio del difetto, come il parametro FM4, ma anche al suo progredire [16]. Infatti, con il progredire del difetto nel numero e nella gravità, la metrica FM4 diventa meno sensibile ai nuovi difetti. Sono pertanto state apportate due modifiche alla metrica FM4 per sviluppare la metrica NA4: la prima consiste nel calcolo della metrica a partire dal segnale residuo e non, come nel caso di FM4, a partire dal segnale differenza; la seconda è la capacità dell'analisi della tendenza, tenendo conto dei record precedenti alla misura corrente. Queste due modifiche fanno la metrica NA4 una metrica maggiormente sensibile e robusta. Quindi NA4 è definito come il rapporto tra il momento statistico del quart'ordine del segnale residuo e la media corrente del quadrato della varianza del segnale residuo stesso; tale media è calcolata su tutti i record precedenti alla misura corrente.

$$NA4 = \frac{\frac{1}{N}\sum_{i=1}^{N}(r_i - \overline{r})^4}{\frac{1}{M}\sum_{j=1}^{M}[\frac{1}{N}\sum_{i}(r_{ij} - \overline{r_j})^2]^2} \tag{2}$$

dove

- r_i è l'i-esimo punto nella registrazione temporale del segnale residuo
- r è il valore medio del segnale residuo
- r_{ij} è l'i-esimo punto nella j-esima registrazione temporale del segnale residuo
- j è la registrazione attuale
- i è l'indice del dato in lettura
- M è la registrazione corrente nel run ensemble
- N è il numero di punti nella registrazione temporale

NA4*

Il parametro NA4$*$ fu sviluppato nel 1994 da Decker, Handschuh e Zakrajsek [16] come un miglioramento dell'indice NA4. In questo caso, il denominatore di NA4 è stato modificato statisticamente. Questa modifica venne effettuata sulla base dell'osservazione che, con il progredire del difetto sulla ruota dentata da localizzato a distribuito, il valore medio della varianza aumenta rapidamente, con la conseguenza che il parametro NA4 cala. Per ovviare a questo problema è stata introdotta la normalizzazione del quarto momento sul quadrato della varianza di segnali di riferimento acquisiti all'inizio in condizioni operative nominali, ottenendo un miglioramento nella tendenza. Quindi, il quarto momento centrale del segnale residuo è normalizzato con il quadrato della varianza media per un riduttore in buone condizioni, questo consente al parametro $NA4*$ di crescere con il progredire del difetto.

$$NA4* = \frac{N\sum_{i=1}^{N}(r_i - \overline{r})^4}{(var(r_{OK}))^2} \tag{3}$$

dove

- $var(r_{OK})$ è la varianza per un riduttore in buone condizioni

NA4mod

Questa è una nuova metrica che si aggiunge a quelle proposte recentemente [17] dal gruppo di ricerca dell'Università degli Studi di Ferrara.

Il parametro originale presentato in questo lavoro è una modifica della metrica NA4. Analogamente a NA*, si è pensato di modificare in modo diverso il parametro NA4 per ottenere un'indicazione correlata alla severità di un difetto su una ruota dentata, anche quando nel suo progredire questo passa da localizzato a distribuito. Invece di utilizzare a denominatore la varianza del segnale residuo, si è deciso di normalizzare il quarto momento statistico del residuo con la media corrente del quadrato della varianza del segnale regolare. Lo scopo, oltre ad una maggiore stabilità, è quello di legare l'indice alla condizione dell'ingranamento utilizzando il segnale regolare ad esso associato.

$$NA4mod = \frac{\frac{1}{N}\sum_{i=1}^{N}(r_{iM} - \overline{r}_M)^4}{\frac{1}{M}\sum_{j=1}^{M}[\frac{1}{N}\sum_{i=1}^{N}(sr_{ij} - \overline{sr_j})^2]^2} \tag{4}$$

dove

- r è il segnale residuo
- $\overline{r}$ è valore medio del segnale residuo
- sr è il segnale regolare
- $\overline{sr}$ il valore medio del segnale regolare
- j è la registrazione attuale
- i è l'indice del dato in lettura
- M è la registrazione corrente nel run ensemble
- N è il numero di punti nella registrazione temporale

3. PROVE SPERIMENTALI

Apparato sperimentale e metodologia

Per studiare il comportamento degli indicatori di condizione si sono utilizzati i dati acquisiti durante la prova utilizzata anche per il lavoro presentato da D'Elia et al. [17]. Questo test è stato realizzato per simulare un caso reale di danneggiamento durante il funzionamento del riduttore. Con questa prova si vuole portare il riduttore al massimo danneggiamento possibile, dato dal pitting, senza comprometterne la funzionalità e creare problemi nell'area di prova.

La prova di durata è stata eseguita utilizzando due riduttori Bonfiglioli 304 L3 220 P CP100, chiamati rispettivamente "Riduttore A" e "Riduttore B", in una configurazione denominata back to back (Fig. 2(a)). I dati del riduttore sono riportati in Tab. 1 mentre lo schema del riduttore è visibile in Fig. 2(b).

Per poter avere il massimo controllo della prova ed ottenere elevati carichi applicati si è scelta una configurazione a riduttori contrapposti con ricircolo di potenza elettrica (Fig. 2(a)), dove uno dei due riduttori lavora come moltiplicatore. I due riduttori identici sono collegati attraverso l'albero lento, mediante un doppio giunto cardanico. Ognuno di essi è

Tabella 1. Dati del riduttore.

Data	Stadio 1	Stadio 2	Stadio 3
Denti del solare	10	10	24
Denti del satellite	25	25	26
Denti della corona	62	62	78
♯ di Pianeti	3	3	4
Rapporto Stadio	7.2	7.2	4.25
Rapporto Totale	220		
N_{reset}	25	25	4

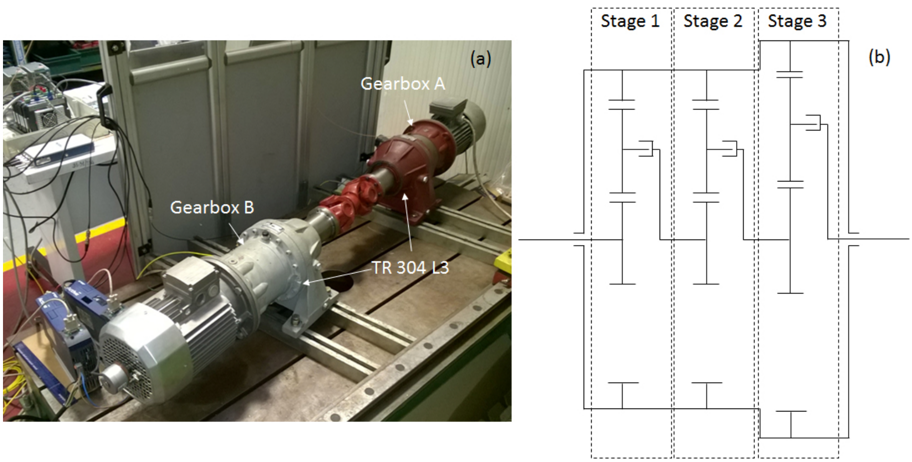

Figura 2. (a) Apparato sperimentale; (b) Schema del riduttore.

azionato da un motore elettrico asincrono trifase da 4 kW (Bonfiglioli BN 112 L4) dotato di un encoder incrementale Sick a 1024 linee, utilizzato per il controllo in retroazione. Per gestire la potenza in maniera efficace si sono impiegati due inverter Bonfiglioli Active-CUBE: il primo aziona un motore elettrico per portare in trascinamento i due riduttori controllandone la velocità attraverso l'encoder di estremità; il secondo inverter comanda il motore collegato al riduttore in moltiplica. Questo secondo motore lavora come un generatore di corrente e attraverso l'inverter è possibile regolare l'assorbimento di corrente grazie al controllo di posizione fornito dall'encoder.

Due accelerometri piezoelettrici B&K 4507 sono stati incollati sulle casse dei due riduttori in corrispondenza della corona del secondo stadio. I segnali di vibrazione sono stati poi acquisiti in continuo con una frequenza di campionamento di 25600Hz mediante una scheda National Instruments NI9234.

Il segnale tachimetrico è stato ottenuto attraverso la funzione dell'inverter di duplicare il segnale dell'encoder riducendo di un trentesimo il numero di linee. Infatti, 1024 linee a 1500 rpm, considerando dieci armoniche delle frequenza di rotazione, richiedono una frequenza di campionamento in analogico molto maggiore della capacità della scheda utilizzata (500 kHz contro i 51 kHz).

Per velocizzare la prova a fine vita si è riempito il moltiplicatore (Riduttore B) con l'olio standard previsto a catalogo e un olio con viscosità minore per il riduttore oggetto della prova di danneggiamento (Riduttore A). Si è poi incrementato il carico oltre quello nominale di catalogo per ottenere un'usura maggiore. Dopo circa 700 ore ad una velocità costante di 1500rpm con una coppia applicata di 4400Nm (superiore del 30% alla coppia nominale riportata a catalogo per questa velocità) si è ottenuto un danneggiamento per pitting del solare del secondo stadio del riduttore A .

Evoluzione delle metriche: risultati e discussione

A causa della scarsa lubrificazione, alla fine della prova (circa 700 ore) quando si sono ispezionati i riduttori per verificarne lo stato di usura, si è riscontrato il pitting distribuito nel secondo solare del Riduttore A. Nella Fig. 3 si possono vedere i solari del primo e del secondo stadio a confronto. Gli effetti della prova di fatica accelerata (danneggiamento per pitting) sono molto evidenti sul solare del secondo stadio (cfr. Fig. 4(a)): questo presenta una forte ricalcatura nell'area di contatto dovuta alla pressione dell'ingranamento con i satelliti e un pitting che ha interessato anche il profilo di testa della dentatura e il fianco non in presa (crushing). Analizzando il Riduttore B, si è riscontrato un leggero pitting alla base del dente sul secondo solare 4(b).

L'analisi dei segnali ha visto il calcolo di numerosi indici statistici applicati sia al segnale temporale complessivo sia ai segnali TSA di tutte le ruote. Di seguito vengono presentati solamente quelli relativi al solare del secondo stadio. Inoltre, per visualizzare i risultati del test ogni sei ore, i grafici sono stati creati con un sottoinsieme di 107 acquisizioni.

Innanzitutto si mostra l'evoluzione dei più comuni parametri statistici, quali RMS e Kurtosis, valutati sui segnali originali (non mediati) nel dominio del tempo. È ben noto che il valore RMS sia correlato all'energia media del segnale, mentre il Kurtosis sia sensibile ai contenuti impulsivi. La Fig. 5 mostra il risultato di questa analisi. I valori RMS di Riduttore A relativi ai segnali nel tempo sono maggiori di quelli di Riduttore B (Fig. 5 (a)); questo effetto potrebbe essere correlato ai diversi oli utilizzati nei riduttori. Poiché i valori dell'energia principale dei segnali nel tempo sono differenti e l'evoluzione del danneggiamento sulla

Figura 3. Condizione del solare del primo e del secondo stadio per il Riduttore A alla fine della prova.

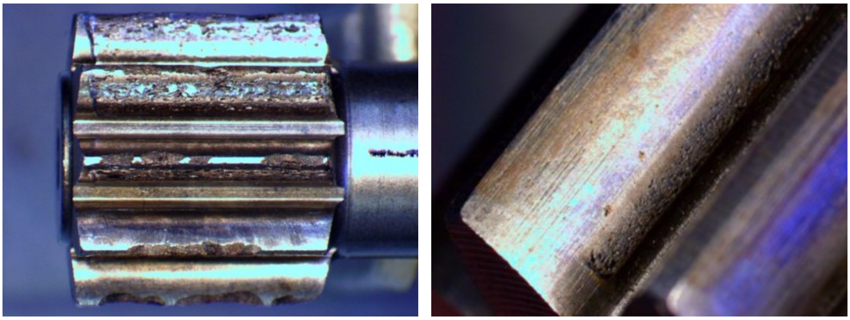

(a) (b)

Figura 4. Dettaglio dell'usura sui denti del solare del secondo stadio: (a) del Riduttore A; (b) del Riduttore B.

ruota è relativo ad un aumento dell'energia del segnale, per poter confrontare i valori dei trends RMS dei riduttori A e B, si è deciso di normalizzarli, dividendoli per il primo valore dell'evoluzione temporale. Il risultato di questa normalizzazione è riportato in Fig. 5 (b) dove si può vedere un aumento nella tendenza del valore RMS del segnale del riduttore A rispetto a B nell'intervallo temporale 100-400 ore, mentre le tendenze sono paragonabili alla fine della prova. Da questo risultato, non si può rilevare l'usura verificatasi nel Riduttore A. L'ultima statistica valutata sui segnali nel tempo è graficata in Fig. 5(c); I risultati mostrano un aumento dei valori di Kurtosis nel riduttore A rispetto a B nell'intervallo temporale 150-350 ore, mentre sono paragonabili alla fine della prova. L'incremento dei valori di Kurtosis potrebbe essere collegata all'innesco del pitting. In realtà, la formazione di pitting è correlata

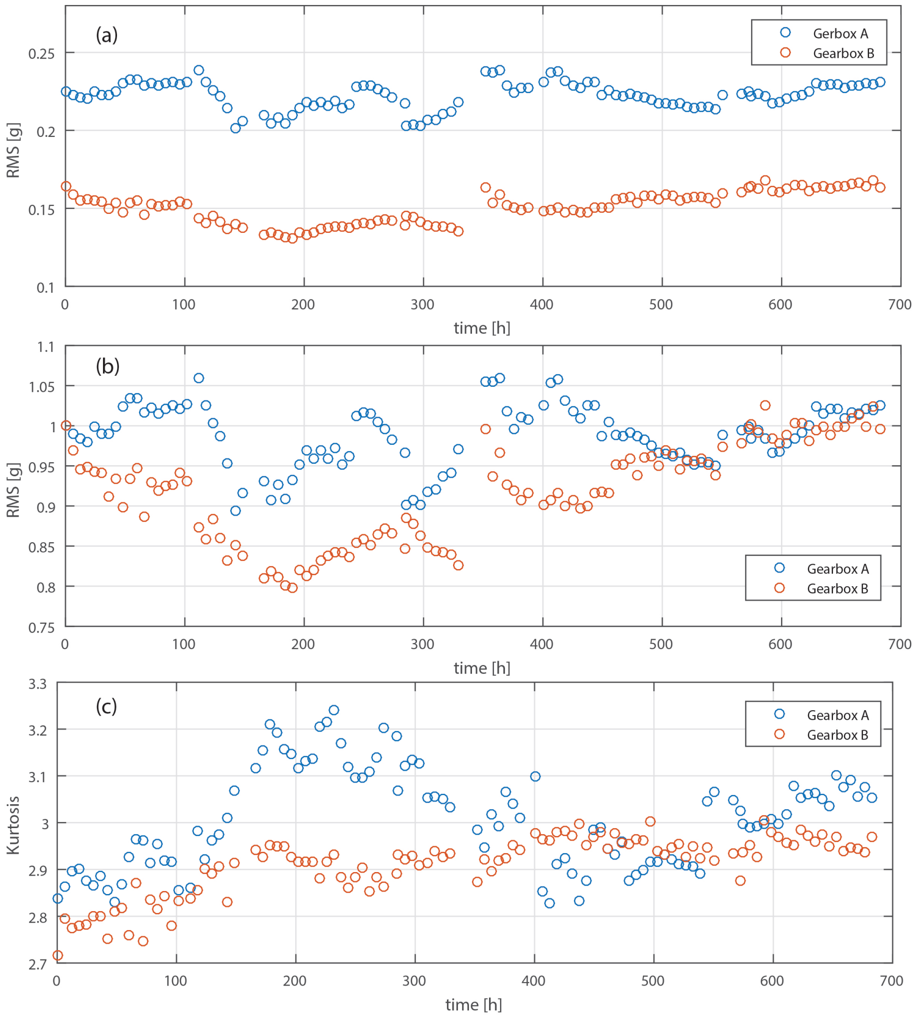

Figura 5. Metriche calcolate sul segnale vibrazionale originale: (a) RMS, (b) RMS normalizzato con il valore del primo campione, (c) Kurtosis.

ad un aumento del contenuto impulsivo nel segnale temporale. Questo comportamento viene rilevato dal Kurtosis, tuttavia, con l'avanzare del difetto i contenuti impulsivi del segnale diminuiscono e il valore Kurtosis crolla. Pertanto, questa statistica può anche rilevare l'innesco del guasto ma non la sua propagazione.

Per meglio evidenziare l'evoluzione del guasto, le metriche precedentemente descritte, calcolate sulla media sincrona (TSA), sono state applicate a tuttii solari ed i satelliti di entrambi i riduttori. Qui si presentano i risultati relativi al solare del secondo stadio del Riduttore A e del Riduttore B.

Il valore della metrica FM4 (Fig. 6(a)) mostra un aumento del suo valore alla fine del test

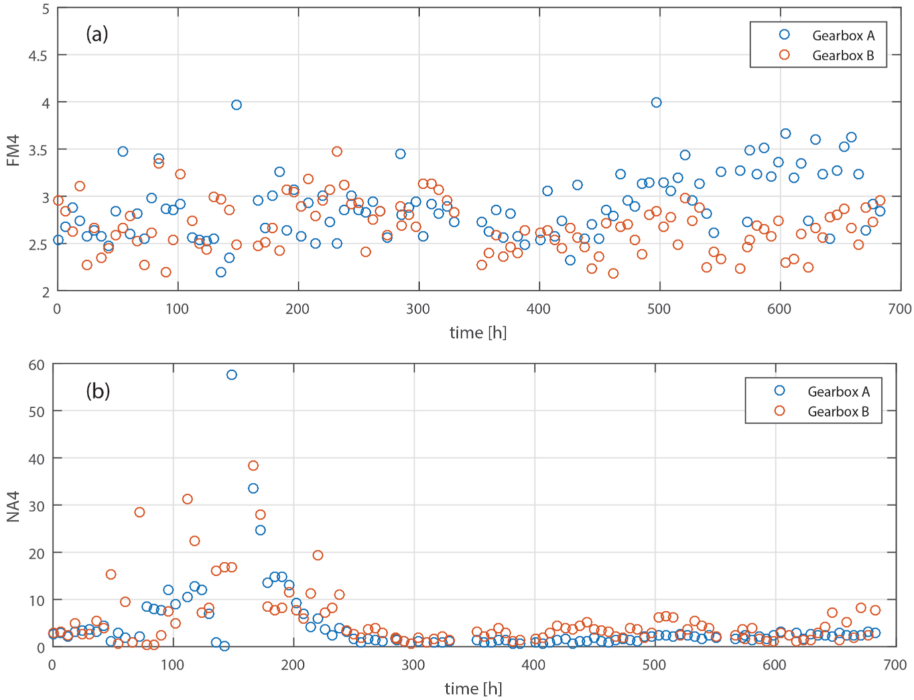

Figura 6. Metriche calcolate sulla media sincrona (TSA) del solare del secondo stadio: (a) FM4, (b) NA4.

nel Riduttore A rispetto al B, tuttavia questo aumento non indica con chiarezza la presenza di un guasto distribuito. Informazioni diagnostiche interessanti possono essere ottenute con l'analisi della metrica NA4. È possibile vedere, in particolare dalla Fig. 6(b), un aumento della metrica in entrambi i Riduttori A e B dopo circa 200 ore, che potrebbe essere connesso all'inizio del guasto. Questo comportamento è ben correlato con la tendenza del Kurtosis, che mostra un aumento dei valori del riduttore A a circa 200 ore. Analogamente queste metriche potrebbero rilevare l'inizio del guasto, ma non la sua crescita.

Oltre alle metriche appena citate si sono calcolate anche le evoluzioni per NA4* e NA4mod.Gli andamenti di questi due indici sono mostrati in Fig. 7 e Fig. 8. Il parametro NA4* del Riduttore A evidenzia bene l'innesco del pitting e mantiene un leggero trend crescente che potrebbe essere coerente con il tipo di usura. Tuttavia non risulta essere un indice affidabile per identificare l'innesco e la propagazione del pitting. Infatti, come è stato evidenziato in Fig. 7, il Riduttore B ha valori molto più alti che il Riduttore A, e questo non è accettabile.

La tendenza dell'indice NA4mod invece risulta molto più interessante e promettente (cfr. Fig. 8). Infatti il valore per il Riduttore A presenta un aumento tra le 150 e le 200 ore, assente per il Riduttore B, correlabile con l'aumento mostrato da altre metriche e indice di un possibile innesco del pitting. Inoltre questo parametro si dimostra anche abbastanza affidabile per il monitoraggio dell'avanzamento del difetto in quanto il suo valore per il Riduttore A rimane sempre superiore a quello relativo al Riduttore B. L'unico aspetto negativo risulta

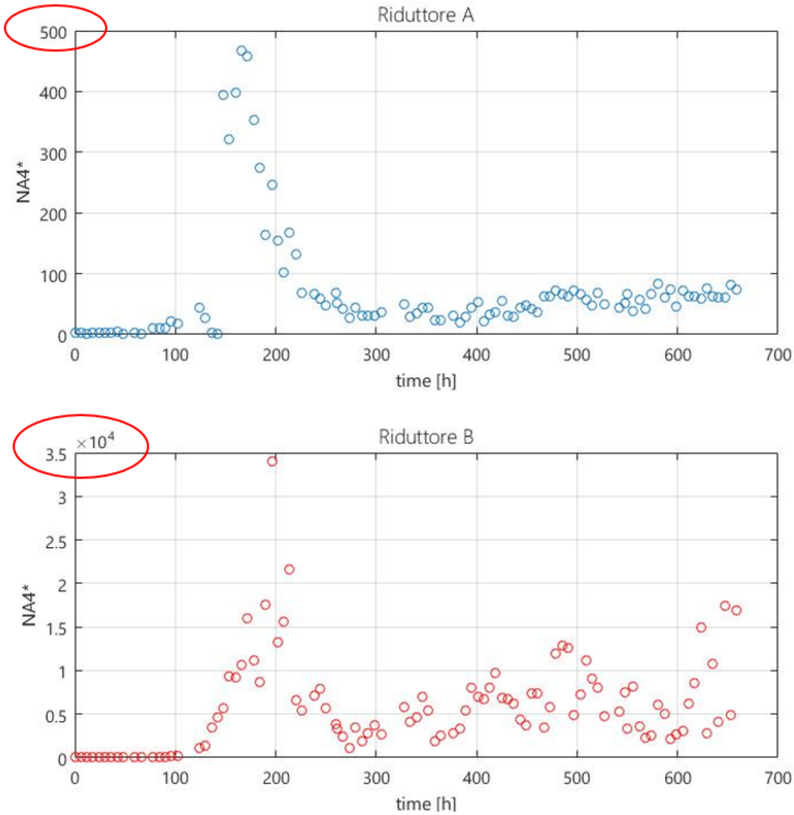

Figura 7. Metrica NA4* calcolata sul segnale TSA del solare del secondo stadio per il Riduttore A e il Riduttore B. *N.B. Si faccia attenzione alla diversa scala delle ordinate.*

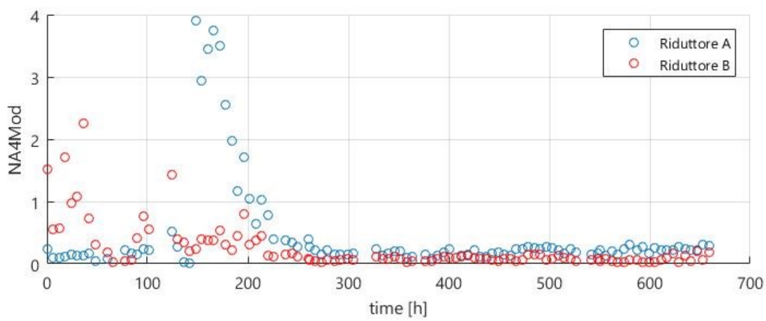

Figura 8. Metrica NA4mod calcolata sul segnale TSA del solare del secondo stadio per il Riduttore A e il Riduttore B.

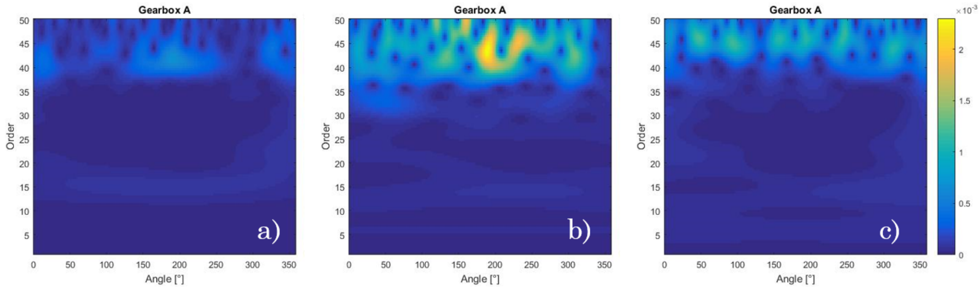

Figura 9. Trasformata Wavelet calcolata sul segnale TSA del solare del secondo stadio per il Riduttore A in tre condizioni diverse: (a) inizio prova, (b) innesco del pitting, (c) fine della prova.

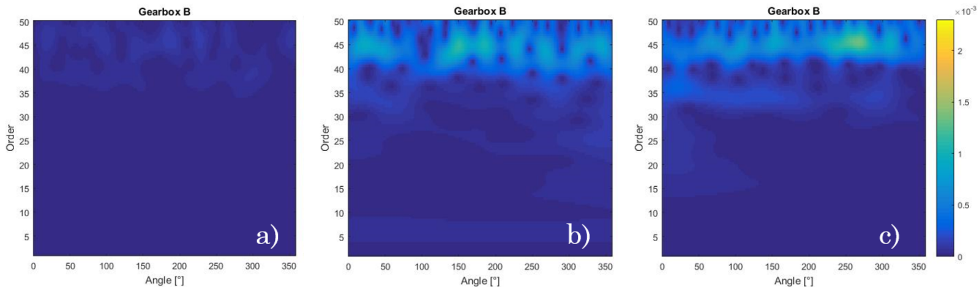

Figura 10. Trasformata Wavelet calcolata sul segnale TSA del solare del secondo stadio per il Riduttore B in tre condizioni diverse: (a) inizio prova, (b) innesco del pitting sul Riduttore A, (c) fine della prova.

nella parte iniziale della prova dove il Riduttore B ha valori maggiori del Riduttore A a fine vita e questo ne limita l'utilizzo.

Si osserva inoltre che le condizioni di usura tra i due solari del secondo stadio sono molto diverse mentre non si riscontra questa grande differenza nel parametro NA4mod alla fine della prova. Calcolando la Trasformata Wavelet (Fig. 9, Fig. 10) in tre momenti della prova (inizio, innesco pitting a 150 ore, fine), considerando il campo attorno ai 40 - 50 ordini, si può vedere bene come l'innesco del pitting sia avvenuto attorno alle 150 ore (Fig. 9(b)). Confrontando le Wavelet del Riduttore A con quelle del Riduttore B, si può notare come, alla fine della prova, il contenuto ad alta frequenza nel campo 40-50 ordini sia maggiore per il Riduttore A.

4. CONCLUSIONI

Si è condotta una prova di usura accelerata portata a fine vita, finalizzata ad individuare indicatori di condizione per il monitoraggio dei rotismi epicicloidali soggetti ad usura distribuita, adatti all'impiego in ambiente industriale, e a valutarne l'efficacia. I principali risultati possono essere sintetizzati come segue.

Riguardo al monitoraggio dell'insorgere e dell'evoluzione dell'usura di pitting sulla dentatura, si è valutata l'efficacia delle metriche proposte in letteratura e di una originale qui proposta: la metrica NA4mod, definita come il rapporto tra il momento del quart'ordine del segnale residuo e la media al tempo corrente del quadrato della varianza del segnale regolare, ha evidenziato una capacità di rilevamento soddisfacente, con maggiore affidabilità rispetto ad altre metriche presenti in letteratura.

La metrica proposta, inoltre, è sensibile sia all'innesco che all'evoluzione del pitting, ma in maniera meno netta rispetto ai parametri RV e CRV presentati da D'Elia et al. [17].

Risulta confermata la necessità di far seguire al rilevamento mediante gli indici statistici analisi avanzate (come analisi nel dominio Tempo-Frequenza), in grado di diagnosticare la condizione con maggiore sicurezza e precisione.

REFERENCES

[1] Smith, J., 1999. "Gear noise and vibration". *Marcel Dekker Inc.*

[2] Randall, R., 2002. "State of the art in monitoring rotating machinery". In Rotating Machinery: monitoring and diagnostics, Vol. **IV** of *Proceedings of ISMA*, pp. 1457–1478.

[3] Jardine, A., Lin, D., and Banjevic, D., 2006. "A review on machinery diagnostics and prognostics implementing condition-based maintenance". *Mechanical Systems and Signal Processing,* **20**, pp. 1483–1510.

[4] Assaad, B., Eltabach, M., and Antoni, J., 2014. "Vibration based condition monitoring of a multistage epicyclic gearbox in lifting cranes". *Mechanical System and Signal Processing,* **42**(1–2), January, pp. 351–367.

[5] Sawalhi, N., and Randall, R., 2014. "Gear parameter identification in wind turbines using diagnostic analysis of gearbox vibration signals". *Mechanical System and Signal Processing,* **42**(1–2), January, p. 368–376.

[6] Decker, H., and Lewicki, D., 2003. Spiral Bevel Pinion Crack Detection in a Helicopter Gearbox. Technical Memorandum 212327, NASA.

[7] Samuel, P., Conroy, J., and Pines, D., 2004. Planetary Trasmission Diagnostics. Technical report, NASA.

[8] McFadden, P., 1987. "Examination of a technique for the early detection of failure in gears by signal processing of the time domain average of the meshing vibration". *Mechanical Systems and Signal Processing,,* **1**(2), pp. 173–183.

[9] McFadden, P., 1991. "A technique for calculating the time domain averages of the vibration of the individual planet gears and the sun in an epicyclic gearbox". *Journal of Sound and Vibration,* **144**(1), pp. 163–172.

[10] McFadden, P., 1986. "Detecting Fatigue Cracks in Gears by Amplitude and Phase Demodulation of the Meshing Vibration". *Journal of Vibration, Acoustics, Stress and Reliability in Design,* **108**(2), April, pp. 165–170.

[11] D'Elia, G., Mucchi, E., and Dalpiaz, G., 2013. "On the time synchronous average in planetary gearboxes". *Proceeding of International Conference Surveillance 7.*

[12] Dalpiaz, G., Rivola, A., and Rubini, R., 2000. "Effectiveness and sensitivity of vibration processing techniques for local fault detection in gears". *Mechanical Systems and Signal Processing,* **14**(3), pp. 387–412.

[13] Stewart, R., 1977. Some Useful Data Analysis Techniques for Gearbox Diagnostics. Report MHM/R/10/77, Institute of Sound and Vibration Research, University of Southampton, July.

[14] Zakrajsek, J., 1989. An Investigation of Gear Mesh Failure Prediction Techniques. Technical Memorandum 102340, NASA.

[15] Polyshchuk, V., Choy, F., and Braun, M., 2002. "Gear Fault Detection with Time-Frequency Based Parameter NP4". *International Journal of Rotating Machinery,* **8**(1), pp. 57–70.

[16] Decker, H., Handshuh, R., and Zakrajsek, J., 1994. An Enchancement to the NA4 Gear Vibration Diagnostic Parameter. Technical Memorandum 106553, NASA.

[17] D'Elia, G., Cocconcelli, M., Rubini, R., and Dalpiaz, G., 2015. "Evolution of gear condition indicators for diagnostics of planetary gearboxes". *Proceeding of International Conference Surveillance 8*.

[18] Mosher, M., Pryor, A., and Huff, E., 2002. Evaluation of Standard Gear Metrics in Helicopter Flight Operation. 56th Meeting of Society for Machinery Failure Prevention Technology, Institute of Sound and Vibration Research, Virginia Beach, VA, USA.

[19] Randall, R., 2011. "Vibration based condition monitoring". *Wiley*.

[20] D'Elia, G., 2008. "Fault detection in rotating machines by vibration signal processing techniques". PhD Thesis, University of Ferrara.

[21] Wang, W., and McFadden, P., 1996. "Application of wavelets to gearbox vibration signals for fault detection". *Journal of Sound and Vibration,* **192**, pp. 927–939.

[22] Kanneg, D., and Wang, W., 2011. "A Wavelet Spectrum Technique for Machinery Fault Diagnosis". *Journal of Signal and Information Processing,* **2**, pp. 322–329.

[23] Bendjama, H., Bouhouche, S., and Boucherit, M., 2012. "Application of Wavelet Transform for Fault Diagnosis in Rotating Machinery". *International Journal of Machine Learning and Computing,* **2**(1), pp. 82–87.

[24] Wolfgang, M., and Flandrin, P., 1985. "Wigner-Ville spectral analysis of non- stationary process". *IEEE Transactions on Acoustics, Speech, and Signal Processing,* **33**(6), pp. 1461–1470.

[25] Staszewski, W., Worden, K., and Tomlinson, G., 1997. "Time-frequency analysis in gearbox fault detection using the wigner-ville distribution and pattern recognition". *Mechanical Systems and Signal Processing,* **11**(5), pp. 673–692.

[26] Samuel, P., and Pines, D., 2005. "A review of vibration-based techniques for helicopter transmission diagnostics". *Journal of Sound and Vibration,* **282**, p. 475–508.

[27] Večeř, P., Kreidl, M., and Šmíd, R., 2005. "Condition Indicators for Gearbox Condition Monitoring Systems". *Acta Polytechnica,* **45**(6), pp. 35–43.

[28] McClintic, K., Lebold, M., Maynard, K., Byington, C., and Campbell, R., 2000. Residual and Difference Feature Analysis with Transitional Gearbox Data. Tech. rep., 54th Meeting of the Society for Machinery Failure Prevention Technology, Virginia.

EXPERIMENTAL MODEL IDENTIFICATION AND VALIDATION OF STANDARD AND FUNCTIONALLY GRADED MATERIALS FOR AEROSPACE, AUTOMOTIVE AND HIGH SPEED INDUSTRIAL APPLICATIONS

Stefano Amadori
CIRI-MAM Department of Industrial Engineering,
University of Bologna, Italy
E-mail:stefano.amadori4@unibo.it

Giuseppe Catania
CIRI-MAM Department of Industrial Engineering,
University of Bologna, Italy
E-mail:giuseppe.catania@unibo.it

Angelo Casagrande
Department of Industrial Engineering,
University of Bologna, Italy
E-mail:angelo.casagrande@unibo.it

Sergio Valeri
Department of Physics, Informatics and Mathematics,
University of Modena and Reggio Emilia, Italy
E-mail:sergio.valeri@unimore.it

Abstract. *The constitutive equivalent material models of specimens prepared with standard viscoelastic materials and Functionally Graded Materials (FGM) are identified and optimized by means of a robust identification technique. The constitutive relationship is modelled by means of a generalized Kelvin model and expressed in the form of the ratio of two frequency dependent polynomials. The polynomial parameters are identified by means of a least square error formulation adopting Forsythe orthogonal polynomials. The model non-physical components are eliminated in order to obtain a reduced and optimized model. The procedure is applied on force and displacement data obtained by means of dynamic mechanical measurement tests on standard viscoelastic specimens and composite FGM specimens. Various types of FGM specimens are prepared by producing dual-layer coatings of Ti and* TiO_2 *and single-layer coatings of* Al_2O_3 *on different substrate materials and the results are compared and discussed.*

Keywords: *damping, model identification, optimal model fitting, dynamic mechanical measurements.*

1. INTRODUCTION

Coating techniques can be used to obtain composite FGM components with specialized mechanical properties. Notably the damping behaviour of such non-conventional materials is extensively researched [1-5], and some industrial applications, concerning the possibility of designing mechanical component exhibiting high stiffness, high resistance and tailored dissipative properties, are thus made it possible.

When used to describe the non-standard viscoelastic behaviour of these materials, over a wide range of frequencies and in quasi-static conditions, the more common constitutive models, for example the Kelvin and Zener models [6-8], can show limitations and the predicted dynamic behaviour may not be coherent with the measured response. A model that accurately describe the material behaviour at high frequencies may result in a poor approximation at low frequencies or quasi-static conditions. An example of such limitations can be observed by means of the analysis of the creep and stress relaxation material response predicted by the Kelvin model. The relationship between stress (σ) and strain (ε) of a Kelvin model composed of a linear elastic element E and a viscoelastic element μ is given by:

$$\sigma = E \cdot \varepsilon + \mu \cdot \dot{\varepsilon} \tag{1}$$

With $(\dot{\ })$ being the time derivative operator. In a creep (strain relaxation) experiment, when a constant stress $\sigma(t) = \sigma_0$ is applied to the material, the strain response is:

$$\varepsilon(t) = \left(\frac{\sigma_0}{E} \right) \cdot \left[1 - \exp\left(-\frac{t}{\mu/E} \right) \right] \tag{2}$$

In a stress relaxation experiment when a constant stress $\varepsilon(t) = \varepsilon_0$ is imposed to the material, the stress is given by:

$$\sigma(t) = E \cdot \varepsilon_0 = \text{constant} \tag{3}$$

While for many materials Eq.2 can be considered effective in the description of their behaviour and is supported by experimental evidence, Eq.3 predicts a constant stress values as the material response of a stress relaxation test. This last result is negated by experimental evidence as stress relaxation measurements generally exhibit an asymptotic exponential time functional relationship. The Kelvin model is unsuitable to describe the behaviour of a real material under constant strain. Since the more common classical material models show such limitations even for standard material models, for more complex non-standard materials different models can be considered [8-10].

FGM composite components that adopt coating layer technology to increase their dissipative properties [3,11-12] can also be expected to exhibit non-standard damping behaviour and because of their high damping capabilities can be employed to reduce system unwanted vibrations, resulting in improved system efficiency and longer service life. Coating layers composition and structure [2,5,13-14], adhesion to the substrate material [11] and layer formation technique [15-16] are all factors that contribute to define the properties of a coatings and the dissipative properties of a coated component can be increased by means of the deposition of layers with high internal hysteresis or with significant frictional actions between the different layers [3,12,17].

It is known from literature [4,18-19] that dynamic mechanical measurements are an effective experimental tool to study the damping behaviour of coated components, and that both forced and free vibration tests were employed to investigate the dynamic behaviour of a wide range of coating materials and component geometries.

In this work forced vibration dynamic mechanical measurements over a wide frequency range are employed to investigate the behaviour of standard and FGM composite specimens. A robust identification technique [20] is employed to process force and displacements experimental data in order to identify the tested specimens constitutive equivalent material model. A high order generalized Kelvin model is considered for the specimen constitutive equation, the contribution of the inertial forces is also taken into account. The identification procedure make use of Forsythe orthogonal polynomials in order to mitigate the ill-conditioning problems that are a consequence of the use of high order constitutive equations and the identified model is reduced and optimized. The experimental, identification and optimization procedure is first tested on polytetrafluoroethylene (PTFE) specimens and then used to compare different types of composite FGM specimens obtained by applying a dual-layer and single-layer coating solutions to different metallic substrates.

2. IDENTIFICATION PROCEDURE

In this section the identification procedure defined by the authors in [20] is outlined. The procedure employs force and displacement dynamic forced vibration tests data. Specimens in the form of slender beams are tested in a single-cantilever experimental set-up with clamped-sliding boundary conditions (Fig.1).

Experimental estimate of the constitutive relationship

The constitutive relationship between the Fourier transform of stress ($\hat{\sigma}$) and strain ($\hat{\varepsilon}$) is given by Eq.4:

$$\hat{\sigma} = E(\omega) \cdot \hat{\varepsilon} \tag{4}$$

A modal approach is used to estimate *E(ω)* over a wide frequency range, taking into account of the inertial actions contribution. The transverse displacement v at the sliding end of a beam in flexural excitation (Fig.1) with boundary conditions $v = \partial v / \partial x = 0$ for the clamped end and $\partial v / \partial x = \partial^3 v / \partial x^3 = 0$ for the sliding end, when at the sliding end an excitation force $q(t) = q_0 \exp(j\omega t)$ is applied, is given by:

$$\hat{v}(\omega) = \sum_{i=1}^{\infty} \frac{\left(\frac{2 \cdot \sinh k_i \cdot \sin k_i}{\cosh k_i + \cos k_i} \right)^2}{-M \cdot \omega^2 + k_i^4 \cdot E(\omega) \cdot I / L^3} \cdot \hat{q}(\omega) \simeq \sum_{i=1}^{nm} \frac{\left(\frac{2 \cdot \sinh k_i \cdot \sin k_i}{\cosh k_i + \cos k_i} \right)^2}{-M \cdot \omega^2 + k_i^4 \cdot E(\omega) \cdot I / L^3} \cdot \hat{q}(\omega) \tag{5}$$

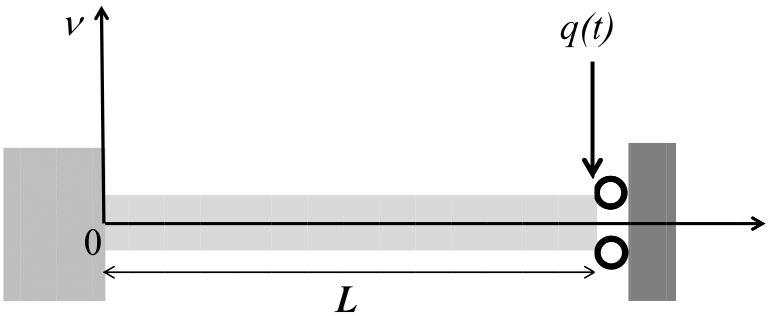

Figure 1. Slender beam in single-cantilever experimental set-up

In Eq.5 k_i are values satisfying $f(k) = \sinh k \cos k + \cosh k \sin k = 0$, $\hat{v}$ and $\hat{q}$ are the Fourier transform of measured transverse displacement and applied force respectively, *M* is the beam mass, *L* is the beam length and *I* the beam section moment. The values of *E(ω)* at any given excitation frequency ω_e can be obtained by finding the root of the non-linear function:

$$\Lambda\left(E\left(\omega_e\right)\right) = \sum_{i=1}^{nm} \frac{\left(\dfrac{2 \cdot \sinh k_i \cdot \sin k_i}{\cosh k_i + \cos k_i}\right)^2}{-M \cdot \omega_e^2 + k_i^4 \cdot E\left(\omega_e\right) \cdot I / L^3} - \frac{\hat{v}\left(\omega_e\right)}{\hat{q}\left(\omega_e\right)} = 0 \tag{6}$$

To find the solution of Eq.6, the Newton-Raphson method can be iteratively adopted at each frequency value and only a few iterations are generally needed for convergence.

Constitutive relationship for a generalized Kelvin model

A generalized Kelvin model [8,20] of order *n* (obtained by connecting *n* single Kelvin model units in series) is considered to define the constitutive equivalent material relationship of the specimen. Application of the Fourier transform to the constitutive relationship of the *n* single kelvin units, with $\hat{\varepsilon}_i$ defined as the strain associated with the i-th Kelvin component:

$$\hat{\sigma} = \left(E_i + j\omega \cdot \mu_i\right) \cdot \hat{\varepsilon}_i \quad , \quad i = 1, \ldots, n \tag{7}$$

leads to the relationship:

$$\frac{\hat{\varepsilon}}{\hat{\sigma}} = \sum_{i=1}^{n} \frac{1}{E_i + j\omega \cdot \mu_i} = \sum_{i=1}^{n} \frac{1/E_i}{1 + j\omega \cdot \left(\mu_i / E_i\right)} \tag{8}$$

Eq.8 can be manipulated [20] to obtain the Fourier transform of the stress in the form:

$$\hat{\sigma} = E_0 \cdot \frac{\alpha_n \cdot \omega^n + \ldots + 1}{\beta_{n-1} \cdot \omega^{n-1} + \ldots + 1} \cdot \hat{\varepsilon} \tag{9}$$

The constitutive relationship is defined as:

$$\hat{\sigma} = E_0 \cdot C(\omega) \cdot \hat{\varepsilon} \quad , \quad E_0 = \left(\sum_{i=1}^{n} \frac{1}{E_i} \right)^{-1} \quad , \quad C(\omega) = \frac{1 + \sum_{r=1}^{n} \alpha_r \cdot \omega^r}{1 + \sum_{s=1}^{n-1} \beta_s \cdot \omega^s} \tag{10}$$

It can be observed that when the frequency is null:

$$C(0) = 1 \quad , \quad \hat{\sigma}(\omega = 0) = E_0 \cdot \hat{\varepsilon}(\omega = 0) \tag{11}$$

The constant E_0 represent the modulus of the material at zero frequency and can be obtained from static experiments (i.e. creep and stress relaxation tests) or extrapolated from dynamical measurement estimates as the frequency goes to zero. $C(\omega)$ is a rational function defined by the ratio of two polynomials.

Identification of the constitutive relationship parameters

An approach based on the least square error technique and making use of orthogonal polynomials is adopted to identify the constitutive equation (Eq.10) parameters [20-22]. Orthogonal polynomials are known in interpolation theory as a useful tool to mitigate ill-conditioning problems in low to high frequency related applications. In Eq.10 $C(\omega)$ is expressed by means of the monomial base, but it can also be expressed by substituting the monomials of the numerator and denominator with two orthogonal polynomial basis:

$$C(\omega) = \frac{1 + \sum_{r=1}^{n} \gamma_r \cdot c_r(\omega)}{1 + \sum_{s=1}^{n-1} \varphi_s \cdot d_s(\omega)} \tag{12}$$

$c_r(\omega)$ and $d_s(\omega)$ are the components of the orthogonal polynomial basis and γ_r and ϕ_s are the corresponding coefficients. Experimentally estimated values V_e of $C(\omega)$ at different frequencies ω_e ($e=1,\ldots,p$) are considered:

$$V_e = C(\omega_e) = \frac{1 + \sum_{r=1}^{n} \gamma_r \cdot c_r(\omega_e)}{1 + \sum_{s=1}^{n-1} \varphi_s \cdot d_s(\omega_e)} \tag{13}$$

The experimental measurements are in the discrete frequency domain, namely obtained by means of the discrete Fourier transform (DFT) operator, and for this reason aliasis symmetry properties are to be considered, i.e. V_e values associated to negative frequencies must also be taken into account:

$$\boldsymbol{\omega} = \left\{ \omega_{-p} \quad \dots \quad \omega_{-1} \quad \omega_1 \quad \dots \quad \omega_p \right\} \quad , \quad V\left(-\omega_e\right) = V^*\left(\omega_e\right) \tag{14}$$

$(\ )^*$ is the complex conjugate operator. By definition orthogonal polynomials satisfy the orthogonality condition:

$$\sum_{i=-p}^{-1} c_k^*\left(\omega_e\right)\cdot c_j\left(\omega_e\right) + \sum_{i=1}^{p} c_k^*\left(\omega_e\right)\cdot c_j\left(\omega_e\right) = \begin{cases} 0 \ , \ k \neq j \\ \mathrm{X} \ , \ k = j \end{cases} \tag{15}$$

Where X is a constant different from zero. From Eq.13:

$$\sum_{r=1}^{n} c_r\left(\omega_e\right)\cdot \gamma_r - \sum_{s=1}^{n-1} d_s\left(\omega_e\right)\cdot V_e \cdot \varphi_s = V_e - 1 \tag{16}$$

An error value H_e can be defined:

$$H_e = \sum_{r=1}^{n} c_k\left(\omega_e\right)\cdot \gamma_r - V_e \cdot \sum_{s=1}^{n-1} d_s\left(\omega_e\right)\cdot \varphi_s - \left(V_e - 1\right) \tag{17}$$

In vector form

$$\mathbf{H} = \left\{ H_1 \quad \dots \quad H_{2p} \right\}^T \quad , \quad \boldsymbol{\varphi} = \left\{ \varphi_1 \quad \dots \quad \varphi_{n-1} \right\}^T \quad , \quad \boldsymbol{\gamma} = \left\{ \gamma_1 \quad \dots \quad \gamma_n \right\}^T \tag{18}$$

$$\mathbf{H} = \mathbf{A}\cdot\boldsymbol{\varphi} - \mathbf{B}\cdot\boldsymbol{\gamma} - \mathbf{D} \tag{19}$$

With:

$$\mathbf{A} = \begin{bmatrix} c_1\left(\omega_1\right) & \dots & c_n\left(\omega_1\right) \\ \dots & \dots & \dots \\ c_1\left(\omega_{2p}\right) & \dots & c_n\left(\omega_{2p}\right) \end{bmatrix} \quad , \quad \mathbf{B} = \begin{bmatrix} V_1 \cdot d_1\left(\omega_1\right) & \dots & V_1 \cdot d_{n-1}\left(\omega_1\right) \\ \dots & \dots & \dots \\ V_{2p} \cdot d_1\left(\omega_{2p}\right) & \dots & V_{2p} \cdot d_{n-1}\left(\omega_{2p}\right) \end{bmatrix} ,$$
$$\mathbf{D} = \left\{ V_1 - 1 \quad \dots \quad V_{2p} - 1 \right\}^T \tag{20}$$

The least square error formulation is applied and a quadratic error functional Ψ is defined:

$$\begin{aligned}\Psi(\boldsymbol{\gamma},\boldsymbol{\varphi}) &= 0.5\cdot\mathbf{H}^*\cdot\mathbf{H} = \\ &= 0.5\cdot\left(\boldsymbol{\gamma}^*\cdot\mathbf{A}^*\cdot\mathbf{A}\cdot\boldsymbol{\gamma}+\boldsymbol{\varphi}^*\cdot\mathbf{B}^*\cdot\mathbf{B}\cdot\boldsymbol{\varphi}+\mathbf{D}^*\cdot\mathbf{D}\right)+ \\ &-\mathrm{Re}\left[\boldsymbol{\gamma}^*\cdot\mathbf{A}^*\cdot\mathbf{B}\cdot\boldsymbol{\varphi}\right]-\mathrm{Re}\left[\boldsymbol{\gamma}^*\cdot\mathbf{A}^*\cdot\mathbf{D}\right]+\mathrm{Re}\left[\boldsymbol{\varphi}^*\cdot\mathbf{B}^*\cdot\mathbf{D}\right]\end{aligned} \tag{21}$$

Ψ is a non-negative real scalar function and the minimum condition with respect to $\boldsymbol{\gamma}$ and $\boldsymbol{\varphi}$ is imposed:

$$\partial\Psi/\partial\boldsymbol{\gamma} = \mathbf{A}^*\cdot\mathbf{A}\cdot\boldsymbol{\gamma}-\mathrm{Re}\left[\mathbf{A}^*\cdot\mathbf{B}\cdot\boldsymbol{\varphi}\right]-\mathrm{Re}\left[\mathbf{A}^*\cdot\mathbf{D}\right]=0 \tag{22}$$

$$\partial\Psi/\partial\boldsymbol{\varphi} = \mathbf{B}^*\cdot\mathbf{B}\cdot\boldsymbol{\varphi}-\mathrm{Re}\left[\boldsymbol{\gamma}^*\cdot\mathbf{A}^*\cdot\mathbf{B}\right]+\mathrm{Re}\left[\mathbf{B}^*\cdot\mathbf{D}\right]=0 \tag{23}$$

The resulting linear equation system is:

$$\begin{Bmatrix}\mathbf{M_A} & \mathbf{G} \\ \mathbf{G^T} & \mathbf{M_B}\end{Bmatrix}\begin{Bmatrix}\boldsymbol{\gamma} \\ \boldsymbol{\varphi}\end{Bmatrix}=\begin{Bmatrix}\mathbf{T} \\ \mathbf{U}\end{Bmatrix} \tag{24}$$

With

$$\begin{aligned}&\mathbf{G}=-\mathrm{Re}\left[\mathbf{A^*}\cdot\mathbf{B}\right] \quad , \quad \mathbf{U}=-\mathrm{Re}\left[\mathbf{B^*}\cdot\mathbf{D}\right] \quad , \quad \mathbf{T}=\mathrm{Re}\left[\mathbf{A^*}\cdot\mathbf{D}\right] \quad , \\ &\mathbf{A^*}\cdot\mathbf{A}=\ \mathbf{M_A} \quad , \quad \mathbf{B^*}\cdot\mathbf{B}=\mathbf{M_B}\end{aligned} \tag{25}$$

As a consequence of the orthogonality condition (Eq.15) $\mathbf{M_A}$ and $\mathbf{M_B}$ are diagonal matrices and the unknown γ_r and φ_s coefficients can be calculated from the two uncoupled systems:

$$\begin{aligned}&\boldsymbol{\gamma}=\mathbf{M_A^{-1}}\cdot\left(\mathbf{T}-\mathbf{G}\cdot\boldsymbol{\varphi}\right) \\ &\boldsymbol{\varphi}=\left(\mathbf{M_B}-\mathbf{G^T}\cdot\mathbf{M_A^{-1}}\cdot\mathbf{G}\right)^{-1}\cdot\left(\mathbf{U}-\mathbf{G^T}\cdot\mathbf{M_A^{-1}}\cdot\mathbf{T}\right)\end{aligned} \tag{26}$$

Any orthogonal polynomial basis can be used with the presented calculations steps (Eq.13-26) but in the specific identification procedure applied in this work, the Forsythe orthogonal polynomial basis is adopted [23]. Here is briefly summarized the well-known recursive algorithm used to generated a basis c_r of Forsythe orthogonal polynomials [22-23]:

$$\begin{aligned}&c_{-1}(\omega_e)=0 \\ &c_0(\omega_e)=1 \\ &c_1(\omega_e)=(j\omega_e-U_1)\cdot c_0 \\ &c_r(\omega_e)=(j\omega_e-U_r)\cdot c_{r-1}-Y_{r-1}\cdot c_{r-2} \\ &r=3,\ldots,n \quad ; \quad e=-p,\ \ldots\ ,\ p\end{aligned} \tag{27}$$

$$U_r = \frac{\sum_{e=-p}^{p} j\omega_e \cdot \left| c_{r-1}\left(\omega_e\right)\right|^2 \cdot W_e}{Z_{r-1}} \quad , \quad Y_r = \frac{\sum_{e=-p}^{p} j\omega_e \cdot c_{r-1}\left(\omega_e\right) c^{*}_{r-2}\left(\omega_e\right) \cdot W_e}{Z_{r-1}} \quad , \tag{28}$$

$$Z_r = \sum_{e=-p}^{p} \left| c_r\left(\omega_e\right)\right|^2 \cdot W_e$$

To increase the computational efficiency, the W_e weight values are chosen as $W_e=1$ for the c_r basis and $W_e=|V_e|^2$ for the d_s basis, the constant value (Eq.15) is $X=Z_0$ and the circular frequency value is normalized to [0,1]. The coefficients γ_r and φ_s obtained from Eq.26 with the adoption of Forsythe polynomials can be unsuitable for further processing and it can be advantageous to convert them into coefficients of an equivalent monomial basis to obtain the material constitutive relationship in the form of Eq.10. A known algorithm [22] can be used for this conversion, and the necessary calculation steps are summarized here (the constant λ is a result of the circular frequency normalization):

$$1+\sum_{r=1}^{n} \gamma_r \cdot c_r\left(\omega_e\right) = 1+\sum_{r=1}^{n} a_r \cdot \omega_e^r \quad , \quad a_r = \lambda^r \cdot \sum_{k=r}^{n} c_k \cdot \beta_r^k \quad , \quad \lambda = \frac{1}{\omega_p} \tag{29}$$

$$\beta_r^k = \begin{cases} 0 & , \ r<0 \\ 0 & , \ r>k \\ 1 & , \ r=k \\ \beta_{r-1}^{k-1} - U_k \cdot \beta_r^{k-1} - Y_{k-1} \cdot \beta_r^{k-2} & , \ 0 \le r < k \end{cases} \tag{30}$$

The use of Forsythe orthogonal polynomials makes the least square error identification approach more accurate than the same approach employing a monomial basis [20-21]. It was shown in the author previous work [20] that the identification of a model by means of coefficients in the derived equivalent monomial basis, i.e. the method employed to obtain the results presented in this paper, became critical only for model of order n above 50 and in the medium to high frequency range.

Constitutive model condensation

Experimental measurements are affected by noise and the lest square error technique cannot distinguish between physical system poles and virtual non-physical poles resulting from noise, as a consequence the constitutive equivalent material model obtained from Eqs.13-30 is generally of high order. It can be useful to reduce the identified model order by means of the elimination of its noise-generated non-physical components.

$C(\omega)$ expressed in the form of Eq.10 is manipulated in order to outline the mathematical dependence on material poles and residues:

$$\frac{1}{C\left(\omega_e\right)} = \frac{b_{n-1}\cdot\left(\omega_e\right)^{n-1}+\ldots+1}{a_n\cdot\left(\omega_e\right)^{n}+\ldots+1} = \frac{b_{n-1}}{a_n}\frac{\left(j\omega_e-\phi_1\right)\cdot\ldots\cdot\left(j\omega_e-\phi_{n-1}\right)}{\left(j\omega_e-\theta_1\right)\cdot\ldots\cdot\left(j\omega_e-\theta_n\right)} \tag{31}$$

Eq.(31) can be expressed in the standard partial fraction form by means of the evaluation the zeros of the numerator (ϕ_s) and denominator (θ_r):

$$\frac{1}{C}(\omega_e) = \sum_{r=1}^{n} \frac{R_r}{j\omega_e - \theta_r} \tag{32}$$

The residues R_r , related to poles θ_r are given by:

$$R_r = \frac{b_{n-1}}{a_n} \cdot \frac{(\theta_r - \phi_1)\cdot \ldots \cdot (\theta_r - \phi_{n-1})}{(\theta_r - \theta_1)\cdot \ldots \cdot (\theta_r - \theta_{r-1})\cdot(\theta_r - \theta_{r+1})\cdot \ldots \cdot (\theta_r - \theta_n)} \tag{33}$$

From Eq.10 and Eq.32:

$$\hat{\varepsilon}(\omega) = \frac{1}{E_0} \cdot \frac{1}{C}(\omega) \cdot \hat{\sigma}(\omega) = \frac{1}{E_0} \cdot \left(\sum_{r=1}^{n} \frac{R_r}{j\omega - \theta_r} \right) \cdot \hat{\sigma}(\omega) \tag{34}$$

It can be observed that poles and residues are expected to appear as complex conjugated pairs or as real values and poles with positive real part can be considered as computational and discarded. Moreover couples of physical poles and residues are expected to present stability as the model order n increases, unstable poles with respect to n can be considered non-physical and discarded. The model condensed to a subset of nc physical pole-residue couples Rc_r and θc_r is expressed as:

$$\frac{1}{C}(\omega_e) \simeq \sum_{r=1}^{nc} \frac{Rc_r}{(j\omega_e - \theta c_r)} \quad , \quad nc < n \tag{35}$$

and the contribution of the discarded $no=n-nc$ computational poles-residue pairs Ro_r and θo_r , can be estimated by a l-th low order polynomial function K_l :

$$\frac{1}{C}(\omega_e) \simeq \sum_{r=1}^{nc} \frac{Rc_r}{j\omega_e - \theta c_r} + \mathrm{K}_l(\omega_e) = \sum_{r=1}^{nc} \frac{Rc_r}{j\omega_e - \theta c_r} + \sum_{m=0}^{l} \eta_m \cdot (j\omega_e)^m \tag{36}$$

For this approach it can be found that $l=1,2$ usually works well. By imposing:

$$\mathrm{K}_l(\bar{\omega}_m) = \sum_{r=1}^{no} \frac{Ro_r}{j\bar{\omega}_m - \theta o_r} \tag{37}$$

$$\bar{\omega}_m = \frac{\left[(l+1-m)\omega_1 + (m-1)\omega_p\right]}{l} \quad , \quad m=1, \ \ldots \ , \ l+1 \tag{38}$$

It results:

$$\{\eta_0 \quad \dots \quad \eta_l\}^T = \left(\Theta^* \cdot \Theta\right)^{-1} \cdot \Theta^* \cdot \left\{ \sum_{r=1}^{no} \frac{Ro_r}{\left(j\bar{\omega}_1 - \theta o_r \right)} \quad \dots \quad \sum_{r=1}^{no} \frac{Ro_r}{j\bar{\omega}_{l+1} - \theta o_r} \right\}^T ,$$

$$\Theta = \begin{bmatrix} 1 & \left(j\bar{\omega}_1\right) & \dots & \left(j\bar{\omega}_1\right)^l \\ \dots & \dots & \dots & \dots \\ 1 & \left(j\bar{\omega}_{l+1}\right) & \dots & \left(j\bar{\omega}_{l+1}\right)^l \end{bmatrix} \tag{39}$$

3. EXPERIMENTAL MEASUREMENT RESULTS

Specimen preparation and experimental measurements

Rectangular specimens are cut from sheets of Polytethrafluoroethylene (PTFE), Al alloy (Al 1000), harmonic steel (C 67) and stainless steel (AISI 304). All tested specimens are in the form of slender beams of rectangular cross section and their data are reported in Tab.1.

The composite FGM specimens are obtained by means of reactive plasma vapour deposition (RPVD) or by means of an anodizing process. The RPVD technique is used to apply a dual-layer coating on the opposite faces of the tree types of metallic beams (Al 1000, C 67, AISI 304). The coating is formed by a 1µm thick metallic bond layer of Ti in direct contact with the substrate material, and by a 1µm thick ceramic coating layer of TiO_2.

The anodizing process is only used on Al 1000 specimen to apply a 40µm single-layer coating of Al_2O_3 on the opposite faces of the beam. The Al anodization is obtained by means of a sulfuric acid bath.

Table 1. Specimens data

material	length (m)	width (m)	thickness (m)	density (kg/m^3)
PTFE	$2.0 \cdot 10^{-2}$	$5.0 \cdot 10^{-3}$	$1 \cdot 10^{-3}$	$2.2 \cdot 10^{3}$
Al 100	$2.0 \cdot 10^{-2}$	$3.0 \cdot 10^{-3}$	$5.0 \cdot 10^{-4}$	$2.68 \cdot 10^{3}$
C 67	$2.0 \cdot 10^{-2}$	$3.0 \cdot 10^{-3}$	$5.0 \cdot 10^{-4}$	$7.85 \cdot 10^{3}$
AISI 304	$2.0 \cdot 10^{-2}$	$3.0 \cdot 10^{-3}$	$5.0 \cdot 10^{-4}$	$7.85 \cdot 10^{3}$

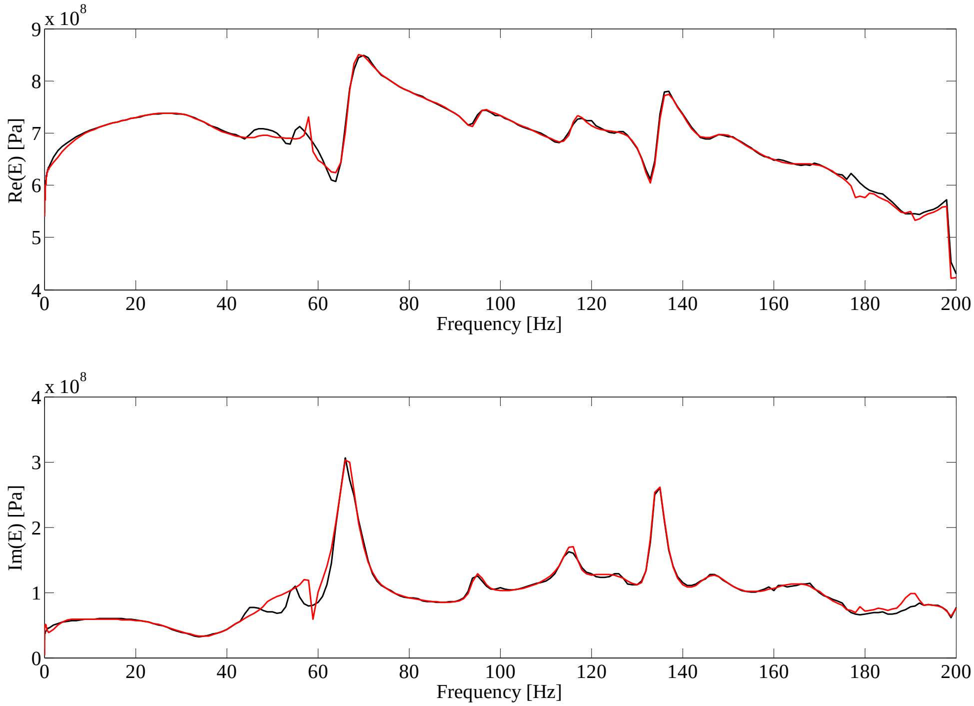

Figure 2. *E(ω)* Experimental estimate (black) and 43th order model fit (red) for a PTFE specimen.

Experimental measurements are carried out with a Dynamic Mechanical Analyzer (DMA). All specimens are tested in a forced flexural excitation experimental set-up, with clamped-sliding boundary conditions. Specimens are tested over a wide frequency range, [0.01-200]Hz at a 35°C constant temperature and with 0.04% maximum imposed strain for the PTFE specimens and 0.01% for the FGM composite specimens. The force and displacement measured data are elaborated following the steps shown in the previous section.

Results

Results obtained for a PTFE specimen are shown in Figs.2-5. In Fig.2 the estimated values of the real and imaginary part of the complex modulus *E(ω)* are reported and compared to a high order (n=43) model fit. It can be seen that the model fitting estimate is an accurate representation of the experimental values. The model is condensed to a 13th order model and the resulting model fitting estimates are shown in Fig.3. The condensed model is obtained from a subset of 11 physical pole-residue (Eq.35) and a grade 2 polynomial residue (Eq.37), poles with positive real parts and unstable with respect to n are discarded, the poles stability is examined by means of a stability diagram (Fig.4). The condensed model fitting estimates is able to maintain a good accuracy while at the same time it significantly reduces the fitting model order. Fig.5 shows the estimated values for a 13th order model fitting estimate.

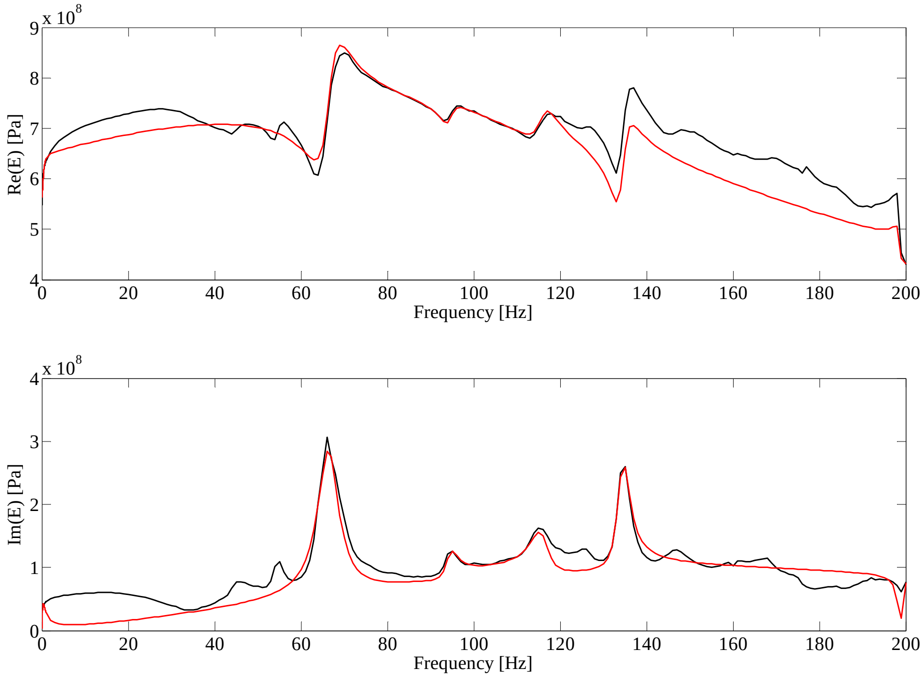

Figure 3. *E(ω)* Experimental estimate (black)
and 13th order condensed model fit (red) for a PTFE specimen.

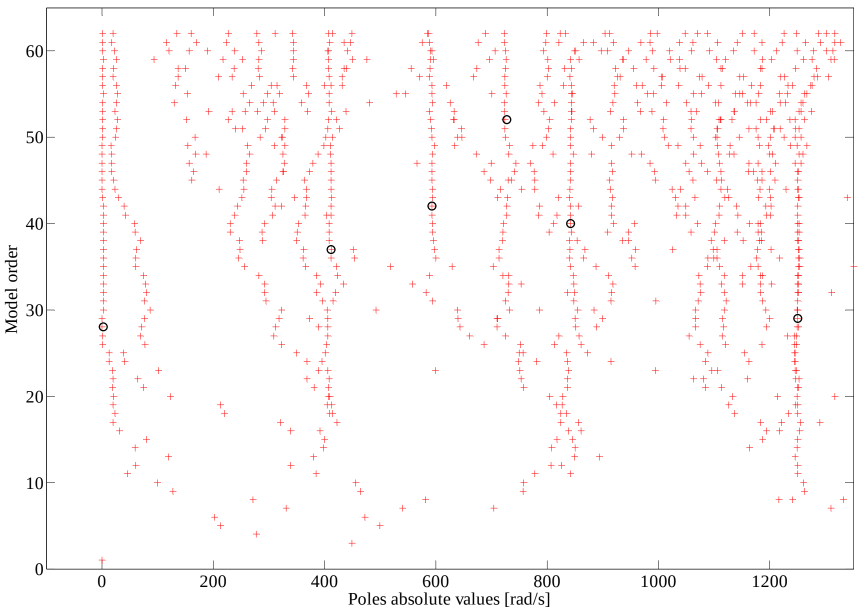

Figure 4. Stability diagram with selected poles of the *n*=13 condensed model of Fig.3.

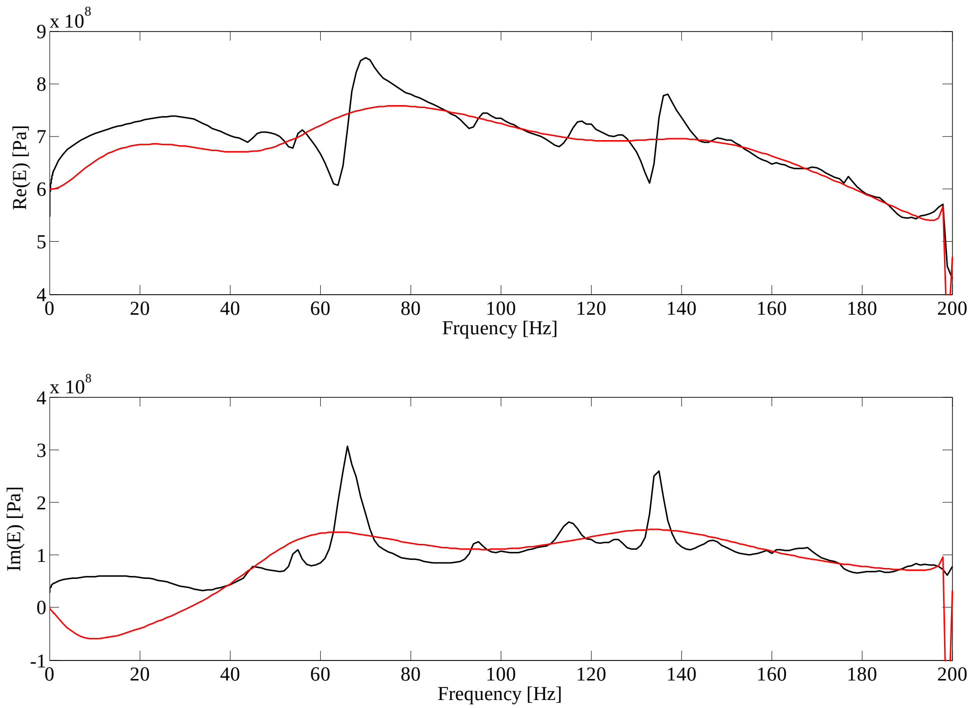

Figure 5. *E(ω)* Experimental estimate (black)
and 13th order model fit (red) for a PTFE specimen.

A comparison with Fig.3 displays the effectiveness of the model condensation procedure, both models are of the same order (n=13) but the condensed one is significantly more accurate. Results reported in Figs.2-3 show how the identification procedure presented in the previous section can be successfully employed to identify the parameters of a high order material model and to condense it to an effective model of significantly lower order. This procedure is now used to elaborate the measurements on FGM composite specimens.

The experimentally estimated values of the complex modulus (Eq.10) are used to calculate the ratio of the imaginary and real part of *E(ω)* for coated and uncoated Al 1000, C 67 and AISI 304 specimens (Figs.6a-6d). The ratio *Im(E)/Re(E)* is considered a measure of the specimen damping capabilities. It can be seen from Figs.6b-6c that on harmonic and stainless steel specimens the application of the Ti based dual-layer coating does not produce any meaningful effects on the dissipative capabilities, the *Im(E)/Re(E)* values for coated and uncoated specimens are almost superimposed. An increase in the dissipative properties can be seen in Fig.6a,6d for coated Al 1000 specimen. The application of the Ti based coating produce a distinct increase in the *Im(E)/Re(E)* ratio for frequencies above 60Hz while application of a single-layer of Al oxide produce an even more significant increase of *Im(E)/Re(E)* at all measured frequencies. The effect of the application of coatings on the three substrates can be better evaluated by observing the relative difference of the coated and uncoated specimens *Im(E)/Re(E)* ratio (Figs.7a-7d). In Figs.7a,7d the increase of the dissipative properties on Al 1000 specimens is clearly visible.

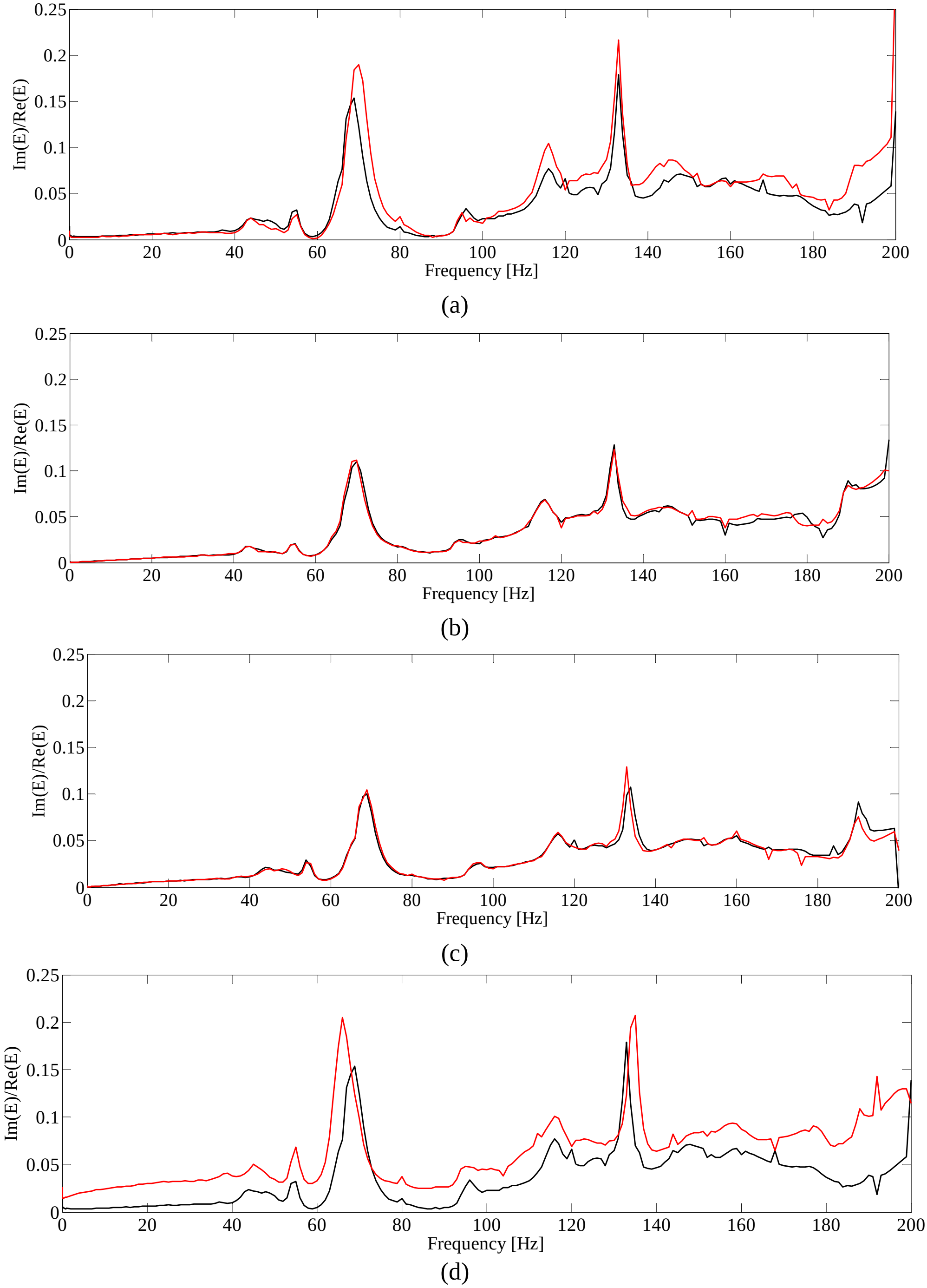

Figure 6. *Im(E)/Re(E) e*stimated values for coated(red) and uncoated (black) specimens. Ti based coating on Al 1000 (a), C 76 (b) and AISI 304 (c), and Al_2O_3 coating on Al 1000 (d).

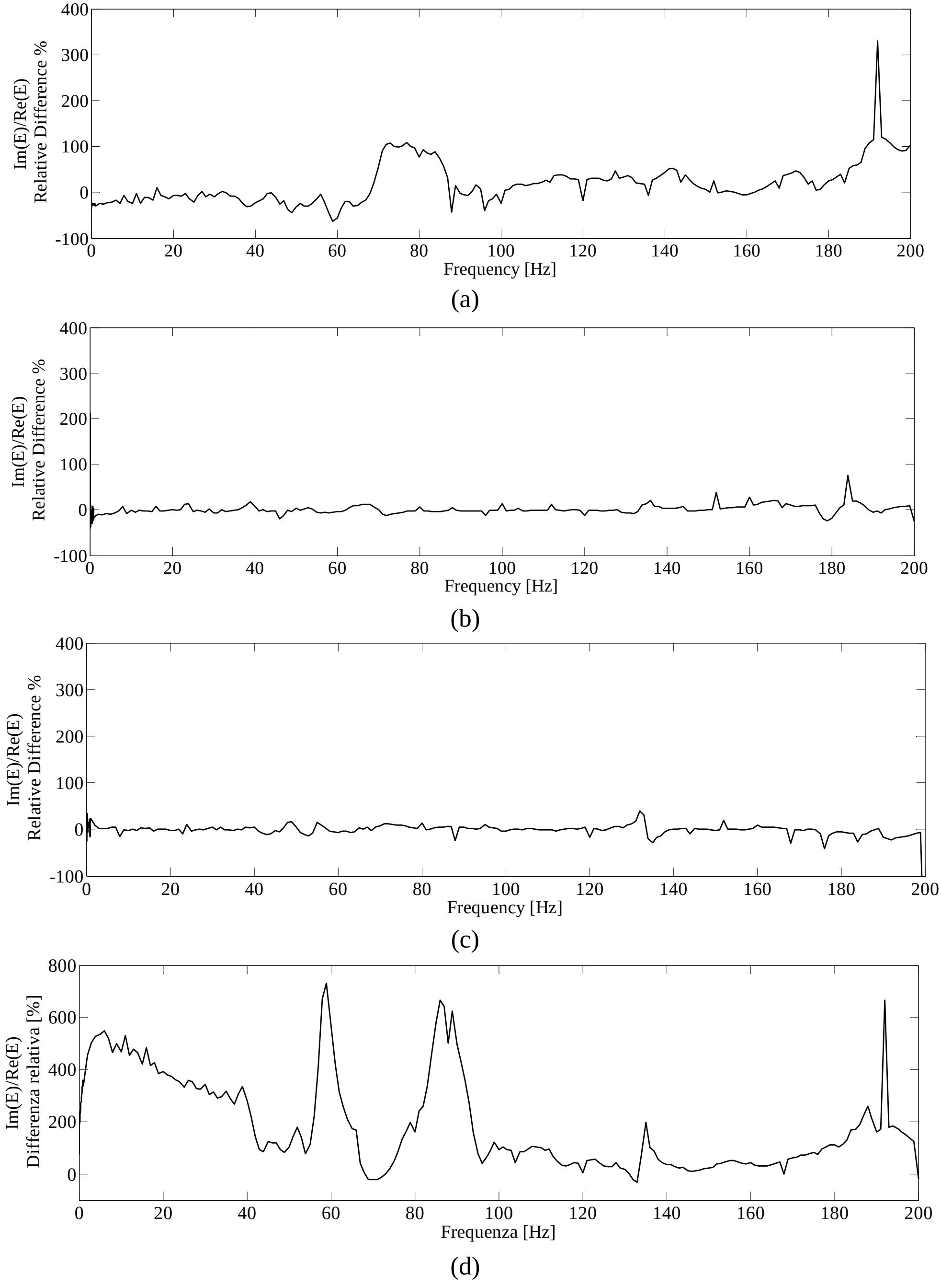

Figure 7. *Im(E)/Re(E)* relative difference for coated and uncoated specimens. Ti based coating on Al 1000 (a), C 76 (b) and AISI 304 (c), and Al_2O_3 coating on Al 1000 (d).

For all of the tested specimens (Al 1000, C 67, AISI 304) coated with Ti and TiO_2., the applied coating structure thickness and compositions are always the same, the obtained results (Figs.6-7) suggest that the damping behaviour improvement observed on coated Al alloy specimens (Figs.6a,7a) might be due to frictional forces acting at the interface between the metallic Ti bond layer and the Al 1000 substrate.

The identification and condensation technique is applied on the $E(\omega)$ experimentally estimated values of coated Al 1000 specimens. A 45th and 43th order models are identified (Figs.8-9) for the two different coating types and by means of the condensation procedure (Eqs.31-39) they are reduced to significantly lower (n=14 and n=13) order models (Fig.10-11). The specimen with dual-layer coating is reduced to a 14th order model with 6 physical pole-residue pairs (Eq.35) and a grade 2 polynomial residue (Eq.37), the one with single-layer coating to a 13th order model with 6 physical pole-residue pairs and a grade 1 polynomial residue. Stability diagrams are used to assess the poles stability with respect to model order n: the stability diagram for the Al 1000 specimen with Ti based coating along with the selected physical poles is shown as an example in Fig.12.

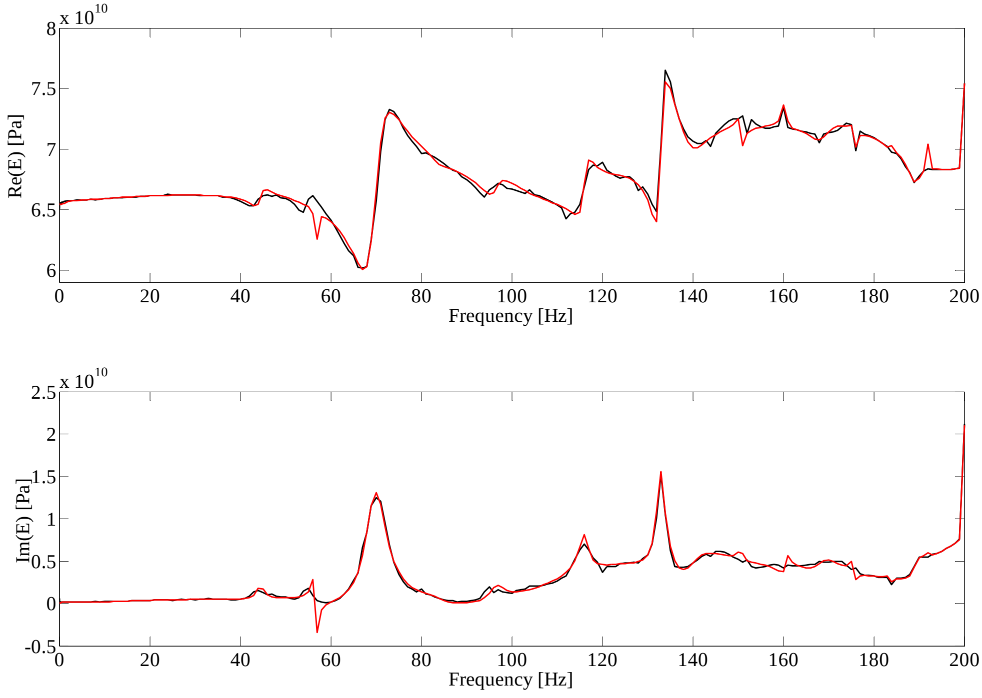

Figure 8. $E(\omega)$ Experimental estimate (black) and 45th order model fit (red) for an Al 1000 specimen with Ti based coating.

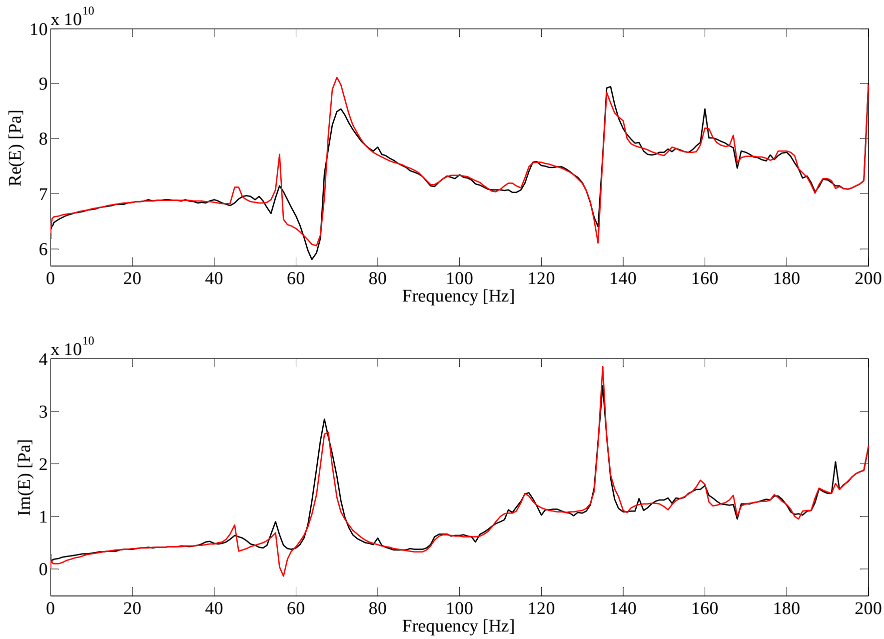

Figure 9. *E(ω)* Experimental estimate (black) and 43th order model fit (red) for an Al 1000 specimen with Al_2O_3 coating

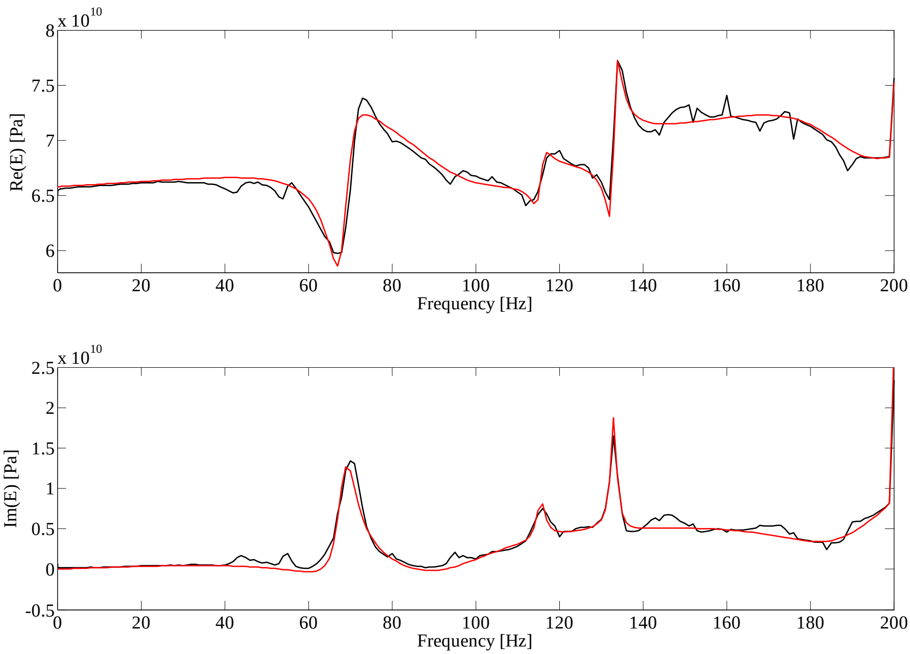

Figure 10. *E(ω)* Experimental estimate (black) and 14th order condensed model fit (red) for an Al 1000 specimen with Ti based coating.

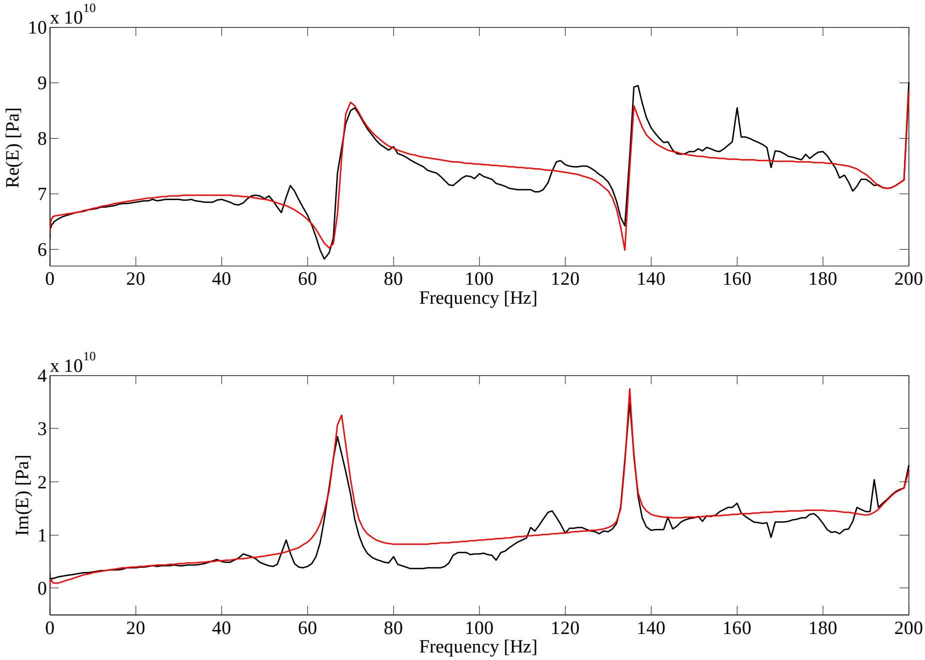

Figure 11. *E(ω)* Experimental estimate (black) and 14th order condensed model fit (red) for an Al 1000 specimen with Al_2O_3 coating.

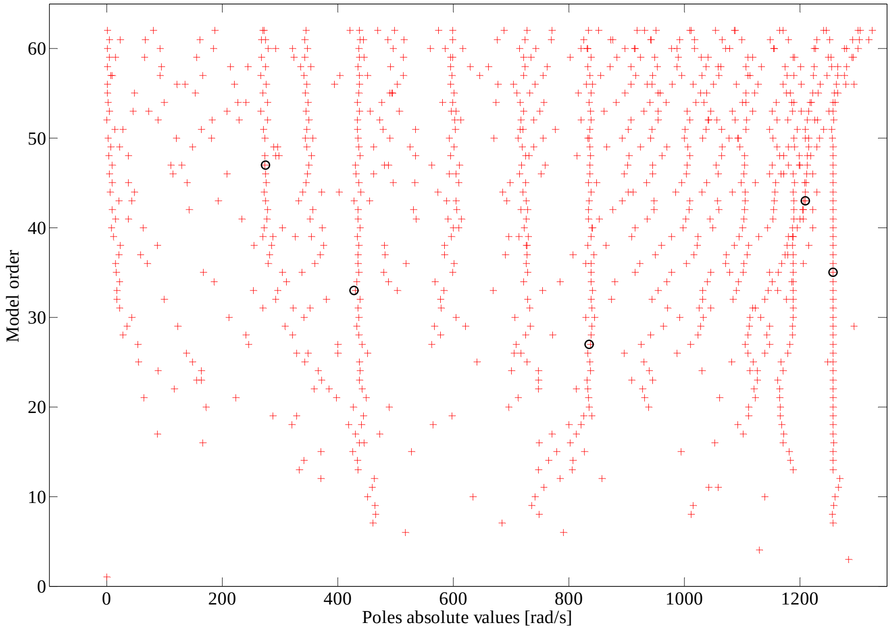

Figure 12. Stability diagram with selected poles of the *n*=14 condensed model of Fig.10.

4. CONCLUSIONS

A robust identification procedure is adopted to obtain the constitutive equivalent material models of PTFE and composite functionally graded materials. The PTFE specimen results demonstrate that the adopted procedure is an effective tool to identify high order material models starting from dynamic mechanical measurements data, and to condense them to optimal lower order models. The condensed model exhibits a significantly lower order but maintains a satisfying accuracy and is computationally more efficient than the original high order model.

Ti based dual-layer coatings and single-layer Al oxide coatings are then produced on three different metallic substrates, i.e. Al alloy, harmonic steel and stainless steel, and the effects on the specimens damping behaviour are investigated. An improvement of the dissipative properties is observed for both coating solutions applied on the Al 1000 metallic substrate.

Condensed constitutive equivalent material models of order 14 and 13 are obtained for coated Al 1000 specimens with Ti based and Al oxide based coating respectively.

This preliminary results justify further investigations on different coating technologies. The effect of the use of different coating materials, different coating structures, i.e. single-layer or multi-layer (with a high number of layers), and different production processes will be investigated in future works.

Aknowledgments

This study was developed within the CIRI-MAM with the contribution of the Regione Emilia Romagna, progetto POR-Fesr-Tecnopoli**.** Support from Mr.Andrea Zucchini and Marzocchi Pompe S.p.A., Casalecchio di Reno, Italy, is also kindly acknowledged.

REFERENCES

[1] Yu L., Ma Y., Zhou C., Xu H., 2005. “Damping efficiency of the coating structure”. *International Journal of Solids and Structures,* 42, June, pp. 3045-3058.

[2] Ustinov A.I., Movchan B.A., 2001. “A study of damping ability of tin-and yttrium-coated flat specimens of Ti-6%Al-4%V titanium alloy”. *Strength of Materials”*, 33(4), pp. 339-343.

[3] Casadei F., Bertoldi K., Clarke D.R., 2014. “Vibration damping of thermal barrier coatings containing ductile metallic layers". ASME *Journal of Applied Mechanics* 81, pp. 101001_1-101001_10.

[4] Torvik P.J., 2009. “Determination of mechanical properties of non-linear coatings from measurements with coated beams” *International Journal of Solids and Structures* 46, pp. 1066-1077.

[5] Colorado H.A., Velez J., Salva H.R., Ghilarducci A.A., 2006. “Damping behavior of physical vapor-deposited TiN coatings on AISI 304 stainless steel and adhesion determination”. *Material Science and Engineering*, A 442, pp. 514-418.

[6] Zener C., 1948. *Elasticity and anelasticity of metals,* The University of Chicago Press, Chicago Illinois, Chap. 1, pp. 7-15.

[7] Nowick A.S., Berry B.S., 1972. *Anelastic Relaxation in Crystalline Solids,* Academic Press Inc., 111 Fifth Evenue New York, New York 10003, Chap. 3, pp. 42-57.

[8] Finley W.N., Lai J.S., Onaran K., 1989 *Creep and relaxation of nonlinear viscoelastic materials,*: Dover Publications, Inc., New York, Chap. 5, pp. 50-64.

[9] Vasques C M A , Moreira R A S , Rodrigues J D., 2010. “Viscoelastic Damping Technologies– Part I: Modeling and Finite Element Implementation”. *Journal of Advanced Research in Mechanical Engineering*, 1(2), pp. 76-95.

[10] Ramirez L E S, Coimbra C F M., 2007. “A variable order constitutive relation for viscoelasticity”. *Ann. Phys*., 16(7-8), pp. 543-552.

[11] Wang X., Pei Y., Ma Y., 2013. “The effect of microstructure at interface between coating and substrate on damping capacity of coating systems”. *Applied Surface Science*,282, pp. 60-66.

[12] Kiretseu M., Hui D., Tomlinson G., 2008. “Advanced shock-resistant and vibration damping of nanoparticle-reinforced composite material”. *Composites: Part B*, 39, pp. 128-138.

[13] Ustinov A.I., Skorodzievskii V.S., 2008. “A study of the dissipative properties of homogeneus materials deposited as coatings part 2. Copper condensates with different microstructural characteristics”. *Strength of Materials*, 40(2), pp. 275-277.

[14] Khor K.A., Chia C.T., Gu Y.W., Boey F.Y.C., 2002. “High temperature damping behavior of plasma sprayed NiCoCrAlY coatings”. *Journal of Thermal Spray Technology*, 11(3), pp. 359-364.

[15] Rongong J.A., Goruppa A.A., Buravalla V.R., Tomlinson G.R., Jones F.R., 2004. “Plasma deposition of constrained layer damping coating”, Proc. Instn Mech. Engrs Vol. 218 Part C: J. of *Mechanical Engineering Science*, pp. 669-680.

[16] Blackwell C., Palazzotto A., George T.J., Cross C.J., 2007. ”The evaluation of the damping characteristics of hard coating on titanium”. *Shock and Vibrations*, 14, pp. 37-51.

[17] Guangyu D., Zhen T., Dechum B., Kun L., Qingkai H., 2014. “Damping properties of a novel porous Mg-Al alloy coating prepared by arc ion plating”. *Surface&Coatings Technology*, 238, pp. 139-142.

[18] Reed S.A., Palazzotto A.N., Baker W.P., 2008. “An experimental technique for the evaluation of strain dependent material properties of hard coatings”, *Shock and Vibration*, 15 pp. 697-712.

[19] Pastias S., Saxton C., Shipton M., 2004. “Hard damping coatings: an experimental procedure for extraction of damping characteristics and modulus of elasticity”. *Material Science and Engineering A*, 370, pp. 412-416.

[20] Amadori S., Catania G., 2017.“Robust identification of the mechanical properties of viscoelatic non-standard materials by means of time and frequency domain experimental measurements" *Composites Structures*, 169, June, pp.79-89.

[21] Richardson M.H., Formenti D.L., 1982 “Parameter estimation from frequency response measurements using rational fraction polynomials”, *1st IMAC Conference*, Orlando Florida.

[22] Kelly L.G., 1967. *Handbook of Numerical Methods and Applications* Addison Wesley Publishing Company, Reading Massachusetts, Chap. 5 , pp.63-71.

[23] Forsythe G.E., 1957. “Generation and use of orthogonal polynomials for data fitting with a digital computer”. *J. Soc. Indust. Appl. Math.*, 5(2), pp. 74-85.

PROTOTIPAZIONE VIRTUALE E SIMULAZIONE DI UN MANDRINO CEDEVOLE PER LA SBAVATURA ROBOTIZZATA

Angelo O. Andrisano
Dipartimento di Ingegneria "Enzo Ferrari"
Università di Modena and Reggio Emilia
E-mail: angelooreste.andrisano@unimore.it

Giovanni Berselli
Dipartimento di Ingegneria meccanica, energetica, gestionale e dei trasporti
Università di Genova
E-mail: giovanni.berselli@unige.it

Gabriele Bigi
Dipartimento di Ingegneria "Enzo Ferrari"
Università di Modena and Reggio Emilia
E-mail: 80629@studenti.unimore.it

Michele Gadaleta
Dipartimento di Ingegneria "Enzo Ferrari"
Università di Modena and Reggio Emilia
E-mail: michele.gadaleta@unimore.it

Marcello Pellicciari
Dipartimento di Ingegneria "Enzo Ferrari"
Università di Modena and Reggio Emilia
E-mail: marcello.pellicciari@unimore.it

Margherita Peruzzini
Dipartimento di Ingegneria "Enzo Ferrari"
Università di Modena and Reggio Emilia
E-mail: marcello.pellicciari@unimore.it

Roberto Razzoli
Dipartimento di Ingegneria meccanica, energetica, gestionale e dei trasporti
Università di Genova
E-mail: roberto.razzoli@unige.it

***Abstract**. Allo stato dell'arte corrente, la Sbavatura Robotizzata (SR) è stata adottata con successo in numerose applicazioni industriali, ma richiede ancora miglioramenti in termini di qualità finale. Infatti, l'efficacia di un processo di SR è altamente influenzata dalla limitata precisione dei movimenti del robot e dalle imprevedibili variazioni di dimensioni e forma delle bave. La cedevolezza dell'utensile risolve parzialmente il problema, nonostante si rendano necessari strumenti dedicati di "engineering design", allo scopo di identificare quei parametri ottimizzati e quelle strategie di SR che consentano di ottenere la miglior qualità e il miglior rapporto costo-efficacia. In questo contesto, il presente lavoro propone un*

Prototipo Virtuale (PV) di un mandrino pneumatico dotato di cedevolezza intrinseca, adatto a valutare l'efficienza del processo in diversi scenari. Il PV proposto è stato creato integrando un modello multi-body della struttura meccanica del mandrino con un modello matematico delle forze di processo. Vengono infine illustrate simulazioni numeriche, atte a prevedere sia le forze di taglio che l'accuratezza della finitura superficiale.

***Parole Chiave**: mandrino cedevole, sbavatura robotizzata, prototipazione virtuale*

1. INTRODUZIONE

Il processo di sbavatura di parti meccaniche con forme complesse e tolleranze ristrette, in genere, coinvolge l'utilizzo di macchine CNC a cinque assi, vale a dire, attrezzature estremamente costose che richiedono lunghi tempi di set-up. Come potenziale alternativa per la medesima attività, i robot industriali offrono grande flessibilità unita ad un investimento iniziale più contenuto, ma sono caratterizzati da una qualità di processo inferiore. Negli ultimi anni, un crescente numero di ricerche è stato indirizzato allo sviluppo di metodi ingegneristici e strumenti atti a migliorare l'efficacia della Sbavatura Robotizzata (SR) e, più in generale, delle lavorazioni meccaniche mediante robot [1].

Focalizzandosi sulle attività di sbavatura, la programmazione offline di una traiettoria ideale del robot non permette di ottenere la miglior qualità finale di prodotto, a causa della limitata accuratezza di movimento di qualsiasi manipolatore industriale e delle condizioni del processo discontinue e non prevedibili (cioè, differente spessore della bava e proprietà del materiale variabili [2,3]).

In pratica, un processo di SR potrebbe portare o ad una sbavatura parziale o ad una sbavatura eccessiva (dove piccole parti strutturali del pezzo vengono accidentalmente rimosse assieme alla bava). In aggiunta, nel caso in cui siano richieste tolleranze molto ristrette ed una buona rugosità superficiale, è necessario garantire in ogni istante una pressione di contatto uniforme tra utensile e pezzo lavorato, a prescindere dallo spessore della bava. In questi casi, vengono di solito utilizzati dispositivi controllati in forza [4], oppure dispositivi passivi dotati di cedevolezza. Quest'ultima soluzione è più diffusa in ambito industriale grazie al buon rapporto costo-efficacia, alla facilità di utilizzo ed al più veloce ed uniforme adattamento a variazioni inaspettate del processo o ad urti. Tuttavia, la regolazione dei parametri del sistema (ad esempio la scelta del *feed-rate* e dalla cedevolezza complessiva) richiede tempo e svariati test su prototipi fisici, con conseguente riduzione della produttività della cella robotica. Per questo, si rende necessario un approccio ingegneristico basato su modelli virtuali, con lo scopo di prevedere le prestazioni della SR senza bisogno di alcun test sul campo e che possibilmente conduca ad una applicazione tecnologica "*first-time-right*", "*plug-and-produce*".

Per quel che riguarda la letteratura pregressa in tema di processi di sbavatura, in [5] viene riportato un sommario di diversi modelli atti alla determinazione delle forze di taglio (ad esempio il modello lineare di Altintas [6] ed il modello esponenziale di Kienzle [7]), mentre in [8] sono stati recentemente proposti metodi assistiti da CAD/CAM. In ogni caso, la maggior parte dei lavori precedenti semplicemente trascura l'influenza della cedevolezza dell'utensile, la cui complessa interazione con il processo di sbavatura viene sperimentata solo su set-up sperimentali. Stando alle considerazioni qui sopra menzionate, il presente lavoro si indirizza allo sviluppo di un Prototipo Virtuale (PV) di un utensile cedevole, il cui scopo è consentire l'ottimizzazione offline delle attività di SR. In particolare, il comportamento della struttura meccanica del mandrino è modellato per mezzo di un software commerciale multibody (*Recurdyn*), mentre le forze del processo sono simultaneamente co-simulate in un ambiente *Simulink*.

Descrizione del mandrino cedevole

Nella SR vengono comunemente impiegati diverse tipologie di mandrini cedevoli disponibili in commercio. Come caso studio, largamente adottato nella pratica, si considera un mandrino caratterizzato da attuazione pneumatica e cedevolezza radiale [3], la cui descrizione dettagliata si può trovare in [9]. Con riferimento al disegno CAD di Fig. 1, l'utensile comprende un motore pneumatico inserito all'interno di un alloggiamento e supportato da un giunto sferico (con centro localizzato sul punto O) e da un da un dispositivo cedevole. Il dispositivo cedevole (Fig. 2) è composto da sette pistoni, aventi corsa limitata, e connessi ad una camera avente un condotto di entrata comune. Inizialmente, come anche riportato in Sez. 3.3, tutti i pistoni sono in contatto diretto con il motore pneumatico. D'altro canto, come mostrato in Fig. 3, il motore pneumatico può inclinarsi durante l'interazione con il pezzo da lavorare. In questo caso, alcuni dei pistoni possono raggiungere il fine corsa inferiore, perdendo così contatto col motore (vedi Fig. 4)

2. BACAKGROUND SUI PROCESSI DI FRESATURA

Si trascuri inizialmente l'influenza della cedevolezza del sistema. In questo caso, un modello matematico del processo di fresatura è stato estensivamente trattato in [7, pp 35-46], la cui nomenclatura viene qui di seguito mantenuta. Con riferimento alla Fig. 5, si consideri un fresa avente diametro D, angolo d'elica β e numero di denti (o scanalature) N. Si definisca c come il feed - rate del processo, ϕ_j l'angolo istantaneo di immersione del j-esimo dente nel al pezzo in lavorazione, $\phi_p = 2\pi/N$ l'angolo di spacing del dente, ϕ_{st}, ϕ_{ex}, $\phi_s = (\phi_{ex} - \phi_{st})$ gli angoli di ingresso, uscita e "*swept*" dell'utensile di taglio.

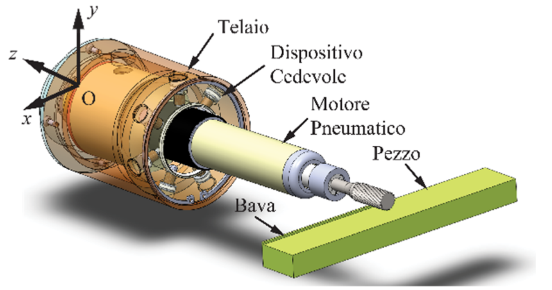

Figura 1. Modello CAD del Mandrino Cedevole.

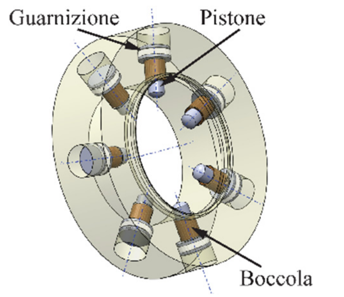

Figura 2. Dispositivo cedevole.

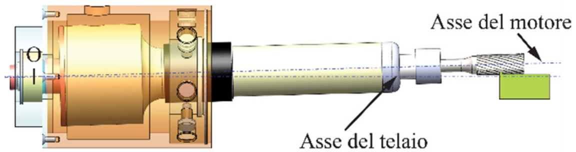

Figura 3. Mandrino con compensazione passiva.

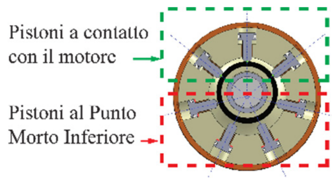

Figura 4. Contatti dei pistoni.

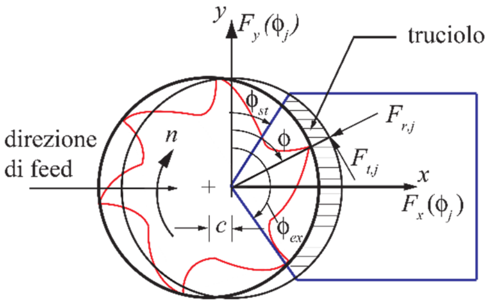

Figura 5. Processo di fresatura/sbavatura [7].

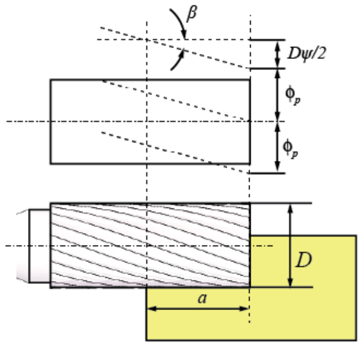

Figura 6. Geometria dell'utensile [7].

Anche se di solito vengono utilizzate frese elicoidali, assumiamo inizialmente β=0 e consideriamo solo il dente j-esimo. In questo caso, lo spessore istantaneo del truciolo , h_j, può essere approssimato come $h_j(\phi_j) = c\ sin\phi_j$, mentre le forze di taglio tangenziale, $F_{t,j}$, radiale, $F_{r,j}$, assiale, $F_{a,j}$, possono essere espresse come funzione della lunghezza del tratto di contatto, a, e dell'area non tagliata del truciolo, $ah(\phi_j)$, così che:

$$F_{q,j}(\phi_j) = K_{q,c}ah(\phi_j) + K_{q,e}a \text{.... per } q = t, r, a \text{ e } j = 0, \dots, N-1 \tag{1}$$

dove $K_{t,c}$, $K_{r,c}$ e $K_{a,c}$ sono rispettivamente definiti come *coefficienti della forza di taglio* dovuti all'azione di taglio nelle direzioni tangenziale, radiale e assiale, mentre $K_{t,e}$, $K_{r,e}$, e $K_{a,e}$ sono le cosiddette "*edge constants*".

Naturalmente, le forze di taglio sono prodotte solo quando lo strumento è nella zona di taglio (immersione), cioè quando $F_{q,j}(\phi_j) > 0$ se $\phi_{st} \leq \phi_j \leq \phi_{ex}$. In aggiunta, denti multipli taglieranno simultaneamente se $\phi_s > \phi_p$, essendo la forza totale data dalla somma del singolo contributo j-esimo.

In caso in cui si utilizzi una fresa elicoidale (cioè $\beta > 0$), il tratto di taglio avanzerà lentamente dietro al fine corsa dell'utensile (vedi Fig. 6). L'angolo di ritardo, ψ, alla profondità assiale di taglio, z, è $\psi = 2zD^{-1}\ tan\beta$. In particolare, come definito in [7], quando il punto inferiore di un dente di riferimento si trova ad un angolo di immersione ϕ, un punto del tratto di taglio localizzato assialmente ad una distanza z al di sopra del dente di riferimento avrà un angolo di immersione di $(\phi - \psi)$. Assumendo che la parte inferiore di un dente sia designata come l'angolo di immersione di riferimento ϕ, essendo l'immersione misurata in senso orario dall'asse normale y, i punti finali inferiori dei denti rimanenti si trovano agli angoli $\phi_j(0) = \phi + j\phi_p$ per $j = 0, \dots, N-1$. L'angolo di immersione per il flauto j-esimo ad una profondità di taglio assiale z è:

$$\phi_j(z) = \phi + j\phi_p - k_\beta z \quad \text{dove } k_\beta = 2D^{-1}\ tan\beta \tag{2}$$

Lo spessore del truciolo, h_j, è ora approssimata come $h_j(\phi_j, z) = c\ \ sin\phi_j(z)$. In modo simile a Eq. 1, il contributo delle forze elementari in direzione tangenziale, $dF_{t,j}$, radiale, $dF_{r,j}$, ed assiale , $dF_{a,j}$, su un elemento elementare del dente con altezza z può essere scritta come:

$$dF_{q,j}(\phi_j, z) = \left[K_{q,c}h_j\left(\phi_j(z)\right) + K_{q,e}\right]dz, \text{ per } q = t, r, a \text{ e } j = 0, \dots, N-1 \tag{3}$$

Dalle condizioni di equilibrio, le forze elementari radiali e tangenziali possono essere proiettate nelle direzioni di avanzamento x e normale, y, utilizzando le seguenti trasformazioni:

$$dF_{x,j} = -dF_{t,j}\, cos\phi_j(z) - dF_{r,j}\, sin\phi_j(z);$$
$$dF_{y,j} = dF_{t,j}\, sin\phi_j(z) - dF_{r,j}\, cos\phi_j(z) \tag{4}$$

La forza totale prodotta dal dente j-esimo può essere ottenuta integrando le forze di taglio differenziali:

$$F_{p,j}(\phi_j(z)) = \int_{z_{j,1}}^{z_{j,2}} dF_{p,j}(\phi_j(z))dz, \quad \text{per } p = x, y, z \tag{5}$$

dove $z_{j,2}(\phi_j(z))$ e $z_{j,2}(\phi_j(z))$ sono i limiti assiali inferiori e superiori di impegno del j-esimo dente nella porzione di fresa impegnata nel taglio. Gli integrali vengono calcolati notando che $d\phi_j(z) = -k_\beta z$,

$$F_{x,j}(\phi_j(z)) = \left\{\frac{c}{4k_\beta}\left[-K_{tc}\, cos2\phi_j(z) + K_{rc}(2\phi_j(z) - sin2\phi_j(z))\right] + \frac{1}{k_\beta}\left[K_{te}\, sin\phi_j(z) - K_{re}\, cos\phi_j(z)\right]\right\}_{z_{j,1}(\phi_j(z))}^{z_{j,2}(\phi_j(z))}$$

$$F_{y,j}(\phi_j(z)) = \left\{\frac{-c}{4k_\beta}\left[-K_{tc}(2\phi_j(z) - sin2\phi_j(z)) + K_{rc}\, cos2\phi_j(z)\right] + \frac{1}{k_\beta}\left[K_{te}\, cos\phi_j(z) + K_{re}\, sin\phi_j(z)\right]\right\}_{z_{j,1}(\phi_j(z))}^{z_{j,2}(\phi_j(z))} \tag{6}$$

$$F_{z,j}(\phi_j(z)) = \frac{1}{k_\beta}\left[K_{ac}c\, cos\phi_j(z) - K_{ae}\phi_j(z)\right]_{z_{j,1}(\phi_j(z))}^{z_{j,2}(\phi_j(z))}.$$

Si noti che l'angolo di ritardo ad una profondità assiale di taglio completa (cioè quando z=a) è $\psi_a = k_\beta a$.

Con riferimento alla Fig. 7, l'algoritmo proposto in [7] per determinare i limiti di integrazione assiale è come segue:

- Se $\phi_{st} < \phi_j(z = 0) < \phi_{ex}$, allora $z_{j,1}$=0;
  Se $\phi_{st} < \phi_j(z = a) < \phi_{ex}$, allora $z_{j,2}$=a;
  Se $\phi_j(z = a) < \phi_{ex}$, allora $z_{j,2}$=$(1/k_\beta)(\phi + j\phi_p - \phi_{st})$;
- Se $\phi_j(z = 0) > \phi_{ex}$ e $\phi_j(z = a) < \phi_{ex}$ allora $z_{j,1}$=$(1/k_\beta)(\phi + j\phi_p - \phi_{ex})$;
  Se $\phi_j(z = a) > \phi_{st}$ allora $z_{j,2}$=a;
  Se $\phi_j(z = a) < \phi_{st}$, allora $z_{j,2}$=$(1/k_\beta)(\phi + j\phi_p - \phi_{st})$;
- Se $\phi_j(z = 0) > \phi_{ex}$ e $\phi_j(z = a) > \phi_{ex}$ allora il dente non sta tagliando.

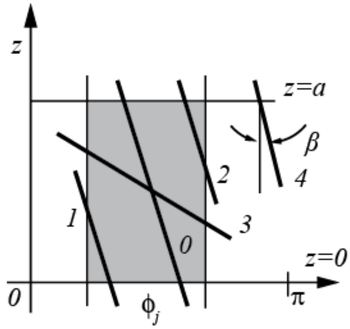

Figura 7. Fresa elicoidale: zona di interfaccia con pezzo in lavorazione [7].

Si noti che queste espressioni possono essere usate se il dente j=0 è allineato a $\phi = 0$ all'inizio dell'algoritmo. Le forze istantanee totali sulla fresa all'immersione sono infine calcolate come segue:

$$F_x(\phi) = \sum_{j=0}^{N-1} F_{x_j}; \quad F_y(\phi) = \sum_{j=0}^{N-1} F_{y_j}; \quad F_z(\phi) = \sum_{j=0}^{N-1} F_{z_j}. \tag{7}$$

3. PROTOTIPO VIRTUALE DEL MANDRINO CEDEVOLE

Il PV del mandrino può essere concettualmente diviso in tre sottosistemi organizzati in una struttura a loop, dove l'output di un sottosistema è l'input di quello successivo. In riferimento a Fig. 8, i sottosistemi del modello sono utilizzati per calcolare: (1) le profondità di taglio del truciolo in direzione radiale p_{rb}, e del pezzo lavorato p_{rp}; (2) le forze di taglio; (3) posizione dell'utensile di taglio e velocità tramite la co-simulazione con un software multi-body.

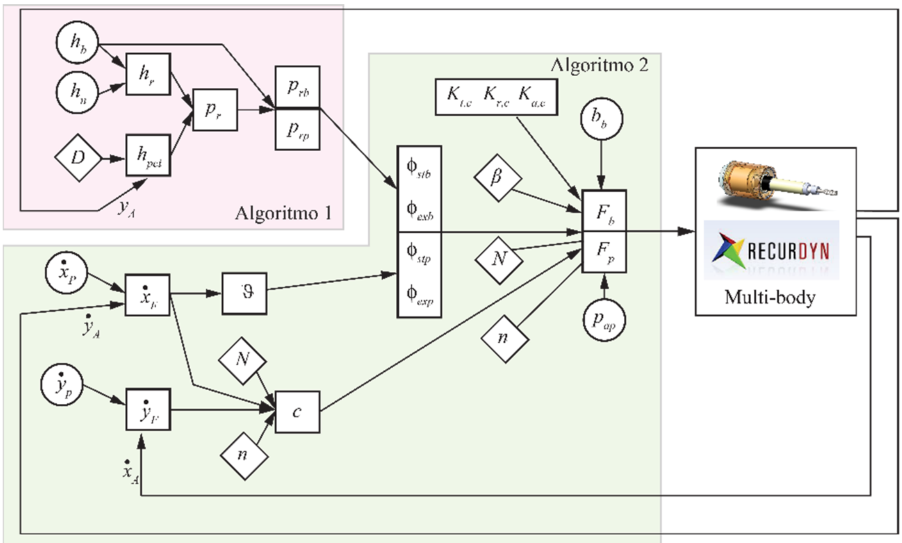

Figura 8. Prototipo Virtuale del mandrino: integrazione tra il modello multibody CAD-based ed i modelli del processo.

Calcolo della profondità di taglio della fresa radiale e del pezzo lavorato

Con riferimento a Fig. 9, si definisca una coordinata spaziale *w* e si supponga di srotolare concettualmente un profilo di bava 3D lungo questa stessa coordinata. L'altezza e la larghezza della bava possono quindi essere definite in funzione di *w*, cioè, rispettivamente, $h_b = h_b(w)$ e $b_b = b_b(w)$. Con riferimento alle Figure 1 e 10, definiamo un sistema di riferimento fisso, localizzato sul punto O, essendo l'asse *z* allineato con l'asse di simmetria dell'alloggiamento, ed indicando come asse *x* la direzione di alimentazione. In modo simile, individuiamo i punti di applicazione delle forze di processo (come calcolato nel prossimo algoritmo) in A e in B. Questi punti giacciono nell'intersezione tra l'asse longitudinale della fresa (Fig. 10) e le due linee parallele all'asse *y* e rispettivamente intersecanti i punti medi di b_b e a (essendo quest'ultima la lunghezza del tratto di contatto tra pezzo lavorato e fresa). Si noti che la posizione di entrambi i punti A e B, rispetto ad O, può variare in base alla cedevolezza del mandrino. In particolare la Fig. 11 presenta una condizione dove il processo di sbavatura è incompleto, mentre la Fig. 12 presenta una condizione dove la fresa sta tagliando sia la bava che il pezzo lavorato. Con riferimento a queste stesse figure, definiamo, per ogni istante di tempo *t*, le variabili x_A e y_A come le coordinate *x* e *y* del punto A nei sistemi di riferimento fissi localizzati sul punto O, h_{pci} come la coordinata *y* del punto di contatto inferiore fresa/pezzo lavorato (punto C), che definisce il profilo del pezzo dopo la sbavatura (cioè $h_{pci} = y_A - D/2$), h_r e h_n come le altezze del pezzo reali e desiderate (nominali) con riferimento a O (cioè $h_r = h_n - h_b$), p_r come la profondità in direzione radiale di sbavatura $p_r = h_r - h_{pci}$.

Ci sono 3 casi possibili:

- **Sbavatura ideale**: $p_r = h_b$, così che $p_{rb} = h_b$ e $p_{rp} = 0$;
- **Sbavatura parziale**: $p_r < h_b$, così che $p_{rb} = p_r$ e $p_{rp} = 0$;
- **Sbavatura eccessiva**: $p_r > h_b$, così che $p_{rb} = h_b$ e $p_{rp} = p_r - h_b$;

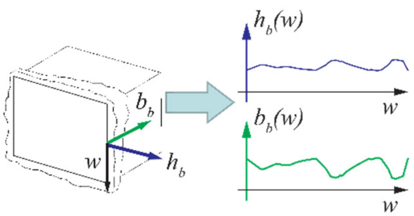

Figura 9. Definizione di altezza e larghezza di bava.

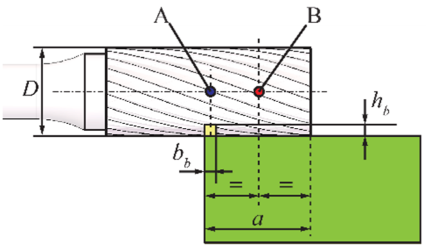

Figura 10. Geometrie di bava e pezzo.

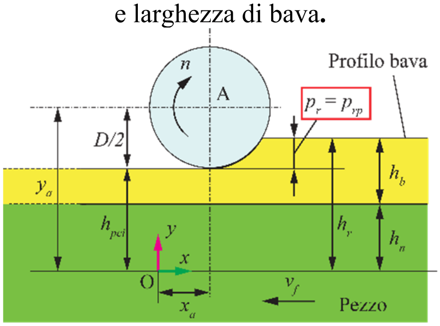

Figura 11. Sbavatura parziale.

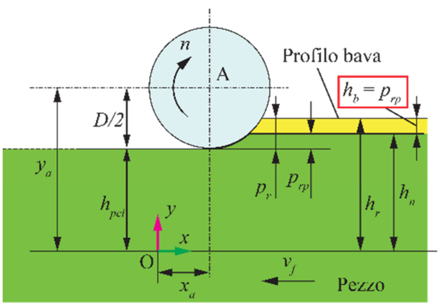

Figura 12. Sbavatura eccessiva.

A causa delle considerazioni qui sopra menzionate, le forze di processo considerate di seguito, $\boldsymbol{F}_b$ e $\boldsymbol{F}_p$, sono rispettivamente dovute o all'interazione fresa-bava o all'interazione fresa-pezzo lavorato. La forza $\boldsymbol{F}_b$, (qui di seguito definita *forza di bava*), è applicata al punto A, mentre la forza $\boldsymbol{F}_p$, (qui di seguito definita *forza di pezzo*), è applicata al punto B.

Calcolo delle forze di sbavatura

A causa della presenza di una struttura cedevole, il vettore della velocità di avanzamento sarà inclinato con riferimento all'asse orizzontale del pezzo lavorato. Si definiscano $\boldsymbol{v}_P = [\dot{x}_P, \dot{y}_P, \dot{z}_P]^T$e $\boldsymbol{v}_A = [\dot{x}_A, \dot{y}_A, \dot{z}_A]^T$come le velocità relative del pezzo e del punto A con riferimento al sistema fisso centrato in O. Il vettore della velocità di alimentazione del pezzo in riferimento alla fresa è $\boldsymbol{v}_F = \boldsymbol{v}_P - \boldsymbol{v}_A = [\dot{x}_F, \dot{y}_F, \dot{z}_F]^T$. Si noti che, per via della cedevolezza del mandrino, $\dot{z}_F \neq 0$. Tuttavia, a patto che $\dot{z}_F$ sia sempre di un ordine di grandezza più basso di $\dot{x}_F$ e $\dot{y}_F$,, il suo contributo è trascurato (cioè $\boldsymbol{v}_F \approx [\dot{x}_F, \dot{y}_F, 0]^T$). L'angolo di inclinazione, ϑ, della velocità del mandrino in riferimento all'asse orizzontale può essere valutato come $\vartheta = \mathrm{atan}(\dot{y}_F/\dot{x}_F)$. Il feed-rate del processo, *c*, è quindi dato da:

$$c = (N\,n)^{-1}(\dot{x}_F{}^2 + \dot{y}_F{}^2)^{1/2} \tag{8}$$

$$h_j(\phi_j) = c \sin(\phi_j - \vartheta) \tag{9}$$

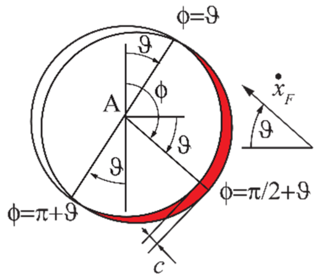

Figura 13. Calcolo di $\boldsymbol{h(\phi_j, \vartheta)}$

Per esempio, con riferimento a Fig. 13, se $\phi_j = \phi_{j,1} = \vartheta$, allora $h(\phi_{j,1}, \vartheta) = 0$. Allo stesso modo, se $\phi_j = \phi_{j,2} = \pi/2 + \vartheta$, allora $h(\phi_{j,2}, \vartheta) = c$. Infine, se $\phi_j = \phi_{j,3} = \pi + \vartheta$, allora $h(\phi_{j,3}, \vartheta) = 0$. Naturalmente, se la cedevolezza del mandrino viene trascurata e conseguentemente $\dot{y}_F = 0$, entrambe le Eq. 8 e 9 si semplificano nelle relazioni date dal modello standard di Altintas [7] (richiamate in Sez. 2), cioè c=$\dot{x}_F$ e $h_j(\phi_j) = c\, sin\phi_j$.

Le forze di taglio possono quindi essere determinate inserendo le Eq. 8 e 9 ed eseguendo i calcoli necessari per l'integrazione delle forze stesse (Eq. 5). Si ricavano così le seguenti espressioni:

$$F_{x,j}(\phi_j(z)) = \left\{ \frac{c}{k_\beta} \left[K_{tc} \left(-\frac{\phi_j(z)\sin(\vartheta)}{2} - \frac{cos(2\phi_j(z) - \vartheta)}{4} \right) + K_{rc} \left(\frac{\phi_j(z)\cos(\vartheta)}{2} - \frac{sin(2\phi_j(z) - \vartheta)}{4} \right) \right] \right\}_{z_{j,1}(\phi_j(z))}^{z_{j,2}(\phi_j(z))}$$

$$F_{x,j}(\phi_j(z)) = \left\{ \frac{c}{k_\beta} \left[K_{tc} \left(-\frac{\phi_j(z)\sin(\vartheta)}{2} - \frac{cos(2\phi_j(z)-\vartheta)}{4} \right) + K_{rc} \left(\frac{\phi_j(z)\cos(\vartheta)}{2} - \frac{sin(2\phi_j(z)-\vartheta)}{4} \right) \right] \right\}_{z_{j,1}(\phi_j(z))}^{z_{j,2}(\phi_j(z))}$$

$$F_{z,j}(\phi_j(z)) = \frac{1}{k_\beta} \left[K_{ac} c\, cos(\phi_j(z)-\vartheta) \right]_{z_{j,1}(\phi_j(z))}^{z_{j,2}(\phi_j(z))} \tag{10}$$

Anche in questo caso, se $\vartheta = 0$, Eq. 10 si riduce a Eq. 6. Come ultimo passaggio per il calcolo delle forze di taglio, occorre calcolare gli estremi di integrazione. In particolare, si possono definire quattro estremi di integrazione, $\phi_{stb}, \phi_{stp}, \phi_{exb}, \phi_{exp}$, che rappresentano l'immersione angolare della fresa o nella bava o nel pezzo. Nel caso esista una componente della velocità nella direzione y, $\dot{y}_F$, i casi istantanei possibili sono mostrati in Tabella 1, in base al valore di ϑ (zero, negativo o positivo) o ai valori di p_{rp} e p_{rb} (Fig. 11 e 12).

Per quel che riguarda i casi mostrati nella terza colonna, non è necessario calcolare alcun estremo di integrazione, poiché la fresa non è in contatto né con la bava né col pezzo (cioè $\boldsymbol{F}_b = \boldsymbol{F}_p = 0$). In parallelo, i casi mostrati nella seconda colonna riportano una situazione in cui la fresa è a contatto solo con la bava, così che ϕ_{stp} e ϕ_{exp} non sono definite (cioè $\boldsymbol{F}_p = 0$). Riassumendo, l'algoritmo complessivo per il calcolo dei limiti integrali, che richiede p_{rp}, p_{rb}, e h_b come input, è formulato come segue:

Tabella 1. Casi possibili per il processo di sbavatura

	$p_{rp} > 0$ e $p_{rb} > 0$	$p_{rp} = 0$ e $p_{rb} > 0$	$p_{rp} = 0$ e $p_{rb} = 0$
$\vartheta = 0$	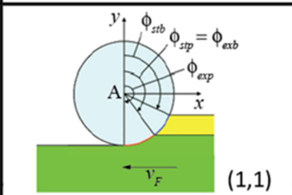	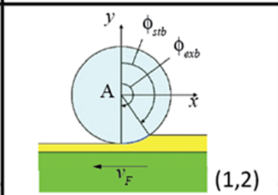	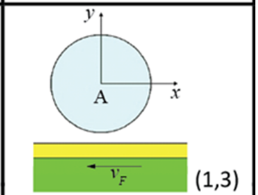
$\vartheta > 0$	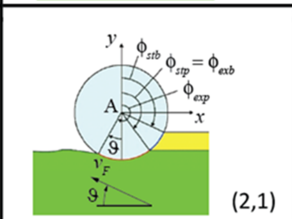	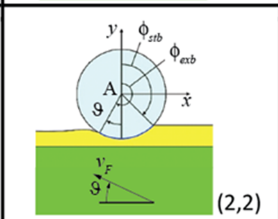	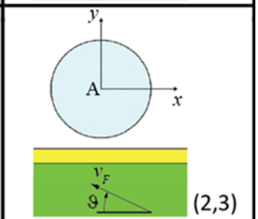
$\vartheta < 0$	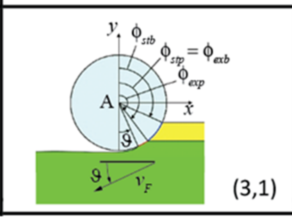	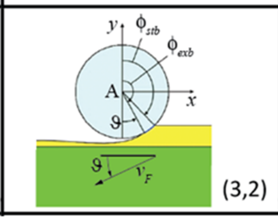	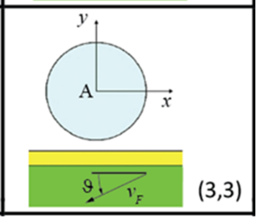

$$\varphi_{stb} = \pi - \mathrm{acos}\left(1 - \frac{2\,p_r}{D}\right), sempre;$$

$$\varphi_{exb} = \begin{cases} \pi - \mathrm{acos}\left(1 - \dfrac{2\,p_{rp}}{D}\right), & if\ p_r > h_b \\ \pi + \vartheta, & if\ 0 < p_r < h_b \end{cases} \tag{11}$$

$$\varphi_{stp} = \pi - \mathrm{acos}\left(1 - \frac{2\,p_{rp}}{D}\right),\ \ if\ p_r > h_b;$$

$$\varphi_{exp} = \pi + \vartheta,\ \ if\ p_r > h_b$$

Modello multibody

Come mostrato in Fig. 8, il modello multy-body della struttura meccanica del mandrino calcola la posizione e la velocità della fresa (specificatamente sul punto A e B) per forze date sul pezzo lavorato $\boldsymbol{F_p}$ e sulla bava $\boldsymbol{F_b}$. Il modello multi-body descrive la struttura cinematica del mandrino, la dinamica di ogni corpo in movimento , e le forze interne dovute agli attriti, ai contatti ed alla pressione interna nella camera del dispositivo cedevole. Così come per la struttura del mandrino, anche l'alloggiamento è considerato fisso, il motore pneumatico è connesso all'alloggiamento per mezzo di un giunto sferico centrato sul punto O, la fresa ruota ad una velocità data, *n*. I sette pistoni possono traslare lungo i loro assi. Ad ogni pistone sono imposti tre possibili contatti, vale a dire il contatto con il motore pneumatico (punto C), e possibili contatti con la camera o al fine corsa inferiore o a quello superiore, si vedano le Fig. 2 e 16. Nella configurazione iniziale del mandrino (non deflesso), tutti i pistoni sono in contatto con il motore. Con riferimento alle forze interne, ne sono state incluse due:

- Pressione sulla volta del pistone, F_{pst}, semplicemente data da $F_{pst} = A_{pst}p$, essendo i parametri A_{pst} e p l'area del cielo del pistone e la pressione nella camera
- Forza di attrito sulle guarnizioni di gomma del pistone F_{sln}. La forza F'_{sln}, di direzione perpendicolare a quella del movimento del pistone e dovuta all'interazione camera-guarnizione, viene calcolata come $F'_{sln} = A_{sln}p$+P ,essendo i parametri A_{sln} e P l'area laterale della guarnizione ed il precarico. La forza, F_{sln}, di direzione parallela a quella del movimento del pistone e dovuta all'attrito, e data da $F_{sln} = \mu F'_{sln}$, essendo il parametro μ il coefficiente di attrito statico o dinamico.

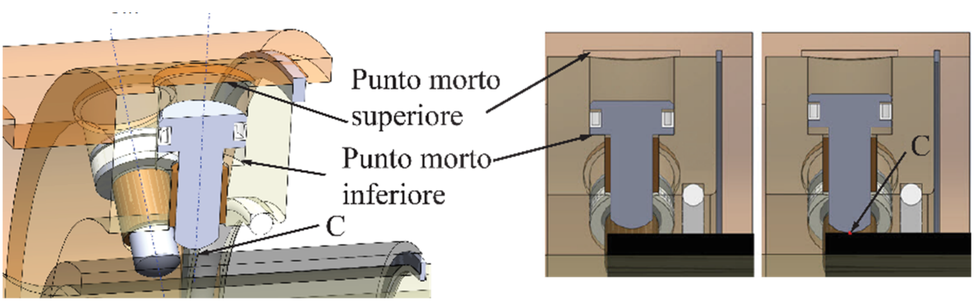

Figura 14. Punti di contatto

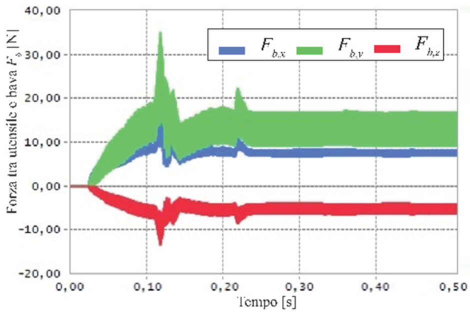

Figura 15. Forza tra pezzo e bava

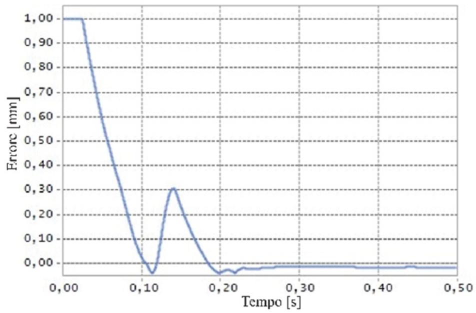

Figura 16. Errore di finitura superficiale

4. SIMULAZIONE NUMERICA

A questo punto, il PV viene validato per mezzo di una serie di simulazioni numeriche. Sono stati utilizzati i seguenti parametri: $K_{t,c}$=2000 N/mm^2, $K_{r,c}$=1200 N/mm^2, $K_{a,c}$=800 N/mm^2, $K_{t,e}$=$K_{r,e}$=$K_{a,e}$=0, N=20, n=40000 rpm, D=8 mm, a=10 mm, $h_b = b_b$=1 mm, h_n=5 mm, v_f=80 mm/s, 80 mm/s, p=5 bar, β=20°, F_{pst}=7.70 N, F_{sln}=3.90 N (attrito statico), F_{sln}=2.80 N (attrito dinamico). Si definisca poi l'errore di processo come:

$$e = \min(h_{pci} - h_n \,, h_b) \tag{12}$$

Un errore positivo indica una sbavatura parziale, mentre un errore negativo indica una sbavatura eccessiva. Come esempio, la Fig. 15 presente un grafico delle componenti di forza sulla bava $F_{b,x}$, $F_{b,z}$, $F_{b,z}$, che sottolinea come le forze del processo si stabilizzino dopo un transitorio iniziale. La Fig. 16 mostra l'errore di processo, che si stabilizza su un valore negativo sufficientemente basso.

5. CONCLUSIONI

In questo lavoro è stato presentato un prototipo virtuale di un mandrino pneumatico cedevole, che utilizza un software multi-body in co-simulazione con *Simulink*. Il prototipo virtuale può efficacemente prevedere sia le forze di sbavatura che gli errori di finitura, permettendo un test virtuale della qualità del processo. In aggiunta, la versatilità dell'ambiente multi-body, basato su modelli CAD del mandrino, permette di valutare facilmente l'influenza di diversi parametri di design (e controllo), come ad esempio la cedevolezza complessiva del mandrino e l'influenza dell'attrito.

BIBLIOGRAFIA

[1] J. Pandremenos, C. Doukas, P. Stavropoulos, G. Chryssolouris, "Machining with Robots: A Critical Review, Proc. of DET2011, 7th Int. Conf. on Digital Enterprise Tech., pp. 1-8, Sept. 28-30, 2011.

[2] M. Mohammad, V. Babriya, T. Sobh, "Modeling A Deburring Process, Using DELMIA V5," Technological Developments in Education and Automation, pp 549-558, 2010.

[3] B. Ryuh and G. R. Pennock, "Robot Automation Systems for Deburring," Industrial Robotics: Programming, Simulation and Applications, L. K. Huat (Ed.), ISBN: 3-86611-286-6, InTech, 2006.

[4] L. Liang, F. Xi, K. Liu, “Modeling and Control of Automated Polishing/deburring Process Using a Dual-Purpose Compliant Toolhead,” International Journal of Machine Tools and Manufacture, vol. 48, no. 12–13, 2008.

[5] B. Denkena e F. Hollmann, Process Machine Interactions - Predicition and Manipulation of Interactions between Manufacturing Processes and Machine Tool Structures, Springer, 2013.

[6] Y. Altintas, Manufacturing automation, Metal Cutting Mechanics, Machine Tool Vibrations, and CNC Design, New York: Cambridge University Press, 2012.

[7] Kienzle, O. and Victor, H., “Spezifische Shnittkraefte bei der Metall-bearbeitung’’, Werkstattstehnik und Maschinenbau, Bd. 47, H.5, 1957.

[8] K. Schützer, E Abele, S Güth, “Simulation-based deburring tool and process development,” CIRP Annals - Manufacturing Technology, vol. 64, no. 1, pp. 357-360, 2015.

[9] D. K. Lawson, “Deburring tool,” U.S. Patent 6,974,286 B2, filed Jul. 25, 2003, and issued Dec. 13, 2005.

OTTIMIZZAZIONE DEI PARAMETRI DI PROCESSO E REALIZZAZIONE DI COMPONENTI CON TECNOLOGIE DI ADDITIVE MANUFACTURING IN MATERIALI METALLICI

Erica Liverani
Dipartimento di Ingegneria Industriale DIN,
Università di Bologna, Italy
E-mail: erica.liverani2@unibo.it

Adrian Lutey
Dipartimento di Ingegneria e Architettura,
Università di Parma, Italy
E-mail: adrianhughalexander.lutey@unipr.it

Andrea Gamberoni
Dipartimento di Ingegneria Industriale DIN,
Università di Bologna, Italy
E-mail: andrea.gamberoni2@unibo.it

Giacomo Guerrini
Dipartimento di Ingegneria Industriale DIN,
Università di Bologna, Italy
E-mail: giacomo.guerrini6@unibo.it

Alessandro Ascari
Dipartimento di Ingegneria Industriale DIN,
Università di Bologna, Italy
E-mail: a.ascari@unibo.it

Alessandro Fortunato
Dipartimento di Ingegneria Industriale DIN,
Università di Bologna, Italy
E-mail: alessandro.fortunato@unibo.it

Luca Tomesani
Dipartimento di Ingegneria Industriale DIN,
Università di Bologna, Italy
E-mail: luca.tomesani@unibo.it

Abstract
Nel seguente articolo viene presentata l'influenza dei parametri di processo sulle caratteristiche finali di componenti metallici ottenuti tramite processo SLM (Selective Laser Melting). I parametri valutati sono: la potenza del laser, la distanza tra due tracce successive eseguite per la fusione di ciascuno strato e la direzione di accrescimento del campione. Per valutare l'influenza sulle proprietà finali sono state eseguite prove di densità, test statici di trazione, misure di durezza ed infine un'indagine microstrutturale preliminare per individuare i difetti e le superfici di frattura dei provini. Le attività sperimentali sono state progettate tramite un approccio statistico (DOE) basato su un piano sperimentale a tre fattori e due livelli. A conclusione del lavoro è stato fabbricato, utilizzando i parametri ottimizzati, un componente reale, presente in una macchina automatica, che mostra i vantaggi industriali legati all'utilizzo di questo processo.

Keyword: *Additive Manufacturing, SLM, proprietà meccaniche, microstruttura*

1. INTRODUZIONE

Il processo di Selective Laser Melting è una tecnologia di produzione additiva (AM) che si pone come alternativa a molte tecniche di produzione convenzionali [1]. Zhang et al. [2] hanno dimostrato che il processo SLM, mediante la fusione e la risolidificazione di polveri metalliche strato per strato, consente la fabbricazione di componenti metallici ad alta resistenza e a piena densità. Componenti meccanici ottenuti tramite questa tecnologia non devono più sottostare a pesanti vincoli geometrici e di forma, con chiari vantaggi in fase di progettazione.

Inoltre, la combinazione di tecnologie AM (Additive Manufacturing) con tecnologie di reverse engineering o imaging consente la personalizzazione di componenti appartenenti a numerosi campi di applicazione, incluse le macchine per l'imballaggio, in cui i manipolatori possono essere facilmente adattati per abbinarsi al prodotto.

Anche se la tecnologia SLM non sembra presentare limitazioni rilevanti dal punto di vista del design, non valgono le stesse considerazioni da un punto di vista tecnologico. Infatti, è stato ampiamente mostrato in letteratura e recentemente mostrato da Olakami et al. [3] in caso di lega di alluminio e da Gu et al. [4] per altri metalli, che le proprietà meccaniche dei componenti prodotti con AM sono fortemente correlate ai parametri di processo utilizzati. Questi parametri influenzano direttamente il ciclo termico [5] e di conseguenza microstruttura e resistenza meccanica sotto carico, sia statico che ciclico. Sono stati presentati diversi studi che evidenziano alcune correlazione tra i parametri di processo, la microstruttura e le proprietà meccaniche dei componenti SLM: dagli effetti degli elementi di lega alla microstruttura di uno strato rifuso [6-7].

L’obiettivo di questo studio è quello di caratterizzare componenti in AISI 316L fabbricati tramite SLM in termini di densità ottenibile, resistenza a trazione, durezza e microstruttura. I parametri di processo in esame includono la potenza del laser, la velocità di scansione, la spaziatura tra tracce successive e la direzione di accrescimento. I risultati ottenuti hanno permesso di individuare delle finestre operative ottimizzate per la produzione di componenti meccanici ad alte prestazioni.

2. MATERIALE E METODI

Fabbricazione dei campioni

La polvere in acciaio inossidabile 316L fornita da LPW, con composizione chimica nominale riportata in Tab. (1), è stata utilizzata come materia prima per la produzione di campioni SLM per la caratterizzazione microstrutturale e meccanica. I grani di polvere, di forma mediamente sferica hanno dimensioni nell'intervallo 15-45 μm.

I campioni sono stati prodotti utilizzando un sistema SISMA MYSINT100 dotato di un laser in fibra con lunghezza d'onda 1030 nm, potenza fino a 150 W e diametro dello spot pari a 50 μm. La produzione è avvenuta in ambiente controllato, riempiendo la camera di Argon con un contenuto di ossigeno residuo pari a 0,5 %.

L'orientamento di ciascun componente, i parametri di processo e la strategia di scansione sono stati definiti tramite il software MARCAM AutoFab. Per la fusione di ciascuno strato è stata scelta la strategia di scansione detta “a scacchiera”: ciascuna superficie viene divisa in blocchi quadrati 3x3 mm^2 (Fig. (1a)), ognuno dei quali etichettato come “bianco” o “nero”.

Tabella 1. Composizione chimica della polvere di AISI 316L.

C	Cr	Cu	Mn	Mo	Ni	P	S	Si	Fe
≤0.03	17.5 - 18	≤0.5	≤2	2.25 - 2.5	12.5 - 13	≤0.025	≤0.01	≤0.75	Bal.

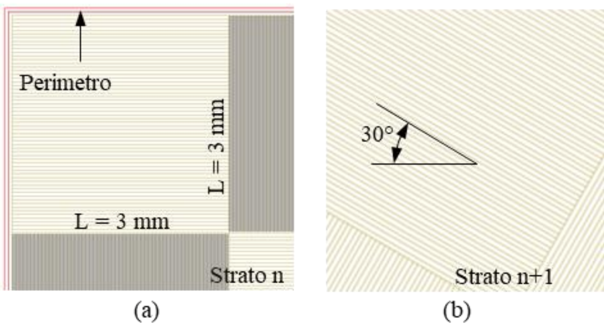

Figura 1. Strategia di scansione a "scacchiera".

Tabella 2. Parametri di processo utilizzati per la fabbricazione dei campioni.

Test	Potenza [W]	Velocità [mm/s]	Distanza tra trace adiacenti [mm]	Direzione di accrescimento [°]	Fluenza [J/mm^3]
1	100	700	0,05	45	142,9
2	100	700	0,05	90	142,9
3	100	700	0,07	45	102,0
4	100	700	0,07	90	102,0
5	150	700	0,05	45	214,3
6	150	700	0,05	90	214,3
7	150	700	0,07	45	153,1
8	150	700	0,07	90	153,1

I blocchi neri vengono fusi per primi, seguiti da quelli bianchi e alla fine il fascio laser percorre il perimetro del componente; ciascun blocco è stato scansionato con tracce parallele. Per minimizzare i gradienti termici, ciascuno strato (n+1) viene ruotato di 30° rispetto allo strato precedente (n) come mostrato in Fig. (1b).

Una corposa campagna sperimentale preliminare è stata condotta per definire la finestra di parametri di processo che permette la fabbricazione di componenti con una densità relativa superiore al 98 %, calcolata prendendo come riferimento 8 kg/dm^3. A partire da questi risultati sono stati costruiti i campioni adatti alla caratterizzazione meccanica e microstrutturale; i parametri scelti sono riportati in Tab. (2).

Caratterizzazione microstrutturale

La composizione chimica pre e post-processo delle polveri di AISI 316L e di alcuni campioni rappresentativi è stata valutata mediante spettroscopia ad emissione ottica (GDOES).

Per la caratterizzazione della microstruttura sono stati scelti gli stessi provini utilizzati per le prove di trazione; tagliandone entrambe le zone di afferraggio e una parte del tratto utile. Per osservarne le caratteristiche microstrutturali, i campioni sono stati attaccati elettrochimicamente utilizzando una soluzione con il 10% in peso di acido oxalico e 90% di acqua deionizzata, applicando 6 V DC per 60 s. Dopo l'attacco, i campioni sono stati sciacquati con acqua e acetone e infine essiccati.

La caratterizzazione microstrutturale è stata effettuata tramite microscopio ottico (OM) e microscopio elettronico a scansione equipaggiato con uno spettroscopio a dispersione di energia (SEM-EDS).

Misure di densità e caratterizzazione meccanica

La densità dei campioni SLM è stata determinata, sulla base del principio di Archimede, utilizzando una bilancia analitica con una precisione di ± 0,0001 g.

I test di trazione sono stati eseguiti su provini a sezione circolare con diametro del tratto utile pari a 6 mm e lunghezza di 30 mm, in rispetto della norma ISO 6892-1, utilizzando una pressa idraulica con una cella di carico di 250 kN. La geometria scelta dei campioni di trazione è stata ottenuta per tornitura partendo da provini con geometria analoga per i quali era stato previsto, in fase di progettazione della stampa, un sovrametallo di 1 mm sul diametro. La velocità di deformazione è stata fissata, in accordo con la normativa, a $2{,}4 \cdot 10^{-4}$ s^{-1} ed è stata mantenuta costante con una velocità di separazione di 0,5 mm/min. Dopo la determinazione della tensione di snervamento, la velocità di deformazione è stata innalzata al valore di $9{,}5 \cdot 10^{-4}$ s^{-1} usando una velocità di separazione di 2 mm/min. Al fine di confrontare i risultati con un valore di riferimento, sono stati eseguiti test di trazione anche su tre campioni ricavati da una barra commerciale ricotta dello stesso materiale.

I test di durezza Vickers sono stati eseguiti con un carico di 1 kg (HV1) su campioni metallografici ricavati da entrambe le estremità dei provini di trazione, per valutare i possibili effetti dovuti alle differenti velocità di raffreddamento che possono verificarsi in zone differenti dei componenti fabbricati con SLM.

Infine, la morfologia delle superfici di frattura è stata analizzata tramite SEM-EDS.

3. RISULTATI

Composizione chimica

La composizione chimica dei campioni SLM in 316L, misurata tramite GDOES, è riportata in Tab. (3). Confrontando i valori con quelli mostrati in Tab. (1) si può affermare che non esiste alcuna variazione significativa dalla composizione nominale.

Caratterizzazione microstrutturale e difetti

Le prime analisi effettuate sono state quelle a basso ingrandimento ottenute tramite microscopio ottico; in Fig. (2) sono mostrate le sezioni di due campioni rappresentativi fabbricati con direzione di accrescimento a 45 ° e 90 ° e con gli stessi parametri di processo (potenza 150 W, velocità di scansione 700 mm / s, distanza tra tracce adiacenti 0,07 mm). I campioni presentano la microstruttura stratificata tipica dei processi additivi, con pozze di fusione generate dal passaggio del fascio laser.

Le immagini ottiche mostrano anche la presenza di grandi grani colonnari all'interno delle pozze di fusione, cresciuti nella direzione del flusso termico attraverso i confini della pozza fusa.

Tabella 3. Composizione chimica misurata tramite GDOES.

C	Cr	Cu	Mn	Mo	Ni	P	S	Si	Fe
0,008	17,492	≤0,066	1,219	2,776	12,576	0,0156	0,0074	0,647	Bal.

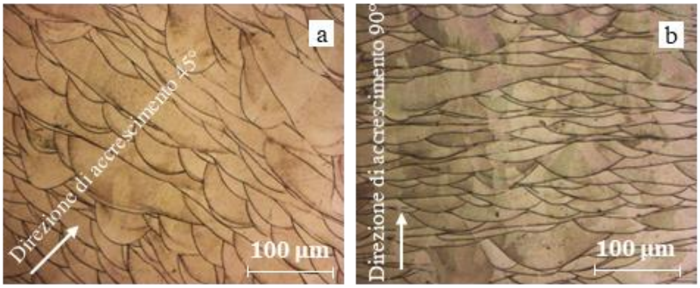

Figura 2. Microscopia ottica di due campioni rappresentativi cresciuti a 45° (a) e a 90° (b).

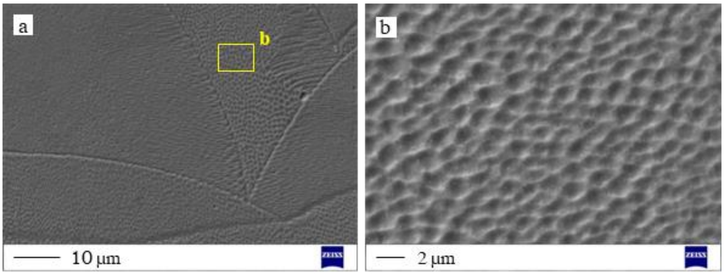

Figura 3. Analisi microstrutturale al SEM ad alto ingrandimento.

A maggiore ingrandimento è possibile osservare che le pozze di fusione sono caratterizzate da una struttura cellulare (Fig. (3)) attribuibile all'elevata velocità di raffreddamento, che induce condizioni di solidificazione di non equilibrio [8]. La dimensione delle celle varia all'interno delle pozze di fusione, ma generalmente non supera i 2 µm di dimensione. Le celle mostrano due diverse geometrie: equiassiche-poligonali o allungate, a seconda della direzione di crescita rispetto alla sezione metallografica.

Per quanto riguarda i difetti di solidificazione presenti nei campioni SLM, le analisi sono state eseguite tramite SEM-EDS. I parametri di processo utilizzati per la produzione dei campioni per i test di trazione e per l'analisi microstrutturale sono stati definiti sulla base di uno studio di ottimizzazione volto a produrre campioni con densità > 98%; di conseguenza, nonostante i campioni presentassero valori di densità diversi tra loro, tutti erano caratterizzati da un limitato contenuto di difetti. Nella finestra di processo studiata non è stata identificata nessuna correlazione specifica tra le dimensioni del difetto, il tipo e i parametri di processo. Tuttavia, sono stati osservati tre principali tipi di difetti: (i) mancata fusione, (ii) pori e (iii) fessurazioni. Le immagini SEM rappresentative di ciascuna tipologia elencata sono riportate in Fig. (4).

In relazione alle zone a mancata fusione, sono state osservate cavità irregolari associate a particelle metalliche non fuse (Fig. (4a)); questi difetti possono essere causati da un'insufficiente energia del laser, o da fenomeni di balling [9]. Per quanto riguarda le porosità (Fig. (4b)), esse hanno una geometria sferica e quindi sono facilmente associabili alla presenza di gas che rimane intrappolato nel bagno di fusione. In questo caso, la dimensione del difetto è generalmente compresa nell'intervallo 10-20 µm.

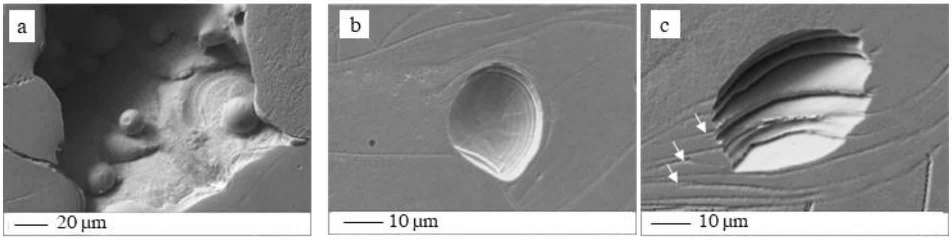

Figura 4. Difetti presenti nei campioni SLM: zone a mancata fusione (a), porosità da gas (b) e strappi (c).

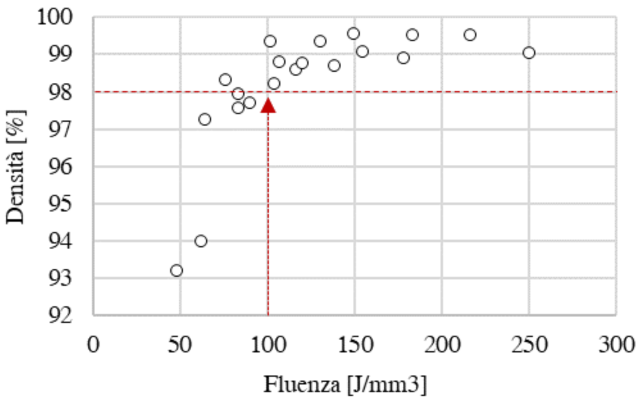

Figura 5. Densità misurate durante la campagna sperimentale preliminare.

Infine, sono stati osservati vuoti di circa 30-50 μm, caratterizzati da una morfologia interna a strati (Fig. (5c)). Poiché la struttura interna del vuoto segue chiaramente i bordi delle pozze ri-solidificate, è possibile che tali difetti siano generati dalle elevate tensioni residue indotte dal ciclo termico, che potrebbero promuovere la formazione di fessure lungo i confini della pozza, portando a strappi e conseguente formazione di vuoti nel materiale.

Densità e proprietà meccaniche

La Figura 5 mostra le combinazioni tra i parametri di processo con cui si sono raggiunte densità relative superiori al 98%, a partire da un ampio spettro di parametri selezionati durante i test preliminari. È stato trovato che i componenti caratterizzati da ρ_{rel}> 98% possono essere prodotti solo utilizzando un'energia per unità di volume (fluenza) maggiore di 100 J/mm^3, ovvero per potenze nell'intervallo 90-150 W e velocità di scansione tra 500 e 900 mm/s.

A valle di questo risultato i campioni per i test di trazione sono stati prodotti utilizzando i parametri di processo riportati in Tab. (2) e le proprietà meccaniche a trazione sono state misurate e confrontate con quelle ottenute per campioni da una barra convenzionale ricotta. I campioni SLM non sono stati trattati termicamente per poter valutare l'influenza dell'orientamento evidenziando ovvero il comportamento anisotropo tipico di campioni fabbricati tramite processi additivi.

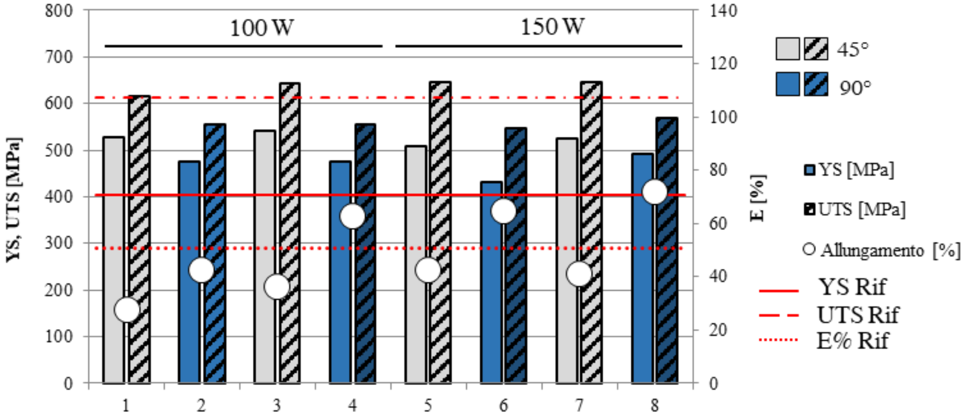

Figura 6. Proprietà meccaniche a trazione dei campioni SLM a confronto con i valori di riferimento.

I risultati delle prove di trazione sono mostrati in Fig. (6). La potenza laser influenza l'allungamento a rottura (E%), mentre ha effetti trascurabili su YS e UTS; in particolare, la diminuzione della potenza laser causa una riduzione del 10% circa dell'allungamento a rottura per entrambe le direzioni di accrescimento. Questo risultato potrebbe essere correlato alla minore densità di campioni prodotti a 100 W: vuoti e cavità riducono fortemente l'allungamento a rottura [3] Va inoltre sottolineato che la direzione di accrescimento ha un'influenza notevole sulle proprietà meccaniche: provini cresciuti con α = 45° vedono un aumento del 10-20% della tensione di snervamento e del 12-13% di UTS per entrambi i livelli di potenza; al contrario l'allungamento diminuisce di circa il 50% rispetto a quelli costruiti a 90°. Lo stesso comportamento è stato osservato per entrambe le distanze imposte tra tracce consecutive. I risultati ottenuti mostrano che la resistenza massima (UTS) e l'allungamento a rottura (E%) sono stati ottenuti, rispettivamente, con i campioni 7 e 8.

Durezze

Lo scopo delle prove di durezza è stato quello di evidenziare eventuali differenze indotte da differenti velocità di raffreddamento tra la parte superiore e quella inferiore, a contatto con i supporti, dei campioni SLM. Le misure di durezza sono state eseguite su campioni fabbricati con distanza tra le tracce pari a 0,07 mm, potenza di 100 W e 150 W e direzione di accrescimento 45° e 90°.

I valori medi delle misure sono mostrati in Fig. (7): la durezza della parte superiore e inferiore di ciascun campione è indicata rispettivamente da una croce e da un rombo. Tali valori non mostrano variazioni sostanziali se si osservano i risultati relativi ai campioni costruiti a 100 W; tuttavia ad alta potenza la differenza è più evidente. Le parti inferiori, infatti, sono più vicine alla piattaforma e sono sottoposte a velocità di raffreddamento superiori che giustificano valori di durezza più elevati.

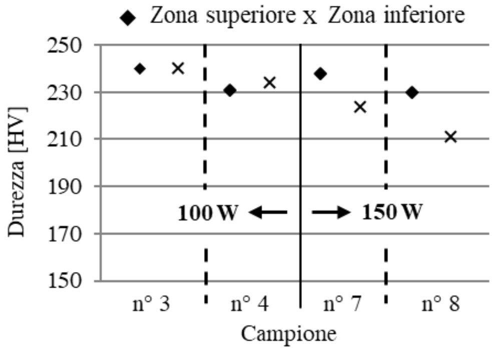

Figura 7. Durezza dei campioni misurata ai due estremi dei campioni di trazione.

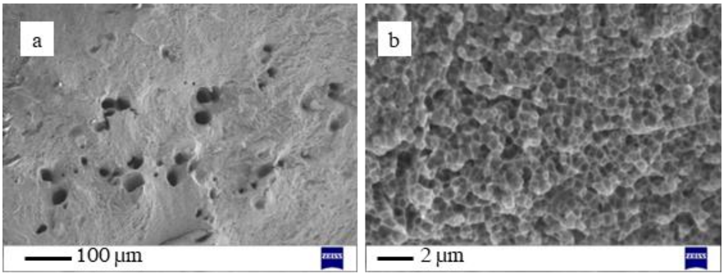

Figura 8. Analisi frattografica che mostra la presenza di vuoti (a) e di dimples (b).

Analisi frattografica

Le superfici di frattura dei campioni sottoposti a prove di trazione sono caratterizzate da un numero notevole di vuoti circolari di dimensioni comprese tra 10 e 50 μm, come mostrato in Fig. (8a). È possibile che tali vuoti siano correlati a difetti di solidificazione (pori e cavità) indotti dal processo SLM, come descritto precedentemente. Durante la deformazione del provino a trazione, la cricca si genera a partire da tali discontinuità, inducendo una concentrazione degli sforzi e successivamente la rottura.

A ingrandimenti maggiori, indipendentemente dai parametri di processo impiegati, sono stati osservati dimples molto piccoli, tipici delle rotture duttili (Fig. (8b)). Come riportato da diversi autori, la dimensione sub-micrometrica/micrometrica dei dimples è legata alle dimensioni delle celle della microstruttura di solidificazione tipica dei componenti SLM; la frattura duttile è correlata alla coalescenza di questi nano-vuoti.

4. APPLICAZIONE

Uno degli obiettivi della tecnologia additiva nel campo dell'ingegneria meccanica e, in particolare, nel mondo del packaging è la produzione di componenti leggeri fabbricati in materiale compatibile con i prodotti alimentari. I componenti attualmente realizzati in alluminio, infatti, devono essere rivestiti con fogli di Teflon per consentire il contatto con prodotti alimentari.

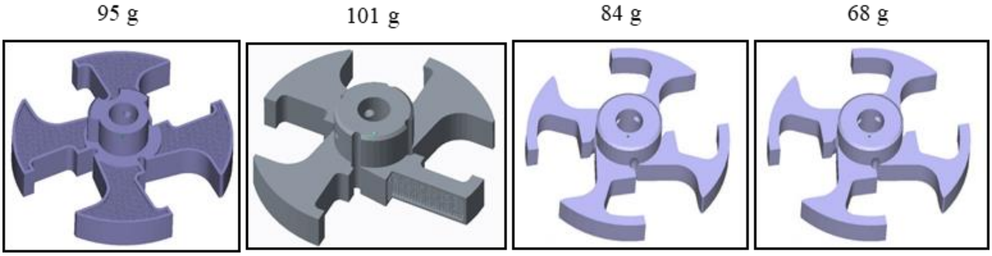

Figura 9. Evoluzione del progetto di alleggerimento di un rotatore per la movimentazione di cioccolatini.

L’obiettivo nello studio proposto è stato quello di ridisegnare un rotatore di alluminio per il movimento di cioccolatini, utilizzando la polvere AISI 316L, ma garantendo almeno lo stesso peso finale del componente: 85,2 g. L'evoluzione del progetto si è sviluppata in quattro fasi:

1. Geometria esterna simile al componente originale, ma con il volume interno sostituito da una struttura reticolare (Fig. 9(a)). Questa scelta ha permesso la riduzione del peso del componente (95 g), rispetto al pieno, ma non in modo sufficiente. Inoltre durante il passaggio del cioccolatino, il prodotto poteva rovinarsi a contatto con il reticolo.
2. Geometria esterna simile al caso (1), ma ricoperta da un guscio di spessore di 1 mm (Fig. 9(b)) per evitare il rischio di accumulo di materiale alimentare tra i reticoli. Il peso finale era 101 g quindi troppo elevato.
3. La geometria del componente è stata modificata al fine di ridurre al minimo le inerzie del sistema lasciando inalterate le superfici funzionali e garantendo una sufficiente resistenza del componente (Fig. 9(c)). Il peso finale era 84 g.
4. Geometria simile al caso precedente, ma con parti interne completamente vuote e senza strutture reticolari (Fig. 9(d)). Il peso finale del componente in questo caso era di 68 g.

Il risultato finale è quindi la fabbricazione di un rotatore in AISI 316L con le stesse prestazioni meccaniche di quello in alluminio, ma con un peso inferiore. Inoltre l'uso dell'acciaio inossidabile ha permesso l'eliminazione del rivestimento, riducendo così i costi e tempi di produzione.

5. CONCLUSIONI

In questo articolo è stata presentata una campagna sperimentale per la caratterizzazione microstrutturale e meccanica di campioni in AISI 316L prodotti con tecnologia additiva a letto di polvere (SLM). Tramite le prove proposte sono state studiate le correlazioni tra potenza laser, distanza tra tracce adiacenti e orientamento dei componenti sulla microstruttura e sulle proprietà meccaniche risultanti. I risultati sperimentali dimostrano che è possibile ottenere campioni ad elevata densità e con resistenza a snervamento e allungamento a rottura superiori a quelli ottenuti su provini in AISI 316L convenzionali. I risultati evidenziano anche il fatto che la potenza laser ha forte influenza sulla densità, con la massima densità relativa ottenuta al più alto livello di potenza esaminata (150 W). Inoltre, la variazione della direzione di accrescimento induce comportamenti meccanici a trazione anche molto diversi: maggiori resistenze e minori allungamenti si sono registrati per provini orientati a 45° rispetto a quelli cresciuti con asse verticale.

A livello microstrutturale i campioni SLM in AISI 316L sono caratterizzati da una microstruttura completamente austenitica e mostrano una morfologia stratificata costituita da pozze di fusione e celle sub micrometriche. Sono stati individuati tre tipi principali di difetti di solidificazione, indipendentemente dai parametri di processo, vale a dire: (i) zone a mancata fusione, (ii) porosità e (iii) strappo associati alle tensioni residue.

Infine, le potenzialità tecnologiche del processo sono state messe in evidenza nella fabbricazione di un rotatore per la movimentazione di cioccolatini. In questo caso la possibilità di produrre componenti internamente cavi ha permesso di effettuare un cambiamento di materiale con un conseguente abbattimento dei costi di produzione.

BIBLIOGRAFIA

[1] Gao, W., Zhanga, Y., Ramanujana, D., Ramani, K., Chenc, Y., Williamsd, C. B., Wange, C. C. L., Shina, Y. C., Zhanga, S., Zavattierif, P. D., 2015. "The Status, Challenges, and Future of Additive Manufacturing in Engineering". *Computer-Aided Design*. 69, pp. 65–89.

[2] Zhang, B., Dembinski, L., Coddet, C., 2013. "The study of the laser parameters and environment variables effect on mechanical properties of high compact parts elaborated by selective laser melting 316L powder". *Materials Science & Engineering A*. 584, pp. 21-31.

[3] Olakanmi, E. O., Cochrane, R. F., Dalgarno, K. W., 2015. "A review on selective laser sintering/melting (SLS/SLM) of aluminium alloy powders: Processing, microstructure, and properties". *Progress in Materials Science*. 74, 401–477.

[4] Gu, D. D., Meiners, W., Wissenbach, K., Poprawe, R., 2012. "Laser additive manufacturing of metallic components: materials, processes and mechanisms". *International Materials Reviews*. 57, pp. 133-164.

[5] Yadollahi, A., Sjamsaei, N., Thompson, S. M., Seely, D. W., 2015. "Effects of process time interval and heat treatment on the mechanical and microstructural properties of direct laser deposited 316L stainless steel". *Material Science & Engineering A*. 644, pp. 171-183.

[6] Rombouts, M., Kruth, J. P., Froyen, L., Mercelis, P., 2006. "Fundamentals of Selective Laser Melting of alloyed steel powders". *CIRP Annals - Manufacturing Technology*. 55, pp. 187-192.

[7] Yasa, E., Kruth, J. P., 2011. "Microstructural investigation of Selective Laser Melting 316L stainless steel parts exposed to laser re-melting". *Procedia Engineering*. 19, pp. 389-395.

[8] Wang, D., Song, C., Yang, Y., Bai, Y., 2016. "Investigation of crystal growth mechanism during selective laser melting and mechanical property characterization of 316L stainless steel parts". *Materials and Design*. 100, pp. 291–299.

[9] Li, R., Shi, Y., Wang, Z., Wang, L., Liu, J., Jiang, W., 2010. "Densification behavior of gas and water atomized 316L stainless steel powder during selective laser melting". *Applied Surface Science*. 256, pp. 4350–4356.

DESIGN OF HIGH ENERGY DENSITY FLYWHEELS: NEW SOLUTIONS TO A CLASSICAL PROBLEM

Eugenio Dragoni
Department of Engineering Sciences and Methods
University of Modena e Reggio Emilia
E-mail: eugenio.dragoni@unimore.it

Abstract. *For years, engineers and designers have focused on electrochemical batteries for long term energy storage which can only last for a finite number of charge-discharge cycles. More recently, compressed hydrogen is being scrutinized as a large-scale storage medium but this poses the risk of spreading high-pressure vessels with inflammable content. Historically, flywheels have provided an effective way to smooth out speed fluctuations in irregular machines and mechanisms. With advancements in composite materials, magnetic bearings and mechatronic drives, flywheels have become the subject of extensive research as power storage devices for mobile or fixed installations. Flywheel energy storage systems are considered to be an attractive alternative to electrochemical batteries due to higher stored energy density, higher life term, deterministic state of charge and ecological operation. The mechanical performance of a flywheel can be attributed to three factors: material strength, geometry and rotational speed. Focussing on this simple relationship, this paper explores the merits of four simple but unconventional flywheel configurations that have not been examined so far. Two geometries assume the use of monolithic isotropic materials, two solutions are based on the use of high-strength strips or tapes wound up to form a composite structure.*

Keywords: *Flywheel, energy storage, finite element method, winding, optimization.*

1. INTRODUCTION

By many accounts renewable energy will have an important part to play in the electricity grid of the future. Fossil fuels are in limited supply and evidence is mounting of its detrimental effect on our environment. This forces us to rethink the way we supply energy. The generation of renewable energy has been shown to be possible but since most renewable sources are inherently intermittent, the question arises of how to marry a fluctuating energy supply with a rather indifferent consumer demand. Energy storage helps to alleviate this problem by providing a mechanism by which surplus energy can be stored during periods of low demand and supplied back to the grid when needed. When energy storage is implemented with renewable resources it decreases the intermittency of supply and adds value to the overall system [1].

The use of flywheels to store energy is not a new technology. Basic flywheels such as stone wheels were used to craft pottery thousands years ago. Under the industrial revolution the use of the flywheel increased significantly when the steam engine was introduced. In that context, the technological development of flywheels started as a means to smoothen the output velocity of machinery under fluctuating input torque. The first milestone was when A. Stodola [2] showed that certain shapes yield uniform stress distribution for isotropic materials. The next milestone in flywheel development took place during 1970's when applications for backup-power and electric vehicles were proposed. During this period flywheels made of composite material were proposed and built. The development continued through the 1980's when magnetic bearings were introduced. Recent developments in materials, magnetic bearings, microcomputers and power electronics have made it possible to consider flywheels as competitive option for electric energy storage [3, 4]. Other modern application of flywheels span a wide range as uninterruptible power supply systems at several industries worldwide and kinetic energy recovery systems in electric or hybrid vehicles.

There are many advantages that make flywheels attractive for applications where other storing units are now used (typically electrochemical batteries and supercapacitors): a) fast charge/discharge transients; b) high energy density; c) no capacity degradation with use; d) the state of charge can easily be measured; e) low periodic maintenance is required; f) short recharge time; g) scalable technology and universal localization; h) tolerance to temperature extremes; i) low environmental impact. Among the above assets, one of the major advantages of flywheels is the ability to handle high power levels. There are, of course, also some disadvantages to using flywheels for energy storage, mainly linked to the need of complicated and heavy auxiliary equipment: vacuum enclosures and magnetic bearing systems are required to minimize aerodynamic and friction losses; mechanical containment systems have to be adopted for safety reason to limit the risk of flywheel fragmentation. This makes for high initial costs and can also lower the efficiency and energy density of the system.

Among the many parameters that have been introduced to measure the mechanical performance of a flywheel, the most significant from the energy standpoint is the kinetic energy per unit mass, e_m , defined as

$$e_m = \frac{E_{k\,max}}{m} \tag{1}$$

where $E_{k\,max}$ is the maximum kinetic energy that can be stored in the flywheel and m is the mass. The higher e_m , the higher the energy that the flywheel can store for given mass. Under very general conditions, it is easily shown that parameter e_m can be written as

$$e_m = K\frac{\sigma_{adm}}{\rho} \tag{2}$$

where K is a shape factor depending on the geometry of the flywheel, σ_{adm} is the allowable stress of the flywheel material and ρ is the material density. Table 1 lists the K values for typical shapes of homogeneous isotropic flywheels. Table 2 give the characteristic σ_{adm}/ρ ratios for metals and alternative flywheel materials.

This paper calculates the kinetic efficiency efficiency of four non-conventional flywheel concept: 1) interference-fitted homogeneous hollow disc; 2) centrally coined homogeneous solid disc; 3) prestretched metal coil; 4) filament-wound composite disc with optimized layup. The literature on flywheels is vast and stretches back to the beginning of 20th century. Comprehensive readings are the books by Genta [5] and by Vullo and Vivio [6] and the more recent papers by Bolund et al. [7] and by Pedrolli et al. [8].

2. INTERFERENCE-FITTED HOMOGENEOUS HOLLOW DISC

From Table 1 we see that the shape ratio for the constant-thickness pierced disc is $K = 0.303$. This section calculates the shape ratio of the disc when it is mounted onto a solid shaft by means of an interference fit as shown in Fig. 1.

Table 1. Shape factor K for typical geometries of homogeneous isotropic flywheels.

Description	Profile	Shape factor K
Constant-stress disc (infinite O.D.)	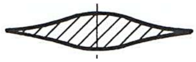	1.0
Constant-stress disc (finite O.D.)		0.7– 0.98
Conical disc	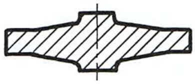	0.7– 0.95
Constant thickness disc		0.606
Thin ring	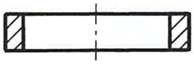	0.5
Rimmed pierced disc	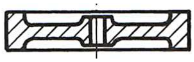	0.4 – 0.5
Pierced constant thickness disc	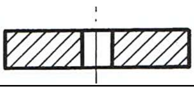	0.303

Table 2. Characteristic σ_{adm}/ρ ratios for metals and alternative flywheel materials.

Material	Ultimate tensile strength (MPa)	Specific strength σ_{adm}/ρ (Wh/kg)
Cast iron	150	5
Carbon steel	340	12
Alloy steel	1000	36
Wood (beech)	120	36
Aluminium alloy	600	61
Maraging steel	1900	66
Wood (mahogany)	160	86
Spring steel (wires)	3000	110
Glass-reinforced plastic (1D)	1300	180
Graphite-reinforced plastic (1D)	1300	230
Kevlar-reinforced plastic (1D)	1200	240

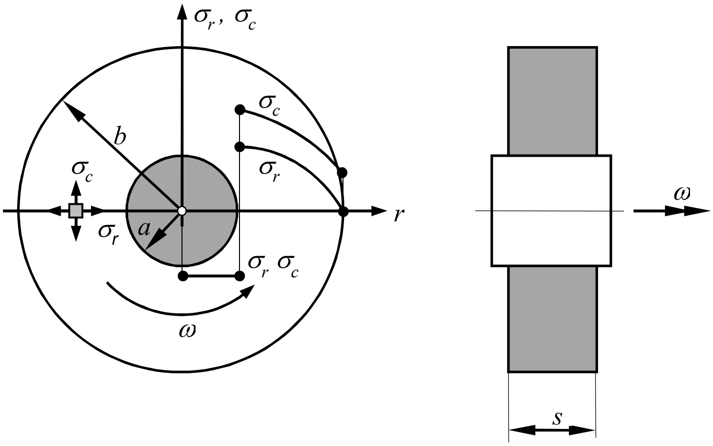

Figure 1. Reference geometry of the homogeneous disc coupled by interference fit with a solid shaft (not shown in figure, *i* is the diametral interference between shaft and disc).

If *i* is the diametral interference between shaft and disc, and *E* is their elastic modulus, from [9] the maximum Tresca equivalent stress at the inner radius *a* of the disc is

$$\sigma_{Ti} = E\frac{i}{2a} \tag{3}$$

Upon rotation, the combined shaft-disc system behaves as a single solid disc. From [9], the circumferential stress, σ_{ca}, and radial stress, σ_{ra}, produced by centrifugal forces at the radius *a* of the disc are given by

$$\sigma_{c\omega} = \frac{3+\nu}{8}\rho\omega^2 b^2 - \frac{1+3\nu}{8}\rho\omega^2 a^2 \tag{4}$$

$$\sigma_{r\omega} = \frac{3+\nu}{8}\rho\omega^2 b^2 - \frac{3+\nu}{8}\rho\omega^2 a^2 \tag{5}$$

where ν is the Poisson's ratio. From (4) and (5) the increment of the Tresca equivalent stress at radius *a* of the disc due to centrifugation, $\Delta\sigma_{T\omega} = \sigma_{c\omega} - \sigma_{r\omega}$, becomes

$$\Delta\sigma_{T\omega} = \frac{1-\nu}{4}\rho\omega^2 a^2 \tag{6}$$

giving the total Tresca stress, σ_T, at radius *a* due to interference fit and centrifugation as

$$\sigma_T = \sigma_{Ti} + \Delta\sigma_{T\omega} = E\frac{i}{2a} + \frac{1-\nu}{4}\rho\omega^2 a^2 \tag{7}$$

Equation (7) holds true up to the overspeed velocity, ω_o , that is the angular velocity at which the radial pressure between shaft and disc is eliminated by the centrifugal deformation of the disc. If ρ is the mass density of shaft and disc, the overspeed velocity is given by [10]

$$\omega_f = \sqrt{\frac{2}{3+\nu}\frac{E\,i}{\rho a b^2}} \tag{8}$$

Using (8), for $\omega = \omega_f$ the Tresca stress (7) becomes

$$\sigma_T = E\frac{i}{2a}\left\{1+\frac{1-\nu}{3+\nu}\left(\frac{a}{b}\right)^2\right\} \approx E\frac{i}{2a}\left\{1+0.2\left(\frac{a}{b}\right)^2\right\} \tag{9}$$

Assuming $\nu = 0.3$ and $a/b \le 0.5$, a shape ratio that covers all reasonable shaft/disc proportions, the term between braces in (9) is less than 1.05. In other terms, the Tresca stress for any rotational speed up to ω_f is approximately constant and coincides with the Tresca stress introduced in the disc at assembly by the interference alone

$$\sigma_T \approx \sigma_{Ti} = E\frac{i}{2a} \tag{10}$$

If σ_{adm} is the admissible working stress of the disc, from (10) the strength condition $\sigma_T = \sigma_{adm}$ gives the maximum admissible interference as

$$i = 2a\frac{\sigma_{adm}}{E} \tag{11}$$

Substituting expression (11) for i in (8) gives the overspeed velocity as

$$\omega_o = \sqrt{\frac{4}{3+\nu}\frac{\sigma_{adm}}{\rho b^2}} \tag{12}$$

The moment of inertia of the disc, including a length s (see Fig. 1) of the mating shaft, is

$$J = \frac{1}{2}mb^2 \tag{13}$$

where $m = \pi\rho s b^2$ is the mass of the shaft-disc system. Using (13), the kinetic energy stored in the flywheel is

$$E_k = \frac{1}{2} J\omega^2 = \frac{1}{4} mb^2\omega^2 \tag{14}$$

Letting $\omega = \omega_o$ in (14) and remembering (12), the maximum kinetic energy that can be stored in the system at the onset of overspeed is

$$E_{k\,max} = \frac{m}{3+\nu} \frac{\sigma_{adm}}{\rho} \tag{15}$$

From (15) the kinetic energy density defined in (1) is obtained as

$$e_m = \frac{1}{3+\nu} \frac{\sigma_{adm}}{\rho} \approx 0.303 \frac{\sigma_{adm}}{\rho} \tag{16}$$

3. CENTRALLY COINED HOMOGENEOUS SOLID DISC

The shape ratio in Table 1 for the constant-thickness solid disc is $K = 0.606$. This section calculates the shape ratio of the disc when an inner core of radius a is coined axially as shown in Fig. 2 (the dashed line oulines the core before coining). Upon coining, the core is compressed axially beyond its yield point. As a result, the core expands radially and generates a virtual diametral interference i. With the flywheel at rest, the core is compressed equibiaxially and the outer layer is expanded as a pressurized thick pipe. The difference with respect to the case in Section 2 is represented by the material continuity at radius a , which allows for tensile radial stresses to arise between core and outer rim after centrifugation.

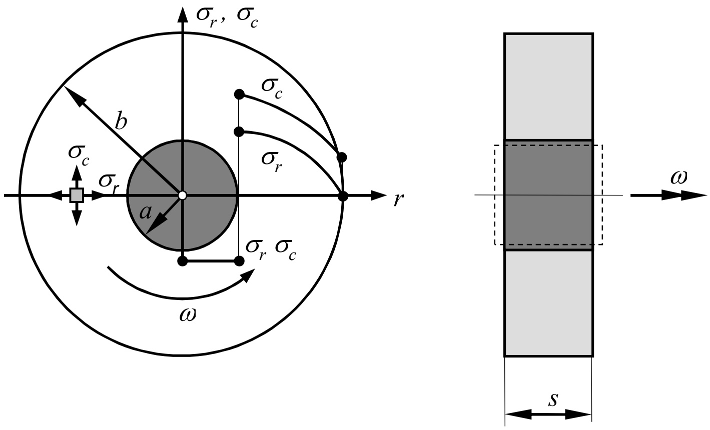

Figure 2. Reference geometry of the homogeneous solid disc coined axially over the radius a. Not shown in figure, i is the virtual diametral interference arising between the coined inner core and the outer crown of the disc.

Stresses due to coining

The radial pressure at radius a consequent upon coining amounts to [10]

$$p_i = E\frac{i}{2a}\cdot\frac{1-\left(\frac{a}{b}\right)^2}{2} = E\frac{i}{4a}\cdot\left[1-\left(\frac{a}{b}\right)^2\right] \tag{17}$$

The isotropic stress state induced by p_i in the coined inner core is defined by identical radial and circumferential stresses given by

$$\sigma_{rit} = \sigma_{cit} = -p_i = E\frac{i}{4a}\cdot\left[\left(\frac{a}{b}\right)^2 - 1\right] \tag{18}$$

The radial stress induced by coining at radius a of the outer layer of the disc is

$$\sigma_{riae} = -p_i = E\frac{i}{4a}\cdot\left[\left(\frac{a}{b}\right)^2 - 1\right] \tag{19}$$

The circumferential stress induced by coining at radius a of the outer layer of the disc is

$$\sigma_{ciae} = p_i\left[\frac{1+\left(\frac{a}{b}\right)^2}{1-\left(\frac{a}{b}\right)^2}\right] = E\frac{i}{4a}\cdot\left[1-\left(\frac{a}{b}\right)^2\right]\left[\frac{1+\left(\frac{a}{b}\right)^2}{1-\left(\frac{a}{b}\right)^2}\right] = E\frac{i}{4a}\cdot\left[1+\left(\frac{a}{b}\right)^2\right] \tag{20}$$

Stresses due to centrifugation

Under the effect of the centrifugal forces the disc behaves as a rotating homogeneous solid disc with stress solutions given in textbooks [9]. The radial and circumferential stresses at the centrepoint of the disc are

$$\sigma_{r\omega ot} = \sigma_{c\omega ot} = \frac{3+\nu}{8}\rho\omega^2 b^2 \tag{21}$$

The radial stress at radius a of the outer layer is

$$\sigma_{r\omega ae} = \frac{3+\nu}{8}\rho\omega^2 b^2 - \frac{3+\nu}{8}\rho\omega^2 a^2 \tag{22}$$

The circumferential stress at radius *a* of the outer layer is

$$\sigma_{c\omega\,ae} = \frac{3+\nu}{8}\rho\omega^2 b^2 - \frac{1+3\nu}{8}\rho\omega^2 a^2 \tag{23}$$

Stresses due to coining and centrifugation

The stresses due to both coining and centrifugations are obtained by superimposing the effects of the previous two sections. The radial and circumferential stresses at the centrepoint of the disc are given by summing (18) and (21) as

$$\sigma_{r\,ot} = \sigma_{c\,ot} = \sigma_{ri\,t} + \sigma_{r\omega\,ot} = \sigma_{ci\,t} + \sigma_{c\omega\,ot} = E\frac{i}{4a}\cdot\left[\left(\frac{a}{b}\right)^2 - 1\right] + \frac{3+\nu}{8}\rho\omega^2 b^2 \tag{24}$$

The Tresca equivalent stress at the centrepoint of the disc is

$$\sigma_{id\,ot} = \left|\sigma_{r\,ot}\right| \equiv \left|\sigma_{c\,ot}\right| = \mathrm{ABS}\left\{E\frac{i}{4a}\cdot\left[\left(\frac{a}{b}\right)^2 - 1\right] + \frac{3+\nu}{8}\rho\omega^2 b^2\right\} \tag{25}$$

The total radial stress at radius *a* of the outer layer of the disc is

$$\sigma_{r\,ae} = \sigma_{ri\,ae} + \sigma_{r\omega\,ae} = E\frac{i}{4a}\cdot\left[\left(\frac{a}{b}\right)^2 - 1\right] + \frac{3+\nu}{8}\rho\omega^2 b^2 - \frac{3+\nu}{8}\rho\omega^2 a^2 \tag{26}$$

The total circumferential stress at radius *a* of the outer layer of the disc is

$$\sigma_{c\,ae} = \sigma_{ci\,ae} + \sigma_{c\omega\,ae} = E\frac{i}{4a}\cdot\left[1 + \left(\frac{a}{b}\right)^2\right] + \frac{3+\nu}{8}\rho\omega^2 b^2 - \frac{1+3\nu}{8}\rho\omega^2 a^2 \tag{27}$$

The Tresca equivalent stress at radius *a* of the outer layer of the disc is

$$\begin{aligned}\sigma_{id\,ae} &= \mathrm{MAX}\left\{\sigma_{c\,ae} - \sigma_{r\,ae};\sigma_{c\,ae}\right\} = \\ &= \mathrm{MAX}\begin{cases} E\dfrac{i}{2a} + \dfrac{1-\nu}{4}\rho\omega^2 a^2 \\ E\dfrac{i}{4a}\cdot\left[1 + \left(\dfrac{a}{b}\right)^2\right] + \dfrac{3+\nu}{8}\rho\omega^2 b^2 - \dfrac{1+3\nu}{8}\rho\omega^2 a^2 \end{cases}\end{aligned} \tag{28}$$

Equation (28) shows that for $\omega = 0$ the equivalent stress at radius *a* reduces to

$$\sigma_{id\,ae0} = E\frac{i}{2a} \tag{29}$$

This stress cannot be greater than the admissible stress of the material, lest the admissible stress would be overcome as soon as the disc is put in motion. By requiring $\sigma_{id\,ae\,0} = k\sigma_{adm}$, with $k < 1$, using (29), the following condition holds true

$$E\frac{i}{2a} = k\,\sigma_{adm} \tag{30}$$

The angular velocity that makes equal the two equivalent stresses (28) is the speed that extinguishes the radial pressure at radius a. This coincides with the overspeed velocity, ω_o, of a pierced disc mounted with interference i over a solid disc of radius a, given by (8). Combining (8) and (30) gives

$$\omega_o^2 = \frac{4\sigma_{adm}}{\rho b^2}\cdot\frac{k}{3+\nu} \tag{31}$$

Using again equation (30), the second of equations (28) becomes

$$\sigma_{id\,ae} = \frac{k\,\sigma_{adm}}{2}\left[1+\left(\frac{a}{b}\right)^2\right] + \frac{3+\nu}{8}\rho\omega^2 b^2 - \frac{1+3\nu}{8}\rho\omega^2 a^2 \tag{32}$$

Letting the strength condition of the outer layer, $\sigma_{id\,ae} = \sigma_{adm}$, from (32) the admissible angular velocity, $\omega_{adm\,e}$, allowed by the outer layer obtains as

$$\omega_{adm\,e}^2 = \frac{4}{3+\nu}\cdot\frac{\sigma_{am}}{\rho b^2}\cdot\frac{2-k\left[1+\left(\frac{a}{b}\right)^2\right]}{1-\left(\frac{1+3\nu}{3+\nu}\right)\left(\frac{a}{b}\right)^2} \tag{33}$$

Remembering (25) and using (30), the strength condition for the inner core of the rotating disc, $\sigma_{id\,ot} = \sigma_{am}$, gives the admissible angular velocity, $\omega_{adm\,ot}$, allowed by the inner core as

$$\omega_{adm\,ot}^2 = \frac{4}{3+\nu}\frac{\sigma_{adm}}{\rho b^2}\left\{2+k\left[1-\left(\frac{a}{b}\right)^2\right]\right\} \tag{34}$$

Equating (33) and (34) gives the following optimal value of k^* that ensures uniform strength for inner core and outer layer

$$k^* = \frac{2\mu x}{2 - \mu x + \mu x^2} \tag{35}$$

where

$$x = \left(\frac{a}{b}\right)^2 \tag{36}$$

and

$$\mu = \frac{1+3\nu}{3+\nu} \tag{37}$$

Entering (35) for k into (33) and (34) gives the limit velocity as

$$\omega_{lim}^2 = \omega_{adm\,ot}^2\Big|_{k=k^*} = \omega_{adm\,e}^2\Big|_{k=k^*} = \frac{8}{3+\nu}\frac{\sigma_{adm}}{\rho b^2}\left(\frac{2}{2-\mu x+\mu x^2}\right) \tag{38}$$

The limit velocity (38) is maximum for $x = x_{opt} = 0.5$. Recalling (36), the optimal aspect ratio, $(a/b)_{opt}$, for the coined disc is

$$\left(\frac{a}{b}\right)_{opt} = \sqrt{0.5} \approx 0.707 \tag{39}$$

The optimal proportions of the disc are shown in Fig. 2. Letting $x = x_{opt} = 0.5$ in (38) and remembering (37), gives the optimal limit velocity

$$\left(\omega_{lim}^2\right)_{opt} = \omega_{lim}^2\Big|_{x=x_{opt}} = \frac{\sigma_{adm}}{\rho b^2}\left(\frac{64}{23+5\nu}\right) \tag{40}$$

Calculating the kinetic energy (14) for optimal limit velocity (40) and combining with (1), gives the following kinetic energy density for the centrally coined solid disc

$$e_m = \frac{16}{23+5\nu}\frac{\sigma_{adm}}{\rho} \approx 0.653\frac{\sigma_{adm}}{\rho} \tag{41}$$

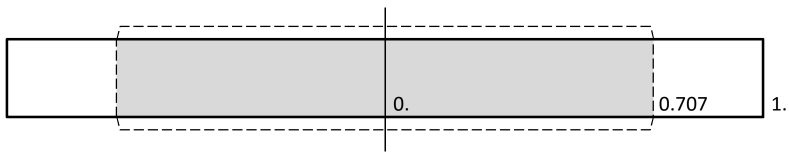

Figure 3. Optimal proportions of the coined inner core for the maximum energy density.

4. PRESTRETCHED METAL COIL

Figure 4 depicts the flywheel obtained by coiling a stretched metal strip over a solid shaft of radius a. Upon incremental addition of the outer layers, the inner layer become more and more compressed both radially and circumfetentially. The stress distribution in wound rolls of thin tapes, strips or sheets has been deeply investigated in the technical literature [11-13]. If the winding tension of the strip is maintained constant at the value $\sigma_o = k\ \sigma_{adm}$, with $k \leq 1$, from [13] the radial and circumferential stresses in the wound layers ($a < r < b$) are given by

$$\begin{aligned} \sigma_{ro\,n} &= -\sigma_o \ln\left(\frac{b}{r}\right) = -k\sigma_{adm} \ln\left(\frac{b}{r}\right) = \\ \sigma_{co\,n} &= \sigma_o \left[1 - \ln\left(\frac{b}{r}\right)\right] = k\sigma_{adm} \left[1 - \ln\left(\frac{b}{r}\right)\right] \end{aligned} \tag{42}$$

The stress state in the solid shaft ($r < a$) is hydrostatic with both radial and circumferential stresses obtained by letting $r = a$ in the first of (42)

$$\sigma_{ro\,a} = \sigma_{co\,a} = -\sigma_o \ln\left(\frac{b}{a}\right) = -k\sigma_{adm} \ln\left(\frac{b}{a}\right) \tag{43}$$

Figure 5 plots the stresses (42) and (43), divided by the stretching stress σ_o , as a function of the dimensionless radius r/a. We see that the first layers of the coil around the shaft are compressed both radially and circumferentially. This is an advantage since this is the position where the highest tensile circumferential stresses due to rotation take place. As far as the radial stresses remain compressive, upon rotation the flywheel behaves as a solid disc. Assuming that the condition of compressive radial stresses is satisfied for the entire disc, the incremental radial and circumferential stresses due to rotation are given by [9]

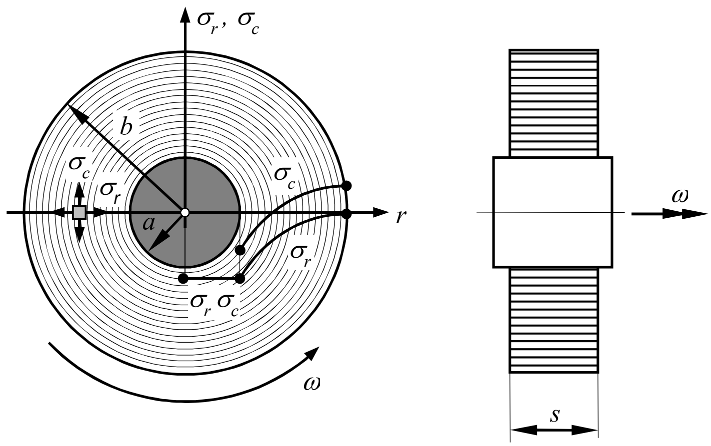

Figure 4. Reference geometry of the prestretched wound-coil flywheel.

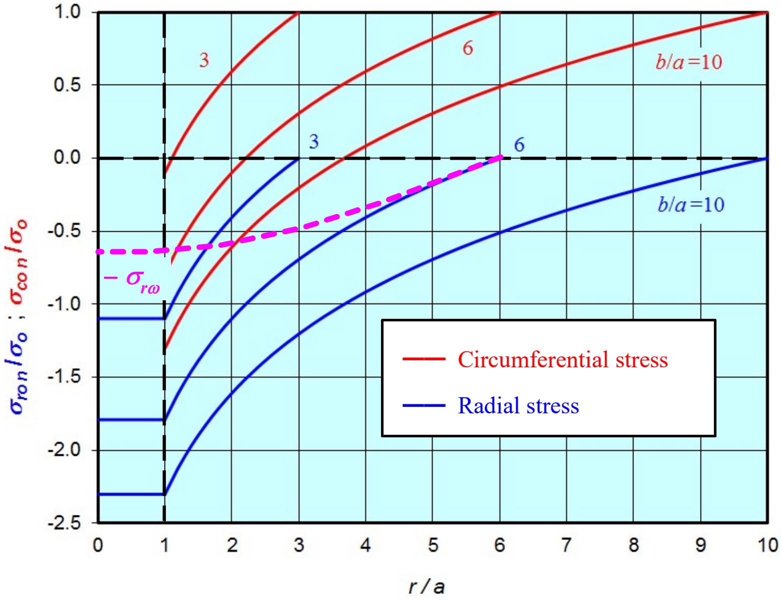

Figure 5. Distribution of radial and circumferential stresses in the prestretched wound coil.

$$\begin{aligned}\sigma_{r\omega} &= \frac{3+\nu}{8}\rho\omega^2\left(b^2 - r^2\right)\\ \sigma_{c\omega} &= \frac{3+\nu}{8}\rho\omega^2 b^2 - \frac{1+3\nu}{8}\rho\omega^2 r^2\end{aligned} \tag{44}$$

The stresses (44) are both tensile and add algebraically to the corresponding prestretching components (42). For $0 \le r \le$ a , the radial and circumferential stresses (44) are nearly equal and the ideal stress in the strip changes negligibly upon centrifugation because the same quantity is added to both prestretch stresses (42). For $r = b$, the radial stress vanishes both in (42) and in (44) and the strip is stresses uniaxially by the sum of the second components in equations (42) and (44).

From Figure 1 we see that the total radial stress, $\sigma_{r\omega} - \sigma_{ro\,n}$, (see pink curve and blue curve for the particular case $b/a = 6$) is negative (compressive) when

$$\left.\frac{\mathrm{d}\sigma_{ro\,n}}{\mathrm{d}r}\right|_{r=b} \ge -\left.\frac{\mathrm{d}\sigma_{r\omega}}{\mathrm{d}r}\right|_{r=b} \tag{45}$$

Calculating the derivatives of the radial components (42) and (44), equation (5) gives the following expression for the limit velocity, ω_{lim} , which ensures compressive radial stresses betwen the coils for ($a \le r \le b$)

$$\omega_{lim}^2 = \frac{4}{3+\nu}\frac{k\sigma_{am}}{\rho b^2} \tag{46}$$

Calculating the kinetic energy (14) for limit velocity (46) and combining with (1), gives the maximum kinetic energy density for the wound flywheel as

$$e_m = \frac{1}{3+\nu}\frac{k\sigma_{am}}{\rho} \approx \left(0.303k\right)\frac{\sigma_{adm}}{\rho} \tag{47}$$

5. FILAMENT-WOUND COMPOSITE DISC WITH OPTIMIZED LAYUP

Modern flywheels are built from advanced fiber-reinforced composite materials with the highest strength-to-density ratios technically available today (Table 2). Though many architectures have been proposed [14], the commonest and most straightforward technology to manufacture the composite flywheel is by filament winding [15]. Depending on the winding angle of the fibres, the wound flywheel can fail either in the radial (matrix failure) or in the circumferential direction (fibre failure), but the predicted durability of the latter is generally much greater than that of the former [16].

This section investigates whether the radial stresses beween the plies of a filament wound disc (Fig. 6) can be cancelled by optimizing the winding angle of the lay-up.

Theory

Let's assume that the disc in Fig. 6 is made by winding around the disc axis a unidirectional tape with mass density ρ, longitudinal-transversal Poisson's ratio ν, longitudinal Young's modulus E_L and transverse Young's modulus E_T. By varying the winding angle α shown in Fig. 6, the circumferential Young's modulus E_c can be varied continuously, as a function of radius *r*, between the limit values E_L ($\alpha = 0°$) and E_T ($\alpha = 90°$).

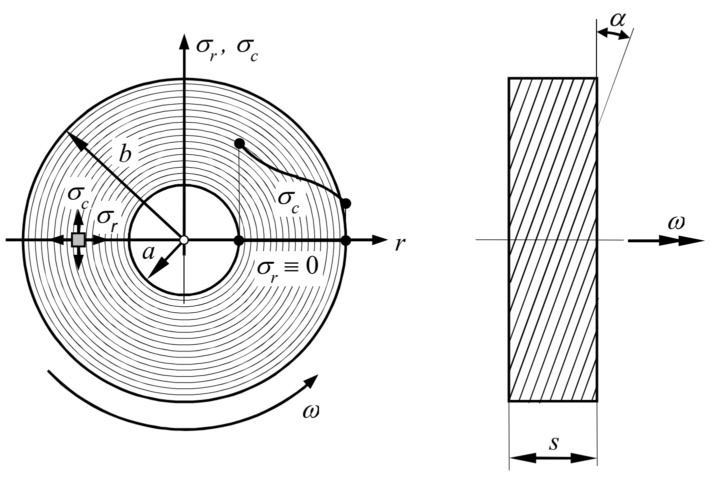

Figure 6. Reference geometry of the filament-wound flywheel with zero radial stresses.

For a disc of constant axial thickness (s in Fig. 6) rotating at angular velocity ω, equilibrium of stresses and inertia forces requires that [17]

$$\frac{\mathrm{d}}{\mathrm{d}r}(r\sigma_r) - \sigma_c + \rho\omega^2 r^2 = 0 \tag{48}$$

Assuming

$$\sigma_r(r) \equiv 0 \quad \forall r \tag{49}$$

equation (48) becomes

$$\sigma_c = \rho\omega^2 r^2 \tag{50}$$

Likewise, the general compatibility equation in terms of circumferential strain, ε_c, and radial strain, ε_r, reads [17]

$$\frac{\mathrm{d}}{\mathrm{d}r}(r\varepsilon_c) = \varepsilon_r \tag{51}$$

Because of (49), neglecting the axial stress throughout the disc ($\sigma_a = 0 \ \forall r$) and introducing the radius-dependent circumferential Young's modulus $E_c = E_c(r)$, the stress-strain relationship for the single layer gives

$$\begin{aligned} \varepsilon_c &= \frac{\sigma_c}{E_c(r)} \\ \varepsilon_r &= -\nu\varepsilon_c = -\nu\frac{\sigma_c}{E_c(r)} \end{aligned} \tag{52}$$

Combination of (50), (51) and (52) yields after some rearrangement

$$\frac{\mathrm{d}\,E_c(r)}{E_c(r)} = (3+\nu)\frac{\mathrm{d}r}{r} \tag{53}$$

Integration of (53) with respect to radius r gives

$$E_c(r) = E_{cb}\left(\frac{r}{b}\right)^{3+\nu} \tag{54}$$

where E_{cb} is the circumferential Young's modulus of the layer at the outer radius $r = b$.

Finite element validation

The result of the previous section has been applied to a filament-wound flywheel made from glass fibre and epoxy resin with internal diameter of 200 mm (a = 100 mm) and external diameter of 298 mm (b = 149 mm). The properties of the cured composite were [18]: mass density $\rho = 2000$ kg/m^3, longitudinal-transversal Poisson's ratio $\nu = 0.3$, longitudinal Young's modulus E_L = 45 GPa (assigned to the material as circumferential modulus at $r = a$), transverse Young's modulus E_T = 12 GPa (assigned to the material as circumferential modulus at $r = b$). The circumferential Young's modulus at radius r was defined by equation (54). In particular, for $E_{cb} = E_L = 45$ GPa, from (54) we calculate $E_c\,(r=a) = E_{cb}\,(a/b)^{3+\nu} = 45\times(100/149)^{3+0.3} = 12\ \text{GPa} \equiv E_T$. The moduli in the radial and axial directions were assumed equal to the transverse value of the composite E_T. The mesh was built using a grid of 50×5 axisymmetric, quadratic orthotropic elements with 50 elements along the radial wall of the flywheel and 5 elements along the axial half-thickness of 50 mm. The nodes on one of the radial sides of the meridional section were constrained in the axial direction to enforce simmetry. Figure 7 shows the distribution of radial and circumferential stresses for an angular velocity of 30 000 rpm (3 141.6 rad/s).

6. DISCUSSION

Equation (16) shows that the interference fitted disc has the same efficiency as the pierced free disc, but with the advantage of having a means for transferring the energy from and to a shaft. The transmissible torque at overspeed can be ensured by reinforcing the interference fit with anaerobic adhesives [19, 20].

Equation (41) shows that the coined solid disc has a slightly higher efficiency than its uncoined counterpart. The advantage is obtained by the centrepoint of the disc being initially compressed at the expense of a slight tension in the outer layer just outside the coined inner core (radius a) where the centrifugal stresses are lower than in the centre. However, the improvement is not very big and can be obtained only for the rather large optimal coined radius equation given by (39) (see also Fig. 3).

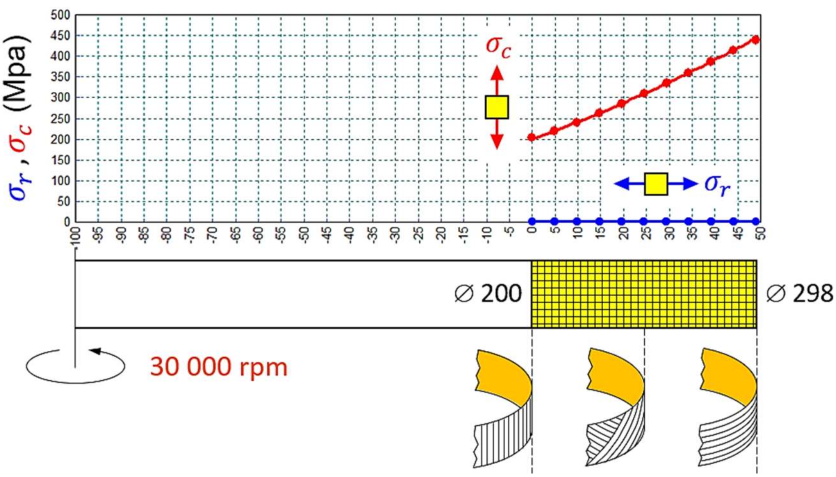

Figure 7. Finite element results for the filament-wound flywheel with zero radial stresses.

Equation (47) and Table 1 show that, geometrically, the wound coil flywheel is worse than the pierced free disc and achieves exactly the same shape ratio (K = 0,303) only for k = 1 (winding stress equal to the admissible stress of the material). However, with respect to the monolithic disc, the wound coil has the advantage of a greater working stress because ribbons and strips are more readily and less expensively available in high grade steels (greater σ_{adm}) than bulk discs. The performance of the wound flywheel could be improved if, at least for the outer radii of the roll, the layers could be joined together (for example by laser welding) so as to react to tensile radial stresses that would occur beyond the limit velocity (46).

Figure 7 demonstrates that the radialstresses vanish in the filament-wound flywheel with a radial distribution of circumferential Young's modulus given by equation (54). At the same time, the radial stresses increase quadratically with the radius across the radial wall of the disc. Tayloring of the circumferential Young's modulus to relationship (54) can be achieved by acting on the winding angle α (Fig. 6) according to the formulas for the properties of the orthotropic ply [18]

$$E_c = \frac{1}{\dfrac{\cos^4\alpha}{E_L} + \dfrac{\sin^4\alpha}{E_T} + 2\cos^2\alpha\sin^2\alpha\left(\dfrac{1}{2G_{LT}} - \dfrac{\nu_{LT}}{E_L}\right)} \tag{55}$$

where G_{LT} and ν_{LT} are the in-plane shear modulus and Poisson's ratio of the ply.

The weakest point of this solution is the decrease of the circumferential strength of the ply when the winding angle α approaches 90° (axially oriented fibres) close to the inner radius a. Though decreasing (see Fig. 7), the circumferential stresses originated by centrifugation could overcome the reduced strength in that position.

7. CONCLUSIONS

Flywheels as energy storage systems are emerging as an attractive alternative to electrochemical batteries due to higher stored energy density, higher life term, deterministic state of charge and ecological operation. The mechanical performance of a flywheel can be attributed to three factors: material strength, geometry and rotational speed. Focussing on the simple relationship between these three variables, this paper has explore the merits of four simple but unconventional flywheel configurations that cannot be traced in the technical literature: 1) interference-fitted homogeneous hollow disc; 2) centrally coined homogeneous solid disc; 3) prestretched metal coil; 4) filament-wound composite disc with optimized layup. The results of the investigation can be summarized as follows:

- the interference-fitted hollow disc is as efficient as the pierced disc with the advantage of providing a convenient means of being joined to the driving shaft;
- the shape factor of the centrally-coined homogeneous solid disc is slightly greater than its homogeneous counterpart's, but the advantage hardly justifies the increased manufacturing complexity;
- geometrically, the prestretched wound coil flywheel matches the pierced free disc of equal size, but it can be operated at higher angular velocities because ribbons and strips are available with higher mechanical properties than bulk discs;
- the lay-up of the filament-wound composite disc can be optimized to cancel the radial stresses between plies that tipically undermine the strength of anisotropic flywheels.

REFERENCES

[1] R. Baxter, R., 2006. *Energy Storage: A Nontechnical guide*. Oklahoma: Pennwell Corporation.

[2] Stodola, A., 1910. *Die Dampfturbinen: Mit einem Anhang über die Aussichten der Wärmekraftmaschinen und über die Gasturbine*. Berlin, Springer.

[3] Bitterly, J., 1997. "Flywheel technology past, present, and 21st Century projections". Energy Conversion Engineering Conference, Proceedings of the 32nd Intersociety, 4, pp. 2312–2315.

[4] Post, F.R, Fowler, T.K., and Post S.F., 1993. "A High-Efficiency Electromechanical battery", *Proceedings of the IEEE*, **81**(4), pp. 462–474.

[5] Genta, G., 1985. *Kinetic energy storage*. Butterworth.

[6] Vullo, V., and Vivio, F., 2013. Rotors: Stress Analysis and Design. Berlin. Springer.

[7] Bolund, B., Bernhoff, H., and Leijon, M., 2007. "Flywheel energy and power storage systems". *Renewable and Sustainable Energy Reviews*, **11**(2), pp. 235–258.

[8] Pedrolli, L., Zanfei, A., 2, Ancellotti, S., Fontanari, V., and Benedetti M., 2016. "Shape optimization of a metallic flywheel using an evolutive system method: Design of an asymmetrical shape for mechanical interface". *Proc IMechE Part C: J Mechanical Engineering Science*, (in press). DOI: 10.1177/0954406216682054.

[9] Timoshenko, S.P., and Goodier, J.N., 1970. *Theory of elasticity*. NewYork: McGraw- Hill.

[10] Niemann, G., Winter, H., and Höhn B-R., 2005. *Maschinenelemente*. Vol. I Berlin, Germany: Springer.

[11] Roisum, D.R., 1994. *The mechanics of winding*. Tappi Press.

[12] de Hoog, F.R., Cozijnsen, M., Yuen, W.Y.D., and Huynh, H-N., 2004. "Predicting winding stresses for wound coils of linear orthotropic material". *Proc IMechE Part C: J Mechanical Engineering Science*, **218**, pp.13–25.

[13] Huber, J.E., Nowell, D., and Hills, D.A., 2007. "On the stress analysis of a wound coil with application to electromagnet manufacture". *J. Strain Analysis*, **42**(6), pp. 447–460.

[14] Moorlat, P.A., and Portnov, G.G., 1984. "Calculation of the stress-strain state of a chord flywheel with spokes". *Mechanics of Composite Materials*, 19(5), pp. 631–639.

[15] Arvin, A.C., and Bakis, C.E., 2006. "Optimal design of press-fitted filament wound composite flywheel rotors". *Composite Structures*, **72**(1), pp. 47–57.

[16] Koyanagi, J., 2012. "Durability of filament-wound composite flywheel rotors". *Mechanics of Time-Dependent Materials*, **16**(1), pp. 71–83.

[17] Jain, R., Ramachandra, K., and Simha, K.R.Y., 1999. "Rotating anisotropic disc of uniform strength", *Int. J Mech. Sci.*, **41**(6), pp. 639–648.

[18] Gay, D., Hoa, S. V., and Tsai, S. W., 2003. *Composite materials: design and applications*. London, UK, CRC Press.

[19] Dragoni, E., and Mauri, P., 2002. "Cumulative static strength of tightened joints bonded with anaerobic adhesives", *Proc. Instn Mech. Engrs*, *Part L*, **216**(1), 9–15.

[20] Dragoni, E., and Mauri, P., 2011. "Science of Friction–Adhesive Joints", in Book: *Hybrid Adhesive Joints* (da Silva, L.F.M., Pirondi, A. and Öchsner, A.), pp. 201–225

A REPERTOIRE OF FAILURES IN GUDGEON PINS FOR INTERNAL COMBUSTION ENGINES

Antonio Strozzi
Department of Engineering Enzo Ferrari,
University of Modena and Reggio-Emilia, Italy
E-mail: antonio.strozzi@ unimore.it

Andrea Baldini
Department of Engineering Enzo Ferrari,
University of Modena and Reggio-Emilia, Italy
E-mail: andrea.baldini@ unimore.it

Matteo Giacopini
Department of Engineering Enzo Ferrari,
University of Modena and Reggio-Emilia, Italy
E-mail: matteo.giacopini@ unimore.it

Enrico Bertocchi
Department of Engineering Enzo Ferrari,
University of Modena and Reggio-Emilia, Italy
E-mail: enrico.bertocchi@ unimore.it

Sara Mantovani
Department of Engineering Enzo Ferrari,
University of Modena and Reggio-Emilia, Italy
E-mail: sara.mantovani@unimore.it

Abstract. *The geometries commonly employed in gudgeon pins for internal combustion engines are examined. In particular, various methods for reducing the pin weight are considered. The selection of the appropriate clearance is addressed. The most typical failure modes are classified and interpreted in the light of stress analysis.*

Keywords: *gudgeon pin, failure, contact pressure, weight reduction, clearance.*

1. INTRODUCTION

Gudgeon pins (or piston pins, or wrist pins) play a vital, literally pivotal, role in a reciprocating internal combustion engine, [1]. In fact, the gudgeon pin connects the piston to the con-rod; it allows the con-rod to rotate with respect to the piston and, therefore, it provides a bearing for the con-rod to pivot upon as the piston undergoes its reciprocating motion.

Piston pins are arguably one of the most highly stressed engine components, and, therefore, they deserve special attention by the designer [2–5].

The forces applied to the pin include those due to the combustion pressure, as well as the inertial forces exerted by the mass of the piston and, partially, of the pin itself, [6-7]. In this paper, the combustion load refers to a loading due to both the combustion and the inertial forces, globally compressing the con-rod shank, whereas the induction load describes a loading pulling the con-rod shank.

Moving along the pin axis direction, the pin central part is in contact with the bore of the con-rod small end, whereas the pin lateral parts are supported by the piston bosses.

The outline of this paper is as follows. The currently employed pin geometries and clearances are examined, and the shapes aiming at reducing the pin weight are classified. The pin commonest failure modes are ranked, and the existing information on the fatigue crack initiation point and evolution directions is discussed.

The collapsed gudgeon pins illustrated in this paper form part of the collection of the Engineering Department Enzo Ferrari, Modena, Italy; the gudgeon pins mainly originate from a long-lasting collaboration of the Engineering Department with several vehicle industries of the territory; the gudgeon pins also constitute a teaching support to the courses offered on the structural design of internal combustion engine components.

2. PIN GEOMETRY

The gudgeon pin basic geometry is essentially cylindrical and hollow. To limit the contact pressure, in non demanding applications the pin length is as long as possible, often in the region of 0.8 times the piston bore. Conversely, to limit weight, in high performance engines the pin is considerably shorter, down to 0.4 times the piston bore.

In automotive applications, the pin outer diameter is often in the region of 20 mm. In addition, in a four stroke engine, the pin inner diameter is about 0.5 times its outer equivalent, *e.g.* [6].

The available indications on the admissible pressure between the pin and the piston bosses are as follows. According to [8] and [9], the admissible pressure between the steel pin and the aluminum piston bosses is 35 MPa, whereas its analogue between the pin and the steel con-rod small end is 45 MPa. To achieve the same mean pressure along the lateral and central pin supports, the axial length of the pin lateral supports should be 1.3 times that of the central support. According to [10, 11], the maximum permissible value for the contact pressure is about 40 MPa. In [12], the admissible contact pressure is 40 MPa for small engines, and 20 MPa for large engines. In [13], a diagram is presented that reports the development trend for the admissible contact pressure in con-rod bearings along the years 1990–2005; see also Chapter 3.5 of [5]. It appears that the technological developments currently allow the employment of contact pressures up to 180 MPa in year 2005, approximately doubled with respect to those of, say, 20 years ago.

Nowadays the gudgeon pins are mainly fully floating, *e.g.* [5] p. 35. Their advantages are: *i*) they provide a dual pivot to the pin, thus more uniformly distributing wear and reducing the incidence of seizure; *ii*) they avoid the insurgence of mainly axial internal stresses connected to the differential thermal expansion of the steel pin and of the aluminium piston, especially during the engine warm-up phase. In past years, pins fixed into the piston bosses (stationary pins) or into the con-rod small end (semi-floating pins) were used, since they did not require the employment of circlips to avoid undesired sideways movements of the pin, [14] p. 274. In addition, in not fully floating pins the effort of designing a lubricated contact can be restricted to the pivoting mating surfaces. It is also observed that in fully floating pins the fatigue cycle of the ovalizing stresses is more detrimental than that in non freely rotating pins. Considerations on the press fit pressure distribution in stationary and semi-floating assemblies are reported in [15].

Pin weight containment

To reduce weight, the engine pin is always hollow, where the inner to outer radii aspect ratio is often in the region of 0.5 in a four stroke engine, *e.g.* [6]. With this geometry, the weight reduction with respect to a solid pin is 25 per cent, whereas the increase in bending stresses is a mere 6 per cent. However, the presence of a bore causes the insurgence of a pin ovalization and, therefore, of undesired ovalizing stresses, which are absent in a solid pin. For this reason, it is not convenient to lighten the pin by increasing the bore radius beyond a certain limit, since the pin weight reduction, within a substantial constancy of the pin bending stresses, would be counterbalanced by a noticeable undesired increase of the ovalizing stresses, see [2], p.570 and [16].

In high performance engines, the gudgeon pin basic cylindrical hollow geometry is often modified to further reduce the pin mass and, consequently, the inertial forces affecting the pin, in the respect of the condition that the pin strength be not significantly compromized. The commonest pin geometry modification is to introduce a taper along the extremities of the inner surface of the hollow pin, see [2, p. 570, 5, 7, 16–17, 18, p. 98] and [19]. Fig. 1(a) shows a tapered pin. Since this tapered zone falls at the pin extremities, the bending moment affecting such pin zones is small and, therefore, the introduction of tapers does not appreciably jeopardize the pin strength. The taper is usually described by a conical surface; however, more complex taper shapes are sometimes employed, Fig. 1(b).

An alternative pin geometry modification aimed at reducing the pin mass, is to lower the radial thickness of the hollow pin, apart from the pin transition zones in which the pin support passes from the piston bosses to the con-rod small end (referred to in the following as "gap"), Fig. 1(c). This geometry has been proposed in Fig. 17 of [7], and in [20–22]. The boring of this shape is time consuming, since cantilever tools would be needed that, being flexible, demand low rates of metal removal. A cold extrusion process for making internal bulges in pins is patented in [20].

The pin geometry of Fig. 1(c) is expected to improve the pin strength at the gaps by reducing the shear stresses, and, therefore, it should be particularly effective when the pin shear stresses prevail over the bending and ovalizing stresses. The present authors are aware of applications of this pin geometry in high performance motorcycle engines.

Additional pin inner profiles have been numerically investigated in [23].

Clearance

An initial clearance must be provided between the pin outer surface on one side, and the small end bore and piston boss bores on the other side. This clearance must fall within a certain interval.

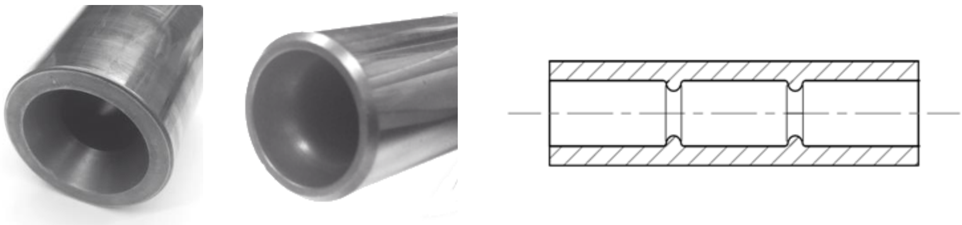

(a) (b) (c)

Figure 1. (a) conical taper; (b) rounded taper; (c) reinforcements at the gap.

In fact, if the clearance at operating temperature is too small, seizure might occur, whereas too high an initial play may cause deterioration in the lubricating regime [6] as well as pin related noise [24, 25]. Based upon an extensive literature review, in [6] the diametral clearance between eye and pin is suggested to fall within the interval 0.0008–0.003 times the pin radius. For a commonplace 20 mm diameter pin, the acceptable diametrical clearance should range from 0.008 to 0.03 mm. In [24] a tighter clearance range is suggested, from 0.002 to 0.012 mm; however, detailed indications on the pin outer diameter interval to which such clearances are applicable have not been provided.

The outer edges of the pin are radiused or chamfered to limit the presence of pressure spikes at the pin extremities. Suggestions on such geometry corrections are provided in [26], p. 7.

In high power engines, the bore surface of the small end is generally inverse barrelled, where the barrelling serves to accommodate for the pin bending and, consequently, to limit the untoward pressure peaks at the contact extremities, [27]. For a 20 mm diameter steel pin, the axially profiled con-rod bore consists of a central cylindrical surface blending with two lateral arcs of a circle, whose radius is about 30 times the pin diameter. The axial length of the cylindrical portion is about one third of the con-rod small end thickness in the pin axial direction; its aim is to avoid any undesired piston pivoting about the pin midpoint.

In high tech pistons, pin bosses are adopted whose pin bores exhibit a diameter (partially) varying along the bore axis, [5, 24, 28]. In particular, a boss splayed seat whose diameter increases towards the small end lateral faces, is frequently employed to achieve a pin-hub contact pressure that stays more uniform in the pin axial direction, [29]. The splayed portion of the boss bore is generally limited to the zone closer to the small end lateral faces; its axial length is about one fourth of the pin diameter, and, for a 20 mm diameter pin, the increase in the bore diameter is about 30 μm, with a fine tolerance range smaller than 10 μm. The splayed profile is supplied to the CNC by reporting the coordinates of a series of subsequent points, whose axial step is in the region of 1 mm.

In race applications, a non axisymmetric splayed profile is sometimes adopted, to account for the differences in intensity of the forces during combustion and induction, and the consequent differences in the pin bending. In such high tech applications, a detailed knowledge of the temperature distribution in working conditions is required.

It is noted that the advantages deriving from inverse barelling are more relevant than the boss splayed seat modification; in fact the piston is made of a relatively deformable aluminum alloy, and it deflects accompanying the steel pin bending, and adapting its deformation to the bent pin.

In [24], trumpet-shaped, profiled pin bores are examined from the viewpoint of noise occurrence.

It is admirable that the potential usefulness of an inverse barrelled small end bore surface had lucidly been understood in year 1941 in [7], before formula 17, together with the advantages of a conical-ovoidal profile of the piston bosses.

The modelling of the effect of clearance, [27], or of interference fits, [30], requires advanced mathematical tools. It is therefore a demanding task to develop models capable of accounting for the pin being floating or not. An attempt is made in the following to perfunctorily review the main available information on the clearance effects within the con-rod assembly realm.

In the presence of an initial clearance, the contact between the pin and the small end bore is progressive, and, therefore, it is non linear, see [4] p. 9 and [31]. It has been shown in [30] that the extent of the contact arc depends on the ratio between the load the and

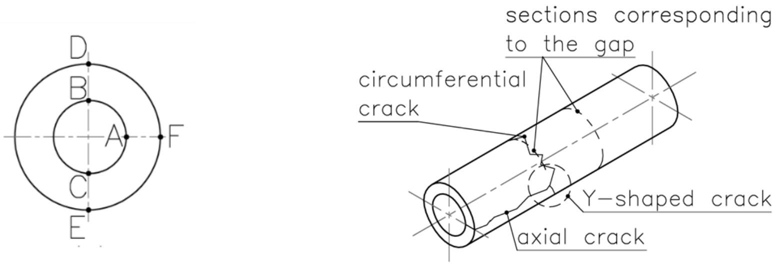

(a) (b)

Figure 2. (a) location of six points lying on a general pin cross section, defined by letters, (b) the main crack propagations in a gudgeon pin.

clearance; consequently, the above ratio may be treated as a single variable. In addition, in two geometries for which the above ratio is the same, the stress pattern remains the same, see [32, 33] for details, and Fig. 11 of [34].

The material employed for the pin is a case-hardened, low carbon, alloyed steel, see [35–36] and Appendix A of [26]. Titanium pins are also commercially available, although their life expectation is very limited, [1]. Anti-wear coatings are frequently employed, see Chapter 3 of [5] and [37].

3. PIN FAILURE MODES

The knowledge of the commonest pin failure loci and modes is particularly useful from the designer viewpoint. In fact, a detailed stress analysis should focus on these loci, and design formulae should be developed for the most detrimental stresses.

Many studies concur in locating the pin failure initiation point, with respect to its radial position, along the pin bore; with respect to its axial position, at the gap, *i.e.* at the axial transitional zone where the pin support passes from a pin lateral to its central zone; with respect to its angular position, along the pin neutral axis, *i.e.* at the bore sides. Fig. 2(a) denotes with letters six points lying on a general pin cross section; the letters are useful for identifying the loci at which the pin stresses are evaluated. In Fig. 2(a) the lettering employed in Fig. 1 of [38] is adopted as an homage. The crack initiation point falls at the point *A* of Fig. 2(a), [5, 16, 19, 23, 36, 39, 40]. This result agrees with the circumstance that the point *A* is generally the most stressed zone, see Section 4.

A contrasting opinion is expressed in [7], Fig. 8, where the crack initiation point is assumed to be located along the pin outer surface. In [41] it is stated that, in the presence of case hardening along the pin outer surface but in its absence along the pin bore, failure initiates at the bore, although not at the bore sides; in the presence of case hardening along the pin inner and outer surface, failure starts at the outside surface. This result may be rationalized by observing that bore hardening improves the fatigue strength of the material, [16].

In [7] it is noted that the crack initiates with an inclination of about 45° with respect to the pin axis, and this fact is interpreted as a result of high shear stresses at the pin bore sides. The presence of two 45° inclined cracks, forming the two branches of a *Y*-shaped crack, see Fig. 2(b) and Fig. 12 of [7]. Fig. 14 of [7] reports experimental contour curves expressing the principal directions, which are about 45° inclined at the gap.

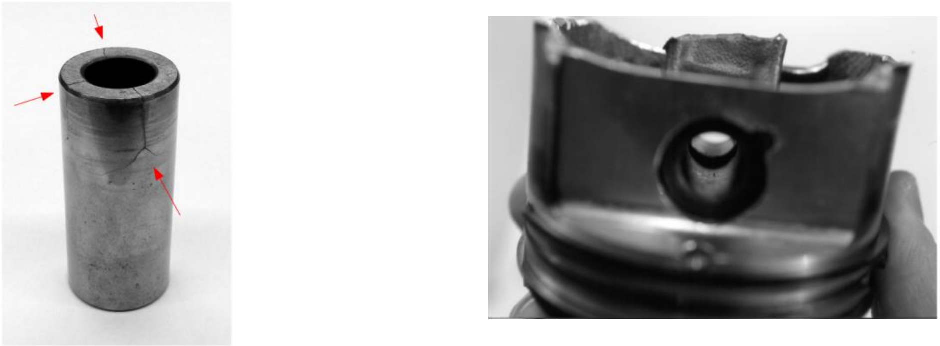

(a) (b)

Figure 3. (a) the *Y*-shaped crack, and three axial cracks; (b) gudgeon pin fractured along a plane perpendicular to its axis, passing through the gap.

Starting from the typical crack initiation at the bore sides, point *A*, the crack evolves in the circumferential direction and/or in the axial direction, propagating towards the pin outer surface, [36], and Fig. 2(b). The first crack evolution mode produces a fracture along a surface perpendicular to the pin axis, and it is mainly imputable to the shear force; in [7] it is noted that this crack evolves circumferentially according to a serrated pattern, see their Fig. 10, initially formed by the two branches of the *Y*-shaped crack. The second mode produces axial cracks, and it is mainly attributable to the ovalizing stresses; in [7], Fig. 15, it is noted that the crack evolves axially according to a straight line. The two fracture modes often coexist in a cracked pin, see [7], [36].

The axial cracks usually evolve along the pin axial portions outside the con-rod small end, and they eventually reach the pin extremities.
Axially cracked pins, in which the cracks do not reach the pin extremities, are rarely encountered. In fact, it is noted in [7] that the pin cracks evolve very rapidly.

The angular distance among different axial cracks due to ovalization varies depending on whether the pin is fully floating or not. If the pin is fully floating, it is free to rotate about its axis, [42], and, consequently, the angular distance among the longitudinal cracks does not possess any privileged value. In addition, as a result of the pin rotation, the ovalizing stresses, see Section 4 below, should be conservatively modelled as reversed. If the pin is not fully floating, it cannot freely rotate about its axis, and four longitudinal cracks generally develop at an angular interval of 90°, consistent with the four angularly equidistant loci of maximum ovalizing moment encountered in an ovalized ring. Fig. 3(a) displays three axial cracks at a relative angular distance of 90°, the fourth crack being absent. When the pin cannot rotate, the ovalizing stresses are repeated and not reversed.

The usual absence of axial cracks in the pin central zone may be rationalized by noting that the pin ovalization in its central part is confined by *the restraint of the central lug*, [38]. Consequently, the small end in some way protects the pin from excessive ovalization. In [2], p.571, it is similarly noted that *experience demonstrates that the pin collapse does not occur at the pin centre*.

It has been noted that the crack evolves both in the circumferential and in the axial direction. Two fracture modes, in which only one of the two above cracks evolves, are displayed in Figs. 3(a) and (b). Fig. 3(a) shows the axial cracks. Fig. 3(b) reports a gudgeon pin fractured along a plane perpendicular to its axis, passing through the gap between the piston bosses and the con-rod small end, in the manifest absence of axial cracks.

(a)

(b)

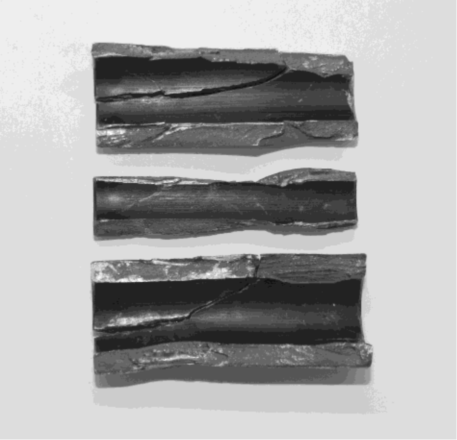

(c)

Figure 4. (a) pin collapsed along the pin central cross section, (b) two unusually contiguous axial cracks; (c) pin axially cracked along its whole length.

Three unusual failure modes are documented in the following. Fig. 4(a) shows a pin collapsed along the pin central cross section. Fig. 4(b) details two unusually contiguous axial cracks evolving from the *Y*-shaped crack. Fig. 4(c) shows a pin axially cracked along its whole length, in the absence of cracks developing along circumferential directions.

In [43] and [44], naval gudgeon pin failures are examined. These pins possess lubrication holes, which act as stress raisers. Crack propagation therefore generally differs from the classical pin collapses examined in this paper.

4. CONCLUSIONS

The geometries commonly adopted in gudgeon pins for internal combustion engines have been examined. Various methods for reducing the pin weight have been considered. The selection of the appropriate clearance has been addressed. The most typical failure modes have been classified and interpreted in the light of stress analysis. A critical review of the available approximate analytical formulae versus FE forecasts are reserved for later work with regard to a reference pin geometry and loading.

REFERENCES

[1] Ward, W., 2012. “Piston pins - material choices”. *Race Engine Technology*, June/July.

[2] Giovannozzi R., 1965. *Costruzione di Macchine.* Patron Editrice, Bologna.

[3] Maass, H., 1975. “Der Kolbenbolzen, ein einfaches Maschinenelement”. VDI-Verlag.

[4] Klebanov, B.M., Barlam, D.M., and Nystrom, F.E., 2007. *Machine elements: life and design.* CRC Press.

[5] MAHLE GmbH, 2010. *Cylinder components, Piston pins and piston pin circlips***.** MAHLE GmbH, pp. 27–47.

[6] Strozzi, A. and De Bona, F., 2005. "Hoop stresses in the con-rod small end". *Proc. Ints. Mech. Eng. D: J Automob. Eng.*, **219**(11), pp. 1331–1345.

[7] Mickel, E., and Sommer, P., 1941. "Zur Festigkeit von Kolbenbolzen", *MTZ-Motortechnische Zeitschrift.* **11**, pp. 352–356.

[8] Caboni, F., 1974. *Costruzione di Macchine.* Pitagora, Bologna.

[9] Strozzi, A., 1998. *Costruzione di Macchine.* Pitagora, Bologna.

[10] Hunt, T.O., 1957. "Gudgeon Pin Loading". *Automob. Eng.* **47**, pp. 177–178.

[11] Rothmann, G., 1963. "Berechnung der Kolbenbolzen von Fahrzeugdiesel-motoren". *Mitteilungen aus den Forschungsanstalten von GHH— Konzern*, **4**, pp. 231–238.

[12] Lawton, B. and Crutcher, D.E.G., 1966. "Paper 7: Mechanical Stresses in Pistons, Gudgeon Pins, and Connecting Rods". *Proc. Inst. Mech. Engs.*, SAGE Pub. **181**(8), pp. 20–30.

[13] Deicke, K. and Schubert, W., 2005. "PVD-coated high-performance bearings". *Auto Technology*, **2**(5) pp. 72–74.

[14] Garro, A., 1992. *Progettazione Strutturale del Motore.* Torino: Levrotto & Bella.

[15] Serban, I., Ispas, N.,Bobescu, G., and Arama, C., 2012. "The experimental research of the combustion engine piston pin stress". In *Proceedings of the 4th Int. Conf. Advanced Composite Mats Eng.*, (COMAT 2012), Brasov, Romania 2012, pp. 433–438.

[16] Giovannozzi, R., 1943. "Sul calcolo dello spinotto del pistone". *L'Aerotecnica*, **23,** pp.146–155.

[17] Buty, L., and Petricenko, M., 1964. L'Attelage mobile des moteurs rapides. *Société des Editions Technique*, Paris.

[18] Vignocchi, D., 2002. *Elementi di Progettazione del Motore.* Athena, Modena.

[19] Ji, B.W., Li, J.L. and Chen, X.P., 2011. "Research on Piston Pin's Strength Calculation Based on FEA". *Advanced Materials Research*, **341–342**, pp. 296–300.

[20] Fefeu, M.A., and Perrin G., 1991. U.S. Patent No. 5,027,996. Washington, DC: U.S. Patent and Trademark Office.

[21] Serban, I., Ispas, N., Bobescu, G., and Arama, C., 2012. "Theoretical investigations about the influence of the piston pin stress on the combustion engine performances". In Proceedings of the 4th Int Conf Advanced Composite Mats. Eng., (COMAT 2012), Brasov, Romania 2012, pp. 439–443.

[22] Bachelor Thesis, Lauria, S., 2004. "Riduzione della massa dello spinotto automobilistico tramite la definizione di una geometria innovativa: analisi agli elementi finiti". University of Modena and Reggio-Emilia, Italy.

[23] Folęga, P., Burdzik, R. and Konieczny, Ł., 2015. State of stress analysis for structural solutions

of combustion engine piston pins. *Solid State Phenomena,* **236**, pp. 70–77.

[24] Werkmann, M., Tunsch, M. and Kuenzel, R., 2005. Piston Pin Related Noise-Quantification Procedure and Influence of Pin Bore Geometry. No. 2005-01-3967, *SAE Technical Paper*.

[25] Dini, D., Mastrandrea, L.N., Giacopini, M., and Bertocchi, E., 2014. "Numerical investigation of the cavitation damage in a high performance engine conrod big end bearing via a mass-conserving complementarity algorithm". In *Proceedings of the Soc. of Tribologists and Lubric. Engs. Annual Meeting and Exhibition*, pp. 586–589.

[26] BS3537:1979. Specification for gudgeon pins up to 200 mm diameter.

[27] Pioli, A., Strozzi, A., Baldini, A., Giacopini, M. and Rosi, R., 2009. "Influence of the initial clearance on the peak stress in connecting-rod small ends". *Proc. Inst. Mech. Eng. D: J. Automob. Eng.,* **223**, pp. 769–782.

[28] W. Ward, Dec/Jan 2010. "Reciprocating ideas". *Race Engine Technology*, pp. 40–48.

[29] Strozzi, A., Baldini, A., Giacopini, M., Bertocchi, E., and Bertocchi, L., 2013."Achievement of a uniform contact pressure in a shaft–hub press-fit". *Proc. Inst. Mech. Eng, C: J. Mech. Eng. Science,* **227**(3), pp. 405–419.

[30] Marmorini, L., Baldini, A., Bertocchi, E., Giacopini, M., Rosi, R. and Strozzi, A., 2011."On the loosening mechanism of a bush press-fitted in the small end of a connecting rod". *Proc. Inst. Mech. Eng. D: J. Automob. Eng.* (0954407011417498).

[31] Master Thesis, Parlamento, M., 2001. "Soluzione teorica esatta per la pressione di contatto tra spinotto e piede di biella: applicazione all'ottimizzazione della geometria del piede", University of Modena and Reggio-Emilia, Italy.

[32] Ciavarella, M., and Decuzzi, P., 2001. "The state of stress induced by the plane frictionless cylindrical contact. I. The case of elastic similarity". *Int. J. Solids and Structs.*, **38**(26), pp. 4507-4523.

[33] Ciavarella, M., Baldini, A., Barber, J.R., and Strozzi, A. 2006. "Reduced dependence on loading parameters in almost conforming contacts". *Int. J. Mech. Sci.,* **48**(9), pp. 917–925.

[34] Strozzi, A., Baldini, A., Giacopini, M., Bertocchi, E. and Mantovani, S., 2015. "A repertoire of failures in connecting rods for internal combustion engines, and indications on traditional and advanced design methods". *Eng. Failure Anal.,* **60**, pp. 20–39.

[35] L'vovskii, A.Y. and Beilina, O.Y., 1981. "Increasing the rigidity of wrist pins". *Metal Sci. and Heat Treatment*, **23**(2), pp. 136–137.

[36] Yu, Z., Xu, X. and Ding, H., 2007. "Failure analysis of a diesel engine piston-pin". *Eng. Failure Anal.,* **14**(1), pp. 110–117.

[37] Etsion, I., Halperin, G., and Becker, E., 2006. "The effect of various surface treatments on piston pin scuffing resistence". *Wear*, **261**, pp. 785–791.

[38] H. Fessler, H., and Padgham, H.B., 1966. "A contribution to the stress analysis of piston pins". *Strain Anal. Eng. Des.,* **1**(5), pp. 422–428.

[39] Grieve, D.J., 2003. DMME-Stresses in a Gudgeon Pin. See also URL

http://www.tech.plym.ac.uk/sme/desnotes/gudgeon.htm.

[40] Wang, Y. and Gao, H., 2011. “Research on optimization for the piston pin and the piston pin boss”. *Open Mech. Eng. J.*, **5**, pp.186–193.

[41] Robinson, J.E., 1965. “Piston-Boss and Wrist-Pin Design”. *J. Eng. for Gas Turbines and Power,* **87**(4), pp. 412–420.

[42] Di Paola, G., Maglioni, C., Molari, P.G., and Spuria, M., 2004. “Verifica del danno e riprogettazione delle zone di contatto biella-spinotto-pistone in un motore da competizione”. In *Proceedings of Convegno Nazionale XIV ADM-XXXIII AIAS, Innovazione nella Progettazione Industriale*, Bari, Italy.

[43] Franco, F., 2008. “Fatica ad alto numero di cicli per motori alternativi di grandi dimensioni”. In *Proceedings of Giornata di studio IGF*, Torino, Italy.

[44] Bejger, A., Gawdzińska,K., Berczyński,S., 2012. “Application of Pareto analysis for the description of faults and failures of marine medium power engines with self ignition”. *Archives of Mech. Technology and Automation,* **32**(3), pp. 7–13.

SHEAR STRENGTH CHARACTERIZATION OF METAL-ELASTOMER BONDED JOINTS

Marina Ragni
Department of Science and Methods for Engineering,
University of Modena and Reggio Emilia, Italy
E-mail: marina.ragni@unimore.it

Davide Castagnetti
Department of Science and Methods for Engineering,
University of Modena and Reggio Emilia, Italy
E-mail: davide.castagnetti@unimore.it

Andrea Spaggiari
Department of Science and Methods for Engineering,
University of Modena and Reggio Emilia, Italy
E-mail: andrea.spaggiari@unimore.it

Filippo Muccini
Department of Science and Methods for Engineering,
University of Modena and Reggio Emilia, Italy
E-mail: 177723@studenti.unimore.it

Eugenio Dragoni
Department of Science and Methods for Engineering,
University of Modena and Reggio Emilia, Italy
E-mail: eugenio.dragoni@studenti.unimore.it

Matteo Milelli
Tellure Rôta S.p.A., Formigine (MO), Italy
E-mail: matteo.milelli@tellurerota.com

Simone Girlando
Tellure Rôta S.p.A., Formigine (MO), Italy
E-mail: simone.girlando@tellurerota.com

Pierluigi Borghi
Tellure Rôta S.p.A., Formigine (MO), Italy
E-mail: pierluigi.borghi@tellurerota.com

Abstract. *The shear strength characterization of bonded joints involving adherends with a remarkably different stiffness has a peculiar interest in industrial applications. This work proposes and investigates three innovative specimens (an axisymmetric annular, a tensile and a torsional one) purposely developed to manage dissimilar adherends bonded with adhesive in thin film. A Thick Adherend Shear Test specimen between rigid adherends is used* *for the assessment of the adhesive by itself. The work focuses on metal-elastomeric polyurethane bonded joints with a solvent-based adhesive. All the tests are performed through an axial dynamometer, using a purposely developed fixture to convert the tensile load in a torque for the torsional specimen. The tensile and the torsional specimens provide the most reliable shear strength characterization.*

Keywords: *bonded joints, dissimilar adherends, thin film adhesive, elastomer, specimen*

1. INTRODUCTION

Bonded joints between dissimilar adherends, in particular metal and elastomer with a thin adhesive layer in-between, can be found in many industrial applications. For example, pallet truck wheels feature a coating of a solid elastomeric layer bonded to the metal body (cast iron or steel). In the offshore oil industry, rubber-metal bonded composites are used to protect the structure from seawater. This paper deals with the experimental characterization of the shear strength of this type of bonded joints.

A few works can be traced in the literature about metal-elastomer joints. Stevenson [1], Hamade [2] and Liechti et al. [3] evaluated the joint strength for metal-rubber adherends in corrosive environment. Othman [4] studied the drawbacks of peel test for the assessment of metal-rubber joints. The ASTM D429 standard [5]-[6] suggests some specimens for testing metal-elastomer joints. Many works in the literature deal with the development of bonded specimens for the characterization of thin adhesive films between rigid adherends [6]-[10].

This work aims to develop and experimentally assess innovative specimens for the shear strength characterization of bonded joints involving adherends with a remarkably different stiffness and with adhesive in thin film. Four different joint specimens are proposed and investigated. First, a Thick Adherend Shear Test (TAST) [11] specimen to assess the shear strength of the adhesive between rigid adherends. Second, an axisymmetric specimen featuring an annular elastomeric ring which is bonded, on the inner diameter, to a rigid hollow shaft: an annular fixture applies an axial load to the elastomeric ring. Third, a tensile specimen, resembling the TAST specimen [11]. This specimen features a sandwich metal-elastomer-metal configuration, bonded one each other, and undergoes shear load. Fourth, a torsional specimen, where an elastomeric annular ring is bonded internally and externally to a rigid shaft and a hub, respectively: a torque is applied between the shaft and the hub.

Three are the steps of the work. The first step describes the conceptual design of the specimens. The second step presents the design and the development of the proposed specimens. The third step reports the experimental assessment of the most promising specimens, which involves a thermoplastic solvent-based adhesive. The results highlight that the TAST-like specimen and the torsional specimen provide the simplest and reliable evaluation of the shear strength between adherends with a remarkably different stiffness. In addition, these specimens can be fruitfully applied to a wide range of dissimilar adherends and adhesives.

2. MATERIAL AND METHODS

2.1 Conceptual design

Table 1 presents the client needs identified for the metal-elastomer bonded specimens and the corresponding weight.

By keeping into account the above client needs, this section proposes and qualitatively compares four specimen configurations for the shear stress characterization of a thermoplastic solvent-based adhesive, which is peculiar for bonding of steel or cast iron to elastomeric polyurethane.

Figure 1 shows a TAST specimen [7], with metallic adherends. This specimen gives the shear strength of the adhesive by itself, disregarding the effect of a stiffness mismatch between the adherends. Due to the experimental constraints, the specimen dimensions (Figure 1a) slightly differ from those prescribed by the standard [7].

An axial load is applied to the specimen through fork pin fixtures on each ends, so as to obtain a pure shear loading on the bonded joint the bonded joint (Figure 1b).

Figure 2a shows an axisymmetric annular specimen, consisting of a hollow shaft with an annular elastomeric ring bonded outside: the annular ring is casted onto the hollow shaft, where the adhesive is preliminary applied. The dimensions of the specimen (Figure 2a) were mainly chosen considering the manufacturing constraints.

Figure 2b shows a detail of the fixture used in the experimental test to support the specimen. In order to obtain a more uniform stress distribution on the specimen, the test is performed by enclosing the annular ring between a support pipe P1 and a cover plate P2 (Figure 2b). An axial load is applied to the hollow shaft (S in Figure 2b), up to complete failure of the bonded joint.

In order to evaluate the shear stress distribution, we implemented an axisymmetric finite element (FE) model of the specimen, loaded against a rigid annular ring (Figure 3a). The FE analysis shows a remarkable not-uniform shear stress distribution along the bond-line. As expected, a noticeable shear stress concentration occurs in the lower boundary, where the pipe P1 pushes against the elastomeric ring. In addition, the elastomeric ring bends upward thus giving in the same region a remarkable peel stress concentration. On the whole, due to this peculiar behaviour, the specimen can be used only for qualitatively comparing different bonding treatments, without obtaining a quantitative characterization of the shear strength.

Figure 4a shows the sketch of the TAST-like specimen here proposed, consisting in a sandwich obtained by bonding an inner elastomeric layer (D) to a couple of metal adherends (C). These three layers are bonded each other. The plates (*A*) act as connecting elements between the top and bottom cross-head of the testing machine, and the sandwich specimen. The plates *B* join the plates *A* to the sandwich specimen. By applying an axial load to the TAST-like specimen (in the vertical direction), a shear stress distribution arises in the adhesive layer: the stiffer the central sandwich, the more uniform the shear stress distribution on the adhesive. A plane stress FE analysis (Figure 5a-b) confirms that, for a metal-elastomer sandwich, large displacements and large strains occur on the central elastomeric layer (D), for a given axial displacement applied to the specimen. Therefore, a non-uniform shear stress (Figure 5a) and peel stress (Figure 5b) distribution originates on both adhesive layers, with peak stresses on the boundaries: the lower the ratio between the thickness and the length for the elastomeric adherend, the lower the peak stresses in the adhesive.

Despite this drawback, the TAST-like specimen is easy to manufacture and allows performing comparative evaluation between, for example, different pairs of adherends or adhesives, simply by using a tensile testing machine. The specimen dimensions (Figure 4a) mainly come from the production constraints, in particular, with regard to the available mold thickness for polyurethane casting.

Figure 6 shows the sketch of the torsional specimen, composed by an elastomeric annular ring bonded on the inner and outer diameter to a central rigid shaft and an outer rigid hub, respectively. By applying a torque to the specimen, a uniform shear stress originates both on the outer and inner adhesive layer: we highlight that the shear stress field is constant both in the circumferential and in the axial direction.

Table 1. Client needs.

Client needs	Weight
Simple manufacturing	5
Uniform shear stress field	5
Gives information for bonded joints improvement	5
Applicable to an axial dynamometer	4
Low-cost	3

The specimen dimensions, specifically the axial thickness of the elastomeric annular ring (10 mm) and its inner diameter (20 mm) are the best tradeoff between a failure torque that can be applied by our testing machine and the production constraints. Table 2 presents the scoring matrix for a quantitative evaluation of the proposed specimens. The specimens are evaluated according to the client needs and their importance, as described in Table 1. The results show that the TAST-like and the torsional specimens are the most promising solutions.

2.2 Preliminary tests

Despite the lower scoring from the evaluation performed in Table 2, some preliminary tests were performed on the TAST and axisymmetric annular specimen. Figure 7 shows a test on the axisymmetric annular specimen. These tests exhibited many drawbacks for these type of specimens. The TAST specimens showed a poor polymerization since the adhesive formulation is specific for a metallic adherend combined with an elastomeric one, but it is not suitable in case both adherends are metallic.

The annular specimen showed an excessive deformation due to the out-of-plane loading thus giving a premature failure, due to the shear and peel stress concentration on the bottom edge.This confirmed the prediction from the FE analysis. Consequently, we decided to exclude these configurations and focus only the TAST-like specimen (Figure 4) and the torsional specimen (Figure 6).

2.3 Experimental plan

Figure 8a and b show respectively a TAST-like and a torsional specimen. Both specimens were made of mild steel and elastic polyurethane and were manufactured through the same procedure, involving three steps. First, we degreased the bonding surfaces of the steel adherends, then sandblasted by angular steel grit. Second, a solvent-based adhesive was applied manually. Third, the adherends were placed into a preheated mold and polyurethane casting started after the adherends reached the mold temperature.

The tests have been performed on a Galdabini SUN 500, an electromechanical dynamometer with a maximum axial load of 5kN. The tests were quasi-static, by applying a 1mm/min displacement law, up to complete failure of the joint.

The experimental tests on the TAST-like specimens (Figure 9a) investigated the applicability of this specimen in assessing the effect of temperature on the joint strength. Three temperature levels were investigated, from room temperature up to the maximum operating temperature. A thermal chamber installed on the dynamometer was used to set the desired temperature. In order to ensure the desired temperature level, the specimens were stored in the thermal chamber for at least 30 minutes before starting the test.

The tests on the torsional specimens (Figure 9b) were performed on the same dynamometer, using the equipment in Figure 10b. These tests were aimed to assess both the specimen and the kinematism used, and were performed at room temperature. Figure 10a describes the schematic of the kinematism used to perform torsional tests on the specimens of Figure 8b, through the tensile testing machine available in our laboratory. According to the kinematic analysis of the system, the twist angle on the specimen ($\theta = \alpha + \beta$) can be found as a function of the stroke of the top arm, Δ, and of the dimensions l and b, by solving this system of equations:

$$\begin{cases} \Delta + b = l\sin\beta + b\cos\alpha + l\sin\alpha \\ l\cos\beta = l\cos\alpha - b\sin\alpha \end{cases} \tag{1}$$

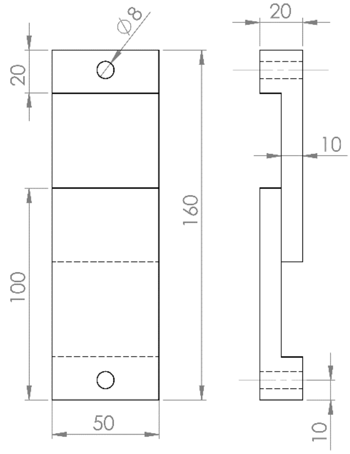

(a)

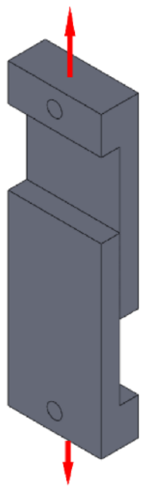

(b)

Figure 1. TAST specimen: (a) technical drawing, (b) 3D model.

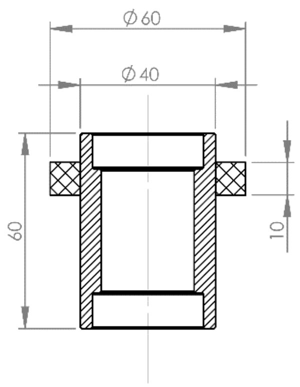

(a)

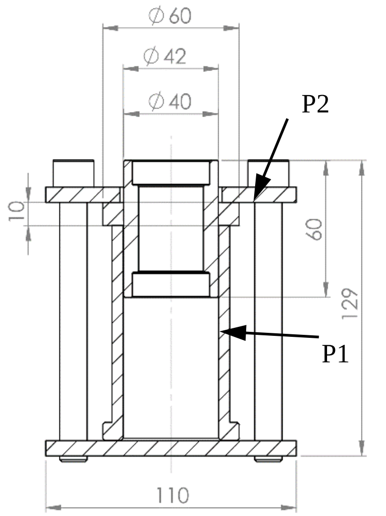

(b)

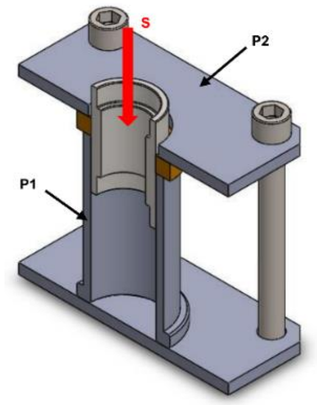

(c)

Figure 2. Annular specimen: (a)-(b) technical drawing, (c) 3D model.

Figure 10b shows a 3D drawing of the kinematism, which was designed accordingly and made of steel. This equipment is composed by a bottom (*A*) and top (*B*) arm, connected, through fork-pin coupling, to the crossheads of the dynamometer. The coupling between the lower arm and the shaft (*C*) of the specimen is performed through a transverse pin. The flange (*F*) is fixed to the top arm through a plate (D) and backplate (E), of equal thickness. The whole system was designed in order to compensate out of plane bending moments on the specimen, and the bolted connections were chosen in accordance with standard design criteria.

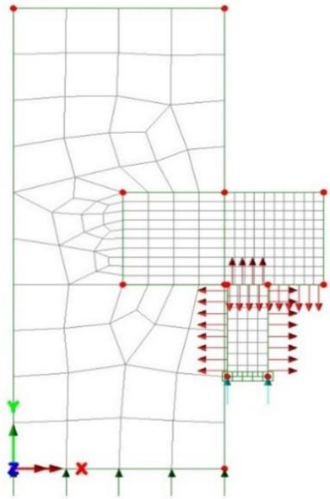

(a)

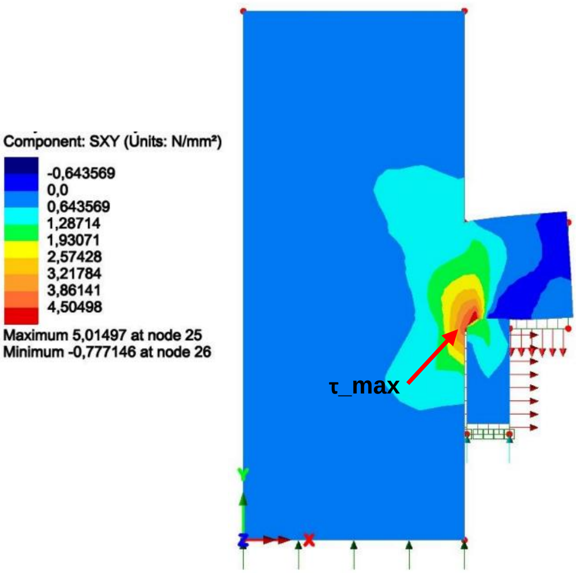

(b)

Figure 3. Annular specimen: (a) FE model, (b) shear stress distribution.

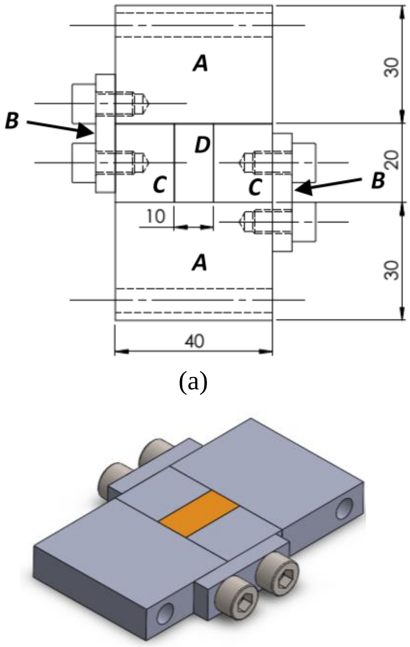

(a)

(b)

Figure 4. TAST-like specimen: (a) technical drawing, (b) 3D model.

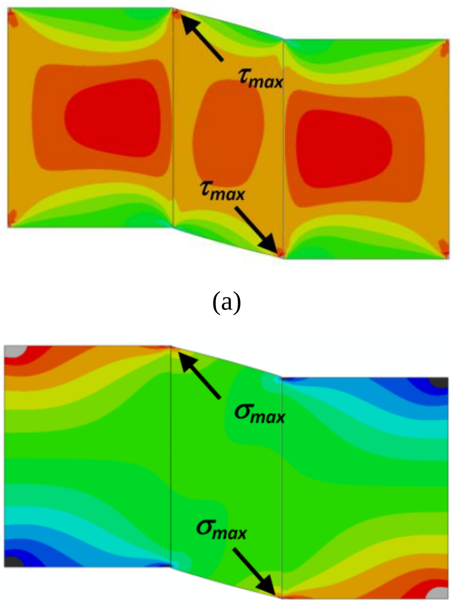

(a)

(b)

Figure 5. TAST-like specimen: (a) shear stress, (b) peel stress.

Table 2. Scoring matrix.

		Specimen			
		TAST	**Annular**	**TAST-like**	**Torsional**
Client needs	*W*	*Score*			
Simple manufacturing	5	5	5	3	1
Uniform shear stress field	5	1	1	4	5
Usefulness	5	1	1	4	5
Applicable to an axial dynamometer	4	5	4	2	2
Low cost	3	3	3	2	2
Total (W x Score)		**64**	**60**	**69**	**69**

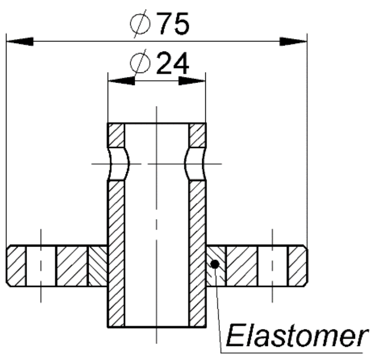

(a)

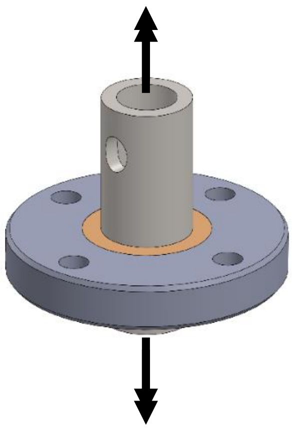

(b)

Figure 6. Torsional specimen: sketch (a) and 3D model (b).

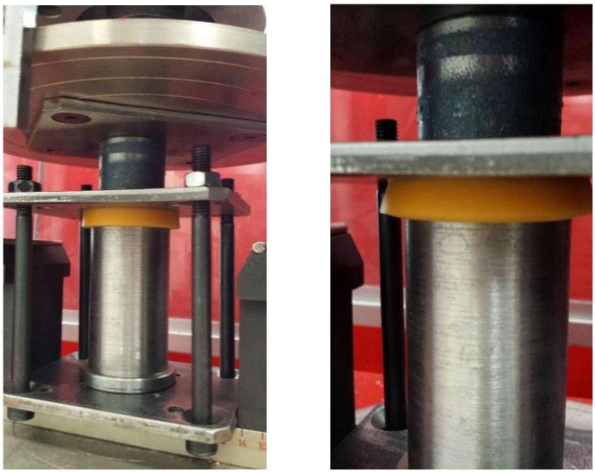

Figure 7. Test on annular specimen.

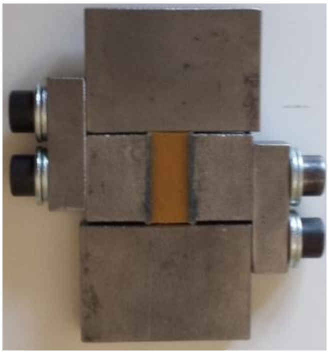

(a)

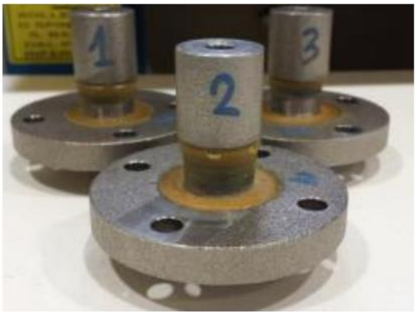

(b)

Figure 8. Sample of Tast-like (a) and torsional (b) specimen.

2.4 Results and discussions

Figure 9a and b show, the debonding on a TAST-like specimen and the large strains occurring on a torsional specimen, respectively: the red lines in Figure 9b were radial straight lines at the beginning of the test. For TAST-like specimens, Figure 11a reports the curves of the average shear stress on the adhesive as a function of the stroke. The average shear stress was calculated as the ratio between the tensile load and the area of the bonded surface of the joint.

Figure 11b reports the peak values of the average shear stress as a function of the test temperature. For torsional specimen, Figure 12 describes the shear stress on the adhesive layer as a function of the twist angle θ. This stress was calculated through the following equation:

$$\tau_t = \frac{2Fl\cos\beta}{\pi h d^2} \tag{2}$$

where F is the instantaneous tensile load, l is the length of the top and bottom arm (A and B in Figure 10b), β is opening angle of the bottom arm, while h and d are the thickness and the inner diameter of polyurethane ring, respectively.

Both the TAST-like and the torsional specimens show a good replicability between the shear stress curves. The TAST-like specimens (Figure 11a), exhibit a remarkable dispersion of the failure stroke, probably caused by a different failure propagation among the specimens. The initial part of the curves shows a stiffer response followed by a stiffness decrease as failure starts, up to a sudden complete failure of the joint.

Figure 11b highlights a remarkable decrease in the shear strength of the joint, as temperature increases. The curves in Figure 12 show an increasing joint stiffness as the twist angle increases, which can be imputed to the large strains occurring to the polyurethane annular ring. On the whole, the proposed specimens are a simple and efficient technique to assess the joint strength of thin film adhesives whose adherends have a remarkably different stiffness.

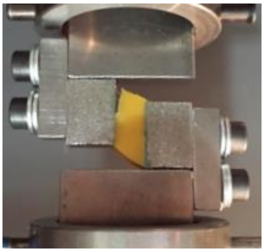

(a)

(b)

Figure 9. Test on a TAST-like (a) and on a torsional (b) specimen.

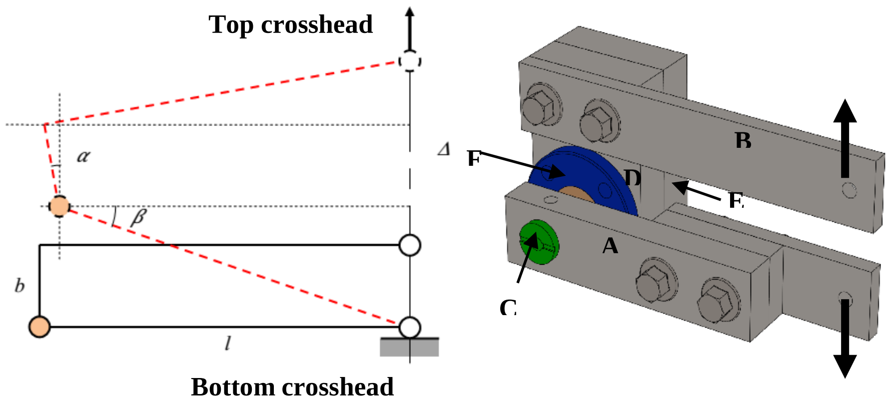

(a) (b)

Figure 10. Schematic of the traction-torsion kinematism (a) and 3D drawing of the designed system (b).

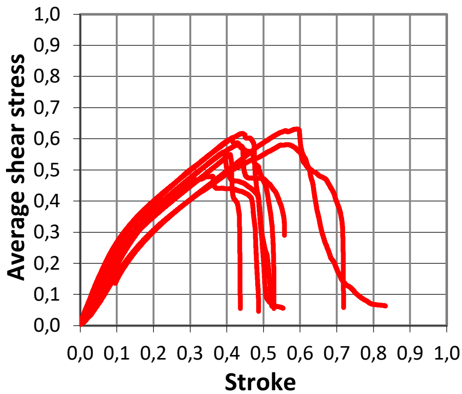

(a)

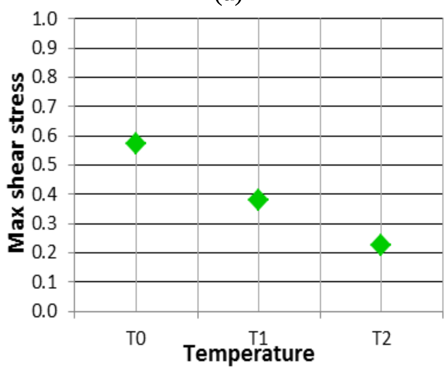

(b)

Figure 11. Normalized TAST-like test results at room temperature (a) and effect of temperature (b).

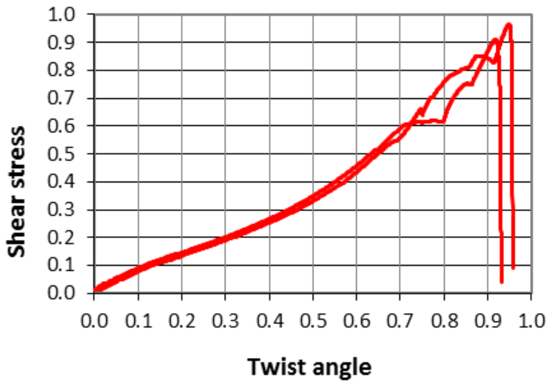

Figure 12. Normalized torsional test curve.

3. CONCLUSIONS

The work proposed, designed and experimentally assessed four specimens for the characterization of thin adhesive films between a metallic and an elastomeric adherend.

According to a conceptual design step and some preliminary assessments, two simple and innovative specimens (a tensile and a torsional one) were investigated in detail, An ad-hoc fixture allowed to test the torsional specimen using a dynamometer.

The proposed TAST-like and torsional specimens are suitable to characterize bonded joints between adherends with different stiffness. In particular, the TAST-like specimen is more suitable for a qualitative comparison between different bonding conditions. On the other hand, the torsional specimen gives an accurate shear strength evaluation.

REFERENCES

[1] Stevenson A., 1985. "On the durability of rubber/metal bond in seawater". *International Journal of Adhesion and Adhesives*, **5**(2), Apr., pp. 81-91.

[2] Hamade R.F., 2009. "Studies on the Prediction of Elastomer to Steel Adhesive Bond Life in Cathodic Environments". *Journal of Adhesion Science and Technology*, **23**(4), pp. 579-600.

[3] Liechti K. M., Becker E.B., Lin. C., Miller T.H., 1989. "A fracture analysis of cathodic delamination in rubber to metal bonds". *International Journal of Fracture*, **39,** pp. 217-234.

[4] Othman A.B., 1989. "Assessment of rubber-to-metal bond strength using the 90-degree peel test". *Polymer Testing*, **8**(4), Apr., pp. 289-299.

[5] http://www.testresources.net/applications/standards/astm/astm-d429-rubber-to-metal-adhesion-tests

[6] www.dowautomotive.com, 299-51993-0612BBI

[7] Castagnetti D., Dragoni E., Spaggiari A., 2010. "Robust shape optimization of tubular butt joints for chatcterizing thin adhesive layers under uniform direct and shear stresses". *Journal of Adhesion Science and Technology*, **24**, pp. 1959-1976.

[8] Castagnetti D., Spaggiari A., Dragoni E., 2011. "Effect of Bondline Thickness on the Static Strength of Structural Adhesives Under Nearly-Homogeneous Shear Stresses". *The Journal of Adhesion*, **87**(7–8), July, pp. 780–803.

[9] Spaggiari A., Castagnetti D., Dragoni E., 2012. "Experimental Tests on Tubular Bonded Butt Specimens: Effect of Relief Grooves on Tensile Strength of the Adhesive". *The Journal of Adhesion*, **88**(4–6), Apr., pp. 499–512.

[10] Spaggiari A, Castagnetti D., Dragoni E., 2013. "Mixed-Mode Strength of Thin Adhesive Films: Experimental Characterization Through a Tubular Specimen with Reduced Edge Effect". *The Journal of Adhesion*, **89**(8), Feb., pp. 660-675.

[11] ASTM International D 5656 - 04, 100 Barr Harbor Drive, West Conshohocken, PA 19428-2959, United States.

AN EFFICIENT FORMAL SYSTEM FOR THREE-DIMENSIONAL KINEMATIC TRANSFORMATIONS USING OPERATOR OVERLOADING

Alessandro Tasora
Dipartimento di Ingegneria ed Architettura,
Università degli Studi di Parma
E-mail: alessandro.tasora@unipr.it

Edzeario Prati
Dipartimento di Ingegneria ed Architettura,
Università degli Studi di Parma
E-mail: edzeario.prati@unipr.it

Dario Mangoni
Dipartimento di Ingegneria ed Architettura,
Università degli Studi di Parma
E-mail: dario.mangoni@studenti.unipr.it

Abstract. *This work presents an efficient way to perform coordinate transformations by computing position, rotation, velocities and accelerations at once, thanks to a custom algebra that maps to synthetic C++ expressions. To this end we took advantage of advanced concepts in object oriented programming, with special emphasis on operator overloading.*

Keywords: *coordinate transformations, Lie groups, kinematics*

1. INTRODUCTION

Coordinate transformation can be computed in many ways [1]. In literature, however, these transformations are mostly mapped to linear algebra expressions that, once implemented in a programming language on a computer, become long and cluttered sequences of operations. The Denavitt-Hartemberg formalism is an attempt at making these operations more readable [2], yet there is room for improvement. In this work, in fact, we show that complex coordinate transformations can be written as compact expression by introducing a new alebra, and we show that such algebra can be typed directly in C++ expressions than to the two concepts of *classes* and *operator overloading*.

In C++, just like in other modern object-oriented languages, mathematical operators such as $+$, $-$, $*$, $/$, can be customized so they can operate over user-objects, not only over scalars [3]. We exploit this feature to the point that overload operators $*$ and $>>$ are used to create an algebra between objects that represent moving frames in space.

This problem often happens in the field of robotics, multibody simulation, kinematics [4].

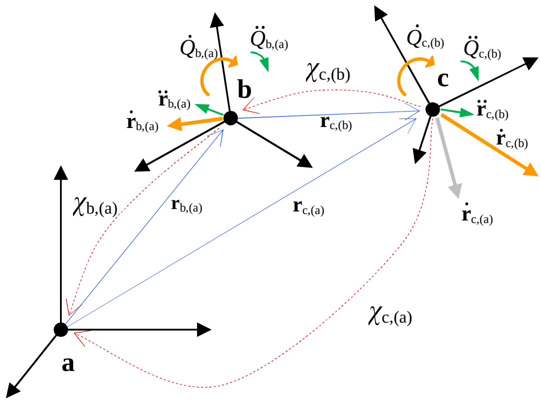

Figure 1. Example of chained transformation.

The algebra discussed in this paper encompasses also speeds and accelerations: for instance if in a sequence of frames the relative speed and relative acceleration of each frame is known respect to the previous frame in the chain, our formalism computes the absolute position, speed and acceleration of the last frame in the chain.

We define a $\succ$ operator such that a sequence of $\succ$ operations corresponds to a sequence of coordinate transformations. An example can explain this: consider $\chi_{i,(j)}$ as a data that represent the position, speed and acceleration (either linear and angular) of the frame i respect to coordinate j; thus, a sequence of transformations as in the example of Fig.1 can be written as:

$$\chi_{c,(a)} = \chi_{a,(b)} \succ \chi_{b,(c)}. \tag{1}$$

2. INTRODUCING THE $\mathcal{T}(\mathbb{T}, \succ)$ ALGEBRA

Aiming at a group algebra that succinctly transforms also velocities and accelerations, we introduce the group $\mathcal{T}^{\mathsf{SO}}(\mathbb{T}^{\mathsf{SO}}, \succ)$ whose non-abelian operator $\succ$, with arity $\bar{\alpha} = 2$, acts over the manifold $\mathbb{T}^{\mathsf{SO}} = \{\mathbb{R}^3 \rtimes \mathsf{SO}(3) \rtimes \mathbb{R}^6 \rtimes \mathbb{R}^6\}$.

Each element $\chi \in \mathbb{T}^{\mathsf{SO}}$ of the group represent a coordinate frame in space, including position, rotation, speed and acceleration information.

We parametrize $\mathsf{SO}(3)$ with unitary quaternions $\mathbf{q} \in \mathsf{S}^3$, i.e. $\mathbf{q} \in \mathbb{H}_1$, for performance reasons. An issue is that S^3 is not exactly isomorphic to $\mathsf{SO}(3)$, being its double cover, but this is not a real problem: the only drawback is that there are two distinct quaternions per a single rotation. In the end we can rather work with an epimorphism of $\mathcal{T}^{\mathsf{SO}}(\mathbb{T}^{\mathsf{SO}}, \succ)$, that is $\mathcal{T}(\mathbb{T}, \succ)$, using quaternions: $\mathbb{T} = \{\mathbb{R}^3 \rtimes \mathsf{S}^3 \rtimes \mathbb{R}^6 \rtimes \mathbb{R}^6\}$..

The speed of the origin of the frame is denoted with $\dot{\mathbf{r}} \in \mathbb{R}^3$, the angular speed is denoted with $\omega \in \mathbb{R}^3$. Acceleration is $\ddot{\mathbf{r}}$ and angular acceleration is α. Note, we decide to express ω and α in the basis of the moving frame. Finally, we introduce $\chi \in \mathbb{T}$ for $\mathbf{r} \in \mathbb{R}^3$, $\mathbf{q} \in \mathsf{S}^3$, $\dot{\mathbf{r}}, \omega, \ddot{\mathbf{r}}, \alpha \in \mathbb{R}^3$, as :

$$\chi = \{\mathbf{r}, \mathbf{q}, \dot{\mathbf{r}}, \omega, \ddot{\mathbf{r}}, \alpha\}.$$

For readability, assuming that position, rotation, speed and acceleration of a frame a in χ_a are expressed relative to another frame b, we will use the notation $\chi_{a,(b)}$. The definition of the $\succ$ operation follows from the requirement that

$$\begin{array}{ccccc} \chi_{a,(c)} = & & \chi_{a,(b)} \succ & & \chi_{b,(c)} \\ \left\{ \begin{array}{c} \mathbf{r}_{a,(c)} \\ \mathbf{q}_{a,(c)} \\ \dot{\mathbf{r}}_{a,(c)} \\ \omega_{a,(c)} \\ \ddot{\mathbf{r}}_{a,(c)} \\ \alpha_{a,(c)} \end{array} \right\} & = & \left\{ \begin{array}{c} \mathbf{r}_{a,(b)} \\ \mathbf{q}_{a,(b)} \\ \dot{\mathbf{r}}_{a,(b)} \\ \omega_{a,(b)} \\ \ddot{\mathbf{r}}_{a,(b)} \\ \alpha_{a,(b)} \end{array} \right\} & \succ & \left\{ \begin{array}{c} \mathbf{r}_{b,(c)} \\ \mathbf{q}_{b,(c)} \\ \dot{\mathbf{r}}_{b,(c)} \\ \omega_{b,(c)} \\ \ddot{\mathbf{r}}_{b,(c)} \\ \alpha_{b,(c)} \end{array} \right\} \end{array} \tag{2}$$

In the remaining paragraphs we develop the expressions for the terms in Eq.(2).

2.1 Position and rotation

As known [5], quaternion morphisms $\mathbf{q}_r^o = \mathbf{q}_e \mathbf{q}_r \mathbf{q}_e^*$ can be used to rotate points in space, with rotation represented in form of Euler parameters $\mathbf{q}_e$ and $\mathbf{q}_r = \mathbb{I}(\mathbf{r}) \equiv \{0, r_x, r_y, r_z\}$ being a *pure* quaternion with imaginary part as the cartesian coordinates of a point.

Hence the affine transformation of the point $\mathbf{r}_{a,(b)}$ after rotation $\mathbf{q}_{b,(c)}$ and translation $\mathbf{r}_{b,(c)}$ can be expressed as:

$$\mathbb{I}(\mathbf{r}_{a,(c)}) = \mathbb{I}(\mathbf{r}_{b,(c)}) + \mathbf{q}_{b,(c)} \mathbb{I}(\mathbf{r}_{a,(b)}) \mathbf{q}_{b,(c)}^*. \tag{3}$$

This Eq.(3) has a counterpart in linear algebra:

$$\mathbf{r}_{a,(c)} = \mathbf{r}_{b,(c)} + [A(\mathbf{q}_{b,(c)})] \mathbf{r}_{a,(b)}. \tag{4}$$

where we introduced the rotation matrix $[A(\mathbf{q}_{b,(c)})]$ function of a quaternion $\mathbf{q}_{b,(c)}$.

The term $\mathbf{q}_{a,(c)}$, representing the rotation of the reference a respect to the reference c, can be easily obtained with a single quaternion product:

$$\mathbf{q}_{a,(c)} = \mathbf{q}_{b,(c)} \mathbf{q}_{a,(b)} \tag{5}$$

2.2 Velocity

Speed terms $\dot{\mathbf{r}}_{a,(c)}$ and $\omega_{a,(c)}$ can be obtained from symbolic differentiation of Eq.(3) and Eq.(5):

$$\begin{aligned} \dot{\mathbb{I}}(\mathbf{r}_{a,(c)}) =& \dot{\mathbb{I}}(\mathbf{r}_{b,(c)}) + \dot{\mathbf{q}}_{b,(c)} \mathbb{I}(\mathbf{r}_{a,(b)}) \mathbf{q}_{b,(c)}^* + \\ & \mathbf{q}_{b,(c)} \dot{\mathbb{I}}(\mathbf{r}_{a,(b)}) \mathbf{q}_{b,(c)}^* + \mathbf{q}_{b,(c)} \mathbb{I}(\mathbf{r}_{a,(b)}) \dot{\mathbf{q}}_{b,(c)}^* \\ \dot{\mathbb{I}}(\mathbf{r}_{a,(c)}) =& \dot{\mathbb{I}}(\mathbf{r}_{b,(c)}) + 2\dot{\mathbf{q}}_{b,(c)} \mathbb{I}(\mathbf{r}_{a,(b)}) \mathbf{q}_{b,(c)}^* + \\ & \mathbf{q}_{b,(c)} \dot{\mathbb{I}}(\mathbf{r}_{a,(b)}) \mathbf{q}_{b,(c)}^* \end{aligned}$$

We note that $\dot{\mathbb{I}}(\mathbf{r}) = \mathbb{I}(\dot{\mathbf{r}})$, hence we get:

$$\begin{aligned} \mathbb{I}(\dot{\mathbf{r}}_{a,(c)}) =& \mathbb{I}(\dot{\mathbf{r}}_{b,(c)}) + 2\dot{\mathbf{q}}_{b,(c)} \mathbb{I}(\mathbf{r}_{a,(b)}) \mathbf{q}_{b,(c)}^* + \\ & \mathbf{q}_{b,(c)} \mathbb{I}(\dot{\mathbf{r}}_{a,(b)}) \mathbf{q}_{b,(c)}^*. \end{aligned} \tag{6}$$

Then we differentiate also Eq.(5):

$$\dot{\mathbf{q}}_{a,(c)} = \dot{\mathbf{q}}_{b,(c)}\mathbf{q}_{a,(b)} + \mathbf{q}_{b,(c)}\dot{\mathbf{q}}_{a,(b)}. \tag{7}$$

The angular velocity $\omega_{a,(c)}$ of $\chi_{a,(c)}$, expressed in the coordinates of reference a, follows the quaternion derivative $\dot{\mathbf{q}}_{a,(c)}$ obtained with Eq.(7) using the following formula:

$$\mathbb{I}(\omega_{a,(c)}) = 2\mathbf{q}^*_{a,(c)}\dot{\mathbf{q}}_{a,(c)}. \tag{8}$$

2.3 Acceleration

By differentiation of Eq.(6):

$$\begin{aligned}
\ddot{\mathbb{I}}(\mathbf{r}_{a,(c)}) =& \ddot{\mathbb{I}}(\mathbf{r}_{b,(c)}) + \\
& 2\ddot{\mathbf{q}}_{b,(c)}\mathbb{I}(\mathbf{r}_{a,(b)})\mathbf{q}^*_{b,(c)} + \\
& 2\dot{\mathbf{q}}_{b,(c)}\dot{\mathbb{I}}(\mathbf{r}_{a,(b)})\mathbf{q}^*_{b,(c)} + \\
& 2\dot{\mathbf{q}}_{b,(c)}\mathbb{I}(\mathbf{r}_{a,(b)})\dot{\mathbf{q}}^*_{b,(c)} + \\
& + \dot{\mathbf{q}}_{b,(c)}\dot{\mathbb{I}}(\mathbf{r}_{a,(b)})\mathbf{q}^*_{b,(c)} + \\
& \mathbf{q}_{b,(c)}\ddot{\mathbb{I}}(\mathbf{r}_{a,(b)})\mathbf{q}^*_{b,(c)} + \\
& \mathbf{q}_{b,(c)}\dot{\mathbb{I}}(\mathbf{r}_{a,(b)})\dot{\mathbf{q}}^*_{b,(c)} \\
=& \ddot{\mathbb{I}}(\mathbf{r}_{b,(c)}) + \\
& 2\ddot{\mathbf{q}}_{b,(c)}\mathbb{I}(\mathbf{r}_{a,(b)})\mathbf{q}^*_{b,(c)} + \\
& 4\dot{\mathbf{q}}_{b,(c)}\dot{\mathbb{I}}(\mathbf{r}_{a,(b)})\mathbf{q}^*_{b,(c)} + \\
& + 2\dot{\mathbf{q}}_{b,(c)}\mathbb{I}(\mathbf{r}_{a,(b)})\dot{\mathbf{q}}^*_{b,(c)} + \\
& \mathbf{q}_{b,(c)}\ddot{\mathbb{I}}(\mathbf{r}_{a,(b)})\mathbf{q}^*_{b,(c)}
\end{aligned}$$

and finally, as $\ddot{\mathbb{I}}(\mathbf{r}_{a,(c)}) = \mathbb{I}(\ddot{\mathbf{r}}_{a,(c)})$, it is:

$$\begin{aligned}
\mathbb{I}(\ddot{\mathbf{r}}_{a,(c)}) =& \mathbb{I}(\ddot{\mathbf{r}}_{b,(c)}) + 2\ddot{\mathbf{q}}_{b,(c)}\mathbb{I}(\mathbf{r}_{a,(b)})\mathbf{q}^*_{b,(c)} + \\
& 4\dot{\mathbf{q}}_{b,(c)}\mathbb{I}(\dot{\mathbf{r}}_{a,(b)})\mathbf{q}^*_{b,(c)} + \\
& + 2\dot{\mathbf{q}}_{b,(c)}\mathbb{I}(\mathbf{r}_{a,(b)})\dot{\mathbf{q}}^*_{b,(c)} + \\
& \mathbf{q}_{b,(c)}\mathbb{I}(\ddot{\mathbf{r}}_{a,(b)})\mathbf{q}^*_{b,(c)}
\end{aligned} \tag{9}$$

Angular acceleration, in quaternion space, follows the differentiation of the epression of Eq.(7):

$$\begin{aligned}
\ddot{\mathbf{q}}_{a,(c)} =& \ddot{\mathbf{q}}_{b,(c)}\mathbf{q}_{a,(b)} + \dot{\mathbf{q}}_{b,(c)}\dot{\mathbf{q}}_{a,(b)} + \\
& \dot{\mathbf{q}}_{b,(c)}\dot{\mathbf{q}}_{a,(b)} + \mathbf{q}_{b,(c)}\ddot{\mathbf{q}}_{a,(b)} \\
=& \ddot{\mathbf{q}}_{b,(c)}\mathbf{q}_{a,(b)} + 2\dot{\mathbf{q}}_{b,(c)}\dot{\mathbf{q}}_{a,(b)} + \mathbf{q}_{b,(c)}\ddot{\mathbf{q}}_{a,(b)}
\end{aligned} \tag{10}$$

As a vector, the angular acceleration $\alpha_{a,(c)}$ of $\chi_{a,(c)}$, is obtained from the quaternion $\ddot{\mathbf{q}}_{a,(c)}$ of Eq.(10) and from the differentiation of Eq.(8):

$$\mathbb{I}(\alpha_{a,(c)}) = 2\dot{\mathbf{q}}^*_{a,(c)}\dot{\mathbf{q}}_{a,(c)} + 2\mathbf{q}^*_{a,(c)}\ddot{\mathbf{q}}_{a,(c)} \tag{11}$$

3. SOME PROPERTIES OF THE $\mathcal{T}(\mathbb{T}, \succ)$ ALGEBRA

In the following we present two theorems showing the fact that, as a Lie group, $\mathcal{T}(\mathbb{T}, \succ)$ has a neutral element and an inverse element.

THEOREM 1

The $\mathcal{T}(\mathbb{T}, \succ)$ algebra has an identity element $\chi_I \in \mathbb{T}$.

(Proof omitted for compactness)

Note: the $\mathcal{T}(\mathbb{T}, \succ)$ magma has both right and left-neutral elements, so it is also a monoid with $\chi_b \succ \chi_I = \chi_I \succ \chi_b = \chi_b$.

The proof of the following theorem is also useful to get an explicit expression for the inverse element. Moreover, as expected, the commutative property does not hold:

THEOREM 2

The $\mathcal{T}(\mathbb{T}, \succ)$ algebra is a non-abelian group.

Proof.

For the $\mathcal{T}(\mathbb{T}, \succ)$ monoid algebra to be a group, each element χ must have an inverse element χ^{-1} such that $\chi^{-1} \succ \chi = \chi_I$, where χ_I is the neutral elment introduced in Theorem 1.

For semplicity, let's recall the notation of the product in Eq.(2). If $\chi_{a,(b)} \succ \chi_{b,(c)} = \chi_I$, then $\chi_{a,(b)}$ is the left-inverse of $\chi_{b,(c)}$, and will be denoted as $\chi^{-1L}_{b,(c)}$. Also, $\chi_{b,(c)}$ is the right-inverse of $\chi_{a,(b)}$, and will be denoted as $\chi^{-1R}_{a,(b)}$. Thus, if right and left inverses exist,

$$\chi_{a,(b)} \succ \chi^{-1R}_{a,(b)} = \chi_I, \quad \chi^{-1L}_{b,(c)} \succ \chi_{b,(c)} = \chi_I$$

Imposing $\chi_{a,(c)} = \chi_I$ in the product of Eq.(2), one can write $\chi_{a,(b)} \succ \chi_{b,(c)} = \chi_I$, then it will be possible to manipulate the definitions in Eq.(3-10) to find the expression of the left-inverse by explicitating the terms belonging to $\chi_{a,(b)}$.

Let start from the transformation of positions. We rewrite Eq.(3) as:

$$\mathbb{I}(\mathbf{r}_{b,(c)}) + \mathbf{q}_{b,(c)} \mathbb{I}(\mathbf{r}_{a,(b)}) \mathbf{q}^*_{b,(c)} = \mathbb{I}(\mathbf{0}).$$

Let left-multiply all terms by quaternion $\mathbf{q}^{-1}_{b,(c)}$ and right-multiply all terms by $\mathbf{q}^{*-1}_{b,(c)}$. By remembering quaternion algebra properties $\mathbf{q}\mathbf{q}^{-1} = \{1,0,0,0\}$ and $\mathbf{q}\{1,0,0,0\} = \mathbf{q}$, $\mathbf{q} \in \mathbb{H}_1$, it is easy to find:

$$\mathbb{I}(\mathbf{r}_{a,(b)}) = -\mathbf{q}^{-1}_{b,(c)} \mathbb{I}(\mathbf{r}_{b,(c)}) \mathbf{q}^{*-1}_{b,(c)}. \tag{12}$$

This is the first element of the left-inverse vector, that in our proof is $\chi_{a,(b)} = \chi^{-1L}_{b,(c)}$.

Coming to rotations, remembering that the rotation part $\mathbf{q}$ in the neutral element χ_I is the unit quaternion $\{1,0,0,0\}$ as demonstrated in Theorem 1, we rewrite Eq.(5) as follows:

$$\mathbf{q}_{b,(c)} \mathbf{q}_{a,(b)} = \{1,0,0,0\}.$$

Therefore, using quaternion inverses, premultiplying the terms by $\mathbf{q}_{b,(c)}^{-1}$ and simplifying, one gets the rotational part of the left-inverse:

$$\mathbf{q}_{a,(b)} = \mathbf{q}_{b,(c)}^{-1}. \tag{13}$$

Now set Eq.(6) to zero in order to compute the speed part of the inverse:

$$\begin{aligned}&\mathbb{I}(\dot{\mathbf{r}}_{b,(c)}) + 2\dot{\mathbf{q}}_{b,(c)}\mathbb{I}(\mathbf{r}_{a,(b)})\mathbf{q}_{b,(c)}^{*} + \\ &\mathbf{q}_{b,(c)}\mathbb{I}(\dot{\mathbf{r}}_{a,(b)})\mathbf{q}_{b,(c)}^{*} = \mathbb{I}(\mathbf{0})\end{aligned}$$

Here, few manipulations with quaternion algebra will produce the following result:

$$\begin{aligned}\mathbb{I}(\dot{\mathbf{r}}_{a,(b)}) =&\mathbf{q}_{b,(c)}^{-1}(-\mathbb{I}(\dot{\mathbf{r}}_{b,(c)}) + \\ &2\dot{\mathbf{q}}_{b,(c)}\mathbf{q}_{b,(c)}^{-1}\mathbb{I}(\mathbf{r}_{b,(c)}))\mathbf{q}_{b,(c)}^{*-1}.\end{aligned} \tag{14}$$

Also, imposing that $\dot{\mathbf{q}}_{a,(c)}$ is null in Eq.(7), it follows:

$$\dot{\mathbf{q}}_{a,(b)} = -\mathbf{q}_{b,(c)}^{-1}\dot{\mathbf{q}}_{b,(c)}\mathbf{q}_{b,(c)}^{-1}. \tag{15}$$

With similar algebraic manipulations, and remembering that $\mathbf{q}^{*-1}\mathbf{q}^{*} = \{1,0,0,0\}$, one can get the accleration part of the left inverse, obtaining:

$$\begin{aligned}\mathbb{I}(\ddot{\mathbf{r}}_{a,(b)}) =&\mathbf{q}_{b,(c)}^{-1}[-\mathbb{I}(\ddot{\mathbf{r}}_{b,(c)}) + 2\ddot{\mathbf{q}}_{b,(c)}\mathbf{q}_{b,(c)}^{-1}\mathbb{I}(\mathbf{r}_{b,(c)}) \\ &+ 4\dot{\mathbf{q}}_{b,(c)}\mathbf{q}_{b,(c)}^{-1}(\mathbb{I}(\dot{\mathbf{r}}_{b,(c)}) \\ &- 2\dot{\mathbf{q}}_{b,(c)}\mathbf{q}_{b,(c)}^{-1}\mathbb{I}(\mathbf{r}_{b,(c)})) \\ &+ 2\dot{\mathbf{q}}_{b,(c)}\mathbf{q}_{b,(c)}^{-1}\mathbb{I}(\mathbf{r}_{b,(c)})\mathbf{q}_{b,(c)}^{-1}\dot{\mathbf{q}}_{b,(c)}^{*}]\mathbf{q}_{b,(c)}^{*-1}\end{aligned}$$

and

$$\ddot{\mathbf{q}}_{a,(b)} = \mathbf{q}_{b,(c)}^{-1}(\ddot{\mathbf{q}}_{b,(c)} - 2\dot{\mathbf{q}}_{b,(c)}\mathbf{q}_{b,(c)}^{-1}\dot{\mathbf{q}}_{b,(c)})\mathbf{q}_{b,(c)}^{-1}. \tag{16}$$

Finally, using Eq.(8) and Eq.(11), one can merge Eq.(12-16) into $\chi_{a,(b)}$, that is the left-inverse $\chi_{b,(c)}^{-1L}$ which satisfies $\chi_{a,(b)} \succ \chi_{b,(c)} = \chi_{b,(c)}^{-1L} \succ \chi_{b,(c)} = \chi_I$.

Similarly, we could solve $\chi_{a,(b)} \succ \chi_{b,(c)} = \chi_I$ for $\chi_{b,(c)}$: after symbolic manipulation (not reported here) we would obtain the same results of Eq.(12-16), but with inverted subscripts, that is with $a,(b)$ swapped with $b,(c)$. Therefore, we built the right-inverse $\chi_{a,(b)}^{-1R}$ and we conclude that, for a generic element $\chi \in \mathbb{T}$, right- and left-inverses are the same, that is $\chi^{-1R} = \chi^{-1L} = \chi^{-1}$. Since there is the inverse, the algebra is a group. QED.

A remark: although associative, the group is non-abelian since the $\succ$ operation is non commutative.

4. SOFTWARE IMPLEMENTATION

We implemented a C++ library that implements the above discussed approach to coordinate transformations. We exploit the object oriented paradigm, hence χ elements are represented by objects inherited from a C++ class. We called this class `ChMovingFrame`. In detail, each `ChMovingFrame` object contains three vectors, three quaternions and an auxiliary

3x3 matrix (the latter is redundant, given the $\mathbf{q}$ quaternion, but it allows speeding up some computations in special cases):

$$\chi_{c++} = \{\mathbf{r}, \mathbf{q}, [A(\mathbf{q})], \dot{\mathbf{r}}, \dot{\mathbf{q}}, \ddot{\mathbf{r}}, \ddot{\mathbf{q}}\}.$$

For such class, we overloaded C++ binary and unary operators; this allows us to express group products using a simple syntax.

The following operators have been implemented:

- The $\cdot$ right-to-left transformation is mapped to the $\star$ operator, so that $\chi_c = \chi_a \cdot \chi_b$ is becomes `c = a * b`.
- The $\succ$ left-to-right transformation is mapped to the >> operator, so that $\chi_c = \chi_a \succ \chi_b$ becomes `c = a >> b`.
- The $\star$= on-place operator has been used for an efficient implementation of self right-multiplication, so $\chi_a := \chi_a \cdot \chi_b$ becomes `a*=b`,
- The >>= on-place operator has been used for an efficient implementation of self left-multiplication, so $\chi_a := \chi_a \succ \chi_b$ becomes `a>>=b`,
- The inversion χ^{-1} is implemented in C++ language by redefining the `!` unary operator,
- The vector-by-frame *heterogeneous* binary operators are implemented, for example as in `v_a = v_b >> frame`, or `v_a = frame * v_b`.

For instance if one must transform a simple point through two frames in sequence using a single line of C++ code, one would type:

```
v_a = frame2 * frame1 * v_b
```

or

```
v_a = v_b >> frame1 >> frame2
```

Therefore the example of Eq.(1), shown in Fig.1, could be written with the following lines of code:

```
ChMovingFrame<> cs_30, cs_32, cs_21, cs_10;
cs_10.coord.pos = ChVector<>(2,4,1);
... etc ...
cs_30 = cs_32 >> cs_21 >> cs_10;
```

We also implemented the $(\cdot)^{-1}$ operation by overloading the `!` C++ unary operator. This requires the in-place evaluation of Eq.(12-16). Thank to this inversion operator, it is possible, in example of Fig.1, to obtain `cs_32` if other frames are known: we multiply both sides by `!cs_10` and `!cs_21`, and we simply write

```
cs_32 = cs_30 >> !cs_10 >> !cs_21;
```

The libraries for the $\mathcal{T}$ algebra has been extensively used in our Project Chrono C++ library for multi body simulation [6] [7]. After testing and profiling we got satisfying results in terms of clean code, ease of development and fast computation. Such a library has been successfully used in various engineering projects by many programmers and users.

5. SEMANTICS

If we follow the abovementioned notation, where second subscript of an element represents the frame to whom the coordinates are expressed, one can see that the subscripts of the elements in the expressions must be chained.

For instance, in $\chi_{3,(0)} = \chi_{3,(2)} \succ \chi_{2,(1)} \succ \chi_{1,(0)}$ the two operands share respectively the second subscript and the first subscript, and the result has the remaining two subscripts, respectively the first of the first operand, and the second of the second operand.

This property can be used to implement an additional, optional functionality that takes care of validating if the programmer is writing transformations that make sense.

This is a set of semantic rules:

- Right to left transformation:
  $\chi_{c,(a)} = \chi_{b,(a)} \cdot \chi_{c,(b)}$
  (the (b) subscript must match the b subscript, and the result gets the remaining two subscripts c and (a), in reverse order).

- Left to right transofrmation:
  $\chi_{c,(a)} = \chi_{c,(b)} \succ \chi_{b,(a)}$
  (the (b) subscript must match the b subscript, and the result gets the remaining two subscripts c and (a), in exact order).

- Inversion:
  $\chi_{b,(a)} = \chi_{a,(b)}^{-1}$
  (the a and (b) subscripts are swapped to b and (a)).

Note that a semantic check can be enforced either at run-time, using tests on subscripts as transient data, or even at compile-time using static asserts and template metaprogramming, wiht zero overhead on CPU time.

6. EXAMPLE

Figure 2 depicts an industrial robot and a conveyor belt. Assume that one must compute the position, speed and acceleration of an item on a conveyor belt respect to the end effector, assuming that position, speed and acceleration of the item (frame n.8) is known respect to the conveyor belt (frame n.7), and all frames of the parts of the robot are known respect to the previous joint (frame n.0). Using the $\mathcal{T}$ algebra, we can instantly compute position, rotation, velocity, angular velocity, acceleration, angular acceleration of frame n.8 respect to frame n.6 using a single expression:

$$\chi_{8,(6)} = \chi_{8,(7)} \succ \chi_{7,(0)} \succ \chi_{1,(0)}^{-1} \succ \chi_{2,(1)}^{-1} \succ \chi_{3,(2)}^{-1} \succ \chi_{4,(3)}^{-1} \succ \chi_{5,(4)}^{-1} \succ \chi_{6,(5)}^{-1}$$

Similarly, one could write instead:

$$\chi_{8,(6)} = \chi_{8,(7)} \succ \chi_{7,(0)} \succ (\chi_{6,(5)} \succ \chi_{5,(4)} \succ \chi_{4,(3)} \succ \chi_{3,(2)} \succ \chi_{2,(1)} \succ \chi_{1,(0)})^{-1}$$

that is, by doing the product of two groups of factors, also:

$$\chi_{8,(6)} = \chi_{8,(0)} \succ \chi_{6,(0)}^{-1} = \chi_{8,(0)} \succ \chi_{0,(6)}$$

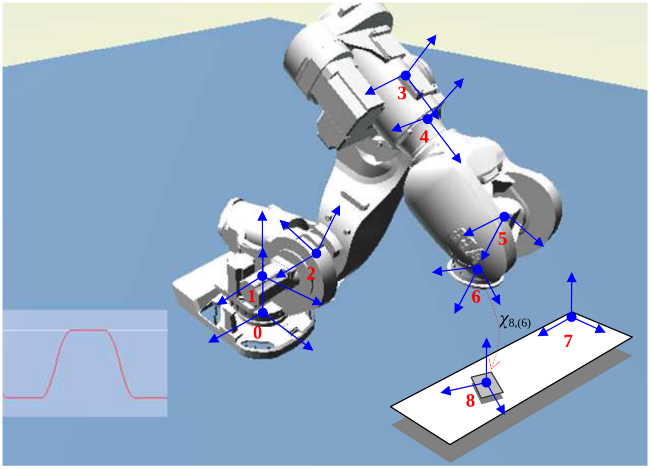

Figure 2. Example. Computing position, speed and acceleration of an item on a conveyor belt, respect to an end effector.

7. CONCLUSION

We introduced the $\mathcal{T}(\mathbb{T}, \succ)$ algebra as a compact formalism that represents kinematic transformations. Thanks to the operator-overloading capabilities of the C++ language, this formal framework maps well into a software implementation. In detail, this algebra is implemented in our open source library Project Chrono.

REFERENCES

[1] Hervé, J., 1994. "The mathematical group structure of the set of displacements". *Mechanism and Machine Theory,* **29**(1), pp. 73 – 81.

[2] Legnani, G., Casolo, F., Righettini, P., and Zappa, B., 1996. "A homogeneous matrix approach to 3d kinematics and dynamics–ii. applications to chains of rigid bodies and serial manipulators". *Mechanism and Machine Theory,* **31**(5), pp. 589 – 605.

[3] H. Sutter, A. A., 2004. *C++ Coding Standards: 101 Rules, Guidelines, and Best Practices*. Addison-Wesley, New York.

[4] Tasora, A., and Righettini, P., 2003. "Sliding contact between freeform surfaces". *Multibody System Dynamics,* **10**(3), pp. 239–262.

[5] Shabana, A., 1989. *Multibody Systems*. John Wiley and Sons, New York.

[6] Tasora, A., 2011. Chrono::engine project, web page.

[7] Tasora, A., and Anitescu, M., 2011. "A matrix-free cone complementarity approach for solving large-scale, nonsmooth, rigid body dynamics". *Computer Methods in Applied Mechanics and Engineering,* **200**(5-8), pp. 439 – 453.

A MESHLESS APPROACH IN FLEXIBLE MULTIBODY SYSTEM MODELLING

Giuseppe Catania
Department of Industrial Engineering,
University of Bologna, Italy
E-mail: giuseppe.catania@unibo.it

Alessandro Zanarini
Department of Industrial Engineering,
University of Bologna, Italy
E-mail: a.zanarini@unibo.it

Abstract. *Flexible multibody dynamics is often approached in case of small flexible deformations by means of the finite-element modelling method in component mode synthesis techniques. In these approaches the size of the motion equations can be high or the general description can be poor.*
In this paper a linearly independent set of shape functions is introduced to continuously model the flexible components of local reference displacements as a superposition of shape functions; a novel formulation of the flexible properties of beam-like components then follows, with a reduced size motion equation set and no restriction in the geometrical model. All of the modelling aspects, such as kinematics, inertia and stiffness distribution and generalised forces, are extensively discussed. Test cases prove the effectiveness of the proposed approach.

Keywords: *flexible multibody, meshless flexible components, flexible floating frame, shape functions*

1. INTRODUCTION

In [1] different approaches are discussed, leaving the classical FE modelling approach as a viable method to include flexibility. In many flexible multibody dynamics approaches for small local deflections the Craig-Bampton [2] reduction scheme has been adopted to take into account the flexibility of bodies, once a proper linear FE model has produced the reduced set of component modes. Craig-Bampton approach might not be efficient, since for every dof of the constraint subset the restraining statical modeshapes need to be added to the base of fixed-constraint flexible shapes; therefore, the number of statical modeshapes rapidly increases with the spatial discretisation of the constraint interfaces, with a multiplicity 3 in planar systems and 6 in three dimensional systems for each FE node, with associated high computational costs. Furthermore, the proper selection of the effective dynamic modeshapes to be included in the reduced set requires a highly skilled attention, becoming a kind of art of trained personnel. While the authors have already worked on kinematics dependant models of mechanisms [3–8], where the elasticity was lumped mainly in between the rigid parts, the approach here presented is focused on modelling the inner elasticity of each moving parts, giving a relevant contribution on the whole system behaviour in the time domain.

2. KINEMATICAL CONSTRAINTS WITH RIGID BODIES

In the present paper the planar dynamics of multibody systems will be modelled, recalling the formalism introduced in literature [9–11]. The generalised coordinates of the i-th floating frame are $\mathbf{q}_i = [x_i, y_i, \phi_i]^T = \left[{\mathbf{r}^O_{G,i}}^T, \phi_i\right]^T$. The position $\mathbf{r}^P_{G,i}$ of a point P on the i-th rigid body in the global coordinate system can be described by:

$$\mathbf{r}^P_{G,i} = \mathbf{r}^O_{G,i} + \mathbf{A}_i \mathbf{s}^P_{O,i}, \tag{1}$$

where $\mathbf{A}_i$ is the 2x2 matrix of the rotational transform, defined in [9–11] by means of the rotation angle ϕ_i:

$$\mathbf{A}_i = \begin{bmatrix} cos(\phi_i) & -sin(\phi_i) \\ sin(\phi_i) & cos(\phi_i) \end{bmatrix}, \tag{2}$$

$\mathbf{r}_{O,i}$ is the centroid location of i-th body, while $\mathbf{s}^P_{O,i}$ is the constant (undeformed) vector in the i-th floating reference frame to locate a point P in respect to the reference origin O_i on the i-th body. For a 90 degrees rotation there follows the orthogonal transform **R**:

$$\mathbf{R} = \begin{bmatrix} 0 & -1 \\ 1 & 0 \end{bmatrix}. \tag{3}$$

If the rotation transform $\mathbf{A}_i$ is derived against ϕ_i, $\mathbf{B}_i$ results in:

$$\mathbf{B}_i = \begin{bmatrix} -sin(\phi_i) & -cos(\phi_i) \\ cos(\phi_i) & -sin(\phi_i) \end{bmatrix}. \tag{4}$$

Revolute joint

The *revolute joint* constraints in the plane is realised by imposing single point coincidence between two points P_i & Q_j belonging to different bodies:

$$\mathbf{\Phi}_{rev} = \mathbf{r}^P_{G,i} - \mathbf{r}^Q_{G,j}. \tag{5}$$

The Jacobian of the revolute joint constraint can be expressed as:

$$\frac{\partial \mathbf{\Phi}_{rev}}{\partial \mathbf{q}_i} = \begin{bmatrix} \mathbf{I} & \mathbf{B}_i \mathbf{s}^P_{O,i} \end{bmatrix}, \tag{6}$$

$$\frac{\partial \mathbf{\Phi}_{rev}}{\partial \mathbf{q}_j} = \begin{bmatrix} -\mathbf{I} & -\mathbf{B}_j \mathbf{s}^Q_{O,j} \end{bmatrix}, \tag{7}$$

and $\mathbf{\Gamma}_{rev} = -\frac{\partial}{\partial \mathbf{q}}\left(\frac{\partial \mathbf{\Phi}}{\partial \mathbf{q}}\dot{\mathbf{q}}\right)\dot{\mathbf{q}} = \mathbf{A}_i \mathbf{s}^P_{O,i} \dot{\phi_i}^2 - \mathbf{A}_j \mathbf{s}^P_{O,j} \dot{\phi_j}^2$.

3. GENERALISED FORCES APPLIED ON RIGID BODIES

External forces

An external force applied to a generic point P_i on the i-th body gives rise to the following work:

$$W_{\mathbf{F}_{G,P_i}} = \mathbf{F}_{G,P_i}^T \mathbf{r}_{G,i}^P = \mathbf{F}_{G,P_i}^T (\mathbf{r}_{O,i} + \mathbf{A}_i \mathbf{s}_{O,i}^P) = -U_{\mathbf{F}_{G,P_i}}, \tag{8}$$

where $U_{\mathbf{F}_{G,P_i}}$ is the potential of the external force $\mathbf{F}_{G,P_i}$. By deriving the former expression with regards to the generalised coordinates, there follows:

$$\frac{\partial U_{\mathbf{F}_{G,P_i}}}{\partial \mathbf{q}_i} = -\mathbf{F}_{G,P_i}^T \begin{bmatrix} \mathbf{I} & \mathbf{B}_i \mathbf{s}_{O,i}^P \end{bmatrix} = -\mathbf{Q}_{\mathbf{F}_{G,P_i}}^T, \tag{9}$$

with $\mathbf{Q}_{\mathbf{F}_{G,P_i}}^T$ as the generalised force vector on the $\mathbf{q}_i$ coordinates.

Linear spring-damper-component between bodies

When the linear device is linked to two points P_i and P_j on distinct bodies i and j, the force acting on the bodies can be expressed as follows:

$$f = k_l(l - l_0) + c_l \dot{l} + F(l, \dot{l}, p), \tag{10}$$

where k_l, c_l and l_0 are the stiffness constant, the damping constant and length of the free spring, l is the magnitude of the distance between P_i and P_j and $F(l, \dot{l}, p)$ is the actuating function freely defined and imposed. Being $\mathbf{d}_{ij} = \mathbf{r}_{O,j} + \mathbf{A}_j \mathbf{s}_{O,j}^P - \mathbf{r}_{O,i} - \mathbf{A}_i \mathbf{s}_{O,i}^P$ the segment of relative distance between the points P_i and P_j, and its time derivative $\dot{\mathbf{d}}_{ij} = \dot{\mathbf{r}}_{O,j} + \mathbf{B}_j \mathbf{s}_{O,j}^P \dot{\phi}_j - \dot{\mathbf{r}}_{O,i} - \mathbf{B}_i \mathbf{s}_{O,i}^P \dot{\phi}_i$, the magnitude of the relative distance and the velocity take the following shapes:

$$l = \sqrt{\mathbf{d}_{ij}^T \mathbf{d}_{ij}}, \tag{11}$$

$$\dot{l} = \frac{\mathbf{d}_{ij}^T}{l} \dot{\mathbf{d}}_{ij} = \hat{\mathbf{d}}_{ij}^T \dot{\mathbf{d}}_{ij}. \tag{12}$$

The generalised forces acting on body i and j are therefore:

$$\mathbf{Q}_i^T = f \hat{\mathbf{d}}_{ij}^T \begin{bmatrix} \mathbf{I} & \mathbf{B}_i \mathbf{s}_{O,i}^P \end{bmatrix}, \tag{13}$$

$$\mathbf{Q}_j^T = -f \hat{\mathbf{d}}_{ij}^T \begin{bmatrix} \mathbf{I} & \mathbf{B}_j \mathbf{s}_{O,j}^P \end{bmatrix}. \tag{14}$$

4. MOTION EQUATIONS WITH RIGID BODIES

With L being the *Lagrangian function*, the motion equations of unconstrained bodies can be formulated as follows:

$$\frac{d}{dt}\left(\frac{\partial L}{\partial \dot{\mathbf{q}}}\right) - \frac{\partial L}{\partial \mathbf{q}} = \mathbf{0}, \tag{15}$$

while for constrained motion, by means of *Lagrangian multipliers* $\mathbf{\Lambda}$ there follows:

$$\frac{d}{dt}\left(\frac{\partial L}{\partial \dot{\mathbf{q}}}\right) - \frac{\partial L}{\partial \mathbf{q}} + \left(\frac{\partial \mathbf{\Phi}}{\partial \mathbf{q}}\right)^T \mathbf{\Lambda} = \mathbf{0}, \tag{16}$$

which can be rewritten if the *Lagrangian function* is explicitly highlighted in its kinetic T and potential energy U contributions, once no potentials U depend on generalised velocities and time:

$$\frac{d}{dt}\left(\frac{\partial T}{\partial \dot{\mathbf{q}}}\right) - \frac{\partial T}{\partial \mathbf{q}} + \left(\frac{\partial \mathbf{\Phi}}{\partial \mathbf{q}}\right)^T \mathbf{\Lambda} = -\frac{\partial U}{\partial \mathbf{q}}. \tag{17}$$

As expressed in paragraphs 3., the potentials can be related to the generalised forces, thus coming to the final form of the motion equations:

$$\frac{d}{dt}\left(\frac{\partial T}{\partial \dot{\mathbf{q}}}\right) - \frac{\partial T}{\partial \mathbf{q}} + \left(\frac{\partial \mathbf{\Phi}}{\partial \mathbf{q}}\right)^T \mathbf{\Lambda} = \mathbf{Q}^a, \tag{18}$$

where $\mathbf{Q}^a$ is the sum of generalised force vectors applied to the bodies.

The motion equations in Eqs.18 have to be fulfilled together with the constraint equations $\mathbf{\Phi}(\mathbf{q}) = \mathbf{0}$ in paragraph 2.. It these latter are twice differentiated, with regards to time, a new set of algebraic equations is obtained:

$$\frac{\partial \mathbf{\Phi}}{\partial \mathbf{q}}\ddot{\mathbf{q}} + \frac{\partial}{\partial \mathbf{q}}\left(\frac{\partial \mathbf{\Phi}}{\partial \mathbf{q}}\dot{\mathbf{q}}\right)\dot{\mathbf{q}} = \frac{\partial \mathbf{\Phi}}{\partial \mathbf{q}}\ddot{\mathbf{q}} - \mathbf{\Gamma} = \mathbf{0}, \tag{19}$$

where $\mathbf{\Gamma} = -\frac{\partial}{\partial \mathbf{q}}\left(\frac{\partial \mathbf{\Phi}}{\partial \mathbf{q}}\dot{\mathbf{q}}\right)\dot{\mathbf{q}}$.

Introducing the following assumptions

$$\frac{d}{dt}\left(\frac{\partial T}{\partial \dot{\mathbf{q}}}\right) = \mathbf{M}\ddot{\mathbf{q}}, \qquad \frac{\partial T}{\partial \mathbf{q}} = \mathbf{0}, \tag{20}$$

and by arranging together Eqs.18 and Eqs.19, a mixed differential-algebraic equation (DAE) system can be written:

$$\begin{cases} \mathbf{M}\ddot{\mathbf{q}} + \left(\frac{\partial \mathbf{\Phi}}{\partial \mathbf{q}}\right)^T \mathbf{\Lambda} = \mathbf{Q}^a \\ \frac{\partial \mathbf{\Phi}}{\partial \mathbf{q}}\ddot{\mathbf{q}} = \mathbf{\Gamma} \end{cases}, \tag{21}$$

or in matrix assembly:

$$\begin{bmatrix} \mathbf{M} & \left(\frac{\partial \mathbf{\Phi}}{\partial \mathbf{q}}\right)^T \\ \frac{\partial \mathbf{\Phi}}{\partial \mathbf{q}} & \mathbf{0} \end{bmatrix} \begin{Bmatrix} \ddot{\mathbf{q}} \\ \mathbf{\Lambda} \end{Bmatrix} = \begin{Bmatrix} \mathbf{Q}^a \\ \mathbf{\Gamma} \end{Bmatrix}. \tag{22}$$

5. MESHLESS DECOMPOSITION OF THE CONTINUUM

The evaluation of the modeshapes of flexible bodies is based on the following simplifying hypotheses:

- continuous, homogeneous and isotropic bodies;
- small flexible displacements;
- elastic strain - stress constitutive relationship, according to Hooke's law.

Axial modes of a homogeneous and uniform beam

With the notation of section S and mass density ρ of the beam at specific axis position, the equilibrium equation to translational forces N along x direction, acting on a infinitesimal element dx, gives:

$$\rho S \frac{\partial^2 u}{\partial t^2} dx - \frac{\partial N}{\partial x} dx = 0, \tag{23}$$

where $\frac{\partial}{\partial t} = (\dot{})$ is the time derivative, and $\frac{\partial}{\partial x} = (')$ is the space domain derivative. Introducing the elastic relation $N = ES\frac{\partial u}{\partial x} = ESu'$ with E as Young's modulus and being $\ddot{u} = \frac{\partial^2 u}{\partial t^2}$, Eq.23 is condensed in the following form:

$$Eu'' = \rho \ddot{u}. \tag{24}$$

The solution of the differential equation Eq.24 is sought ([12] and also [13]) in the domain of the functions with separating variables of the type:

$$u(x,t) = \psi_u(x) p_u(t), \tag{25}$$

where $\psi_u(x)$ describes the space domain and $p_u(t)$ the time domain. The substitution of Eq.25 in Eq.24, with the separation of the terms in x on the left and in t on the right, yields:

$$\frac{E}{\rho} \frac{\psi_u''(x)}{\psi_u(x)} = \frac{\ddot{p_u}(t)}{p_u(t)}. \tag{26}$$

In Eq.26 each member must be equal to a constant function $z(x,t)$. By posing $C = -\omega_u^2$ and $\gamma_u^2 = \omega_u^2 \frac{\rho}{E}$, Eq.26 yields to a set of ordinary differential equations in their separate variables of time and spatial domain:

$$\begin{cases} \ddot{p_u}(t) + \omega_u^2 p_u(t) = 0, \\ \psi_u''(x) + \gamma_u^2 \psi_u(x) = 0, \end{cases} \tag{27}$$

for which a solution of the following type is sought:

$$\begin{cases} p_u(t) = P_u e^{\alpha_u t}, \\ \psi_u(x) = \Psi_u e^{\beta_u x}. \end{cases} \tag{28}$$

The general integrals of the differential equations in Eq.27 can be thus deployed in:

$$\begin{cases} p_u(t) = C_{u_1} e^{-j\omega_u t} + C_{u_2} e^{j\omega_u t}, \\ \psi_u(x) = C_{u_3} e^{-j\gamma_u x} + C_{u_4} e^{j\gamma_u x}, \end{cases} \tag{29}$$

where the complex-valued coefficients C_{u_1}, C_{u_2}, C_{u_3} and C_{u_4} can be further simplified with the Eulero relations, leading to the reformulation of Eq.29 with the real-valued coefficients P_{u_s}, P_{u_c}, Ψ_{u_s} and Ψ_{u_c} that need to be determined with the boundary conditions:

$$\begin{cases} p_u(t) = P_{u_s} \sin(\omega_u t) + P_{u_c} \cos(\omega_u t), \\ \psi_u(x) = \Psi_{u_s} \sin(\gamma_u x) + \Psi_{u_c} \cos(\gamma_u x). \end{cases} \tag{30}$$

Axial modeshape solution in free - free condition. The boundary conditions can be sketched as follows by imposing the forces at the extremes to be null at every instant:

$$\begin{cases} Q(0,t) = 0, \\ Q(L,t) = 0. \end{cases} \tag{31}$$

Recalling Eq.25 and that $Q = ES\frac{\partial u}{\partial x}$, with some passages it yields:

$$\begin{cases} \frac{\partial \psi_u(0)}{\partial x} = \gamma_u \Psi_{u_s} = 0, \\ \frac{\partial \psi_u(L)}{\partial x} = -\gamma_u \Psi_{u_c} \sin(\gamma_u L) = 0. \end{cases} \tag{32}$$

Therefore $\Psi_{u_s} = 0$ and the following results are obtained for the r-th ($r = 1, \ldots, N$) axial modeshape, after normalisation with appropriate selection of $\Psi_{u_{c_r}}$:

$$\begin{cases} \gamma_{u_r} = \frac{r\pi}{L}, \qquad \Psi_{u_{c_r}} = 1/\sqrt{\int_0^L \cos^2(\gamma_{u_r} x)dx}, \\ \psi_{u_r}(x) = \Psi_{u_{c_r}} \cos(\gamma_{u_r} x). \end{cases} \tag{33}$$

Bending modes of a homogeneous and uniform beam

From the Bernoulli-Euler beam theory, with the assumption of small transversal displacements (detached from axial ones), there follows that the rotation of an infinitesimal part of the beam is close to its first derivative, thus $\theta(x) \cong \frac{dv}{dx} = v'$; also, the rotation of the section produces an axial displacement for a generic point at y distance from the neutral axis, therefore $u(x) \cong y\theta(x) = yv'$, raising a strain $\epsilon(y) \cong \frac{\partial u}{\partial x} = \frac{\partial}{\partial x}(yv') = y\frac{\partial v'}{\partial x} = yv''$ and a tension $\sigma(y) = E\epsilon(y) = Eyv''$, thus a bending moment $M = \int_S \sigma y dS = EIv''$, where S is the section and ρ the mass density along the beam axis.

According to Timoshenko theory [12,14], the equilibrium equation to transversal motion along y direction, acting on a infinitesimal element dx, gives:

$$\rho S \frac{\partial^2 v}{\partial t^2} dx - T + \left(T + \frac{\partial T}{\partial x} dx \right) = 0. \tag{34}$$

For the equilibrium equation to rotational motion along z direction, acting on a infinitesimal element dx, follows:

$$\rho I dx \frac{\partial^2 \theta}{\partial t^2} + M - \left(M + \frac{\partial M}{\partial x} dx \right) + T dx = 0. \tag{35}$$

If the inertial torque can be disregarded, the Eqs.34-35 can be simplified with the elastic relations and joined to:

$$Ev'''' = -\rho S \ddot{v}. \tag{36}$$

The solution of the differential equation Eq.36 is sought in the domain of the functions with separating variables of the type:

$$v(x,t) = \psi_v(x) p_v(t), \tag{37}$$

where $\psi_v(x)$ describes the space domain and $p_v(t)$ the time domain. The substitution of Eq.37 in Eq.36, with the separation of the terms in x on the left and in t on the right, yields:

$$\frac{EI}{\rho S} \frac{\psi_v''''(x)}{\psi_v(x)} = -\frac{\ddot{p_v}(t)}{p_v(t)}. \tag{38}$$

In Eq.38 each member must be equal to a constant function $z(x,t)$. By posing $C = \omega_v^2$ and $\gamma_v^4 = \omega_v^2 \frac{\rho S}{EI}$, Eq.38 yields to a set of ordinary differential equations in their separate variables of time and spatial domain:

$$\begin{cases} \ddot{p_v}(t) + \omega_v^2 p_v(t) = 0, \\ \psi_v''''(x) - \gamma_v^4 \psi_v(x) = 0, \end{cases} \tag{39}$$

for which a solution of the following type is sought:

$$\begin{cases} p_v(t) = P_v e^{\alpha_v t}, \\ \psi_v(x) = \Psi_v e^{\beta_v x}. \end{cases} \tag{40}$$

The general integrals of the differential equations in Eq.39 can be thus deployed in:

$$\begin{cases} p_v(t) = C_{v_1} e^{-j\omega_v t} + C_{v_2} e^{j\omega_v t}, \\ \psi_v(x) = C_{v_3} e^{-j\gamma_v x} + C_{v_4} e^{j\gamma_v x} + C_{v_5} e^{-\gamma_v x} + C_{v_6} e^{\gamma_v x}, \end{cases} \tag{41}$$

where the complex-valued coefficients C_{v_1}, C_{v_2}, C_{v_3}, C_{v_4}, C_{v_5} and C_{v_6} can be further simplified with the Eulero relations, leading to the reformulation of Eq.41 with the real-valued coefficients P_{v_s}, P_{v_c}, Ψ_{v_s} and Ψ_{v_c} that need to be determined with the boundary conditions:

$$\begin{cases} p_v(t) = P_{v_s} \sin(\omega_v t) + P_{v_c} \cos(\omega_v t), \\ \psi_v(x) = \Psi_{v_s} \sin(\gamma_v x) + \Psi_{v_c} \cos(\gamma_v x) + \Psi_{v_{sh}} \sinh(\gamma_v x) + \Psi_{v_{ch}} \cosh(\gamma_v x). \end{cases} \tag{42}$$

Bending modeshapes solution in free-free condition. The boundary conditions can be sketched as follows by imposing the shear forces and torques at the extremes to be null at every instant:

$$\begin{cases} T(0,t) = 0, \quad M(0,t) = 0, \\ T(L,t) = 0, \quad M(L,t) = 0. \end{cases} \tag{43}$$

Recalling Eq.37 and that $M = EIv''$, $T = M'$, the previous conditions can be rewritten as:

$$\begin{cases} \frac{\partial^3 \psi_v(0)}{\partial x^3} = 0, \quad \frac{\partial^2 \psi_v(0)}{\partial x^2} = 0, \\ \frac{\partial^3 \psi_v(L)}{\partial x^3} = 0, \quad \frac{\partial^2 \psi_v(L)}{\partial x^2} = 0. \end{cases} \tag{44}$$

This homogeneous system admits non-trivial solutions for those γ_v values that make the determinant of the system null, with $\omega_{v_r} = \gamma_{v_r}^2 \sqrt{\frac{EI}{\rho S}}$:

$$1 - cos(\gamma_v L) cosh(\gamma_v L) = 0. \tag{45}$$

The solution of the system in Eq.45 gives the r-th ($r = 1, \ldots, N$) normalised bending modeshape in Eqs.39 and 42:

$$\begin{cases} \alpha_r = \frac{cosh(\gamma_{v_r} L) - cos(\gamma_{v_r} L)}{sinh(\gamma_{v_r} L) - sin(\gamma_{v_r} L)}, \\ \psi_{v_r}(x) = cosh(\gamma_{v_r} x) + cos(\gamma_{v_r} x) - \alpha_r (sinh(\gamma_{v_r} x) + sin(\gamma_{v_r} x)). \end{cases} \tag{46}$$

Modeshape usage in motion equations.

The orthogonality property of the modeshapes permits them to become a linearly independent vector base for the representation of the bi-dimensional displacement in the local reference frame:

$$u(x,t) = \sum_{r=1}^{\infty} \psi_{u_r}(x) p_{u_r}(t), \tag{47}$$

$$v(x,t) = \sum_{r=1}^{\infty} \psi_{v_r}(x) p_{v_r}(t), \tag{48}$$

where the modal base might be truncated to a finite number of m axial and n transversal modeshapes:

$$u(x,t) = \sum_{r=1}^{m} \psi_{u_r}(x) p_{u_r}(t), \tag{49}$$

$$v(x,t) = \sum_{r=1}^{n} \psi_{v_r}(x) p_{v_r}(t), \tag{50}$$

compacted in

$$\mathbf{u}(x,t) = \mathbf{\Psi}(x)\mathbf{p}(t), \tag{51}$$

where:

$$\mathbf{u}^T(x,t) = \begin{bmatrix} u(x,t) & v(x,t) \end{bmatrix}, \tag{52}$$

$$\mathbf{\Psi}(x) = \begin{bmatrix} \mathbf{\Psi}_u & \mathbf{0}_n \\ \mathbf{0}_m & \mathbf{\Psi}_v \end{bmatrix} = \begin{bmatrix} \psi_{u_1}(x) & \dots & \psi_{u_m}(x) & 0 & \dots & 0 \\ 0 & \dots & 0 & \psi_{v_1}(x) & \dots & \psi_{v_n}(x) \end{bmatrix}, \tag{53}$$

$$\mathbf{p}^T(t) = \begin{bmatrix} p_{u_1}(t) & \dots & p_{u_m}(t) & p_{v_1}(t) & \dots & p_{v_n}(t) \end{bmatrix}. \tag{54}$$

The *Lagrangian* formulation of the motion equations requires the evaluation of the *kinetic energy* T, of the *potential* of the *elastic* forces U_{el} and of the distributed *applied* forces U_{app}, as follows:

$$T = \frac{1}{2}\int_V \dot{\mathbf{u}}^T \begin{bmatrix} \rho & 0 \\ 0 & \rho \end{bmatrix} \dot{\mathbf{u}} dV = \frac{1}{2}\int_0^L \dot{\mathbf{u}}^T(x,t) \begin{bmatrix} \rho S & 0 \\ 0 & \rho S \end{bmatrix} \dot{\mathbf{u}}(x,t) dx, \tag{55}$$

$$U_{el} = \frac{1}{2}\int_V \sigma^T \epsilon dV = \frac{1}{2}\int_0^L \begin{bmatrix} u'(x,t) & v''(x,t) \end{bmatrix} \begin{bmatrix} ES & 0 \\ 0 & EI \end{bmatrix} \begin{bmatrix} u'(x,t) \\ v''(x,t) \end{bmatrix} dx, \tag{56}$$

$$U_{app} = -\int_V \mathbf{f}^T \mathbf{u} dV = -\int_{x_a}^{x_b} \mathbf{f}^T(x) \mathbf{u}(x,t) dx. \tag{57}$$

The above energies can be therefore rewritten as functions of the modal base of Eq.51:

$$T = \frac{1}{2}\dot{\mathbf{p}}(t)^T \left(\int_0^L \mathbf{\Psi}^T(x) \begin{bmatrix} \rho S & 0 \\ 0 & \rho S \end{bmatrix} \mathbf{\Psi}(x) dx \right) \dot{\mathbf{p}}(t) = \frac{1}{2}\dot{\mathbf{p}}^T(t)\hat{\mathbf{M}}\dot{\mathbf{p}}(t), \tag{58}$$

$$U_{el} = \frac{1}{2}\mathbf{p}(t)^T \left(\int_0^L \begin{bmatrix} \mathbf{\Psi}'_u(x) & \mathbf{0}_n \\ \mathbf{0}_m & \mathbf{\Psi}''_v(x) \end{bmatrix}^T \begin{bmatrix} ES & 0 \\ 0 & EI \end{bmatrix} \begin{bmatrix} \mathbf{\Psi}'_u(x) & \mathbf{0}_n \\ \mathbf{0}_m & \mathbf{\Psi}''_v(x) \end{bmatrix} dx \right) \mathbf{p}(t) = , \\ = \frac{1}{2}\mathbf{p}(t)^T \hat{\mathbf{K}} \mathbf{p}(t) \tag{59}$$

$$U_{app} = -\left(\int_{x_a}^{x_b} \mathbf{f}^T(x)\mathbf{\Psi}(x)dx \right) \mathbf{p}(t) = -\hat{\mathbf{Q}}\mathbf{p}(t), \tag{60}$$

where $\hat{\mathbf{M}}$ is the *mass matrix*, $\hat{\mathbf{K}}$ is the *stiffness matrix* and $\hat{\mathbf{Q}}$ is the *external force vector*. In particular, due to the orthogonality property and the selected normalisations, $\hat{\mathbf{M}}$ and $\hat{\mathbf{K}}$ are diagonal, with the following values for the r-th diagonal terms: $m_r = \rho SL = m$, $k_{u_r} = ES\gamma_{u_r}^2 L = \rho SL\omega_{u_r}^2 = m\omega_{u_r}^2$ and $k_{v_r} = EI\gamma_{v_r}^4 L = \rho SL\omega_{v_r}^2 = m\omega_{v_r}^2$.

With the *Lagrangian function* $L = T - U_{el} + U_{app}$ and being $\mathbf{\Psi}(x)$ constant properties of the elastic body, the bi-dimensional motions in the form of ordinary differential equation as in Eq.15 follow:

$$\frac{d}{dt}\left(\frac{\partial L}{\partial \dot{\mathbf{p}}}\right) - \frac{\partial L}{\partial \mathbf{p}} = \mathbf{0}, \tag{61}$$

$$\hat{\mathbf{M}}\ddot{\mathbf{p}}(t) + \hat{\mathbf{K}}\mathbf{p}(t) = \hat{\mathbf{Q}}. \tag{62}$$

6. KINEMATICAL CONSTRAINTS WITH FLEXIBLE BODIES

The generalised coordinates of the i-th floating frame are $\mathbf{q}_i = [x_i, y_i, \phi_i]^T = \left[\mathbf{r}_{O,i}^T, \phi_i\right]^T$. With the modelling of the beam flexibility, a point P at coordinate x along the beam axis, sees a further elastic motion $\mathbf{w}_{O,i}^P(x,t) = \mathbf{w}_{O,i}^P(t) = [u(x,t), v(x,t)]^T$. The position $\mathbf{r}_{G,i}^P$ of a point P on the i-th body in the global coordinate system can then be described by:

$$\mathbf{r}_{G,i}^P = \mathbf{r}_{O,i} + \mathbf{A}_i\left(\mathbf{s}_{O,i}^P + \mathbf{w}_{O,i}^P(t)\right). \tag{63}$$

As in Eq.49 and Eq.50, an approximation of the axial and transversal motion can be achieved by means of a finite number (of evaluated modeshapes:

$$u(x,t) = \sum_{r=1}^{m} \psi_r^a(x)p_r^a(t), \tag{64}$$

$$v(x,t) = \sum_{k=1}^{n} \psi_k^b(x)p_k^b(t). \tag{65}$$

Therefore the elastic motion $\mathbf{w}_{O,i}^P(x,t) = \mathbf{w}_{O,i}^P(t)$ can be expressed as $\mathbf{N}_i^P\mathbf{p}_i$, where:

$$\mathbf{N}_i^P = \begin{bmatrix} (\psi_1^a(x))_i & \dots & (\psi_m^a(x))_i & 0 & \dots & 0 \\ 0 & \dots & 0 & (\psi_1^b(x))_i & \dots & (\psi_n^b(x))_i \end{bmatrix}, \tag{66}$$

$$\mathbf{p}_i^T = \begin{bmatrix} p_{1i}^a(t) & \dots & p_{mi}^a(t) & p_{1i}^b(t) & \dots & p_{ni}^b(t) \end{bmatrix}^T, \tag{67}$$

and Eq.63 becomes:

$$\mathbf{r}_{G,i}^{P}=\mathbf{r}_{O,i}+\mathbf{A}_{i}\left(\mathbf{s}_{O,i}^{P}+\mathbf{N}_{i}^{P}\mathbf{p}_{i}\right), \tag{68}$$

written using the set of generalised coordinates for the i-th flexible body:

$$\mathbf{q}_{i}^{f}=\begin{bmatrix}x_{i} & y_{i} & \phi_{i} & p_{1i}^{a} & \dots & p_{mi}^{a} & p_{1i}^{b} & \dots & p_{ni}^{b}\end{bmatrix}^{T}. \tag{69}$$

Once derived in respect to time, the previous expression yields the velocity formulation of a point P in the global coordinate system:

$$=\dot{\mathbf{r}}_{O,i}+\dot{\phi}_{i}\mathbf{B}_{i}\left(\mathbf{s}_{O,i}^{P}+\mathbf{N}_{i}^{P}\mathbf{p}_{i}\right)+\mathbf{A}_{i}\mathbf{N}_{i}^{P}\dot{\mathbf{p}}_{i}, \tag{70}$$

which can be compacted with a matrix notation:

$$\dot{\mathbf{r}}_{G,i}^{P}=\begin{bmatrix}\mathbf{I} & \hat{\mathbf{B}}_{i}^{P} & \mathbf{A}_{i}\mathbf{N}_{i}^{P}\end{bmatrix}\begin{bmatrix}\dot{\mathbf{r}}_{O,i}\\ \dot{\phi}_{i}\\ \dot{\mathbf{p}}_{i}\end{bmatrix}, \tag{71}$$

where $\hat{\mathbf{B}}_{i}^{P}=\mathbf{B}_{i}\left(\mathbf{s}_{O,i}^{P}+\mathbf{N}_{i}^{P}\mathbf{p}_{i}\right)$.

Further, as already seen in Paragraph 5., the rotation of the section containing point P is given by:

$$\theta_{i}^{P}=\sum_{k=1}^{n}\left(\frac{\partial\psi_{k}^{b}(x)}{\partial x}\right)_{i}p_{ki}^{b}(t)=\sum_{k=1}^{n}\left({\psi'}_{k}^{b}(x)\right)_{i}p_{ki}^{b}(t)=\mathbf{H}_{i}^{P}\mathbf{p}_{i}, \tag{72}$$

where:

$$\mathbf{H}_{i}^{P}=\begin{bmatrix}0 & \dots & 0 & ({\psi'}_{1}^{b}(x))_{i} & \dots & ({\psi'}_{n}^{b}(x))_{i}\end{bmatrix}. \tag{73}$$

Revolute joint

The *revolute joint* constraints in the plane is realised by imposing single point coincidence between two points P_i & Q_j belonging to different bodies, now modelled with the set of flexible modeshapes:

$$\mathbf{\Phi}_{rev_f}=\mathbf{r}_{G,i}^{P}-\mathbf{r}_{G,j}^{Q}=\mathbf{r}_{O,i}+\mathbf{A}_{i}\left(\mathbf{s}_{O,i}^{P}+\mathbf{N}_{i}^{P}\mathbf{p}_{i}\right)-\mathbf{r}_{O,j}-\mathbf{A}_{j}\left(\mathbf{s}_{O,j}^{Q}+\mathbf{N}_{j}^{Q}\mathbf{p}_{j}\right). \tag{74}$$

According to the generalised coordinates for elastic bodies, the Jacobian of the revolute joint constraint can be expressed as:

$$\frac{\partial\mathbf{\Phi}_{rev_f}}{\partial\mathbf{q}_{i}}=\begin{bmatrix}\mathbf{I} & \mathbf{B}_{i}\left(\mathbf{s}_{O,i}^{P}+\mathbf{N}_{i}^{P}\mathbf{p}_{i}\right) & \mathbf{A}_{i}\mathbf{N}_{i}^{P}\end{bmatrix}, \tag{75}$$

$$\frac{\partial\mathbf{\Phi}_{rev_f}}{\partial\mathbf{q}_{j}}=\begin{bmatrix}-\mathbf{I} & -\mathbf{B}_{j}\left(\mathbf{s}_{O,j}^{Q}+\mathbf{N}_{j}^{Q}\mathbf{p}_{j}\right) & -\mathbf{A}_{j}\mathbf{N}_{j}^{Q}\end{bmatrix}, \tag{76}$$

and $\mathbf{\Gamma}_{rev_f}=-\frac{\partial}{\partial\mathbf{q}}\left(\frac{\partial\mathbf{\Phi}}{\partial\mathbf{q}}\dot{\mathbf{q}}\right)\dot{\mathbf{q}}=$

$$=\mathbf{A}_{i}\left(\mathbf{s}_{O,i}^{P}+\mathbf{N}_{i}^{P}\mathbf{p}_{i}\right)\dot{\phi}_{i}^{2}-2\mathbf{B}_{i}\mathbf{N}_{i}^{P}\dot{\mathbf{p}}_{i}\dot{\phi}_{i}-\mathbf{A}_{j}\left(\mathbf{s}_{O,j}^{Q}+\mathbf{N}_{j}^{Q}\mathbf{p}_{j}\right)\dot{\phi}_{j}^{2}+2\mathbf{B}_{j}\mathbf{N}_{j}^{P}\dot{\mathbf{p}}_{j}\dot{\phi}_{j}.$$

7. GENERALISED FORCES APPLIED ON FLEXIBLE BODIES

External forces

An external force applied to a generic point P_i on the i-th flexible body gives rise to the following work:

$$W_{\mathbf{F}_{G,P_i}} = \mathbf{F}_{G,P_i}^T \mathbf{r}_{G,i}^P = \mathbf{F}_{G,P_i}^T \left(\mathbf{r}_{O,i} + \mathbf{A}_i \left(\mathbf{s}_{O,i}^P + \mathbf{N}_i^P \mathbf{p}_i\right)\right) = -U_{\mathbf{F}_{G,P_i}}, \tag{77}$$

where $U_{\mathbf{F}_{G,P_i}}$ is the potential of the external force $\mathbf{F}_{G,P_i}$. By deriving the former expression with regards to the generalised coordinates for flexible bodies, there follows:

$$\frac{\partial U_{\mathbf{F}_{G,P_i}}}{\partial \mathbf{q}_i} = -\mathbf{F}_{G,P_i}^T \begin{bmatrix} \mathbf{I} & \mathbf{B}_i \left(\mathbf{s}_{O,i}^P + \mathbf{N}_i^P \mathbf{p}_i\right) & \mathbf{A}_i \mathbf{N}_i^P \end{bmatrix} = -\mathbf{Q}_{\mathbf{F}_{G,P_i}}^T, \tag{78}$$

with $\mathbf{Q}_{\mathbf{F}_{G,P_i}}^T$ as the generalised force vector on the $\mathbf{q}_i$ coordinates.

Linear spring-damper-component between bodies

When the linear device is linked to two points P_i and P_j on distinct flexible bodies i and j, the force acting on the bodies can be expressed as follows:

$$f = k_l(l - l_0) + c_l \dot{l} + F(l, \dot{l}, p), \tag{79}$$

where k_l, c_l and l_0 are the stiffness constant, the damping constant and length of the free spring, l is the magnitude of the distance between P_i and P_j and $F(l, \dot{l}, p)$ is the actuating function freely defined and imposed. With flexible bodies, being $\mathbf{r}_{O,i} + \mathbf{A}_i \left(\mathbf{s}_{O,i}^P + \mathbf{N}_i^P \mathbf{p}_i\right) - \mathbf{r}_{O,j} - \mathbf{A}_j \left(\mathbf{s}_{O,j}^P + \mathbf{N}_j^P \mathbf{p}_j\right)$ the segment of relative distance between the points P_i and P_j, and its time derivative actualised to $\dot{\mathbf{d}}_{ij} = \dot{\mathbf{r}}_{O,j} + \dot{\phi}_j \mathbf{B}_j \left(\mathbf{s}_{O,j}^P + \mathbf{N}_j^P \mathbf{p}_j\right) + \mathbf{A}_j \mathbf{N}_j^P \dot{\mathbf{p}}_j - \dot{\mathbf{r}}_{O,i} - \dot{\phi}_i \mathbf{B}_i \left(\mathbf{s}_{O,i}^P + \mathbf{N}_i^P \mathbf{p}_i\right) - \mathbf{A}_i \mathbf{N}_i^P \dot{\mathbf{p}}_i$, the magnitude of the relative distance and the velocity take the following shapes:

$$l = \sqrt{\mathbf{d}_{ij}^T \mathbf{d}_{ij}}, \tag{80}$$

$$\dot{l} = \frac{\mathbf{d}_{ij}^T}{l} \dot{\mathbf{d}}_{ij} = \hat{\mathbf{d}}_{ij}^T \dot{\mathbf{d}}_{ij}. \tag{81}$$

The generalised forces acting on body i and j are therefore:

$$\mathbf{Q}_i^T = f \hat{\mathbf{d}}_{ij}^T \begin{bmatrix} \mathbf{I} & \mathbf{B}_i \left(\mathbf{s}_{O,i}^P + \mathbf{N}_i^P \mathbf{p}_i\right) & \mathbf{A}_i \mathbf{N}_i^P \end{bmatrix}, \tag{82}$$

$$\mathbf{Q}_j^T = -f \hat{\mathbf{d}}_{ij}^T \begin{bmatrix} \mathbf{I} & \mathbf{B}_j \left(\mathbf{s}_{O,j}^P + \mathbf{N}_j^P \mathbf{p}_j\right) & \mathbf{A}_j \mathbf{N}_j^P \end{bmatrix}. \tag{83}$$

8. MOTION EQUATIONS WITH FLEXIBLE BODIES

With $\mathbb{L}$ being the *Lagrangian function*, the motion equations of unconstrained flexible bodies can be formulated as follows:

$$\frac{d}{dt}\left(\frac{\partial \mathbb{L}}{\partial \dot{\mathbf{q}}^f}\right) - \frac{\partial \mathbb{L}}{\partial \mathbf{q}^f} = \mathbf{0}, \tag{84}$$

while for constrained motion, by means of *Lagrangian multipliers* $\mathbf{\Lambda}$ there follows:

$$\frac{d}{dt}\left(\frac{\partial \mathbb{L}}{\partial \dot{\mathbf{q}}^f}\right)-\frac{\partial \mathbb{L}}{\partial \mathbf{q}^f}+\left(\frac{\partial \mathbf{\Phi}}{\partial \mathbf{q}^f}\right)^T \mathbf{\Lambda}=\mathbf{0}, \tag{85}$$

which can be rewritten if the *Lagrangian function* is explicitly highlighted in its kinetic $\mathbb{T}$ and potential energy $\mathbb{U}$ contributions, once no potentials $\mathbb{U}$ depend on generalised velocities and time:

$$\frac{d}{dt}\left(\frac{\partial \mathbb{T}}{\partial \dot{\mathbf{q}}^f}\right)-\frac{\partial \mathbb{T}}{\partial \mathbf{q}^f}+\left(\frac{\partial \mathbf{\Phi}}{\partial \mathbf{q}^f}\right)^T \mathbf{\Lambda}=-\frac{\partial \mathbb{U}}{\partial \mathbf{q}^f}. \tag{86}$$

As expressed in paragraphs 7., the potentials can be related to the generalised forces, thus coming to the final form of the motion equations:

$$\frac{d}{dt}\left(\frac{\partial \mathbb{T}}{\partial \dot{\mathbf{q}}^f}\right)-\frac{\partial \mathbb{T}}{\partial \mathbf{q}^f}+\left(\frac{\partial \mathbf{\Phi}}{\partial \mathbf{q}^f}\right)^T \mathbf{\Lambda}=\mathbf{Q}^a, \tag{87}$$

where $\mathbf{Q}^a$ is the generalised force vector applied to the bodies.

The motion equations in Eqs.87 have to be fulfilled together with the constraint equations $\mathbf{\Phi}(\mathbf{q}^f)=\mathbf{0}$ in paragraph 6.. It these latter are twice differentiated, with regards to time, a new set of algebraic equations is obtained:

$$\frac{\partial \mathbf{\Phi}}{\partial \mathbf{q}^f}\ddot{\mathbf{q}}^f+\frac{\partial}{\partial \mathbf{q}^f}\left(\frac{\partial \mathbf{\Phi}}{\partial \mathbf{q}^f}\dot{\mathbf{q}}^f\right)\dot{\mathbf{q}}^f=\frac{\partial \mathbf{\Phi}}{\partial \mathbf{q}^f}\ddot{\mathbf{q}}^f-\mathbf{\Gamma}=\mathbf{0}, \tag{88}$$

where $\mathbf{\Gamma}=-\frac{\partial}{\partial \mathbf{q}^f}\left(\frac{\partial \mathbf{\Phi}}{\partial \mathbf{q}^f}\dot{\mathbf{q}}^f\right)\dot{\mathbf{q}}^f$.

Total kinetic energy

In the definition of the new *Lagrangian function* $\mathbb{L}=\mathbb{T}-\mathbb{U}$ with flexible bodies, care must be given to the evaluation of the total kinetic energy $\mathbb{T}$ and total potentials $\mathbb{U}$. For the i-th flexible body, the kinetic energy can be expressed as follows:

$$T_i=\frac{1}{2}\int_{V_i}\rho_i\left(\dot{\mathbf{r}}^*_{G,i}\right)^T\dot{\mathbf{r}}^*_{G,i}dV_i, \tag{89}$$

with integration over the volume V_i at locations of every point $*$ of the velocities $\dot{\mathbf{r}}^*_{G,i}$. If the product $\rho_i S_i$ can be supposed constant along the beam axis, the previous expression can be rewritten as:

$$T_i=\frac{1}{2}\dot{\mathbf{q}}_i^{fT}\left(\int_0^{L_i}\rho_i S_i\begin{bmatrix}\mathbf{I}\\ \hat{\mathbf{B}}_i^{*T}\\ \mathbf{N}_i^{*T}\mathbf{A}_i^T\end{bmatrix}\begin{bmatrix}\mathbf{I} & \hat{\mathbf{B}}_i^* & \mathbf{A}_i\mathbf{N}_i^*\end{bmatrix}dx_i\right)\dot{\mathbf{q}}_i^f, \tag{90}$$

where the terms inside the parenthesis can be expanded into the symmetric mass matrix $\mathbf{M}_i^f$ of the i-th flexible body:

$$\mathbf{M}_i^f=\int_0^{L_i}\rho_i S_i\begin{bmatrix}\mathbf{I} & \hat{\mathbf{B}}_i^* & \mathbf{A}_i\mathbf{N}_i^*\\ \hat{\mathbf{B}}_i^{*T} & \hat{\mathbf{B}}_i^{*T}\hat{\mathbf{B}}_i^* & \hat{\mathbf{B}}_i^{*T}\mathbf{A}_i\mathbf{N}_i^*\\ \mathbf{N}_i^{*T}\mathbf{A}_i^T & \mathbf{N}_i^{*T}\mathbf{A}_i^T\hat{\mathbf{B}}_i^* & \mathbf{N}_i^{*^T}\mathbf{N}_i^*\end{bmatrix}dx_i, \tag{91}$$

therefore the kinetic energy contribution of the i-th body results:

$$T_i = \frac{1}{2} \dot{\mathbf{q}}_i^{fT} \mathbf{M}_i^f \dot{\mathbf{q}}_i^f . \tag{92}$$

The total kinetic energy of the whole system, composed of N flexible bodies, can be expressed as follows:

$$\mathbb{T} = \frac{1}{2} \dot{\mathbf{q}}^{fT} \mathbf{M}^f \dot{\mathbf{q}}^f , \tag{93}$$

with the block diagonal mass matrix of the system and the dofs' vector derivatives:

$$\mathbf{M}^f = \begin{bmatrix} \mathbf{M}_1^f & \mathbf{0} & \dots & \mathbf{0} \\ \mathbf{0} & \mathbf{M}_2^f & \ddots & \vdots \\ \vdots & \ddots & \ddots & \mathbf{0} \\ \mathbf{0} & \dots & \mathbf{0} & \mathbf{M}_N^f \end{bmatrix}, \qquad \dot{\mathbf{q}}^f = \begin{bmatrix} \dot{\mathbf{q}}_1^f \\ \dot{\mathbf{q}}_2^f \\ \vdots \\ \dot{\mathbf{q}}_N^f \end{bmatrix}. \tag{94}$$

Total elastic potential

Each flexible body participates to the total elastic potential of the flexible multibody system with a contribution related to the axial and bending related deformations, as follows:

$$U_i^{ef} = \frac{1}{2} \int_{V_i} \left(\sigma_a^T \epsilon_a + \sigma_b^T \epsilon_b \right) dV_i = \frac{1}{2} \int_0^{L_i} \left(E_i S_i \epsilon_i^2 + E_i I_i c_i^2 \right) dx_i , \tag{95}$$

where, with the written modelling assumptions,

$$\epsilon_i = \frac{\partial u_i(x,t)}{\partial x_i} = u_i'(x_i,t), \tag{96}$$

$$c_i = \frac{\partial^2 v_i(x,t)}{\partial x_i^2} = v_i''(x_i,t). \tag{97}$$

Equation 95 can be therefore rewritten as:

$$U_i^{ef} = \frac{1}{2} \int_0^{L_i} \begin{bmatrix} u_i'(x_i,t) & v_i''(x_i,t) \end{bmatrix} \begin{bmatrix} E_i S_i & 0 \\ 0 & E_i I_i \end{bmatrix} \begin{bmatrix} u_i'(x_i,t) \\ v_i''(x_i,t) \end{bmatrix} dx_i . \tag{98}$$

Recalling Eqs.64-65, it follows:

$$u_i'(x_i,t) = \sum_{r=1}^{m} \left(\frac{\partial \psi_r^a(x)}{\partial x} \right)_i p_{ri}^a(t) = \sum_{r=1}^{m} \left({\psi'}_r^a(x) \right)_i p_{ri}^a(t), \tag{99}$$

$$v_i''(x_i,t) = \sum_{k=1}^{n} \left(\frac{\partial^2 \psi_k^b(x)}{\partial x^2} \right)_i p_{ki}^b(t) = \sum_{k=1}^{n} \left({\psi''}_k^b(x) \right)_i p_{ki}^b(t), \tag{100}$$

which in matrix notation can be lumped in:

$$\begin{bmatrix} u_i'(x_i,t) \\ v_i''(x_i,t) \end{bmatrix} = \begin{bmatrix} (\psi'^a_1(x))_i & \dots & (\psi'^a_m(x))_i & 0 & \dots & 0 \\ 0 & \dots & 0 & (\psi''^b_1(x))_i & \dots & (\psi''^b_n(x))_i \end{bmatrix} \begin{bmatrix} p^a_{1i}(t) \\ \vdots \\ p^a_{mi}(t) \\ p^b_{1i}(t) \\ \vdots \\ p^b_{ni}(t) \end{bmatrix} =$$

$$= \mathbf{D}_i^P \mathbf{p}_i. \tag{101}$$

Once in Eq.95 the inner square matrix is posed as

$$\mathbf{C}_i = \begin{bmatrix} E_i S_i & 0 \\ 0 & E_i I_i \end{bmatrix}, \tag{102}$$

there follows:

$$U_i^{ef} = \frac{1}{2} \int_0^{L_i} \mathbf{p}_i^T \mathbf{D}_i^{*T} \mathbf{C}_i \mathbf{D}_i^* \mathbf{p}_i dx_i = \frac{1}{2} \mathbf{p}_i^T \left(\int_0^{L_i} \mathbf{D}_i^{*T} \mathbf{C}_i \mathbf{D}_i^* dx_i \right) \mathbf{p}_i, \tag{103}$$

where $\hat{\mathbf{K}}_i = \int_0^{L_i} \mathbf{D}_i^{*T} \mathbf{C}_i \mathbf{D}_i^* dx_i$ is the stiffness matrix of the i-th flexible member. The expression of the elastic potential can now be represented with the global coordinates of the flexible body in Eq.67 as:

$$U_i^{ef} = \frac{1}{2} \mathbf{q}_i^{fT} \begin{bmatrix} \mathbf{0} & \mathbf{0} \\ \mathbf{0} & \hat{\mathbf{K}}_i \end{bmatrix} \mathbf{q}_i^f = \frac{1}{2} \mathbf{q}_i^{fT} \mathbf{K}_i \mathbf{q}_i^f. \tag{104}$$

The total elastic potential of the whole system, composed of N flexible bodies, can be expressed as follows:

$$\mathbb{U}^{ef} = \frac{1}{2} \mathbf{q}^{fT} \mathbf{K}^f \mathbf{q}^f, \tag{105}$$

with the block diagonal stiffness matrix of the system and the dofs' vector:

$$\mathbf{K}^f = \begin{bmatrix} \mathbf{K}_1^f & \mathbf{0} & \dots & \mathbf{0} \\ \mathbf{0} & \mathbf{K}_2^f & \ddots & \vdots \\ \vdots & \ddots & \ddots & \mathbf{0} \\ \mathbf{0} & \dots & \mathbf{0} & \mathbf{K}_N^f \end{bmatrix}, \qquad \mathbf{q}^f = \begin{bmatrix} \mathbf{q}_1^f \\ \mathbf{q}_2^f \\ \vdots \\ \mathbf{q}_N^f \end{bmatrix}. \tag{106}$$

DAE of motion equations

Introducing the following assumptions

$$\frac{d}{dt}\left(\frac{\partial \mathbb{T}}{\partial \dot{\mathbf{q}}^f}\right) = \mathbf{M}^f \ddot{\mathbf{q}}^f, \qquad \frac{\partial \mathbb{T}}{\partial \mathbf{q}^f} = \frac{\partial \left(\dot{\mathbf{q}}^f \mathbf{M}^f \dot{\mathbf{q}}^f\right)}{\partial \mathbf{q}^f} = \mathbf{Q}^v, \qquad \frac{\partial \mathbb{U}^{ef}}{\partial \mathbf{q}^f} = \mathbf{K}^f \mathbf{q}^f = -\mathbf{Q}^e, \tag{107}$$

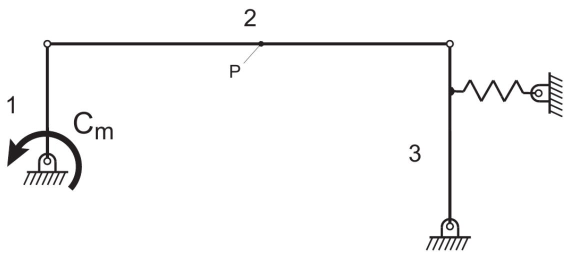

Figure 1. Four bar mechanism scheme

and by arranging together Eq.87 and Eq.88, a mixed differential-algebraic equation (DAE) system can be written:

$$\begin{cases} \mathbf{M}^f \ddot{\mathbf{q}}^f + \left(\frac{\partial \mathbf{\Phi}}{\partial \mathbf{q}^f}\right)^T \mathbf{\Lambda} = \mathbf{Q}^a + \mathbf{Q}^v + \mathbf{Q}^e, \\ \frac{\partial \mathbf{\Phi}}{\partial \mathbf{q}^f} \ddot{\mathbf{q}}^f = \mathbf{\Gamma}, \end{cases} \tag{108}$$

or in matrix assembly:

$$\begin{bmatrix} \mathbf{M}^f & \left(\frac{\partial \mathbf{\Phi}}{\partial \mathbf{q}^f}\right)^T \\ \frac{\partial \mathbf{\Phi}}{\partial \mathbf{q}^f} & \mathbf{0} \end{bmatrix} \begin{Bmatrix} \ddot{\mathbf{q}}^f \\ \mathbf{\Lambda} \end{Bmatrix} = \begin{Bmatrix} \mathbf{Q} \\ \mathbf{\Gamma} \end{Bmatrix}, \tag{109}$$

where $\mathbf{Q} = \mathbf{Q}^a + \mathbf{Q}^v + \mathbf{Q}^e$.

9. TEST CASE: a four bar mechanism

The mechanism selected to prove the approach was the one shown in Fig.1: it was composed of a rotating crankshaft (part 1), a slender (here horizontal) beam (part 2), a connecting beam rod (part 3) and the ground (part 0); revolute joint constraints connected part 1 and part 3 to the ground 0, part 2 to part 1 and part 2 to part 3. A massive flywheel of 1.26 kgm^2 and a rotational damper (active with the relative rotational velocity to ground - part 0) with damping coefficient equal to $1.6Ns/m$ were rigidly attached to part 1. An example for the inertial properties can be found in Tab.2 for steel material (as in Tab.3), while the initial configuration of Fig.2 can be achieved with the positions listed in Tab.4 with all parts of the mechanism as resting (null initial velocity). A linear spring was attached between the ground and part 3, with stiffness equal to $1000N/m$.

Depending on the chosen material, the natural frequencies of part 3 in free-free condition can be evaluated as in Tab.5, where bending and axial eigenmode frequencies are displayed. It can therefore be seen, as expected, how the axial modes have an higher order of magnitude in their frequency content. In the following simulation results, the first 5 bending modes and 1 axial mode were retained. An example of the actuator function C_m is described in its steps in Tab.6. In all the reported examples below, the modelling of the flexible parts with the introduced basis functions increased the calculation times in respect to the rigid body simulations, but left relatively limited the burden of this modelling option, while augmenting the description of real-life vibrational phenomena in flexible mechanisms.

Table 1. Section properties of the mechanism moving parts.

Part	Section Shape	Diameter	Length	Section Area	Section Area Moment
1	circular+flywheel	30 mm	200 mm	7.069E-04 m^2	3.976E-08 m^4
2	circular	15 mm	800 mm	1.767E-04 m^2	2.485E-09 m^4
3	circular	60 mm	300 mm	2.827E-03 m^2	6.362E-07 m^4

Table 2. Inertial properties of the mechanism moving parts, when made of steel.

Part	Section Shape	Mass	Inertia Moment
1	circular+flywheel	1.103 kg	1.26368 kgm^2
2	circular	1.103 kg	0.05881 kgm^2
3	circular	6.616 kg	0.04962 kgm^2

Figure 2 shows the main features of the custom software, which was written in Matlab environment to implement the proposed approach: there results the chance to run a rigid or a flexible body simulation, driven by the actuator and external force functions, as in Eqs.22 or 109. After the evaluation of the evolving time-history of each dof, it is possible to plot the operative deflection shape at each instant in the mechanism plane, together with the graphs of positions, velocities and accelerations of the dofs as functions of time in separate charts. Figure 3 shows an example of the operative deflection shape of the mechanism at a specific time instant, with the superposition of the rigid mechanism sketch at the same time; the same

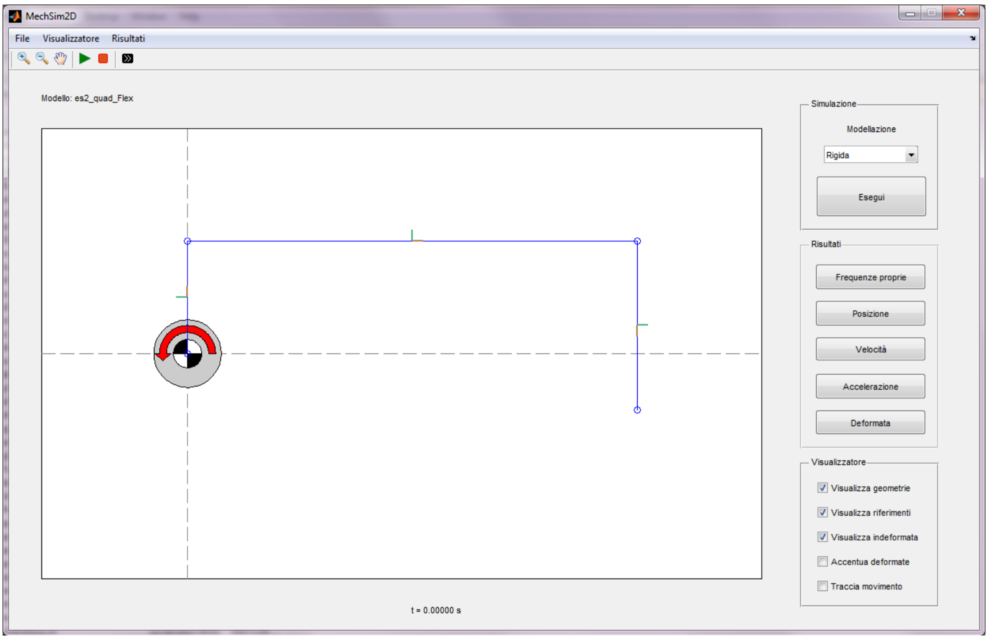

Figure 2. Four bar mechanism in the software console

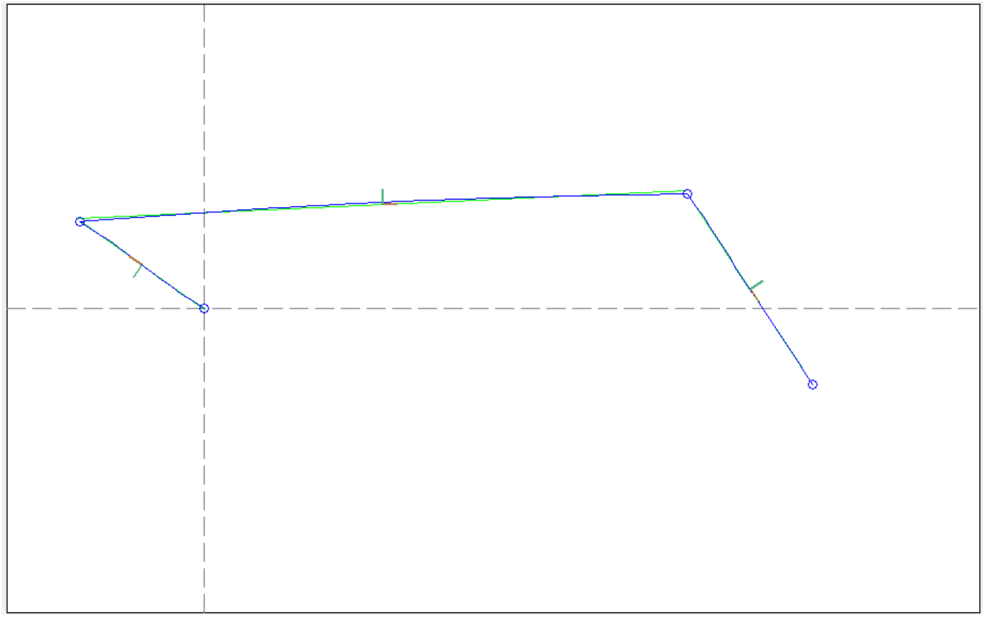

Figure 3. Flexible four bar mechanism during motion: the operative deflection shape with flexible bodies modelled with 5 bending shape functions

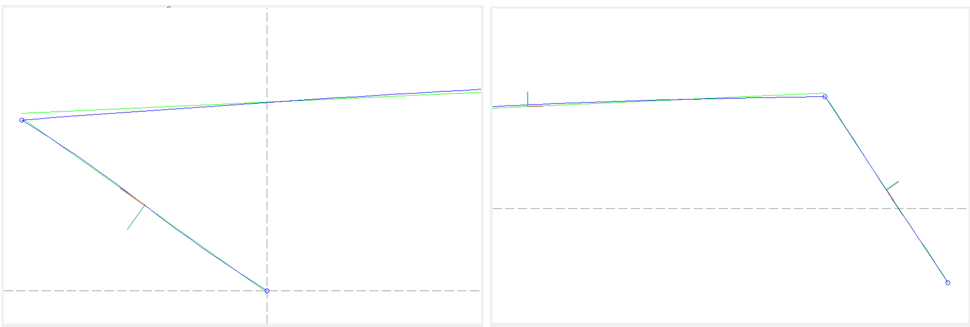

Figure 4. Flexible four bar mechanism during motion: enlargements of the operative deflection shape modelled with 5 bending shape functions

step is enlarged in Fig.4 to highlight the small deflection that the parts are encountering while moving, still respecting the revolute joint constraints. In order to check the convergence of the software algorithms, the stiffness of the parts was reduced to show high deflections in all the flexible parts, as highlighted in Fig.5, where, at different time steps, the superposition of the shape functions of the basis is coherent with the kinematical constraints, while detaching from the small relative displacement's assumption.

In Fig.6 it is shown the influence of the lonely flexible steel part 2, modelled by means

Table 3. Material properties of the mechanism moving parts.

Material	Density	Elasticity Modulus
Steel	7801 kg/m^3	2.07E+11 Pa
Aluminium 6061-O	2700 kg/m^3	6.89E+10 Pa
Polyethylene PE-HD	958 kg/m^3	9.00E+08 Pa

Table 4. Initial positions of the local reference frame in the mechanism moving parts.

Part	x_0	y_0	ϕ_0
1	0.000 m	0.100 m	$\Pi/2\, rad$
2	0.400 m	0.200 m	0 rad
3	0.800 m	0.050 m	$\Pi/2\, rad$

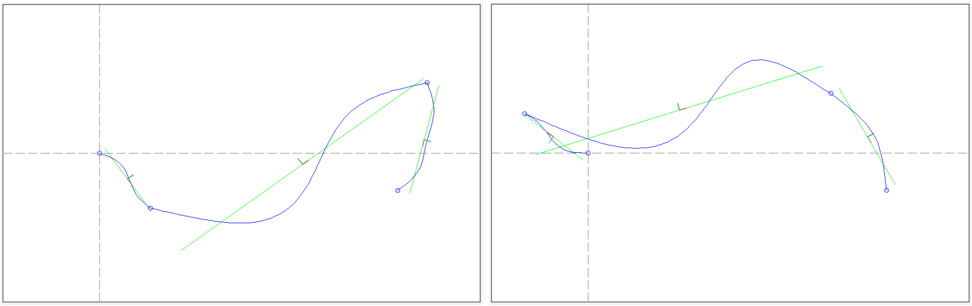

Figure 5. Flexible four bar mechanism during motion: checking the algorithms by high deflections

of 1 axial and 5 bending basis functions in the proposed approach, on the motion of the rigid crankshaft - part 1, under the actuator function of Tab.6. The absolute angular position, velocity and acceleration, especially the two latter, in the ground reference manifest increasing dependence on the introduced flexibility, thus with increasing fluctuations around the corresponding rigid body solutions; the angular position is not clearly distinguishable from that of the rigid case.

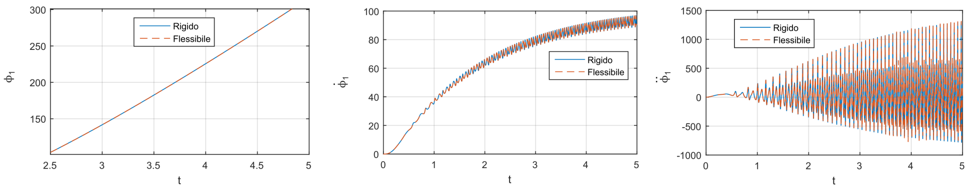

Figure 6. Angular position, velocity and acceleration of rigid body 1 in the global reference, when only body 2 is flexible with 1 axial + 5 bending basis functions, actuation as in Tab.6

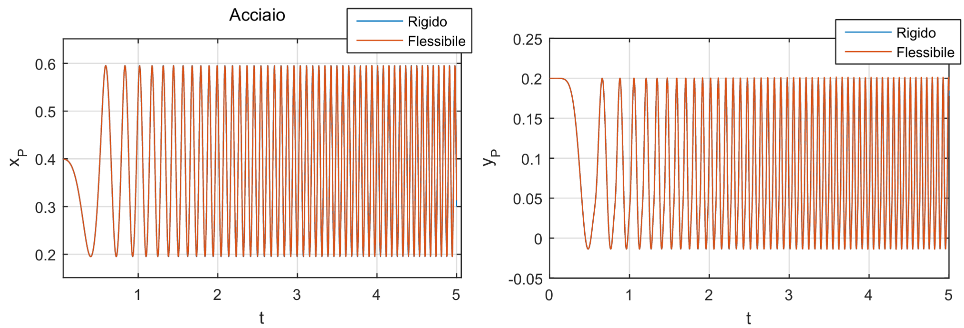

Figure 7. Simulated motion: position of centroid 2 in the global reference with steel body, with horizontal (left) and vertical (right) components

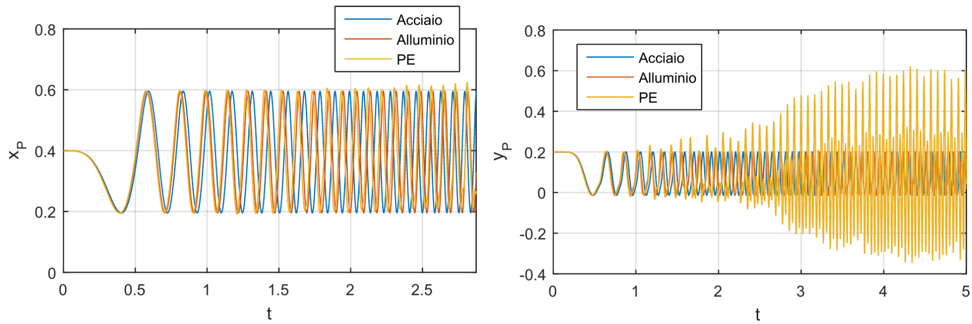

Figure 8. Simulated motion: position of centroid 2 in the global reference with the body made of different materials, with horizontal (left) and vertical (right) components

If the body of part 2 is made of steel, even if modelled as a flexible part among rigid ones, the position of its centroid in the ground frame as in Fig.7 is indeed hardly distinguishable from that of the rigid body option, being the deflection of orders of magnitude lower than the rigid body motion. Instead, when the material changes to aluminium or to polyethylene, a more pronounced relevance of the flexible contribution can be appreciated in the global reference, as depicted in Fig.8; while in the horizontal direction (part 2 rotates much less than the other parts) the addition is limited due to the very low axial contributions, in the vertical direction, approximately close to the direction in which the bending deployment of the flexible part 2 occurs, the flexibility is greatly manifested, in particular with the less rigid materials as polyethylene, whose deflection shape goes beyond the small deflections' assumption.

Looking instead at the deflections along the axial and transversal axis of the local reference frame of part 2, the above statements find a quantitative explanation: in Fig.9 it is evident how the axial flexible deformation has no practical meaning (below $1.0\text{x}10^{-21}m$), while the flexible contribution in the transversal direction reaches an amplitude of $1.5\text{x}10^{-3}m$ in the global reference. Thou, an enlargement of the transversal deflection in Fig.9 puts in evidence

Table 5. Natural frequencies of the flexible component 2.

Mode num.	Flexural frequency [Hz] Steel	Al.6061-O	PE-HD	Axial frequency [Hz] Steel	Al.6061-O	PE-HD
1	50.155	49.185	9.437	3219.512	3157.241	605.785
2	138.255	135.581	26.014	6439.024	6314.482	1211.570
3	271.036	265.793	50.998	9658.536	9471.723	1817.355
4	448.036	439.370	84.303	-	-	-
5	669.288	656.343	125.934	-	-	-
6	934.791	916.711	175.891	-	-	-

Table 6. Actuator torque function on the mechanism moving part 1.

Step	Type	Start time	End time	Characterization
1	Hermite interpolation	0.000 s	0.300 s	Start value = 0; Start tangent = 0; End value = 80 Nm; End tangent = 0
2	Constant	0.300 s	5 s	Value = 80 Nm;

the multi modeshape nature of the vibration, with at least 2 predominant modeshapes. The same conclusions can be drawn also with different materials, as depicted in Fig.10 with the local frame deflection when part 2 is made of aluminium and polyethylene. While with aluminium the deflections stay very close to those manifested with steel, with polyethylene there is a marked increase for both axial and transversal local displacements of about 3 orders of magnitude, thus relevant especially for the transversal deflection.

10. CONCLUSIONS

This paper has introduced a shape function based approach to represent the small deflections in the local frame of each body of a flexible multibody system. The detailed modelling was discussed in terms of the novel equations and in terms of test cases for the approach validation. There resulted a promising viable method to include the flexibility of bodies with a reduced computational burden and meshless description of the problem.

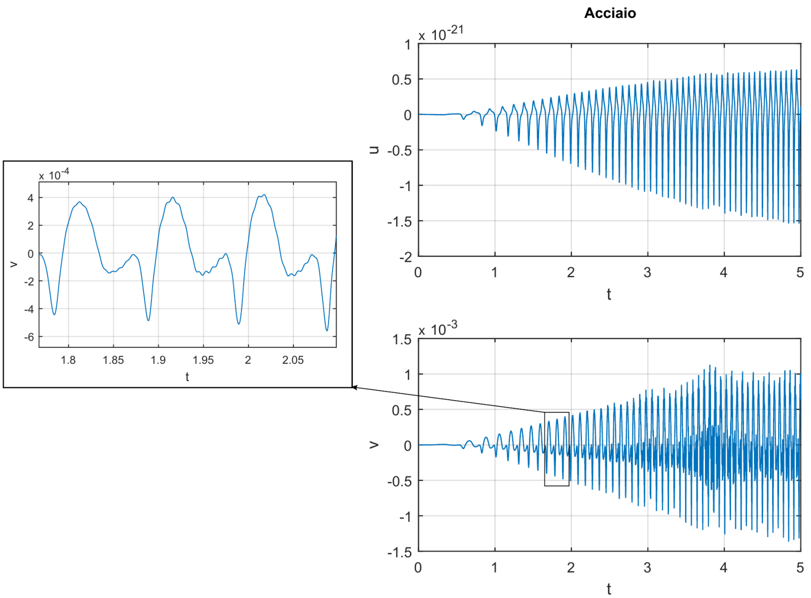

Figure 9. Simulated motion: position of centroid 2 in the local reference with flexible steel body, with axial (upper right) and transversal (lower right) components, and an enlargement of the transversal position (left)

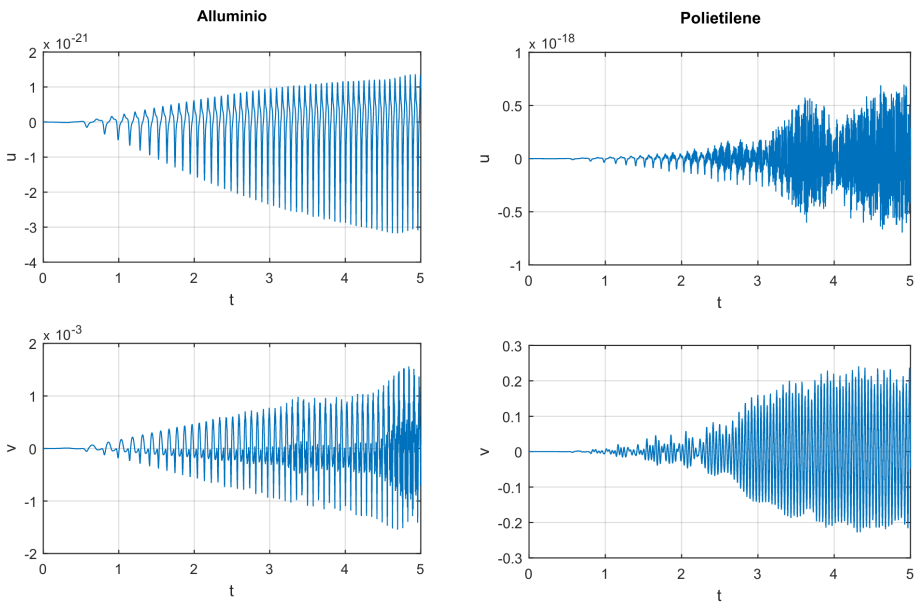

Figure 10. Simulated motion: axial and transversal position of centroid 2 in the local reference with flexible body of aluminium (left) and PE-HD (right)

REFERENCES

[1] Shabana, A. A., 1997. “Flexible multibody dynamics: Review of past and recent developments”. *Multibody System Dynamics,* **1**(2), pp. 189–222. doi:10.1023/A:1009773505418.

[2] Craig, R. R., 1981. *Structural Dynamics: An Introduction to Computer Methods*. John Wiley & Sons Inc., New York, US.

[3] Catania, G., and Zanarini, A., 2003. “Dynamic contribution of tires in vehicle suspension modeling: An experimental approach”. In Proceedings of the ASME International Mechanical Engineering Congress and Exposition, Washington, DC, USA, November 1521, 2003, Design Engineering, Volumes 1 and 2, ASME, pp. 1–8. doi:10.1115/IMECE2003-41255.

[4] Zanarini, A., and Catania, G., 2004. “Evaluation of spatial mechanism eigenproperties with respect to kinematical configuration”. In Proceedings of the 5éme Conférence Internationale Méthodes de Surveillance et Techniques de Diagnostic Acoustiques et Vibratoires, October 11-13 2004, Senlis (France), CETIM, pp. 1–10. `https://www.researchgate.net/publication/266896167_Evaluation_of_spatial_mechanism_eigenproperties_with_respect_to_kinematical_configuration`.

[5] Zanarini, A., 2008. “Kinematics-based variability of the dynamic behaviour in spatial mechanisms”. In Proceedings of the ISMA2008 Conference, September 15-17, Leuven (Belgium), P. Sas, ed., KUL, pp. 2175–2190. Multi-body dynamics and control, Paper 327, doi:10.13140/RG.2.1.2666.5048.

[6] Zanarini, A., and Brugnoni, E., 2012. “Frequency analysis of a motorbike under motion conditions”. In Proceedings of the ISMA2012-USD2012 Conferences, Leuven, Belgium, 2012 September, Sas and Moens, eds., Vol. Multy-body dynamics and control, KUL. doi:10.13140/RG.2.1.2404.3608, `https://www.isma-isaac.be/past/conf/isma2012/proceedings/papers/isma2012_0456.pdf`.

[7] Zanarini, A., 2012. *Analisi cinetostatica grafica di meccanismi piani. Applicazioni per la Meccanica delle Macchine*. Societá Editrice Esculapio, Bologna, Italy. ISBN - 978-88-7488-545-9.

[8] Zanarini, A., and Brugnoni, E., 2013. “A time-varying dynamic problem for the frequency analysis of an off-road motorcycle”. In Proceedings of the Sesta giornata di studio Ettore Funaioli, July 2012, Bologna (Italy). doi:10.6092/unibo/amsacta/3715.

[9] Haug, E., 1989. *Computer aided kinematics and dynamics of mechanical systems. Vol. 1: basic methods*. Allyn & Bacon, Inc. Needham Heights, MA, USA. ISBN:0-205-11669-8.

[10] de Jalon, J. G., and Bayo, E., 1994. *Kinematic and Dynamic Simulation of Multibody Systems: The Real Time Challenge*. Springer-Verlag New York, Inc., Secaucus, NJ, USA.

[11] Shabana, A. A., 2013. *Dynamics of Multibody Systems*, 4 ed. Cambridge University Press, Cambridge, 009. doi:10.1017/CBO9781107337213.

[12] Timoshenko, S., Young, D. H., and Weaver, W., 1974. *Vibration Problems in Engineering*. Wiley, New York.

[13] James, M. L., Smith, G. M., Wolford, J. C., and Whaley, P. W., 1989. *Vibration of Mechanical and Structural Systems: With Microcomputer Applications*. Harper & Row, Publishers, Inc.

[14] Timoshenko, S., and Young, D. H., 1965. *Theory of structures*, 2nd ed. ed. McGraw-Hill.

SYMMETRIC SUBSPACES OF EUCLIDEAN GROUP: CHARACTERIZATION AND ROBOTIC APPLICATIONS

Yuanqing Wu
Department of Industrial Engineering,
University of Bologna, Italy
E-mail: yuanqing.wu@unibo.it

Marco Carricato
Department of Industrial Engineering,
University of Bologna, Italy
E-mail: marco.carricato@unibo.it

Abstract. *The special Euclidean group* $\mathrm{SE}(3)$ *is a symmetric space under inversion symmetry. It admits seven conjugacy classes of symmetric subspaces, which are submanifolds closed under inversion symmetry. This paper characterizes the symmetric subspaces of* $\mathrm{SE}(3)$ *in three distinct ways, each focusing on some particular applications in robotics. First, they are the exponential of Lie triple systems of the Lie algebra* $\mathfrak{se}(3)$ *of* $\mathrm{SE}(3)$*, leading to a list of Lie theoretical properties which are of crucial importance in mechanism analysis and synthesis. Next, they (except one) are symmetric bundle subspaces of* $\mathrm{TSO}(3)$*, the tangent bundle of* $\mathrm{SO}(3)$*. The non-triviality of these subbundle explains the kinematic behavior of several kinesiological systems, which implies a potential application in rehabilitation robotics. Finally, they (except one) are either projective subspaces or quadrics of the Study quadric under dual quaternion representation. This third characterization is connected to the study of overconstrained linkages and line/plane symmetric motions.*

Keywords: *symmetric subspaces, mechanism theory, robot kinematics*

1. INTRODUCTION

The special Euclidean group $\mathrm{SE}(3)$ consisting of all Euclidean motions is a six dimensional (6-D) Lie group which is neither simple nor solvable. Brockett introduced the product of exponentials (POE) formula [1] (see also *canonical coordinates of the second kind*, [2]) for the characterization of serial robot kinematics (see [3] for a comprehensive development). Hervé first introduced $\mathrm{SE}(3)$ and its ten conjugacy classes of (connected) Lie subgroups to the mechanism and robotics community [4] (originally published in French in 1978).

Mechanical engineers and roboticists use Lie subgroups and more generally submanifolds of $\mathrm{SE}(3)$ to characterize the motion pattern of a mechanism or robot manipulator. As shown in Table 1, each Lie subgroup G of $\mathrm{SE}(3)$ is generated by the exponential of its corresponding Lie subalgebra $\mathfrak{g}$ of $\mathfrak{se}(3)$, which is a linear subspace of $\mathfrak{se}(3)$ closed under the Lie bracket operation $[\cdot,\cdot]$. Application of Lie subgroups in the analysis and synthesis of

Table 1. Connected Lie subgroups of $\mathrm{SE}(3)$. **i**,**j**,**k** denote the unit zero-pitch screws along $\mathbf{x}, \mathbf{y}, \mathbf{z}$-axis respectively. ε denotes the dual number. $\mathbf{p}, \mathbf{u}$ denote a generic point and vector in $\mathbb{R}^3$ respectively.

dim	$G = \exp(\mathfrak{g})$	$\mathfrak{g}$	basis	Gibson-Hunt type	isom. type	isotropy	generic
1	$\mathrm{SO}(2)$	$\mathfrak{l}$	$\mathbf{k}$	—	$\mathfrak{so}(2)$	$\mathfrak{tl}$	$\mathcal{R}(\mathbf{p},\mathbf{u})$
	$\mathrm{SO}_p(2)$	$\mathfrak{l}_p$	$(1+p\varepsilon)\mathbf{k}$	—	$\mathbb{R}$	$\mathfrak{tl}$	$\mathcal{H}_p(\mathbf{p},\mathbf{u})$
	$\mathbb{R}^1$	$\mathfrak{l}_\infty$	$\mathbf{k}\varepsilon$	—	$\mathbb{R}$	$\mathfrak{cl}$	$\mathcal{T}_1(\mathbf{u})$
2	$\mathrm{SO}(2)\times\mathbb{R}^1$	$\mathfrak{tl}$	$\mathbf{k}, \mathbf{k}\varepsilon$	IB^0	$\mathfrak{so}(2)\times\mathbb{R}$	$\mathfrak{tl}$	$\mathcal{C}(\mathbf{p},\mathbf{u})$
	$\mathbb{R}^2$	$\mathfrak{p}_\infty$	$\mathbf{i}\varepsilon, \mathbf{j}\varepsilon$	IIC	$\mathbb{R}^2$	$\mathfrak{cl}$	$\mathcal{T}_2(\mathbf{u})$
3	$\mathrm{SO}(3)$	$\mathfrak{so}(3)$	$\mathbf{i}, \mathbf{j}, \mathbf{k}$	IIA	$\mathfrak{so}(3)$	$\mathfrak{so}(3)$	$\mathcal{S}(\mathbf{p})$
	$\mathrm{SE}(2)$	$\mathfrak{nl}$	$\mathbf{k}, \mathbf{i}\varepsilon, \mathbf{j}\varepsilon$	IIB	$\mathfrak{se}(2)$	$\mathfrak{cl}$	$\mathcal{G}(\mathbf{u})$
	$\mathrm{SE}_p(2)$	$\mathfrak{hp}_p$	$(1+p\varepsilon)\mathbf{k}, \mathbf{i}\varepsilon, \mathbf{j}\varepsilon$	IIC	$\mathfrak{l}_p \ltimes \mathbb{R}^2$	$\mathfrak{cl}$	$\mathcal{Y}(\mathbf{u})$
	$\mathbb{R}^3$	$\mathfrak{t}$	$\mathbf{i}\varepsilon, \mathbf{j}\varepsilon, \mathbf{k}\varepsilon$	IID	$\mathbb{R}^3$	$\mathfrak{se}(3)$	$\mathcal{T}_3$
4	$\mathrm{SE}(2)\times\mathbb{R}^1$	$\mathfrak{cl}$	$\mathbf{k}, \mathbf{i}\varepsilon, \mathbf{j}\varepsilon, \mathbf{k}\varepsilon$	—	$\mathfrak{so}(2)\ltimes\mathbb{R}^3$	$\mathfrak{cl}$	$\mathcal{X}(\mathbf{u})$

Table 2. Some typical POE submanifolds $\mathrm{SE}(3)$ resulting from the product of two Lie subgroups. $\mathbf{p}, \mathbf{q}$: generic points in $\mathbb{R}^3$; $\mathbf{u}, \mathbf{v}$: generic vectors in $\mathbb{R}^3$.

dim	submanifold	mechanical realization	bundle characterization
2	$\mathcal{R}(\mathbf{p},\mathbf{u})\cdot\mathcal{R}(\mathbf{p},\mathbf{v})$	Cardan joint	T^2
5	$\mathcal{C}(\mathbf{p},\mathbf{u})\cdot\mathcal{S}(\mathbf{q})$	CS dyad	$\mathbb{R}\mathrm{P}^3\times(\mathbb{R}\times S^1)$
5	$\mathcal{G}(\mathbf{u})\cdot\mathcal{G}(\mathbf{v})$	doubly-planar bond	$T^2\times\mathbb{R}^3$
5	$\mathcal{G}(\mathbf{u})\cdot\mathcal{S}(\mathbf{p})$	planar-spherical bond	$\mathbb{R}\mathrm{P}^3\times\mathbb{R}^2$
5	$\mathcal{S}(\mathbf{p})\cdot\mathcal{S}(\mathbf{q})$	SS dyad	$\mathbb{R}\mathrm{P}^3\times S^2$

mechanisms is well documented in the literature (see [5] and the references therein). General submanifolds of $\mathrm{SE}(3)$, on the other hand, are impossible to classify and may not be useful for robotic applications. In practice, some special submanifolds have been studied.

Hervé introduced the notion of mechanical bond to characterize a connected subset of $\mathrm{SE}(3)$ as an element-wise product of two or more Lie subgroups of $\mathrm{SE}(3)$ [4] (see Table 2 for some typical instances). This is the same as a submanifold generated by the POE formula, since each Lie subgroup itself admits a POE representation. We shall refer to such submanifolds as *POE submanifolds*. In general, POE submanifolds are only locally well defined due to presence of singularity (degeneracy of tangent space). However, the product of two Lie subgroups $G_1 \cdot G_2$ does admit the global differential structure of a regular submanifold with dimension $\dim G_1 + \dim G_2 - \dim(G_1 \cap G_2)$ [5]. Besides, Carricato *et al.* investigated a special class of POE submanifolds whose tangent spaces are mutually congruent, thus defining what is called a *persistent screw system* (PSS) [6–10]. Wu *et al.* considered the application of local sections of homogeneous spaces G/H of $\mathrm{SE}(3)$ in analysis and synthesis of mechanisms with two cooperating modules [11].

Recently, we reported the discovery of another special family of submanifolds of $\mathrm{SE}(3)$ and illustrated their potential applications in robot kinematics [12, 13]. These are the *sym-*

Table 3. Symmetric subspaces of $\mathrm{SE}(3)$. The naming convention of the symmetric subspaces in the second column is explained in Section 3.

dim	$\mathrm{M} = \exp(\mathfrak{m})$	$\mathfrak{m}$	basis	Gibson-Hunt type	$\mathfrak{h}_\mathfrak{m}$	$\mathfrak{g}_\mathfrak{m}$	isotropy	chain symmetry
2	$\mathrm{N_P L}$	$\mathfrak{n}_\mathfrak{p}\mathfrak{l}$	$\mathbf{i}, \mathbf{k}\varepsilon$	IIB	$\mathfrak{l}_\infty$	$\mathfrak{nl}$	$\mathfrak{p}_\infty$	plane symmetry
	E_p	$\mathfrak{e}_p$	$(1+p\varepsilon)\mathbf{i}, \mathbf{k}\varepsilon$			$\mathfrak{hp}_p$		
	P	$\mathfrak{p}$	$\mathbf{j}, \mathbf{k}$	IIA		$\mathfrak{s}$	$\mathfrak{l}$	
3	$\mathrm{C_P L}$	$\mathfrak{c}_\mathfrak{p}\mathfrak{l}$	$\mathbf{i}, \mathbf{i}\varepsilon, \mathbf{k}\varepsilon$	IIC	$\mathfrak{l}_\infty$	$\mathfrak{cl}$	$\mathfrak{p}_\infty$	
	NP	$\mathfrak{np}$	$\mathbf{i}, \mathbf{j}, \mathbf{k}\varepsilon$	IIB	$\mathfrak{nl}$	$\mathfrak{se}(3)$	$\mathfrak{nl}$	
4	TP	$\mathfrak{tp}$	$\mathbf{i}, \mathbf{j}, \mathbf{i}\varepsilon, \mathbf{j}\varepsilon$	—	$\mathfrak{tl}$	$\mathfrak{se}(3)$	$\mathfrak{tl}$	line symmetry
5	CP	$\mathfrak{cp}$	$\mathbf{i}, \mathbf{j}, \mathbf{i}\varepsilon, \mathbf{j}\varepsilon, \mathbf{k}\varepsilon$	—	$\mathfrak{cl}$	$\mathfrak{se}(3)$	$\mathfrak{cl}$	both of above

metric subspaces of $\mathrm{SE}(3)$ considered as a *symmetric space* [14]. We are mainly interested in symmetric subspaces containing the identity $\mathbf{1}$. These subspaces are both similar to and different from the Lie subgroups. On the one hand, just like a connected Lie subgroup being generated by the exponential (see *canonical coordinates of the first kind*, [2]) of its corresponding Lie subalgebra, a symmetric subspace is generated by the exponential of its corresponding *Lie triple system* (LTS) of the Lie algebra $\mathfrak{se}(3)$ of $\mathrm{SE}(3)$. An LTS is a linear subspace $\mathfrak{m}$ of $\mathfrak{se}(3)$ which is closed under the triple product $[[\cdot,\cdot],\cdot] : \mathfrak{se}(3) \times \mathfrak{se}(3) \times \mathfrak{se}(3) \to \mathfrak{se}(3), (\boldsymbol{\xi}, \boldsymbol{\zeta}, \boldsymbol{\varsigma}) \mapsto [[\boldsymbol{\xi}, \boldsymbol{\zeta}], \boldsymbol{\varsigma}]$. Seven conjugacy classes of symmetric subspaces are found by equivalently classifying LTSs of $\mathfrak{se}(3)$ (see Table 3 and also [13, 15]). This result is later confirmed [16] by a systematic investigation of triple product closure property of general and special screw systems of order two to five [17].

On the other hand, symmetric subspaces also entail several distinct characteristics not shared by the Lie subgroups or POE submanifolds. First, since they do not admit POE representation, they do not admit any serial mechanical realization. In other words, it is only possible to generate a symmetric subspace motion by parallel mechanisms. We have shown that the joint screws in each kinematic chain of these parallel mechanisms must satisfy certain symmetry conditions and therefore are referred to as *symmetric chains* (see Section 2.); the type of symmetry depends on the underlying LTS (see last column of Table 3 and also [13]). Second, symmetric subspaces are invariant under conjugation by elements of the Lie subgroup $\exp(\mathfrak{h}_\mathfrak{m})$ generated by the derived algebra $\mathfrak{h}_\mathfrak{m} := [\mathfrak{m}, \mathfrak{m}]$ (also referred to as the *torsion algebra* in [13] for its relevance to torsional rotation). This property is important for type synthesis of parallel mechanisms. Finally, the tangent space of a symmetric subspace obeys the half angle property, namely $\mathrm{T}R^{-1}_{e^{\boldsymbol{\xi}}}(\mathrm{T}_{e^{\boldsymbol{\xi}}} \exp(\mathfrak{m})) = \mathrm{Ad}_{e^{\boldsymbol{\xi}/2}}\mathfrak{m}$ with $R_\mathbf{g}, \mathbf{g} \in \mathrm{SE}(3)$ being the right translation of $\mathrm{SE}(3)$ and Ad the Adjoint representation of $\mathrm{SE}(3)$. This property simplifies the kinematic analysis of parallel mechanisms generating symmetric subspace motions, and sometimes also helps to identify a symmetric subspace motion. All these Lie theoretic properties of symmetric subspaces have been systematically studied in [13].

This paper serves as both a tutorial and a summary of existing work from a robotic application viewpoint. We show that by characterizing the symmetric subspaces of $\mathrm{SE}(3)$ in three different ways, we enable their applications in several different problems in robotics. In Section 2., we give a brief review of the classification and Lie theoretical properties of the symmetric subspaces, and consider their applications to mechanism analysis and synthe-

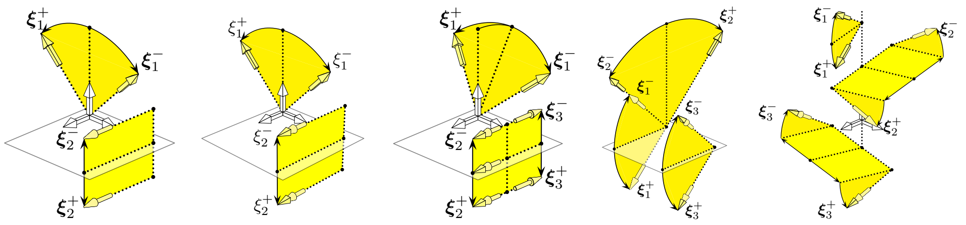

Figure 1. Chain symmetry type of symmetric subspaces. $\mathrm{N_PL}$, E_p, $\mathrm{C_PL}$, NP: plane symmetry; TP: line symmetry. Round arrow: zero-pitch screw (revolute joint), prism arrow: inifite-pitch screw (prismatic joint), round arrow with prism hat: finite non-zero pitch screw (helical joint). Except for NP whose mirror symmetric helical joints should have equal and opposite pitch, symmetric helical joints of E_p, $\mathrm{N_PL}$ and TP should have equal pitch [13]. CP (not shown here) admits both plane symmetry and line symmetry.

sis. In Section 3., we show that symmetric subspaces are nontrivial subbundles of the tangent bundle $\mathrm{TSO}(3)$ of $\mathrm{SO}(3)$, which are in distinct comparison to the trivial subbundles (Lie subgroups and POE submanifolds). The non-triviality of these subbundle is shown to explain the kinematic behavior of several kinesiological systems, which implies a potential application in rehabilitation robotics. In Section 4., we show that the symmetric subspaces along with the Lie subgroups are either linear subspaces or quadrics in the Study quadric. A connection between symmetry of the joint screws in a symmetric chain and line/plane symmetric motions [18] is then revealed. This characterization of the symmetric subspaces is also shown to be connected to the study of overconstrained linkages.

2. SYMMETRIC SUBSPACES OF $\mathrm{SE}(3)$

$\mathrm{SE}(3)$ is a symmetric space under the inversion symmetry $S_{\mathbf{g}}(\mathbf{h}) = \mathbf{g}\mathbf{h}^{-1}\mathbf{g}$ for any $\mathbf{g}, \mathbf{h} \in \mathrm{SE}(3)$ [14]. Its symmetry preserving subsets are called symmetric subspaces. In particular, symmetric subspaces containing the identity $\mathbf{1}$ are generated by the exponential of LTSs of $\mathfrak{se}(3)$ [13,15]. As shown in Table 3, there are seven conjugacy classes of (connected) symmetric subspaces of $\mathrm{SE}(3)$ (excluding Lie subgroups). Here, we have used the dual quaternion representation of $\mathfrak{se}(3)$ so that $\mathbf{i}$, $\mathbf{j}$ and $\mathbf{k}$ denote the unit zero-pitch screws along $\mathbf{x}, \mathbf{y}$ and $\mathbf{z}$-axis respectively and ε is the dual number satisfying $\varepsilon^2 = 0$. The Lie theoretical properties of symmetric subspaces of $\mathrm{SE}(3)$ are systematically investigated in [13] and summarized as follows:

(SS 1) The tangent space $\mathfrak{m} := T_{\mathbf{1}}\mathrm{M}$ of a symmetric subspace M of $\mathrm{SE}(3)$ at identity is a LTS:

$$[[\boldsymbol{\xi}, \boldsymbol{\zeta}], \boldsymbol{\varsigma}] \in \mathfrak{m} \qquad \forall \boldsymbol{\xi}, \boldsymbol{\zeta}, \boldsymbol{\varsigma} \in \mathfrak{m} \tag{1}$$

Moreover, M is given by $\exp(\mathfrak{m}) := \{e^{\boldsymbol{\xi}} \mid \boldsymbol{\xi} \in \mathfrak{m}\}$;

(SS 2) The derived algebra $\mathfrak{h}_{\mathfrak{m}} := [\mathfrak{m}, \mathfrak{m}]$ and the completion algebra $\mathfrak{g}_{\mathfrak{m}} := \mathfrak{m} + [\mathfrak{m}, \mathfrak{m}]$ are both Lie subalgebras of $\mathfrak{se}(3)$;

(SS 3) The tangent space of a symmetric subspace $\exp(\mathfrak{m})$ obeys the half-angle property:

$$\mathrm{T}R_{e^{\boldsymbol{\xi}}}^{-1}(T_{e^{\boldsymbol{\xi}}}\exp(\mathfrak{m})) = \mathrm{Ad}_{e^{\boldsymbol{\xi}/2}}\mathfrak{m} \tag{2}$$

(SS 4) $\mathfrak{m}$ is invariant under the Adjoint action of the subgroup $\exp(\mathfrak{h}_\mathfrak{m})$:

$$Ad_{e^{\boldsymbol{\eta}}}\mathfrak{m} = \mathfrak{m}, \quad \forall \boldsymbol{\eta} \in \mathfrak{h}_\mathfrak{m} \tag{3}$$

and similarly $\exp(\mathfrak{m})$ is invariant under conjugation by elements of the subgroup $\exp(\mathfrak{h}_\mathfrak{m})$:

$$e^{\boldsymbol{\eta}}\exp(\mathfrak{m})e^{-\boldsymbol{\eta}} = \exp(\mathfrak{m}), \quad \forall \boldsymbol{\eta} \in \mathfrak{h}_\mathfrak{m} \tag{4}$$

(SS 5) All LTSs $\mathfrak{m}$ except $\mathfrak{cp}$ satisfy $\mathfrak{m} \cap \mathfrak{h}_\mathfrak{m} = \mathfrak{m} \cap [\mathfrak{m}, \mathfrak{m}] = \mathbf{0}$, leading to the following parameterization for the completion group $\exp(\mathfrak{g}_\mathfrak{m})$ of $\exp(\mathfrak{m})$:

$$\begin{aligned} \mathfrak{m} \times \mathfrak{h}_\mathfrak{m} &\to \exp(\mathfrak{g}_\mathfrak{m}), \\ (\boldsymbol{\xi}, \boldsymbol{\eta}) &\mapsto e^{\boldsymbol{\xi}}e^{\boldsymbol{\eta}} \end{aligned} \tag{5}$$

(SS 6) A symmetric subspace $\exp(\mathfrak{m})$ with $\dim \mathfrak{m} = k$ can be generated by the *symmetric movement* of a *symmetric chain*:

$$e^{\theta_1\boldsymbol{\xi}_1^+}\cdots e^{\theta_k\boldsymbol{\xi}_k^+}\cdot e^{\theta_k\boldsymbol{\xi}_k^-}\cdots e^{\theta_1\boldsymbol{\xi}_1^-} = e^{\theta_1\boldsymbol{\xi}_1^+}\cdots e^{\theta_k\boldsymbol{\xi}_k^+}(e^{-\theta_1\boldsymbol{\xi}_1^-}\cdots e^{-\theta_k\boldsymbol{\xi}_k^-})^{-1} \tag{6}$$

where each *symmetric pair* of joint screws $(\boldsymbol{\xi}_i^+, \boldsymbol{\xi}_i^-), i = 1, \ldots, k$ is given by:

$$\begin{cases} \boldsymbol{\xi}_i^+ = Ad_{e^{\zeta_i}}\boldsymbol{\xi}_i, \\ \boldsymbol{\xi}_i^- = Ad_{e^{-\zeta_i}}\boldsymbol{\xi}_i \end{cases} \qquad \boldsymbol{\zeta}_i, \boldsymbol{\xi}_i \in \mathfrak{m} \qquad \text{(geometric condition)} \tag{7}$$

or

$$\begin{cases} \boldsymbol{\xi}_i^+ = \boldsymbol{\zeta}_i + \boldsymbol{\eta}_i, \\ \boldsymbol{\xi}_i^- = \boldsymbol{\zeta}_i - \boldsymbol{\eta}_i \end{cases} \qquad \boldsymbol{\zeta}_i \in \mathfrak{m}, \boldsymbol{\eta}_i \in \mathfrak{h}_\mathfrak{m} \qquad \text{(algebraic condition)} \tag{8}$$

with

$$\begin{aligned} \mathrm{span}(\boldsymbol{\xi}_1^+, \ldots, \boldsymbol{\xi}_k^+) \oplus \mathfrak{h}_\mathfrak{m} &= \mathfrak{g}_\mathfrak{m} \quad \text{or} \\ \mathrm{span}(\boldsymbol{\xi}_1^-, \ldots, \boldsymbol{\xi}_k^-) \oplus \mathfrak{h}_\mathfrak{m} &= \mathfrak{g}_\mathfrak{m} \quad \text{or} \\ \mathrm{span}(\boldsymbol{\zeta}_1, \ldots, \boldsymbol{\zeta}_k) &= \mathfrak{m} \end{aligned} \tag{9}$$

According to **(SS 6)**, the joint screws of the symmetric chain obey either plane symmetry or line symmetry (see the last column of Table 3 and also Figure 1). a symmetric chain generates symmetric subspace motion only when it is going through a symmetric movement, i.e. ξ_i^+ and ξ_i^- have equal joint movement θ_i for all i's. Additional constraints (for example, forming parallel mechanisms with multiple symmetric chains) are required to enforce a symmetric movement [12, 13].

One important application of the aforesaid properties is to give a rigorous treatment of Hunt's general theory of constant velocity couplings [19], which involves the two symmetric subspaces P (non-plunging type) and NP (plunging type). Properties of P can also be exploited in the synthesis of two degrees-of-freedom (DoF) interconnected parallel wrist that features a large singularity-free rotation range [20]. More generally, a systematic type synthesis method for parallel mechanisms generating symmetric subspaces can be derived from the same procedure used in [20].

3. SYMMETRIC SUBSPACES AS SUBBUNDLES OF $\mathrm{TSO}(3)$

It is well known that $\mathrm{SE}(3)$ is isomorphic as a Lie group to the tangent bundle $\mathrm{TSO}(3)$ of $\mathrm{SO}(3)$. Under homogeneous representation of $\mathrm{SE}(3)$, this is explictly given by:

$$\begin{pmatrix} \mathbf{R} & \mathbf{t} \\ \mathbf{0} & 1 \end{pmatrix} \in \mathrm{SE}(3) \mapsto (\mathbf{R}, \widehat{\mathbf{t}}\mathbf{R}) \in \mathrm{TSO}(3) \tag{10}$$

where $\wedge$ takes the translation vector $\mathbf{t}$ to a skew symmetric matrix $\widehat{\mathbf{t}}$. A direct advantage of the $\mathrm{TSO}(3)$ model is that we can model all but one (namely E_p) symmetric subspaces as subbundles of $\mathrm{TSO}(3)$ [15]. We shall use $\mathrm{T}(), \mathrm{N}()$ and $\mathrm{C}() := \mathrm{T}() \oplus \mathrm{N}()$ to denote the tangent bundle, the normal bundle and the "complete" bundle, respectively.

(1) TP, NP and $\mathrm{CP} = \mathrm{TP} \oplus \mathrm{NP}$ are the tangent bundle, the normal bundle and the complete bundle of the projective plane $\mathrm{P} \simeq \mathbb{R}\mathrm{P}^2$ in $\mathbb{R}\mathrm{P}^3 \simeq \mathrm{SO}(3)$, having typical fiber $\mathbb{R}^2$, $\mathbb{R}^1$ and $\mathbb{R}^3$ respectively. It can be shown that NP is the unique twisting line bundle over P and CP is a trivial vector bundle over P.

(2) $\mathrm{N_P L} = \mathrm{TP} \cap \mathrm{NL}$ is the normal bundle over the projective line $\mathrm{L} \simeq \mathrm{SO}(2)$ in the tangent bundle TP of the projective plane P. It can be shown that this is just the Möbius strip, or the unique twisting line bundle over $\mathbb{R}\mathrm{P}^1 \simeq S^1$.

(3) $\mathrm{C_P L} = \mathrm{TP} \cap \mathrm{CL}$ is the complete bundle over L in TP. It can be shown that $\mathrm{C_P L}$ is the trivial line bundle over the Möbius strip.

Note that with the tangent bundle description $\mathrm{TSO}(3)$ of $\mathrm{SE}(3)$, the Lie subgroups (Table 1) and POE submanifolds (Table 2) mostly reduce to trivial subbundles of $\mathrm{TSO}(3)$, in comparison to the mostly non-trivial subbundles corresponding to the symmetric subspaces listed above.

During our investigation of application of symmetric subspaces of $\mathrm{SE}(3)$ in type synthesis of mechanisms [13], we noticed that the type synthesis of mechanical generators for trivial and non-trivial subbundles are extremely distinct. Trivial subbundles of $\mathrm{TSO}(3)$ with base space $S^1 \simeq \mathbb{R}\mathrm{P}^1$, T^2 (torus) or $\mathrm{SO}(3)$ can usually be generated by a serial chain, while non-trivial subbundles with base space S^1 or $\mathbb{R}\mathrm{P}^2$ do not admit serial chain generators. Moreover, the non-triviality of the symmetric subspaces results in a coupling among multiple DoFs, which fits the motion characteristics of many kinesiological systems such as the human shoulder complex, wrist and knee [12, 13, 21–23]. This suggests that symmetric subspaces have potential applications in rehabilitation robotics (e.g. artificial joints and exoskeletons). Another advantage of this topological characterization is that a practical mechanism design may slightly deviate from the plane or line symmetric configuration required for mechanical generators of symmetric subspaces, without completely altering its motion characteristics.

4. SYMMETRIC SUBSPACES AS SUBVARIETIES OF $\mathbb{R}\mathrm{P}^7$

Elements of $\mathrm{SE}(3)$ can be represented as points in $\mathbb{R}\mathrm{P}^7$ under the dual quaternion representation [24]:

$$\mathbf{g} = a_0 + a_1\mathbf{i} + a_2\mathbf{j} + a_3\mathbf{k} + b_0\varepsilon + b_1\mathbf{i}\varepsilon + b_2\mathbf{j}\varepsilon + b_3\mathbf{k}\varepsilon, \quad \mathbf{g} \in \mathrm{SE}(3) \tag{11}$$

The homogeneous coordinate $(a_0 : a_1 : a_2 : a_3 : b_0 : b_1 : b_2 : b_3)$ satisfies the homogeneous quadratic constraint $a_0b_0 + a_1b_1 + a_2b_2 + a_3b_3 = 0$, which defines a 6-$D$ quadric in

Table 4. Dual quaternion representation of symmetric subspaces of $\mathrm{SE}(3)$.

dim	$\mathfrak{m}$	dual quaternion representation of $\exp(\mathfrak{m})$
2	P	$\{(a_0 : a_1 : a_2 : 0 : 0 : 0 : 0 : 0) \in \mathbb{R}\mathrm{P}^2\}$
	$\mathrm{N_P L}$	$\{(a_0 : a_1 : 0 : 0 : 0 : 0 : 0 : b_3) \in \mathbb{R}\mathrm{P}^2\} - \mathbf{k}\varepsilon$
3	$\mathrm{C_P L}$	$\{(a_0 : a_1 : 0 : 0 : b_0 : b_1 : b_2 : 0) \in \mathbb{R}\mathrm{P}^4 \mid \sum_{i=0}^{1} a_i b_i = 0\} - \varepsilon \wedge \mathbf{i}\varepsilon \wedge \mathbf{j}\varepsilon$
	NP	$\{(a_0 : a_1 : a_2 : 0 : 0 : 0 : 0 : b_3) \in \mathbb{R}\mathrm{P}^3\} - \mathbf{k}\varepsilon$
4	TP	$\{(a_0 : a_1 : a_2 : 0 : b_0 : b_1 : b_2 : 0) \in \mathbb{R}\mathrm{P}^5 \mid \sum_{i=0}^{2} a_i b_i = 0\} - \varepsilon \wedge \mathbf{i}\varepsilon \wedge \mathbf{j}\varepsilon$
5	CP	$\{(a_0 : a_1 : a_2 : 0 : b_0 : b_1 : b_2 : b_3) \in \mathbb{R}\mathrm{P}^6 \mid \sum_{i=0}^{2} a_i b_i = 0\} - \varepsilon \wedge \mathbf{i}\varepsilon \wedge \mathbf{j}\varepsilon \wedge \mathbf{k}\varepsilon$

$\mathbb{R}\mathrm{P}^7$ known as the *Study quadric*. A straightforward computation shows that all symmetric subspaces except E_p are either projective subspaces or quadrics in the Study quadric, with its intersection with the ideal 3-plane $\varepsilon \wedge \mathbf{i}\varepsilon \wedge \mathbf{j}\varepsilon \wedge \mathbf{k}\varepsilon$ removed (see Table 4). Here $\wedge$ denotes wedge product.

The subspace/quadric representation of the symmetric subspaces has several applications in robotics. First, recall that $\exp(\boldsymbol{\xi}(t)), t \in \mathbb{R}^1$ represents a line symmetric motion if and only if the axis of $\boldsymbol{\xi}(t)$ is concurrent and perpendicular with a line $\boldsymbol{l}_0 \in \mathrm{SE}(3)$ considered as a half-turn [18]. Without loss of generality, we take $\boldsymbol{l}_0$ to be $\mathbf{k}$ and the 2-parameter family of lines satisfying these two conditions is exactly the degenerate congruence defined by $\mathfrak{tp}$. Therefore, we may as well refer to TP as the line symmetric subspace. In this case, TP is exactly the quadric defined by the intersection of the Study quadric with the 5-plane $1 \wedge \mathbf{i} \wedge \mathbf{j} \wedge \varepsilon \wedge \mathbf{i}\varepsilon \wedge \mathbf{j}\varepsilon$, excluding the ideal 2-plane $\varepsilon \wedge \mathbf{i}\varepsilon \wedge \mathbf{j}\varepsilon$. All line symmetric motion trajectories studied by Selig [18] are therefore trajectories in TP. An alternative way to understand this is to see that line symmetric motions are closed under inversion symmetry:

$$\forall \mathbf{g} = \boldsymbol{l}_1 \boldsymbol{l}_0, \mathbf{h} = \boldsymbol{l}_2 \boldsymbol{l}_0 \Rightarrow \mathbf{g}\mathbf{h}^{-1}\mathbf{g} = \boldsymbol{l}_1 \boldsymbol{l}_0 (\boldsymbol{l}_2 \boldsymbol{l}_0)^{-1} \boldsymbol{l}_1 \boldsymbol{l}_0 = (\boldsymbol{l}_1 \boldsymbol{l}_2 \boldsymbol{l}_1^{-1}) \boldsymbol{l}_0 \tag{12}$$

where $\boldsymbol{l}_1 \boldsymbol{l}_2 \boldsymbol{l}_1^{-1}$ is a line conjugate to $\boldsymbol{l}_2$. Selig also considered several degenerate line symmetric motions, with the ruled surface given by a cone, a cylinder or a developable of plane curves [18]. When the ruled surface is a cone, the trajectory lies completely in P, which is identified with the 2-plane $1 \wedge \mathbf{i} \wedge \mathbf{j}$. The line symmetric motion generated by a developable of plane curve lies in $\mathrm{N_P L}$, which lies in another 2-plane $1 \wedge \mathbf{i} \wedge \mathbf{k}\varepsilon$.

Similarly, if $\boldsymbol{\pi}_0$ is the reflection about the $\mathbf{xy}$-plane (the defining plane of NP), the corresponding plane symmetric motions [18] reside in the 3-D symmetric subspace NP, which is exactly the $\mathbf{B_1}$-plane $1 \wedge \mathbf{i} \wedge \mathbf{j} \wedge \mathbf{k}\varepsilon$ (with an ideal point $\mathbf{k}\varepsilon$ removed) investigated in [24]. It is obvious that plane symmetric motions are closed under inversion symmetry:

$$\forall \mathbf{g} = \boldsymbol{\pi}_1 \boldsymbol{\pi}_0, \mathbf{h} = \boldsymbol{\pi}_2 \boldsymbol{\pi}_0 \Rightarrow \mathbf{g}\mathbf{h}^{-1}\mathbf{g} = \boldsymbol{\pi}_1 \boldsymbol{\pi}_0 (\boldsymbol{\pi}_2 \boldsymbol{\pi}_0)^{-1} \boldsymbol{\pi}_1 \boldsymbol{\pi}_0 = (\boldsymbol{\pi}_1 \boldsymbol{\pi}_2 \boldsymbol{\pi}_1^{-1}) \boldsymbol{\pi}_0 \tag{13}$$

The fact that line symmetric motions lie in the 5-plane TP of the Study quadric can be used to infer the full-cycle mobility of a line symmetric 6R (R for revolute joint) linkage [25]. The implication of full-cycle mobility of overconstrained linkages using dimensionality of subspaces of $\mathbb{R}\mathrm{P}^7$ is also discussed in [26].

5. CONCLUSIONS

In this paper, we have highlighted three different characterizations of symmetric subspaces of $\mathrm{SE}(3)$, and illustrated their applications in several different problems in robotics. First, as the exponential of LTSs of $\mathfrak{se}(3)$, symmetric subspaces share common properties **(SS 1)–(SS 6)** which lead to a general theory for analysis and synthesis of their mechanical generators [13, 20]. Second, as non-trivial subbundles of $\mathrm{TSO}(3)$, symmetric subspaces admit distinct motion characteristics in comparison to Lie subgroups and POE submanifolds, and are shown to have potential applications in kinesiology and rehabilitation robotics [12]. Finally, as subspaces or quadrics of the Study quadric (under dual quaternion representation), symmetric subspaces are closely related to line symmetric and plane symmetric motions and therefore study of overconstrained linkages [18, 25].

Acknowledgements

Dr. Wu is financially supported by the 2007-2013 ERDF Emilia-Romagna Regional Operational Programme at the Interdepartmental Center for Health Sciences and Technologies. Dr. Carricato gratefully acknowledges the financial support of the Italian Ministry of Education, Universities and Research through the PRIN grant No. 20124SMZ88. This work is also in partial fulfillment to Hong Kong RGC Grant No.616509, No.615610 and No.615212, China National Natural Science Foundation Grant No.51375413 and Shenzhen Municipal Science and Technology Planning Program for Basic Research No.JCYJ 20120618150931822, which supported Dr. Wu when he was working at HKUST.

REFERENCES

[1] Brockett, R., 1984. "Robotic manipulators and the product of exponentials formula". In Mathematical Theory of Networks and Systems, Springer, pp. 120–129.

[2] Knapp, A. W., 2002. *Lie Groups Beyond an Introduction (Progress in Mathematics)*. Springer.

[3] Murray, R., Li, Z., and Sastry, S., 1994. *A Mathematical Introduction to Robotic Manipulation*. CRC press.

[4] Hervé, J., 1999. "The Lie group of rigid body displacements, a fundamental tool for mechanism design". *Mechanism and Machine Theory,* **34**(5), pp. 719–730.

[5] Meng, J., Liu, G., and Li, Z., 2007. "A geometric theory for analysis and synthesis of sub-6 dof parallel manipulators". *IEEE Transactions on Robotics,* **23**(4), pp. 625–649.

[6] Carricato, M., and Rico-Martínez, J. M., 2010. "Persistent screw systems". In *Advances in Robot Kinematics: Motion in Man and Machine*. Springer, pp. 185–194.

[7] Carricato, M., and Rico-Martínez, J., 2011. "Persistent screw systems of dimension three". In Proc. of 13th World Congress in Mechanism and Machine Science, Guanajuato, Mexico, pp. 1–12.

[8] Carricato, M., 2012. "Persistent screw systems of dimension four". In *Latest Advances in Robot Kinematics*. Springer, pp. 147–156.

[9] Carricato, M., and Zlatanov, D., 2014. "Persistent screw systems". *Mechanism and Machine Theory,* **73**, pp. 296–313.

[10] Carricato, M., 2014. "Four-dimensional persistent screw systems of the general type". In *Computational Kinematics*. Springer, pp. 299–306.

[11] Wu, Y., Wang, H., and Li, Z., 2011. "Quotient kinematics machines: concept, analysis, and synthesis". *Journal of Mechanisms and Robotics,* **3**(4), p. 041004.

[12] Wu, Y., Liu, G., Löwe, H., and Li, Z., 2013. "Exponential submanifolds: A new kinematic model for mechanism analysis and synthesis". In IEEE International Conference on Robotics and Automation (ICRA), pp. 4177–4182.

[13] Wu, Y., Löwe, H., and Li, Z., 2014. "Inversion symmetry of the Euclidean group: Theory and application in robot kinematics". submitted to IEEE Transactions on Robotics on Sept. 22, 2014.

[14] Loos, O., 1969. *Symmetric Spaces*. W. A. Benjamin.

[15] Löwe, H., Wu, Y., and Carricato, M., 2015. "Symmetric subspaces of $se(3)$". *Advances in Geometry*. Accepted.

[16] Wu, Y., and Carricato, M., 2015. "Identification and geometric characterization of Lie triple screw systems". 14th IFTOMM World Congress.

[17] Hunt, K. H., 1978. *Kinematic Geometry of Mechanisms (Oxford Engineering Science Series)*. Oxford University Press.

[18] Selig, J., and Husty, M., 2011. "Half-turns and line symmetric motions". *Mechanism and Machine Theory,* **46**(2), pp. 156–167.

[19] Hunt, K., 1973. "Constant-velocity shaft couplings: a general theory". *Journal of Manufacturing Science and Engineering,* **95**(2), pp. 455–464.

[20] Wu, Y., and Carricato, M., 2015. "Design of a novel 3-dof serial-parallel robotic wrist: A symmetric space approach". In Proceedings of International Symposium on Robotics Research, Flagstaff, AZ, Aug.

[21] Schiele, A., and Visentin, G., 2003. "The ESA human arm exoskeleton for space robotics telepresence". In 7th International Symposium on Artificial Intelligence, Robotics and Automation in Space, pp. 19–23.

[22] Rosheim, M., 2006. *Leonardo's Lost Robots*. Springer.

[23] Parenti-Castelli, V., Leardini, A., Di Gregorio, R., and O'Connor, J., 2004. "On the modeling of passive motion of the human knee joint by means of equivalent planar and spatial parallel mechanisms". *Autonomous Robots,* **16**(2), pp. 219–232.

[24] Selig, J., 2004. *Geometric Fundamentals of Robotics (Monographs in Computer Science)*. Springer. 2nd ed.

[25] Selig, J., 2014. "Some remarks on the RRR linkage". In *Advances in Robot Kinematics*. Springer, pp. 77–85.

[26] Hegedüs, G., Schicho, J., and Schröcker, H.-P., 2013. "The theory of bonds: A new method for the analysis of linkages". *Mechanism and Machine Theory,* **70**, pp. 407–424.

MEASUREMENT OF ARTICULAR ANGLES AND GROUND FORCES IN THE SIT-TO-STAND MOVEMENT

Nicola Sancisi
Department of Industrial Engineering,
University of Bologna, Italy
E-mail: nicola.sancisi@unibo.it

Marco Cocconcelli
Department of Sciences and Methods of Engineering,
University of Modena and Reggio Emilia, Italy
E-mail: marco.cocconcelli@unimore.it

Riccardo Rubini
Department of Sciences and Methods of Engineering,
University of Modena and Reggio Emilia, Italy
E-mail: riccardo.rubini@unimore.it

Vincenzo Parenti Castelli
Department of Industrial Engineering,
University of Bologna, Italy
E-mail: vincenzo.parenti@unibo.it

Abstract. *In this paper, two motion protocols are presented that describe the sequence of movements to be complied with by a subject to perform a sit-to-stand movement. In gait analysis, the sit-to-stand movement is the movement a patient does when he/she gets up from a chair and stands in upright position. The protocols are intended to obtain repeatable and reproducible results that can be compared among different studies. The first protocol (standard) is closer to other studies in the literature, in order to improve comparison with previous experimental results. The second protocol (natural) reproduces a sit-to-stand movement more similar to natural conditions. The main differences between the two protocols are in the knee angle, the pose of the arms and the torso at the beginning of the test. The two motion protocols are tested by a volunteer on a gait lab. Results of experimental tests in terms of joint and foot-ground angles, ground reaction force and center of pressure show both the repeatability of the tests and the differences between standard and natural movement during sit-to-stand.*

Keywords: *gait analysis, sit-to-stand movement, motion protocols*

1. INTRODUCTION

In gait analysis, the experimental protocol defines several details of the experiment, such as the initial setup, the execution of the test and the post-processing of the data, in order to obtain repeatability of experimental measurements: the marker position on the patient body, the measurement technique, the local reference systems are all defined by the experimental protocol. Among these aspects, a specific part of this protocol is the so-called motion protocol, which defines the motion tasks and the way it is performed. For common motion tasks such as the walking, different experimental protocols have been proposed so far in the literature [1], but the motion protocol is almost standard. Conversely, several motion tasks do not even have a standard motion protocol.

The sit-to-stand movement, which is the movement a patient does when he/she gets up from a chair and stands in upright position, is one of these. This is a common and important task: it features an eccentric position of the patient center of mass, demanding a complex control and dynamics to reach and maintain the upright position; it generates anterior-posterior loads on the joint that must be compensated by the patient muscles to keep stability at the joint. However, the literature lacks of a standardization of this motion task. Etnyre and Thomas [2] proposed a motion protocol for the sit-to-stand that focused on the position of the arms and its influence during this movement. Portnoy and Morin [3] and Houtz and Walsh [4] studied the electric activity in the muscles, while Schenkman [5] and Kralj [6] divided the sit-to-stand movement into four steps, and analyzed them separately in terms of forces and joint angles. Other studies investigated the effect of the age [7], the speed of the movement [8] and other aspects on the kinematics of the lower limbs. Often the proposed motion protocols are not for general analyses, but are developed with a specific target in mind, e.g. Hirschfeld [9] studied the load transfer from the buttocks to the feet during the movement, while Kawagoe [10] studied the effect of feet positioning and the type of chair on the kinematics of the movement. In particular, Kawagoe proved the importance of two parameters: the positioning of the feet at the beginning of the test and the height of the chair, which influences the position of the femur with respect to the ground. These motion protocols optimize the acquisition of specific data, but the subject natural movement is sacrificed, since it is far from everyday life. This aspect could affect the outcomes of the experimental tests, given the sensitivity of measurements to some parameters [10]: these results could not represent a realistic loading condition.

This paper presents two motion protocols, namely the standard condition protocol (SCP) and natural condition protocol (NCP), for the study of the sit-to-stand movement. Both are developed to maximize the repeatability and the standardization of the tests. The NCP, in particular, is developed to make the movement as close as possible to the real human movement. The protocols are detailed in Section 2, while in Section 3 they are performed by a subject and experimental results from both protocols are compared in Section 4.

2. PROTOCOLS

The SCP and NCP are presented in this Section. The SCP favors the repeatability of the trial and the comparison with results in the literature. The NCP makes the movement as close as possible to everyday life, while maintaining the repeatability of the trial. The main differences between the two protocols are in the knee angle, the pose of the arms and the torso at the beginning of the test.

In this study, since only two platforms are available and are not aligned, the right and

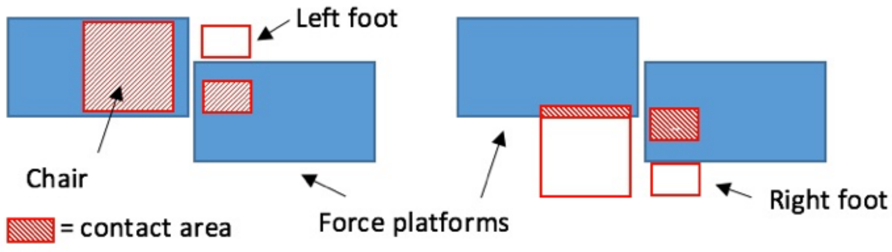

Figure 1. Placement of the chair and feet on the force platforms

left legs are analyzed separately; moreover, the chair is placed on one platform, while the tested foot is in contact with the second one. Just half of the chair load is measured during the left leg test, while the full chair load is measured during the right leg test. A schematic picture of the setup is shown in Fig. 1. It is worth noting, however, that measurements could be simplified if three force platforms are used, one for the chair and two for the feet: in this case, the simultaneous measurements of both legs would be allowed.

Standard Condition Protocol (SCP)
The SCP requirements are listed below:

1. Initial position
    - the subject sits on the chair with knees bent at 90 degrees
    - the feet are in full contact with the ground
    - the hands are placed on the knees
    - the torso and the head are straight and aligned
2. Sit-to-stand movement
    - the torso and the head remain aligned and are bent until the head is vertically aligned with the knees
    - the subject starts getting up from the chair
    - the arms remain extended, while the hands move along the thighs and are placed sideways at the end
    - the subject stands completely straight

Natural Condition Protocol (NCP)
The NCP requirements are listed below:

1. Initial position
    - the subject sits on the chair
    - the feet are in full contact with the ground and are moved back 13 cm compared to the SCP

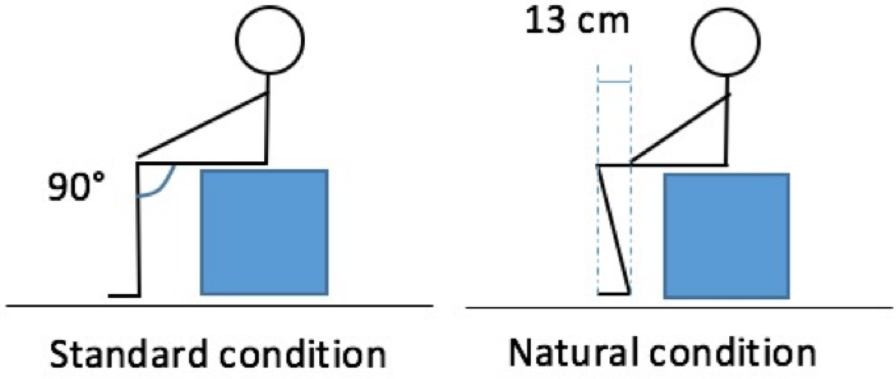

Figure 2. Different initial conditions for the standard and natural protocols

- the hands are placed on the thighs, vertically aligned with the heels
- the torso is in a natural position
- the head is straight

2. Sit-to-stand movement

   - the torso and the head remain aligned and are bent until the head is vertically aligned with the knees
   - the subject starts getting up from the chair
   - the arms remain extended, while the hands move along the thighs and are placed sideways at the end
   - the subject stands completely straight

The sit-to-stand movement is basically the same for the SCP and NCP: the main differences are in the initial position. A representation of the setup is shown in Fig. 2.

3. EXPERIMENTAL ANALYSES

Experimental tests on a volunteer were performed in a gait analysis laboratory by means of an optoelectronic system (Vicon Motion Systems Ltd) with six infrared cameras, a set of passive reflective markers and two force platforms (AMTI OR6). The two platforms were positioned at the ground level and were not aligned. The markers were placed on the subject body according to the Total3Dgait protocol [1]. Each trial consisted of one sit-to-stand cycle, and was repeated three times for the SCP and three times for the NCP, preceded by two free cycles.

Experimental data were post-processed in order to obtain for both legs the knee and ankle flexion angles, together with the resultant vector (also called the ground reaction force, GRF) and the center of pressure (COP) of the contact force distribution between each foot and the ground. Two reference systems were defined. A global reference system had horizontal plane parallel to the ground. An anatomical reference system was obtained on the

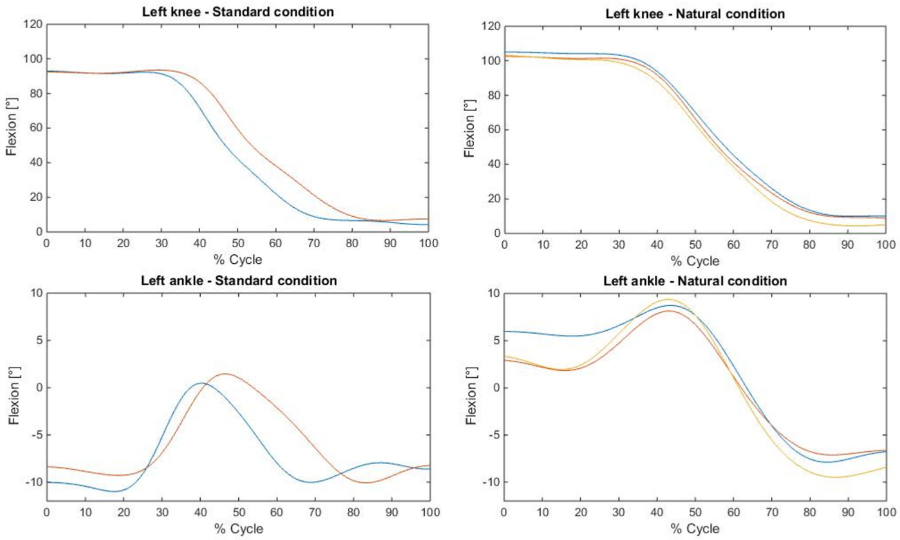

Figure 3. Comparison of the knee and ankle flexion angles for the SCP and NCP in the left leg.

foot from the foot markers, namely the markers on the calcaneus (P1), on the fifth (P2) and on the first (P3) metatarsal heads and the mid-point (P4) between P2 and P3: these points were projected on the global horizontal plane (P1*,...,P4*) and the foot reference system was defined with origin P1*, anterior axis connecting P1* and P4*, medial axis on the horizontal plane, orthogonal to the anterior axis, pointing medially, vertical axis orthogonal to the horizontal plane, pointing up (coincident with the global vertical axis). Thus, the left and right foot reference systems are left and right handed respectively. The GRF and COP were represented with respect to the foot reference system. Flexion angles were defined according to the Total3Dgait protocol. The forces were scaled on the subject's weight, COP trajectories were scaled on the length and width of the subject's feet, while time was scaled on each cycle duration.

4. RESULTS

Only results of left leg are presented for the sake of conciseness. The knee and ankle angles are shown in Fig. 3, where the different curves represent the different repetitions. The curves for the SCP and NCP are similar, but the flexion angles at the beginning of the test are higher for the NCP; this aspect increases the peak flexion angles reached during the movement, with respect to the SCP. Thus, the angles that should be considered during prosthesis and orthosis design are higher than those obtained during standard motion protocols, in order to allow a natural sit-to-stand movement for the subject.

GRF components are shown in Fig. 4, where the different types of line represent the different GRF components, while the different curves for each type are the different repetitions. During the NCP, the peak GRF component values are lower and their overall variation is lower during the movement. Moreover, in these conditions the ratio between the antero/posterior

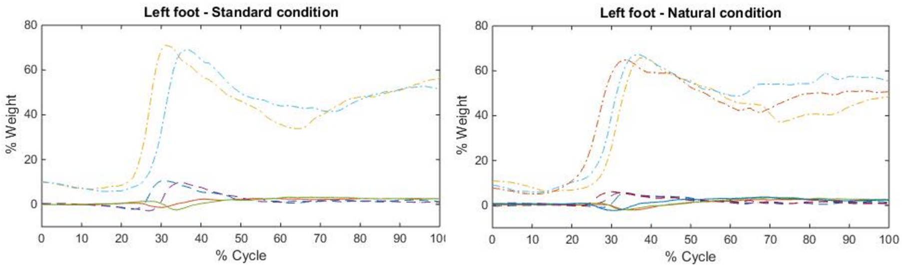

Figure 4. Comparison of the GRF for the SCP and NCP in the left leg. Vertical, antero/posterior and medio/lateral GRF components are represented with dash-dotted, dashed and solid lines respectively.

component peak value and the corresponding GRF magnitude is lower (11% vs 14% obtained during the SCP). All these considerations suggest that the natural conditions are characterized by an optimization (i.e., a reduction) of the force on the leg and on the subject's joints; this optimization affects in particular the antero/posterior components, that usually generate antero/posterior loads on the joint that must be compensated by the subject muscles to keep stability at the joint.

Finally, COP trajectories are shown in Fig. 5. For both the SCP and the NCP, these trajectories are basically lines that coincide with the antero/posterior axis of the foot reference system. The main difference between the two motion protocols is that the COP reaches a more anterior position during the NCP.

In general, the two protocols were easily repeated by the volunteer after a few free trials. A visual inspection of the material recorded during the test shows very similar movements for all repetitions of each protocol. This qualitative analysis is confirmed quantitatively by the results: all curves look similar over different repetitions and very similar peak values are reached. The only significant difference is timing, that was not strictly controlled during each cycle. A first possibility to improve this aspect is to better instruct the volunteer on a specific time sequence or to help him/her by beating the time, at the risk of a less natural movement of the subject. A second possibility is to choose a different parameter to represent different movements (such as the knee flexion angle) or to divide the recorded motion into several events that are synchronized for all repetitions, at the risk of biased data since speed of each test phase influences the results (GRF in particular) due to the different inertial forces.

5. CONCLUSIONS

Two new protocols for the sit-to-stand movement analysis are proposed in this paper. The standard condition protocol is developed to maximize the standardization and the repeatability of the measurements, also with respect to previous studies in the literature. The natural condition protocol maintains the repeatability of the test but, in addition, is closer to the natural sit-to-stand movement. Experimental measurements were performed in a gait analysis lab on a volunteer. The protocols were well accepted and easily learned by the subject. Results show repeatability over several trials and allow the analysis of the joint angles, of the ground reaction force and of the center of pressure. Despite the apparently minor differences

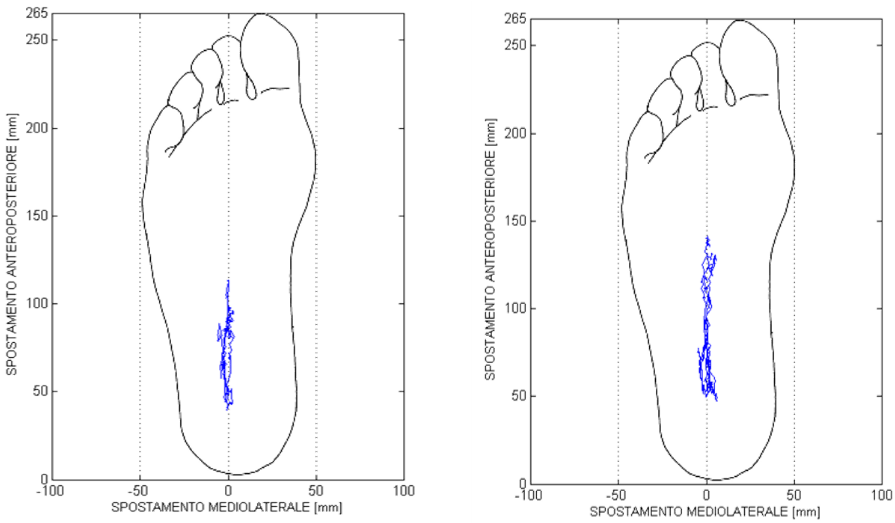

Figure 5. Comparison of the COP for the SCP and NCP in the left leg.

between the two motion protocols, some significant differences could be observed in terms of forces and motion. Timing could be improved, depending on the application of the data. Moreover, the two protocols should be tested and validated on more subjects, for a better statistical analysis of repeatability.

Acknowledgements

The authors want to acknowledge Dr Alberto Ferrari, for his help during experimental measurements.

REFERENCES

[1] Ferrari, A., Benedetti, M., Pavan, E., Frigo, C., Bettinelli, D., Rabuffetti, M., Crenna, P., and Leardini, A., 2008. “Quantitative Comparison of Five Current Protocols in Gait Analysis”. *Gait & Posture,* **28**(2), Aug, pp. 207–216.

[2] Etnyre, B., and D.Q.Thomas, 2007. “Event Standardization of Sit-to-stand Movements”. *Physical Therapy,* **87**(12), Dec, pp. 1651–1666.

[3] Portnoy, H., and Morin, F., 1956. “Electromyographic Study of Postural Muscles in Various Positions and Movements”. *American Journal of Physiology,* **186**(1), Jan, pp. 122–126.

[4] Houtz, S., and Walsh, F., 1959. “Electromyographic Analysis of the Function of the Muscles Acting on the Ankle during Weight-bearing with Special Reference to the Triceps Surae”. *Journal of Bone and Joint Surgery. American Volume,* **41**(A), Dec, pp. 1469–1481.

[5] Schenkman, M., Berger, R., Riley, P., Mann, R., and Hodge, W., 1990. “Whole-body Movements During Rising to Standing from Sitting”. *Physical Therapy,* **70**(10), Oct, pp. 638–648.

[6] Kralj, A., Jaeger, R., and Munih, M., 1990. “Analysis of Standing Up and Sitting Down in Humans: Definitions and Normative Data Presentation”. *Journal of Biomechanics,* **23**(11), Nov, pp. 1123–1138.

[7] Papa, E., and Cappozzo, A., 2000. "Sit-to-stand Motor Strategies Investigated in Able-bodied Young and Elderly Subjects". *Journal of Biomechanics,* **33**(9), Sep, pp. 1113–1122.

[8] Pai, Y., and Rogers, M., 1991. "Speed Variation and Resultant Joint Torques During Sit-to-stand". *Archives of Physical Medicine and Rehabilitation,* **72**(11), Oct, pp. 881–885.

[9] Hirschfeld, H., Thorsteinsdottir, M., and Olsson, E., 1999. "Coordinated Ground Forces Exerted by Buttocks and Feet are Adequately Programmed for Weight Transfer During Sit-to-stand". *Journal of Neurophysiology,* **82**(6), Dec, pp. 3021–3029.

[10] Kawagoe, S., Tajima, N., and Chosa, E., 2000. "Biomechanical Analysis of Effects of Foot Placement with Varying Chair Height on the Motion of Standing Up". *Journal of Orthopedic Science,* **5**(2), Feb, pp. 124–133.

A PROCEDURE FOR THE DEFINITION OF A PATIENT-SPECIFIC KINEMATIC MODEL OF THE KNEE JOINT: AN IN-VIVO VALIDATION

Michele Conconi
Department of Industrial Engineering,
University of Bologna, Italy
E-mail: michele.conconi@unibo.it

Nicola Sancisi
Department of Industrial Engineering,
University of Bologna, Italy
E-mail: nicola.sancisi@unibo.it

Fabrizio Nardini
Department of Industrial Engineering,
University of Bologna, Italy
E-mail: fabrizio.nardini2@unibo.it

Vincenzo Parenti Castelli
Department of Industrial Engineering,
University of Bologna, Italy
E-mail: vincenzo.parenti@unibo.it

Abstract*. The capability to model human joint motion is a fundamental step towards the definition of effective treatments and medical devices, with an increasing request to adapt the devised models to the specificity of each subject. We present an approach for the definition of subject-specific models of the knee natural motion. The approach is the result of a combination of two different techniques and exploits the advantages of both. It relays upon non invasive measurements that can be performed in vivo, based on which a kinematic model of the natural motion is built, suitable to be extended to the definition of static and dynamic models. Comparison of the model outcomes with in-vivo measurements performed on one subject shows promising results supporting the proposed approach.*

Keywords*: Knee; kinematic modelling; subject-specific; non-invasive.*

1. INTRODUZIONE

Il moto naturale del ginocchio è il moto proprio dell'articolazione in assenza di carico. Esso rappresenta quindi lo stato dell’articolazione all’inizio dell’applicazione dei carichi associati a qualsiasi compito motorio. Il moto naturale pertanto fornisce un’importante base anche per lo studio del moto tibio-femorale in esercizio. Per tale ragione, la sua conoscenza è fondamentale in tutte quelle applicazioni che mirano a replicare o ripristinare il comportamento naturale del ginocchio, come nei casi di modellazione dell'arto inferiore, pianificazione chirurgica o progettazione di protesi. I modelli articolari consentono di ottenere informazioni sul moto dell’articolazione, ma anche sullo stato delle strutture articolari in assenza o in presenza di carichi, sia in condizione sana che protesizzata, aiutando quindi la comprensione dell'impatto di cure o dispositivi sul paziente.

La definizione del moto naturale medio del ginocchio può basarsi su dati da letteratura [1-3]. Ciò non permette però di catturare le specificità proprie di ciascun individuo, come invece necessario qualora si vogliano personalizzare trattamenti e/o geometria dei dispositivi protesici. Una misura accurata in vivo del moto articolare del singolo paziente, invece, è un operazione difficile ad oggi [4]: le tecniche non invasive possono essere inaccurate (marker cutanei) o troppo complesse (fluoroscopia) per la pratica standard, mentre tecniche più invasive (pin ossei) non sono accettabili nella maggioranza dei casi. La definizione di modelli articolari personalizzati sul paziente, validati sperimentalmente, apre la strada alla ricostruzione del moto naturale dell’articolazione del paziente a partire da misure non invasive. Inoltre, fornisce importanti strumenti di calcolo per studiare l’articolazione sotto diverse condizioni di carico e da diverse prospettive.

In questo lavoro viene presentato un approccio che combina due tecniche complementari al fine di giungere alla definizione di un modello articolare personalizzato. La prima tecnica (T1), sviluppata e validata originariamente per la caviglia [5], predice il moto dell’articolazione tramite ottimizzazione della capacità di distribuzione dei carichi sulle superfici articolari, assumendo che tale condizione sia rappresentativa della fisiologia delle articolazioni umane. T1 richiede una rappresentazione 3D delle superfici articolari, ottenibile con immagini biomediche standard. Il modello prodotto non è però impiegabile nello studio dell’articolazione e delle sue strutture in condizioni di carico generico.

La seconda tecnica (T2) modella il ginocchio come un meccanismo spaziale ad un grado di libertà (gdl). Tale meccanismo include nella sua definizione i vincoli rappresentativi dei due contatti condilari e quelli relativi alle fibre isometriche dei legamenti crociati anteriore (ACL) e posteriore (PCL) e del legamento collaterale mediale (MCL) [2, 6-8]. T2 ha dimostrato grande accuratezza nella replica del moto naturale ed ha il vantaggio di essere facilmente estendibile alla più complessa modellazione statica e dinamica, permettendo quindi di analizzare condizioni di carico generiche. Per contro, richiede un moto di riferimento per l’ottimizzazione dei parametri del modello.

In questo studio si propone di combinare le due tecniche in un nuovo approccio (T1+T2) che permetta di giungere alla definizione di un modello articolare specifico per il paziente (grazie a T2) partendo da una valutazione non invasiva del suo moto naturale (tramite T1). Tale approccio è stato testato in vitro in [9] ed è qui valutato in vivo. Lo scopo di questo lavoro è pertanto duplice: valutare l'attendibilità di T1 applicata all'articolazione di ginocchio e testare l'applicabilità di T1+T2 sulla stessa articolazione, a partire da misure eseguite in vivo. A tal fine, è stato esaminato un singolo paziente, ottenendo il moto naturale tramite T1 a partire da immagini da risonanza magnetica (MRI) e tomografia assiale computerizzata (CT). Sfruttando le informazioni sull'anatomia del paziente ricavate da queste immagini e il moto determinato da T1, il modello personalizzato è stato ottenuto applicando T2. Infine i risultati sia di T1 che della combinazione T1+T2 sono stati validati confrontandoli con il moto misurato sul paziente tramite fluoroscopia monoplanare.

2. METODI

Evidenze sperimentali indicano che la capacità di adattamento ai carichi propria dei tessuti biologici (adattamento funzionale) [10-13] si traduce per le superfici articolari nell'ottimizzazione della distribuzione dei carichi o, in altri termini, nella massimizzazione della congruenza articolare [14, 15]. E' dunque possibile ricostruire il moto dell'articolazione come inviluppo al variare dell'angolo di flessione delle configurazioni articolari a massima congruenza. Questa analisi è teoricamente applicabile a qualsiasi articolazione, compreso quindi il ginocchio.

Se il moto ottenuto massimizzando la congruenza articolare è rappresentativo dell'adattamento funzionale, tale moto dovrebbe essere caratterizzato da un comportamento isometrico dei legamenti del ginocchio. Infatti, l'adattamento funzionale porta nel caso dei legamenti alla minimizzazione della deformazione elastica, e quindi all'isometria, come discusso in [5] e come verificato in [9]. Tale isometria costituisce un importante analogia con il moto naturale di ginocchio: è infatti noto da letteratura che i legamenti ACL, PCL, MCL e LCL mostrano un comportamento isometrico durante il moto naturale. Molti studi hanno mostrato inoltre che il moto naturale relativo tra tibia e femore è caratterizzato da un gdl nello spazio tridimensionale, ovvero è parametrizzabile con un singolo parametro, ad esempio tramite l'angolo di flesso-estensione [2,3]. In definitiva, sulla base di queste osservazioni il moto naturale del ginocchio può essere considerato come un moto a un gdl nello spazio tridimensionale, caratterizzato dall'isometria dei legamenti e dalla massimizzazione della congruenza articolare. Queste informazioni possono essere sfruttate per costruire un modello articolare specifico per il singolo paziente a partire da immagini biomediche, come presentato in vitro in [9].

Per questo studio in vivo, il ginocchio destro di un volontario (maschio, 169 cm, 58 kg) è stato scansionato in CT e MRI. Le immagini così ottenute sono state segmentate ottenendo modelli 3D del femore distale e della tibia prossimale che comprendono ossa, cartilagini e inserzioni di ACL, PCL, MCL e LCL. La tecnica T1 è stata applicata alle scansioni da MRI come mostrato in [5] e [9], impiegando una misura della congruenza articolare [16] basata sul modello di contatto a fondazione elastica proposto da Winkler [17]. La tecnica T2 è stata quindi applicata come in [9] per giungere alla sintesi di un meccanismo spaziale 5-5 ad un gdl che include cinque membri rigidi binari rappresentativi di ACL, PCL, MCL e dei due contatti sfera-sfera approssimanti i contatti condili-piatto tibiale. La geometria iniziale, ricavata dall'anatomia del volontario, è stata ottimizzata per seguire al meglio il moto generato da T1.

Per poter validare i risultati della combinazione T1+T2 contro una misura sperimentale del moto naturale, una fluoroscopia monoplanare è stata registrata durante la flessione passiva del ginocchio del volontario. Modelli ossei da CT sono stati quindi allineati alle immagini fluoroscopiche per ottenere una misura sperimentale del moto tibio-femorale.

3. RISULTATI

Il moto relativo sperimentale tra femore e tibia e quelli risultanti dall'applicazione di T1 e di T1+T2 sono rappresentati in Figura 1, dove ciascuna delle cinque componenti dipendenti del moto (abduzione/adduzione AA, rotazione interna/esterna IE, traslazione antero/posteriore AP, medio/laterale ML e prossimo/distale PD) è mostrata al variare dell'angolo di flessione. In Tabella 1 sono rappresentati gli errori assoluti medi tra T1 e

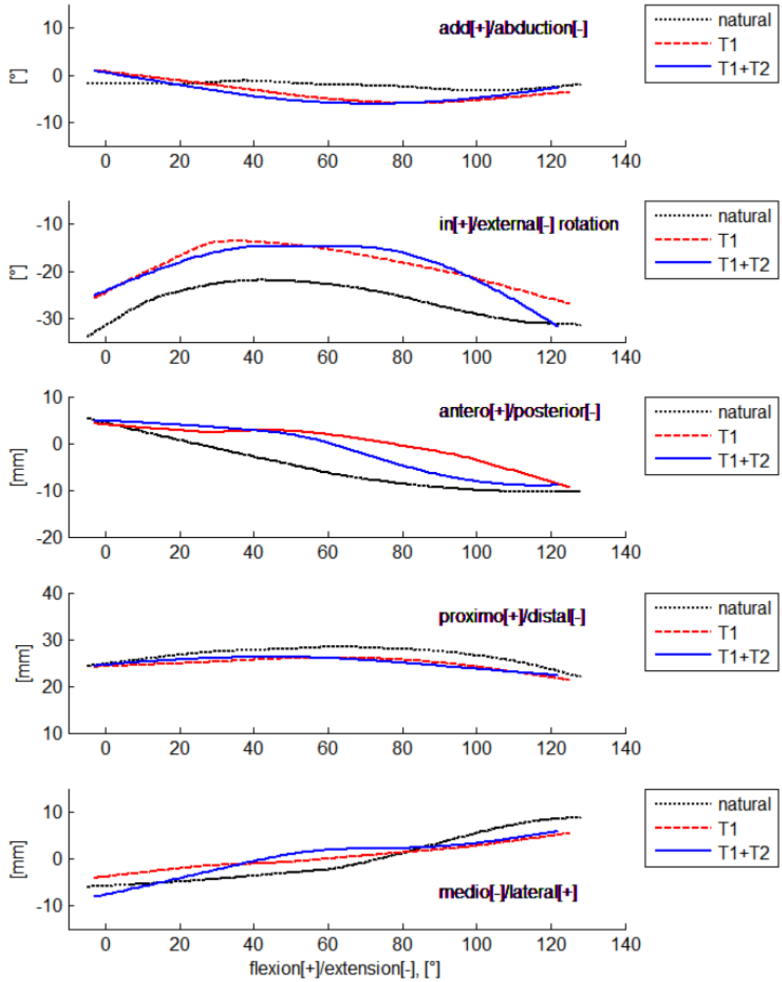

Figura 1. Confronto tra moto calcolato con T1 (linea rossa in tratteggio), moto calcolato con T1+T2 (linea blu continua) e dato sperimentale (linea nera a tratto).

Tabella 1. Errore assoluto medio per le componenti dipendenti del moto di flesso-estensione calcolato fra T1 e moto sperimentale, tra T1 e T1+T2 e infine tra T1+T2 e moto sperimentale.

	AA [°]	IE [°]	AP [mm]	PD [mm]	ML[mm]
T1 vs exp	2.11	7.27	5.02	1.99	2.33
T1 vs T1+T2	0.72	1.37	2.15	048	1.42
T1+T2 vs exp	2.35	7.16	3.64	1.93	2.17

moto sperimentale, tra T1 e T1+T2 e infine tra T1+T2 e moto sperimentale, per ciascuna delle cinque componenti dipendenti.

4. DISCUSSIONI

Il moto tibio-femorale predetto dalla combinazione delle due tecniche T1 e T2 replica bene i dati sperimentali. Ci sono tuttavia alcune differenze significative in IE e in AP. A dispetto delle differenze quantitative, le curve calcolate e misurate mostrano andamenti analoghi, in particolare per la IE che differisce sostanzialmente per un offset. Il tipico screw-home motion del ginocchio è pertanto correttamente predetto dal modello.

E' utile notare che, nonostante contatti e legamenti guidino l'articolazione lungo una traiettoria spaziale ad un gdl, il ginocchio mostra la sua maggiore cedevolezza proprio attorno all'asse di IE [18,19], che pertanto risulta la più sensibile tra le componenti di moto sia nelle misure sperimentali che nei modelli numerici.

Rispetto a quanto ottenuto in vitro in [9], i risultati dell'applicazione di T1 in vivo mostrano un lieve aumento dell'errore. Occorre però considerare che l'analisi qui svolta ha fatto uso per la MRI di sequenze tradizionali 2D FSE nel piano sagittale e non di sequenze 3D isotropic FSE, come accaduto in [9]. Ciò può aver ridotto la qualità della rappresentazione tridimensionale delle superfici articolari, influenzando i risultati di T1. Inoltre, il moto sperimentale è stato acquisito con fluoroscopia monoplanare eseguita su piano sagittale. Tale tecnica è meno precisa di sistemi stereofotogrammetrici quali quelli usati in [9]. Alla luce di queste considerazioni i risultati qui ottenuti possono essere considerati confrontabili con quelli ottenuti in vitro.

5. CONCLUSIONI

Lo scopo di questo lavoro era testare in vivo un approccio per la definizione di un modello del moto naturale di ginocchio specifico per il singolo individuo basato su misure non invasive. L'approccio si basa sulla combinazione di due tecniche definite T1 e T2 che insieme contribuiscono alla definizione del modello finale. In questo modo vengono sfruttati i vantaggi di ciascuna delle due tecniche: T1 fornisce una previsione del moto naturale a partire da una rappresentazione delle superfici articolari ottenibile da misure non invasive quali MRI; quindi, a partire da tale moto e dall'anatomia del paziente, T2 sintetizza un meccanismo che rispetta i vincoli imposti da legamenti e contatti articolari. Il modello finale riproduce il moto naturale del paziente e permette la semplice estensione a più complicati modelli articolari statici e dinamici.

I risultati della combinazione di T1 e T2 sono in buon accordo con i dati sperimentali, anche se alcune differenze sono osservabili. Future osservazioni avranno lo scopo di validare ulteriormente tale approccio ed eventualmente spiegare tali differenze.

BIBLIOGRAFIA

[1]. Blankevoort, L., Huiskes, R., De Lange, A., 1988. "The envelope of passive knee joint motion". *Journal of Biomechanics* **21**(9), 705 – 720.

[2] Ottoboni, A., Parenti-Castelli, V., Sancisi, N., Belvedere, C., Leardini, A., 2010. "Articular surface approximation in equivalent spatial parallel mechanism models of the human knee joint". *Proceedings of the Institution of Mechanical Engineers, Part H: Journal of Engineering in Medicine*, **224**(9), 1121–1132.

[3] Wilson, D., Feikes, J., Zavatsky, A., O'Connor, J., 2000. "The components of passive knee movement are coupled to flexion angle". *Journal of Biomechanics*, **33**(4), 465 – 473.

[4] Masum, M.A., Pickering, M.R., Lambert, A.J., Scarvell, J.M., Smith, P.N., 2014. "A review: Techniques for kinematic analysis of knee joints". In: Australian Biomedical Engineering Conference (ABEC).

[5] Conconi, M., Leardini, A., Parenti-Castelli, V., 2015. "Joint kinematics from functional adaptation: A validation on the tibio-talar articulation". *Journal of Biomechanics*, **48**(12), 2960 – 2967.

[6] Parenti-Castelli, V., Di Gregorio, R., 2000. "Parallel mechanisms applied to the human knee passive motion simulation", pp. 333–344. Kluwer Academic Publishers, Pirano-Portoroz, Slovenia.

[7] Sancisi, N., Parenti-Castelli, V., 2011. "A novel 3d parallel mechanism for the passive motion simulation of the patella-femur-tibia complex". *Meccanica*, **46**(1), 207–220.

[8] Sancisi, N., Parenti-Castelli, V., 2012. "On the role of passive structures in the knee loaded motion", pp. 1–8. Springer, Berlin.

[9] Conconi, M., Sancisi N. and Parenti-Castelli, V., 2016. "Subject-specific model of knee natural motion: a non-invasive approach", 15th conference of Advances in Robot Kinematics - ARK, Grasse, France, June.

[10] Benjamin, M., Ralphs, J.R., 1998. "Fibrocartilage in tendons and ligaments-an adaptation to compressive load". *J. Anat.*, **193** (Pt 4), 481–494.

[11] Eckstein, F., Hudelmaier, M., Putz, R., 2006. "The effects of exercise on human articular cartilage". *J. Anat.*, **208**, 491–512.

[12] Hayashi, K., 1996. "Biomechanical studies of the remodeling of knee joint tendons and ligaments". *J Biomech*, **29**, 707–716.

[13] Robling, A.G., Castillo, A.B., Turner, C.H., 2006. "Biomechanical and molecular regulation of bone remodeling". *Annu Rev Biomed Eng*, **8**, 455–498.

[14] Frost, H.M., 1999. "An approach to estimating bone and joint loads and muscle strength in living subjects and skeletal remains". *Am. J. Hum. Biol*. **11**, 437–455.

[15] Heegaard, J.H., Beaupre, G.S., Carter, D.R., 1999. "Mechanically modulated cartilage growth may regulate joint surface morphogenesis". *J. Orthop. Res*. **17**, 509–517.

[16] Conconi, M., Parenti-Castelli, V., 2014. "A sound and efficient measure of joint congruence". *Proceedings of the Institution of Mechanical Engineers, Part H: Journal of Engineering in Medicine*, **228**(9), 935 – 941.

[17] Johnson, K., 1985. Contact mechanics. Cambridge: Cambridge University Press.

[18] Grood, E.S., Stowers, S.F., Noyes, F.R., 1988. "Limits of movement in the human knee. Effect of sectioning the posterior cruciate ligament and posterolateral structures". *J Bone Joint Surg Am*, **70**(1), 88–97.

[19] Markolf, K.L., Mensch, J.S., Amstutz, H.C., 1976. "Stiffness and laxity of the knee–the contributions of the supporting structures. A quantitative in vitro study". *J Bone Joint Surg Am* **58**(5), 583–594.

RESULTS OF THE TEFFMA EUROPEAN FP7 PROJECT: TOWARDS EXPERIMENTAL FULL FIELD MODAL ANALYSIS

Alessandro Zanarini
Department of Industrial Engineering,
University of Bologna, Italy
e-mail: a.zanarini@unibo.it

Abstract. *The improvements in the electronics of modern cameras have raised the attention on image based technologies also for the measurement of complex vibration patterns for dynamic analyses in a broad extent beyond Holography. The advent of digital cameras has brought ESPI techniques to a recent success. Besides, the production of hi-speed digital cameras has recently raised DIC technique as another competitive technology in the full field domain; the SLDV, thanks to its ability to scan discrete locations over the surface, can also be considered close to the full field technologies. Present dynamic testing and analysis approaches, based on traditional transducers, do not take full advantage of the growing optical measurements, while full field techniques have proved to be increasingly effective in complex dynamic analysis.*

The potential of three completely different technologies was benchmarked in the TEFFMA project. SLDV, dynamic ESPI and hi-speed DIC were here first deployed in a complex and unique test on the estimation of FRFs with high spatial accuracy from a thin vibrating plate. A peculiar pointwise comparison was addressed by means of discrete geometry transforms to put all the three technologies on trial at each physical point of the surface.

These researches numerically evaluated and compared also rotational and dynamic strain FRFs. Thereafter, dynamic stress FRFs can be modelled directly, by means of a constitutive model: spectral fatigue approaches can try to predict the life of a component in many excitation conditions, highlighting benefits and drawbacks of a direct experimental approach to failure & risk assessment.

The identification of EMA models highlighted the increasing quality of shapes that can be obtained nowadays from native full field high resolution gears, against that of a scanning system like the SLDV tested. Model updating results were compared between scanning and native full field technologies, with comments and details on the test rig, on the advantages and drawbacks of the approaches.

Keywords: *Full Field FRFs estimation, rotational FRFs, experimental strain & stress FRFs - fatigue, full field EMA & model updating*

1. INTRODUCTION

From their beginning [1] full field measurements were showing the other side of the structural dynamics: a highly detailed spatial domain against the lumped sensor placement, with surface operative deflection shapes rapidly changing from frequency to frequency, functions of the complex superposition of the eigensolutions in non-conventional patterns.With the recent development of the digital processing of optical measurement results it appears possible to have access to reliable full field quantitative data [2].

The Scanning Laser Doppler Vibrometer (SLDV) is nowadays the reference when the need of spatially detailed FRF measurements for NVH tools is demanded, because SLDV has kept the same peculiarities of previous technologies and proven procedures, extending the concept of the velocity non-contacting sensors to a spatially detailed acquisition. Native full field technologies, those based on an imaging sensor that acquires the whole information synchronously at every dof, showed the acknowledged quality obtainable in the spatial domain, especially in terms of consistency of the deflection field in the neighbouring dofs, as investigated by the author in the recent past [3, 4]. Electronic Speckle Pattern Interferometry (ESPI) gives nowadays [4–6] an extremely accurate displacement field at the single frequency of interest; but having populated data in a broad frequency band can be prohibitive, due to the time-consuming stepped sine excitation/acquisition it requires with today gears. Digital Image Correlation (DIC), with high-speed cameras, has increasingly good detail in the time resolved displacement maps, but can be more limited in the frequency domain, due to the specifications of the cameras, which, though, are seeing rapid electronics improvements; the extraction of the correlated fields is still very time demanding. Therefore, broad frequency band *receptance* FRFs can be successfully extracted also from native full field technologies [6, 7]. Native Full Field FRFs can be the strong link between advanced experimental analysis and numerical modelling, adding highly consistent and detailed fields to proven NVH approaches and fatigue life, reliability or integrity predictions, giving an alternative to the SLDV technology, with successful applications [8–15], especially for lightweight structures.

Extensive and comparative research work has been carried out by the author at Vienna University of Technology, Austria, with the project TEFFMA[1] to assess advantages and drawbacks of today full field measurement techniques (SLDV, ESPI, DIC) on a common experimental set-up, where Full Field FRFs have to be extracted in a broad frequency range, as briefly described in Paragraph 2.. Paragraph 3. introduces a compulsory series of geometrical transforms of the measured domain to be able to attempt a precise comparison between the different technologies on the same set-up and same physical location. The fundamental research contribution of these researches is the extensive overview of accurate & high resolution impedance model for *receptance* FRFs, discussed in Paragraph 4., with emphasis on the accurate pointwise comparisons. It gives thus the opportunity to underline the high quality, benefits and drawbacks of experimental models nowadays obtainable from optical techniques in vibration engineering, starting from the selection of proper test references.

Rotational dofs are recognized as relevant [16, 17] for the successful build of a reliable dynamic model for complex structures. It is common practice to assess dynamic strains by means of lumped strain measurements and finite element models (hopefully updated) to simulate the distribution of strains, eventually of stresses with constitutive parameters of the

[1] A. Zanarini, Experienced researcher in the project TEFFMA - Towards Experimental Full Field Modal Analysis, financed by the Marie Curie FP7-PEOPLE-IEF-2011 PIEF-GA-2011-298543 grant from 1/2/2013 to 31/7/2015

material, but a compromise should be sought for the best gauge placement, FEM reliability against tests, which are, on the contrary, becoming more enhanced in estimating the whole dynamic behaviour [3, 4, 6, 18] and, finally, the structural reliability [7–10, 19, 20].

Failure analysis needs improvements in the numerical models by means of better assumptions in the formulation and a closer geometrical relationship with the actual component, by means of extensive material tests and overall model updating on the structural dynamics responses, such as displacements, velocities or accelerations in many points of the structure, plus the awaited rotations [6, 21] and the dynamic strains [6–9, 20], as the answer to a dynamic event, as outlined in Paragraph 5.. This paper also explores the suitability of full field experimental impedance models for fatigue life prediction, considering the whole structural dynamics of the specimen under real test, extending previous research work [8–10], now taking into account the dynamic contribution at every frequency line of the domain. With a numerical derivation on broad frequency band datasets in [6, 21] and with material appropriate constitutive laws, strain & stress fields can be numerically obtained at each frequency line from any full field optical technique as in Paragraph 6., without the aid of numerical structural models, and taking into account real experiment-related boundary conditions.

Among the many spectral methods in literature, Dirlik's one [22] was applied in Paragraph 7. to show the potentials of the proposed direct experimental full field approach. Dirlik's methodology is well known [19] for high cycle fatigue cumulative damage calculation. Time-to-failure distribution of the test specimen was thus mapped in each measuring location by means of different combination of coloured noise, leading to an experiment-based fatigue life assessment procedure, without the use of any structural virtual model.

While not completely mature, full field technologies are tempting in traditional NVH approaches [23, 24], EMA and model updating to add the spatial sampling needed in increasingly more applications. Besides, without requiring advanced featuring techniques to efficiently exploit the data redundancy [25], it was not completely proved the advantage of having more data, when these might be extended source of variance in the estimations, due to the measurement process quality. The purpose of the activities reported in Paragraph 8. is clearly to assess the impact of high spatial accuracy on the modal base identification; it was thus attempted the processing of full field FRFs in the frame of what can be here called Experimental Full Field Modal Analysis (EFFMA), with modal base identification and FRFs' synthesis. The obtained modal bases then became the references to tune a virtual model of the experimental set-up, as outlined in Paragraph 9., which investigates the impact of the spatial resolution on model updating process by means of an extended comparison of today full field optical technologies, with a focus on SLDV, Hi-Speed DIC and Dynamic ESPI.

2. FULL FIELD FRFS RESEARCH IN TEFFMA PROJECT

The fundamental research project funded by the European Commission and carried out by Dr. Alessandro Zanarini at the Vienna University of Technology aimed at making a comparison between the state-of-the-art in native full field technologies and the SLDV as reference, to understand at which point of their development these experimental procedures can provide NVH applications with enhanced peculiarities. In the well equipped laboratory of the TU-Wien it was possible to build a complex set-up for the comparison of the qualities of the different technologies available in acquiring Full Field FRFs. This paragraph wants to highlight the results obtained on *receptance* map estimation and, further, on *coherence function* maps, on a pointwise comparative scheme at the same physical location on the test specimen.

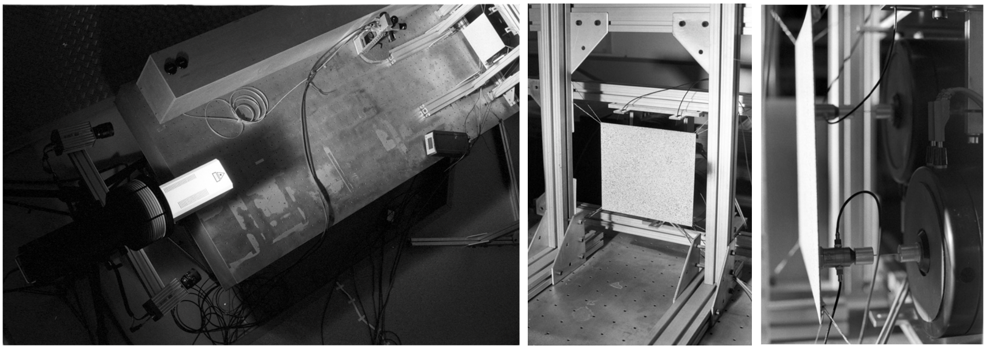

Figure 1. The experimental set-up for vibration measurements by means of optical equipment

2.1 The available equipment in brief

TU-Wien had a dedicated room with seismic floor and air-cushion anti-vibration optical table. A Polytec PSV 300 was at disposal during the TEFFMA project, with 1D (out-of-plane) scanning head OFV-056, as the reference technology. As pure full field equipment there was the Dantec Ettemeyer Q-500 Hi-Res (a specifically developed prototype), the laser speckle pattern interferometer for 3D dynamic measurements in stroboscopic monochromatic light, and the Dantecdynamics Q-450 for 3D dynamic measurements by means of image correlation and hi-speed cameras (Nanosense Mk III, 4 GB of memory - 1040 fps at 1280 x 1024 pixels maximal resolution) in white light. It completed the equipment an LMS-Scadas Mobile SCM05 16 channels acquisition unit, with its dedicated software LMS Test.Lab, B&K shakers and force cells, amplifiers and dedicated waveform generators.

2.2 The experimental set-up

The experimental set-up was designed in order to have high modal density inside the frequency range of interest of all the three measurement technologies. An aluminium rectangular thin plate (250x236x1.5mm) was therefore tightened by wires fixed to a solid frame on the air-spring optical table (see Figure 1) to restrain excessive rigid body movement. The excitation was given orthogonally by electrodynamic shakers on the back of the plate. LMS Test.Lab drove the excitation in SLDV and DIC measurements, while ESPI system, with the the proprietary phase-shifting procedures [26], commanded an external waveform generator. To be able to calculate the *receptance* FRFs, force signal was sampled at the shaker-plate interface. The assumption of linearity was forced, after some comparative test with varying input power, to be able to compare measurements done at three different source power levels; while SLDV and ESPI delivered matching results in the whole range, DIC sensed a slightly different dynamics at higher frequencies, due to the much higher input force level required to let the displacements trespass on the noise floor.

3. THE NEED OF A POINTWISE COMPARATIVE APPROACH

Albeit the optical technologies offer a highly defined description of the geometry under investigation, further alignment, scaling and rotation of the grid need to be considered to project the datasets on the same reference. SLDV data had arbitrary scaling factor and origin, plus a barrel distortion of the geometry, due to the optics through which the scanning grid is sketched. DIC, even if precisely calibrated for the vibration measurements, gave a rotated and slightly perspective distorted grid. ESPI was the only with native rectangular grid of data, thanks to the simple lens & lighting source concept. Unfortunately, even with the best accuracy, there was a slight error on location assessment and size of the measured surface. This means that no pointwise comparison could be made without pre-processing and geometry-based matching of the datasets, as done in [6], where the FRF datasets saw an earlier matching, but limited to a promising qualitative investigation of the operational shapes and single FRFs.

To obtain a precise pointwise comparison, the proposed procedure started with the identification of two common reference points on each dataset, then proceeded to scale, rotate and align the grids to a common coordinate system: the shakers' locations were sought by means of FRFs analysis. Once the three grids were in the wanted position and properly scaled, the common portion of the measured area had to be extracted, based on discrete geometry considerations. Three different reference grids, against which making the pointwise comparison of the other two techniques, by means of spatial interpolation of the datasets, can be adopted. Differences in frequency sampling from the chosen reference technique were coped with interpolation in frequency domain.

4. FRFS FOR A DIRECT EXPERIMENTAL CHARACTERISATION

It will be used the known declination [23] of *receptance* matrix $\mathbf{d}(x, y, j\omega)$ as spectral relation between displacements and forces, describing the dynamic behaviour of a *many*-degree-of-freedom testing system, with potentially multi-input excitation, here by two shakers.

The *coherence function* [23] is here used as index of quality of the FRF estimation. A cause of low *coherence function* which can be appreciated with increased spatial sampling, beyond the not correlated sources, is limited motion against force in areas (e.g. nodal lines), which means that it is related to the dynamics of the component and not to any measurement chain error. The *coherence function* does not take into account the consistency of the measurements with the neighbouring locations, leading to the judgement of very highly coherent (with the excitation force) displacements even when the grid is scattered by relevant uncertainty around a mean, and more physical, shape.

4.1 Higher spatial resolution

Full field technologies can expand structural dynamics analyses in the spatial domain, a region whose potentialities in the past have not been sufficiently explored. The traditional NVH achievements have to be delivered by native full field technologies. On the other side, adding high spatial resolution in dynamic models by means of accurate FRFs will be a valuable addition to the state-of-the-art of the design of complex systems and will surely lead to the exploration of new FRF-based quantities derived from enhanced displacement fields, such as surface rotations, strains [6, 21] & stresses and failure point distributions [7, 20], as later exampled in this brief summary.

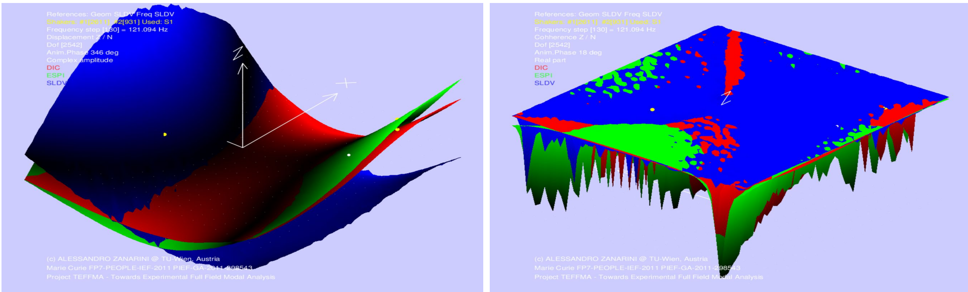

Figure 2. Matching comparison of FRF & Coherence function maps at 121Hz from SLDV, DIC and ESPI, excitation from shaker 1

4.2 Many sensors in a wide frequency band

The selection of locations where to place the sensors becomes increasingly important with wider dynamics, due to the superposition of the eigenshapes and their nodal lines, being these latter the cause of the diminishing of the signal-to-noise ration and of the *coherence function*. Normally this selection might be refined by means of a carefully updated numerical model on the test, causing time and cost increase. Since full field technologies are mostly optical, thus dimensionless, they are not invasive with added mass and cabling, and offer an increased mapping ability. Native full field sensors deliver more consistent fields of data, with more continuity in the field maps due to the synchronous acquisition of all the viewed field: this is of uttermost relevance when dealing with real boundaries and couplings, unstable phenomena, inhomogeneous materials, like compounds or structured layers, to discriminate if unexpected local behaviour was originated by a component or a measurement issue.

4.3 Full field *receptance* and *coherence function* maps

The TEFFMA project raised the overall quality of the experimental results to the new reference level awaited from full field measurements since the early activities of the author [4]. In this paper were briefly summarised pointwise comparisons of the out-of-plane results obtained from all the three technologies (SLDV was 1D limited). The reference grid for all the three technologies was the restricted one from SLDV (57 x 51 dofs), due to the scattering of the data; the frequency axis was limited in the range [20.312 - 1023.438] Hz with spectral spacing of 0.78125 Hz of SLDV, not to add even more error to the SLDV datasets with interpolation, but down-sampling instead the DIC and ESPI measurements in both domains.

SLDV is not a native full-field technology: it requires perfect steady-state conditions during the time consuming high resolution scans. Room heating problems were faced in the tests, the non-synchronous measurements showed unexpected spatial inconsistency, like lost phase correlation or time delay, leading to mistaken bands / behaviours on the measurements. Other causes could be overheating and clock errors in the electronics of the whole system that drove the piezo-actuated mirror. The quality of the measurement map, even if the system gave optimal feedback, was sometime unexpectedly poor, with many dropped datasets.

The acquisition of the time domain signals was very fast by DIC, but required strong power by the shakers, and the off-line work was time-consuming: half an hour was required to download each of the time series from the cameras, about 3 days to evaluate the displacement

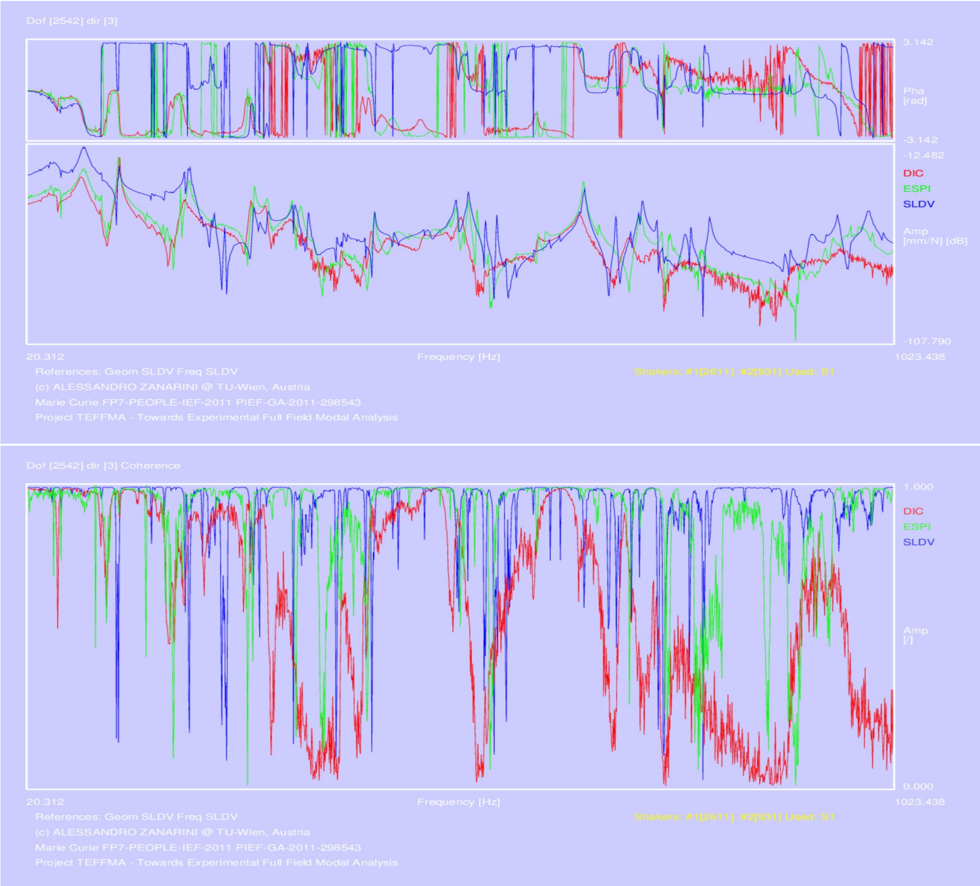

Figure 3. Matching comparison of FRF & Coherence single functions at dof 2542 in the whole frequency domain from SLDV, DIC and ESPI, excitation from shaker 1

fields in the time domain, and 2 days for frequency domain processing.

Each frequency step of interest in ESPI measurements needed about 2 minutes to acquire and evaluate the complex valued displacement maps. A very low input force was calibrated at each narrow frequency interval to obtain the best signal-to-noise ratio and avoid unresolvable areas in the fringe maps.

The quality reached in the processed measurements (on a dual hexa-core Intel®Xeon X5670 2.93GHz and 192GB RAM Linux workstation, by means of a custom software written by the author in C-language & OpenGL and extending proven routines [23, 27, 28]) was indeed promising for all the potential elaborations in frequency domain (see [15, 20, 21] and Paragraphs 5.-9. for some examples). The structural dynamics retained seemed again to play a relevant role in determining the distributions of critical locations and reflect that high modal density wanted at the time of the test design.

In Figure 2 can be seen the superposition of *receptance* and *coherence function* maps from all the three gears; the SLDV results are shown in blue, followed by DIC in red and

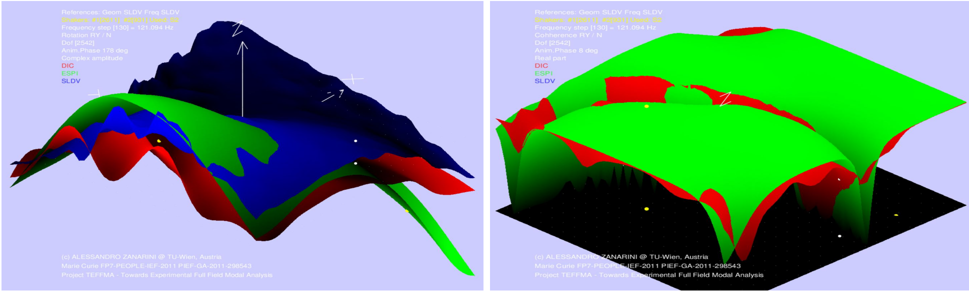

Figure 4. Matching comparison of rotational RY FRF & Coherence maps at 121Hz from SLDV, DIC and ESPI, excitation from shaker 2

ESPI in green tones. The *coherence function* maps show the high quality of measurement and processing obtained with Hi-speed DIC technology in almost the frequency range, starting to rival the more traditional SLDV technology. Thou, *coherence function* did not reveal non-physical inconsistencies on *receptance* maps, especially in SLDV and much less in DIC low-frequency measurements. Instead ESPI *receptance* results outperformed SLDV and DIC in terms of surface consistency in the whole range and in terms of frequency accuracy in most of the domain, coupled with excellent *coherence function* maps. DIC and ESPI manifested a finer treatment of the spikes in the FRFs, with broad dynamic range in the amplitude and added uniformity of the *coherence function* at the maxima of the *receptance* shape. SLDV showed instead some limits (the surface quality of the results), therefore it can be remarked how the *coherence function* was not sensible enough to the scattering on SLDV *receptance* maps that left some troubles for further processing (see [15] and Paragraph 9.).

In Figure 3 there is the superposition of *receptance* and *coherence function* obtained with all the three technologies at the same (with the best precision of the cited pointwise approach) geometry location and shaker excitation. It can again be seen a relevant drop of accuracy in the *coherence function* of DIC measurements above 3/4 of the frequency range of interest, while dynamic ESPI still delivers consistent results at much higher frequencies, due to its sensibility to much lower displacements and proper tuning of the excitation to optimise the measurement quality. The high modal density retained in this experiment plaid a relevant role on the output *coherence functions*, with the nodal lines that moved fast with frequency and crossed many times the points of interest.

5. DYNAMIC EXPERIMENTAL ROTATION & STRAIN DISTRIBUTIONS

Pure full field experimental techniques, like ESPI and DIC, become particularly suited for the numerical derivation of the rotational and strain fields in dynamic events, thanks to the higher continuity of the displacement maps, as highlighted already in the analyses of *receptance* maps in Paragraph 4. and in [4, 6–10, 18].

If the full field reference system is parallel to a flat surface to be measured, at each frequency the dynamic rotations of a locally tangent plane can be calculated by means of a differential operator on the *receptance* map $\mathbf{d}(x, y, j\omega)$ along *x* & *y* directions:

$$\mathbf{r}(x, y, j\omega)_x = \frac{\partial \mathbf{d}(x, y, j\omega)}{\partial y}, \mathbf{r}(x, y, j\omega)_y = -\frac{\partial \mathbf{d}(x, y, j\omega)}{\partial x}. \tag{1}$$

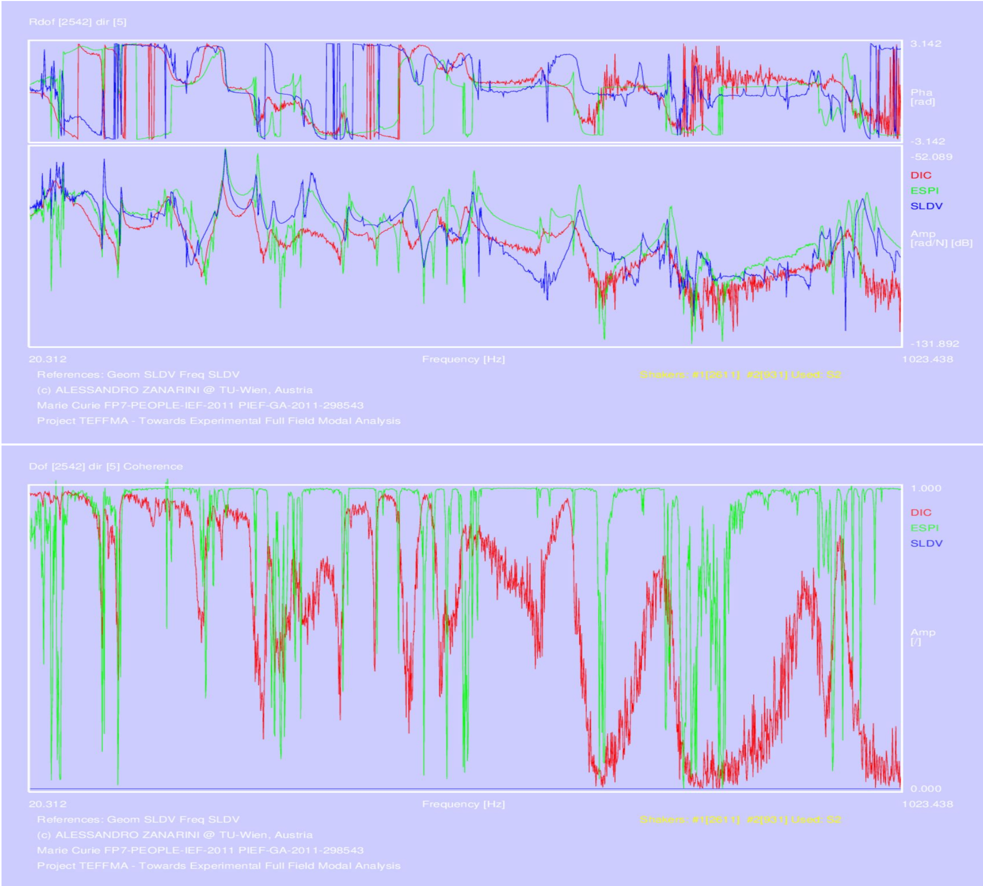

Figure 5. Matching comparison of rotational RY FRF & Coherence single functions at dof 2542 in the whole frequency domain from SLDV, DIC and ESPI, excitation from shaker 2

Strain tensor impedance model components $\varepsilon(x, y, j\omega)_{ik}$ can be calculated from plane stress assumption in strain theory, by means of the successive derivations of the *receptance* map $\mathbf{d}(x, y, j\omega)$ along q directions:

$$\varepsilon(x, y, j\omega)_{ik} = \frac{1}{2}\left(\frac{\partial \mathbf{d}(x, y, j\omega)_i}{\partial q_k} + \frac{\partial \mathbf{d}(x, y, j\omega)_k}{\partial q_i}\right). \tag{2}$$

In the plane stress scenario, the in-plane displacements give their contribution to the tensor components as:

$$\begin{aligned} \varepsilon(x, y, j\omega)_{xx} &= \frac{\partial \mathbf{d}(x, y, j\omega)_x}{\partial x},\ \varepsilon(x, y, j\omega)_{yy} = \frac{\partial \mathbf{d}(x, y, j\omega)_y}{\partial y}, \\ \gamma(x, y, j\omega)_{xy} &= \gamma(x, y, j\omega)_{yx} = \frac{\partial \mathbf{d}(x, y, j\omega)_x}{\partial y} + \frac{\partial \mathbf{d}(x, y, j\omega)_y}{\partial x}, \end{aligned} \tag{3}$$

while, from the out-of-plane displacements, the bending-related in-plane strain results:

$$\varepsilon(x,y,j\omega)_{xx_b} = -\frac{s}{2}\frac{\partial^2 \mathbf{d}(x,y,j\omega)_z}{\partial x^2}, \; \varepsilon(x,y,j\omega)_{yy_b} = -\frac{s}{2}\frac{\partial^2 \mathbf{d}(x,y,j\omega)_z}{\partial y^2},$$
$$\gamma(x,y,j\omega)_{xy_b} = \gamma(x,y,j\omega)_{yx_b} = -s\frac{\partial^2 \mathbf{d}(x,y,j\omega)_z}{\partial x \partial y}, \tag{4}$$

where *s* is the thickness of the bending surface. The principal strains can be then easily evaluated at each frequency line, together with their principal directions, working on the diagonalising transform [27].

5.1 Extending traditional strain gauges

It is sufficient to introduce different inputs in the impedance based model of the dynamic $\varepsilon(x, y, j\omega)$- tensor to obtain the related dynamic strains on the whole measured surface, just as a multiplication of the impedance matrix by the known input in frequency domain or as a convolution to the time domain, without any FE model. This advantage opens promising investigations on the dynamic characterisation of real assemblies, component junctions, weldings, glued compounds and failure locations. Also, full field optical technologies deliver measurements independently of the material type. This is not commonly achieved with conventional instruments, like the widespread strain gauges, which may face some problems, like effective sensor placement, spatial averaging, mass burden and lumped measurements. Multimodal behaviour of the structure under dynamic loading in service increases the strain-gage location uncertainty. Strain gauges, to enhance their sensitivity, may find a better location when this is different from that of other types of sensors. This means that at least two different tests for structural dynamics and strain measurements might be requested, and that strain gauges might not certainly achieve that fine spatial resolution on the whole surface typical of advanced full field technologies. High spatial resolution in full field optical measurements brings also a reduction of sensor area-averaging effect and set-up complexity, in comparison with strain rosettes or other more conventional instruments. For these latter, the analysis across the whole domain must then be completed by means of detailed numerical models, calibrated on the few points of lumped measurements. Therefore obtaining *receptance* maps and dynamic strain tensor impedance model from any full field technologies might have a great relevance to shrink test steps & costs and to gain better accuracy, due to the lack of assumptions required by any numerical model nor having sensor placement issues.

5.2 Full field *rotational impedance* model and *coherence function* maps

The extended details on the *receptance* FRF maps acquisition can be found in [18] and Paragraph 4.. In [6, 18] it was already pointed out how the performances of SLDV were affected by unexpected scattering of the data on the *receptance* maps, when not a total destruction of a clear pattern. The poor continuity of SLDV data across the spatial mapping, not overtaken with smoothing post-processing for a fair comparison with the other techniques, strongly affected the quality of any derived quantity, such as *rotations* and *dynamic strains*. The equipment of SLDV released the *mobility FRFs* only, therefore the rotational *coherence function* was set to null values. Native full field technologies gave instead much higher continuity of the field, especially for ESPI at higher frequencies, where, instead, DIC lost coherence. The unevenness seen in [6, 7, 18] and in Paragraph 4.3 on DIC displacement & *receptance* maps at some low frequencies was amplified in the derivative process.

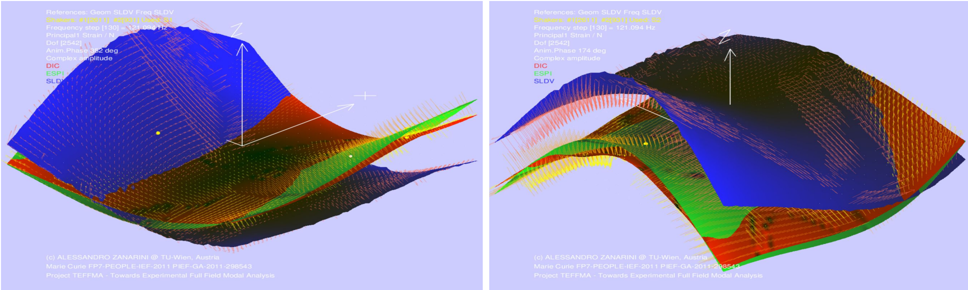

Figure 6. Matching comparison of 1^{st} Principal Strain FRF maps at 121Hz from SLDV, DIC and ESPI, excitation from shaker 1 & 2

Results from the processing of all the techniques data are shown: in Figures 4 all the three *rotational impedance* and *coherence function* maps are superimposed for direct comparison; in Figures 5 are sketched single *rotational FRF and coherence functions* at one location (with the best precision of the pointwise approach). The *coherence function* maps showed the good quality of processing obtainable from DIC technology in only a part (less than a fourth) of the frequency range, amplifying the wide drops already seen in the *coherences* of the *receptance* maps (in [6, 18] and Paragraph 4.3). ESPI *rotational impedance* results outperformed SLDV and DIC in terms of surface consistency and frequency accuracy in the whole range, coupled with excellent *coherence function* maps. ESPI still delivered consistent results at much higher frequencies, thanks to its sensibility to sub-micron displacements and extensive tuning of the single sine excitation it received. The modal density was retained in the derivative quantities, especially in terms of amplitude peaks; especially at higher frequencies ESPI exhibited higher rotational FRF amplitudes.

In some sharp changes in the frequency domain, *rotational coherence functions* from down-sampled DIC & ESPI datasets could show few overshooting little spikes above unity, as numerical error in the reduction done with a simple cubic interpolation.

5.3 *Dynamic strain* full field impedance models

From the high quality *receptance* maps evaluated in [6, 18] and Paragraph 4.3, as with *rotational dofs* of Paragraph 5.2, could come the numerical derivation of the *dynamic strain tensor models* and (later predicted in Paragraphs 6.-7.) fatigue life estimations [20]. In Figure 6 are shown the *first principal strains* in the FRF model from the 3 sensing technologies, using the colours (from dark to bright) for the amplitudes (while the bended surface shape is from the *receptance* data), and related fields of eigenvectors (as bright small arrows).

DIC & ESPI results were down-sampled in the frequency domain to match SLDV frequency axis: the numerical error at low strain amplitudes from the basic interpolation gave some sign reversals with minimal amplitude, highlighted by dark spots on the strain colours, while calculations in native resolutions did not show any issues.

In Figures 7 are also shown the first principal strain FRFs at the highlighted single output dof, denoting their complex-valued nature in an experimental impedance base modelling. While the complex amplitude retained the high modal density of the *receptance* maps, the phasing appeared contaminated by increasing errors, spreading in the second derivation of

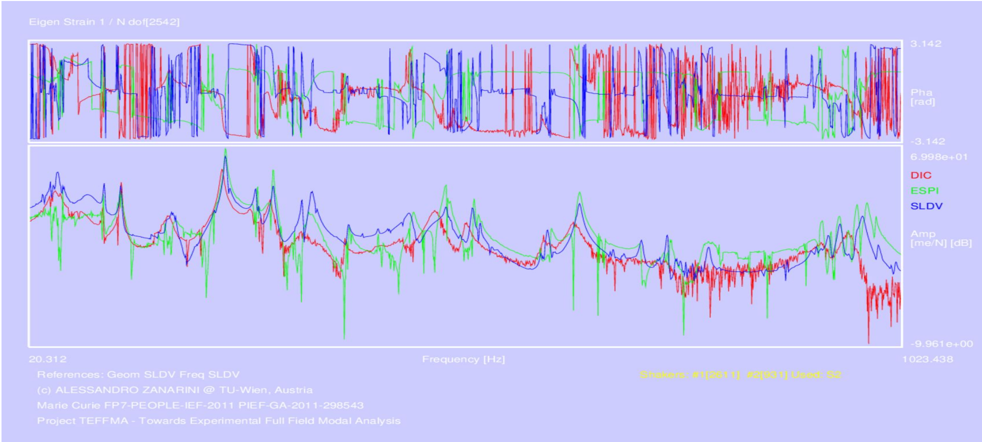

Figure 7. Matching comparison of 1^{st} Principal Strain FRF single functions at dof 2542 in the whole frequency domain from SLDV, DIC and ESPI, excitation from shaker 2

the data fields. No coherence functions were evaluated to simply limit the computational costs and time.

In the whole experimental model there were thousands of principal strain FRF: in this way an advanced dynamic strain evaluation could be run, with much more mapping ability. By comparing the quality of the *receptance* shapes in [18] and in Paragraph 4.3 to the evaluated dynamic principal strain field models in Figures 6 it is possible to appreciate, as with rotational dofs evaluations, the beneficial effects of field consistency that native full field technologies can exploit in numerical derivations.

6. OPTICAL MEASUREMENTS FOR DYNAMIC STRAIN-STRESS FIELDS

The great amount of experimental dofs, typical of full-field techniques for vibration patterns, reduces the uncertainty in choosing the best sensor locations and transducers' number, simply by dramatically increasing the spatial sampling in respect to more traditional equipments, resulting in precise description of the sample dynamics also in the space domain, without any simplification, since complex-shaped patterns are complex-valued measurable at extremely high frequencies, as obtained in Paragraphs 4., 5. and in [6, 18, 21], from which the experimental results were processed. ESPI, as the highest detailed source in space domain here proposed, was yet thoroughly investigated in the past by [5, 29–32] for NVH applications, when the computing power and allocable memory arrays were relatively limited; while strain measurements were searched for by [33], and [34] tried a basic application in automotive. But in [18, 21] the *receptance* FRF acquisition was extended also to SLDV and DIC, as competing optical gears, with a strong emphasis on the pointwise comparison of the FRFs in any location of the reference grid: the same comparative approach is pursued in the results here proposed and later in the Paragraph 7., about fatigue predictions.

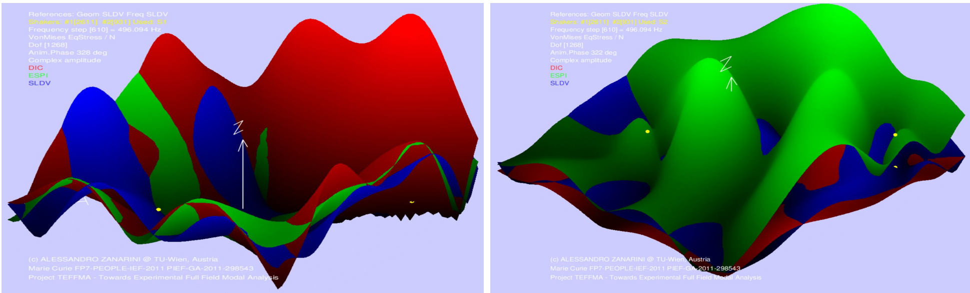

Figure 8. Matching comparison of Von Mises equivalent stress FRF maps at 496Hz from SLDV, DIC and ESPI, excitation from shaker 1 & shaker 2

6.1 Stress impedance model

$\boldsymbol{\sigma}$-tensor FRFs can be evaluated in every point from the experimental $\boldsymbol{\varepsilon}$-tensor impedance model (see [6, 21] and Paragraph 5.) using proper constitutive model. A linear elastic, isotropic and low-strain / high-cycle fatigue behaviour of the material is adopted in the following applications. The experimental full-field *impedance* model can extend the simulations, under the assumption of linearity, to higher response ranges and different excitation spectra. Linear isotropic constitutive relations can be outlined as the complex-valued tensor expression of Hooke's law of Eq.(5), which includes material parameters and transformation between complex-valued strain $\boldsymbol{\varepsilon}$-tensor and stress $\boldsymbol{\sigma}$-tensor components. The complex valued principal strains and stresses can be then easily evaluated by means of a tensor diagonalisation, together with their principal directions coming from the transforming base vectors [27]. The basic material parameters of this simple constitutive model as in Eq.(5) are: E, elastic modulus; ν, Poisson ratio; G, shear modulus; Λ, Lamé constant.

$$\begin{aligned} \sigma_\omega(x,y)_{ii} &= 2G\varepsilon_\omega(x,y)_{ii} + \Lambda\left(\varepsilon_\omega(x,y)_{xx} + \varepsilon_\omega(x,y)_{yy}\right), \\ \sigma_\omega(x,y)_{ij} &= 2G\varepsilon_\omega(x,y)_{ij},\ G = E/2\left(1+\nu\right),\ \Lambda = E\nu/(\left(1+\nu\right)\left(1-2\nu\right)). \end{aligned} \tag{5}$$

6.2 Failure criteria for multi-axes stress

An equivalence criteria has to be formulated to compare the multi-axes loading conditions of real samples with results from mono-axial loading tests on materials [35], even if a comprehensive theory is awaited [36] to relate failure & fatigue limits among different stress states.

In each location of the maps in Figures 8 complex-valued FRFs of Von Mises equivalent stresses were evaluated at one frequency, considering completely reversed-stress and no mean stress effect. From full field experiment based calculations the whole distributions of Von Mises equivalent stress FRFs in Figures 8 could be mapped, as the response to an input at specific shaker location. Full field measurements become an alternative to the assumption of stress concentration factors thanks instead to a detailed mapping.

7. FATIGUE ASSESSMENT DIRECTLY FROM FULL FIELD EXPERIMENTS

Long life fatigue tests are time demanding experiments and ask for accelerated tests to achieve a basic understanding of the behaviour with frequency shifts: an example of the researches carried on this latter aspect is given in [35], where a very fast vibration-based fatigue testing

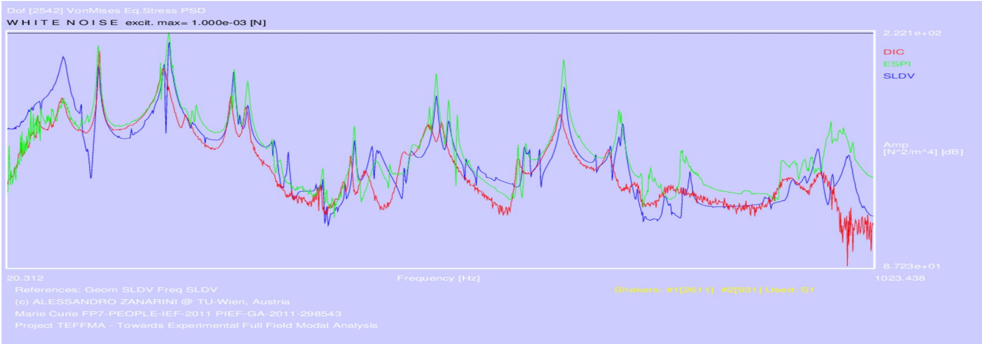

Figure 9. Matching comparison of single Von Mises equivalent stress PSD at dof 2542 in the whole frequency domain from SLDV, DIC and ESPI, white noise excitation from shaker 1

procedure was proposed, exploiting the designed sample & test-rig in a forced vibration-based fatiguing procedure, with bi-axial stress state and stress gradient in bending.

This research stream showed a promising evolution of an accepted procedure [19, 22] towards the direct use of full-field FRFs with a precise experimental characterization of the spatial and frequency domains in the structural dynamics instead of any FE model, pointing to obtain the prediction without selecting *a priori* the location of the sensors on the surface under analysis and without simplifying the dynamic behaviour of the sample, even in high-frequency ranges where complex-shaped patterns are expected due to high modal superposition. This work follows the approach proposed by ESDU [19, 37, 38] in low-stress / high-cycles random loading for isotropic metal alloys, thus extending the evaluations over many experimental measurement points, to come to a mapping ability of critical real locations. Furthermore, full field experiment-based predictions can be developed also in other fatigue assessment frameworks that take advantage of the extremely fine spatial resolution and wide frequency band in these dynamic measurements, together with the complex-valued nature of dynamic strain FRFs [6, 21].

7.1 Cumulative damage evaluation with spectral methods

Spectral methods [19, 37, 38] are applied to evaluate an equivalent range of stress cycles $S_{eq}(x, y)$ representative of the cumulated damage, inferred by the whole spectrum of the retained dynamics. The full field experiment-based approach aimed here at avoiding any simplification of the structural behaviour, taking into account the multi-axial dynamics especially at higher frequencies by means of the broad collection of experiment-based results; no modal identification approach (with its modelling errors) was here applied to extract the strain or stress maps, where complex shaped displacement patterns were expected.

7.1.1 Parameters of the spectral method. In a full field experiment-based procedure the parameters need to be considered as maps, but here the suffix (x, y) is omitted for space limitations. The spectral methods are based on $m_k = \int_0^\infty f^k PSD_{VM}(\omega) d\omega$, k-th order moments of the frequency by $PSD_{VM}(\omega)$, the power spectral density (PSD) of the Von Mises equivalent stress; on characteristic frequencies $F_k = (m_k/m_0)^{1/k}$; and on a whole

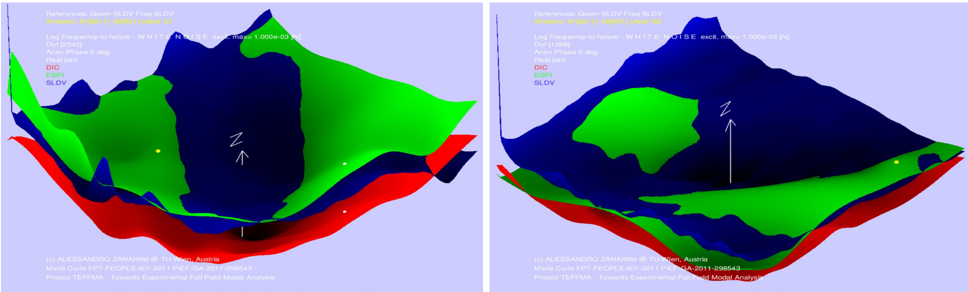

Figure 10. Matching comparison of failure frequencies maps from SLDV, DIC and ESPI, white noise excitation from shaker 1 & shaker 2

class of bandwidth parameters $\gamma_k = m_k / (m_0 m_{2k})^{1/2}$ to describe the distribution of the stationary and Gaussian processes. Some more specific expressions are also evaluated:

effective frequency: $F_{zerocrossing} = F_{zc} = \sqrt{m_2/m_0}$;

expected number of peaks per unit time: $F_{peaks} = F_p = \sqrt{m_4/m_2}$;

irregularity factor: $\gamma = \gamma_2 = F_{zc}/F_p = m_2/\sqrt{m_0 m_4}$.

The Dirlik method [22] is here adopted with the support of full field techniques for the experimental characterisation in a broad frequency range, as suggested in [19], where Dirlik semi-empirical spectral method is regarded as giving the best prediction for the fatigue life, especially for wide band spectra of stress responses. Below is reported the formulation to get the equivalent range of stress cycles $S_{eq}(x, y)$ raised to the fatigue exponent b, representative of the total damage in a specific (x, y) location:

$$\begin{aligned}
&\chi_m = (m_1/m_0)(m_2/m_4)^{1/2}, \quad D_1 = 2\left(\chi_m - \gamma^2\right)/\left(1+\gamma^2\right), \\
&R = \left(\gamma - \chi_m - D_1^2\right)/\left(1-\gamma-D_1+D_1^2\right), \quad D_2 = \left(1-\gamma-D_1+D_1^2\right)/(1-R), \\
&D_3 = 1 - D_1 - D_2, \quad Q = 1.25\,(\gamma - D_3 - D_2 R)/D_1, \\
&S_{eq}^b = D_1 (2\sqrt{m_0} Q)^b \Gamma(b+1) + (2^{3/2}\sqrt{m_0})^b \Gamma(1+b/2)[D_2 R^b + D_3].
\end{aligned} \tag{6}$$

Finally the time-to-failure distribution is given [19] by :

$$T_{failure}(x, y) = K_r / \left(F_p(x, y) S_{eq}^b(x, y)\right). \tag{7}$$

7.1.2 Cumulative fatigue calculation on the plate with coloured noise excitation.

The constitutive model and spectral method parameters (E= 7.0e+10 Pa, ν=0.33, b=4.81, K_r=4.42e+43 Pa^b) of Eq.(5) and of Eq.(7) were taken from the Aluminium 7075-T6 properties [19].

The definition of $PSD_{VM}(\omega)$ [28] took into account the complex-valued nature of Von Mises equivalent stress and the spectra of the input shaping selected as coloured noise, as can be seen in the single dof functions of Figure 9. Dirlik semi-empirical spectral method could be thus followed as in Eq.(6), and the map of time-to-failure was obtained as in Eq.(7) for

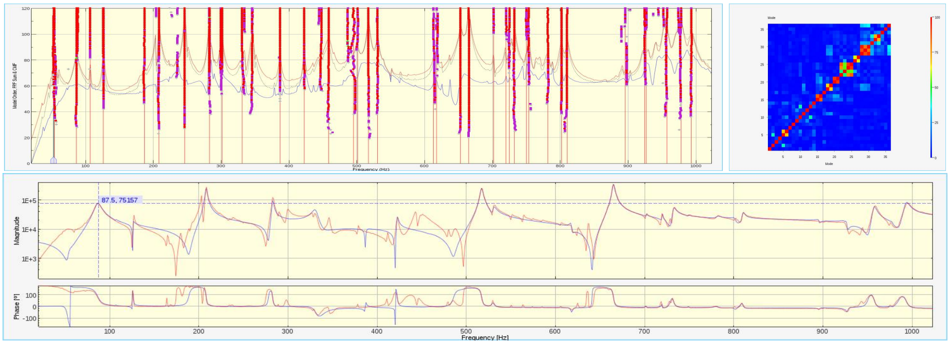

Figure 11. Stabilisation chart, AutoMAC matrix and FRF synthesis from EMA on SLDV dataset

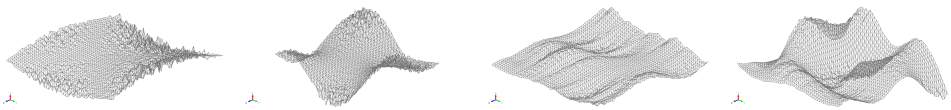

Figure 12. Modeshapes from EMA on SLDV dataset (126.2, 301.3, 724.9 and 978.1 Hz)

each excitation considered. The calculations were run on the *receptance* FRF and impedance strain model maps calculated in [18, 21] and presented in Paragraphs 4. and 5., to assess the fatigue life of the component as subjected to an input force with coloured (here only white) noise spectrum of 1 millinewton maximum amplitude. The location of the calculated failing points (corresponding to the minimum time-to-failure or maximal frequency-to-failure, as its inverse) was always on the corners of the grid, followed by the borders; nevertheless the distributions of critical locations inside the area demonstrated to be deeply linked with the dynamic behaviour retained in the elaborated data, in terms of emphasised spectral part and excitation point, as shown in Figures 10 for a matching comparison of the previous results, by sketching the frequency-to-failure distribution as the inverse of Eq.(7), in a logarithmic scale (the brighter is the colour or higher is the point on the z-axis, the shorter is the time-to-failure or higher is the damage reached in the corresponding point).

It could be noted a marked dependency on the full field technology adopted to extract the *receptances*, not only in terms of extrema, but also in terms of simulated distribution of damage (see Figures 10): the scattering of SLDV maps and some artefacts of DIC, highlighted in [6, 18, 21] and Paragraph 4., increased the uncertainty of the predictions; ESPI, with its superior continuity in spatial domain, released much smoother cumulated damage surfaces.

8. FULL FIELD EXPERIMENTAL MODAL ANALYSIS FROM OPTICAL MEASUREMENTS

The *receptance* FRF datasets were taken from the two shaker excitations on the experimental set-up of the TEFFMA project, widely described in [6, 7, 14, 18] and reported in Paragraph 2. and 4.. No extra smoothing was applied to the data, neither in space domain nor in frequency domain, to obtain a fair comparison of the three optical technologies. For all the identifications, the same parameters were kept in the Least Squares Frequency Domain

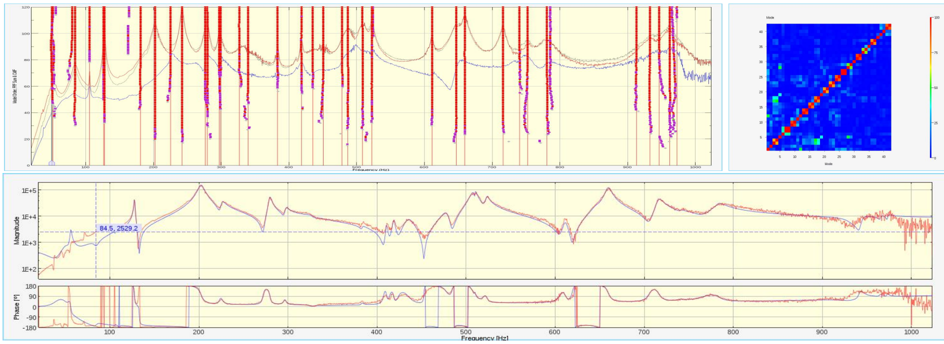

Figure 13. Stabilisation chart, AutoMAC matrix and FRF synthesis from EMA on DIC dataset

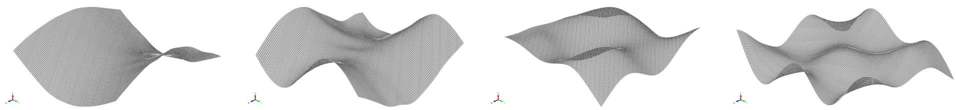

Figure 14. Modeshapes from EMA on DIC dataset (126.6, 299.5, 716.1 and 973.2 Hz)

(LSFD) modal extractor of the commercial software FEMtools 3.8 [39], which was able to deal with the relevant dimensions of all the datasets in reasonable time, except for ESPI at native frequency resolution (as explained below). Therefore, the modal bases first extracted were minimising any effect of a reducing interpolation scheme in spatial domain, to show the results the three technologies could give at their best. Later, instead, to make the pointwise comparison, new modal bases would have been evaluated, starting from properly reduced FRFs datasets, as explained in Paragraph 9.3.

8.1 The modal model from SLDV-based FRFs

The SLDV datasets were taken in their native spatial (2907 dofs) and frequency (0.78125 Hz) resolution, only limited [18] to the common measured area among all the three optical gears. Though, since the first analysis of acquired data, they appeared to have relevant scattering on the out-of-plane direction of the FRF maps, with potential repercussion on the quality of modal base identification steps.

In Figure 11 are briefly reported the steps of the modal identification from the SLDV datasets, with stabilisation diagram highlighting the FRF sum and the CMIF functions, with the AutoMAC matrix [23] emphasising potential similarities among the eigenshapes, and with the driving point FRF at shaker S1 checking the FRF synthesis from the identified modal base. While the AutoMAC matrix appeared cleaner than that from the other optical technologies, it did not take into account the bad continuity, or roughness, of the eigenmode shapes, as depicted in Figure 12, where the shapes appeared heavily scattered by non-physical noise; on the third shape appeared also some bands, as unexpectedly encountered during FRF acquisition [6, 18].

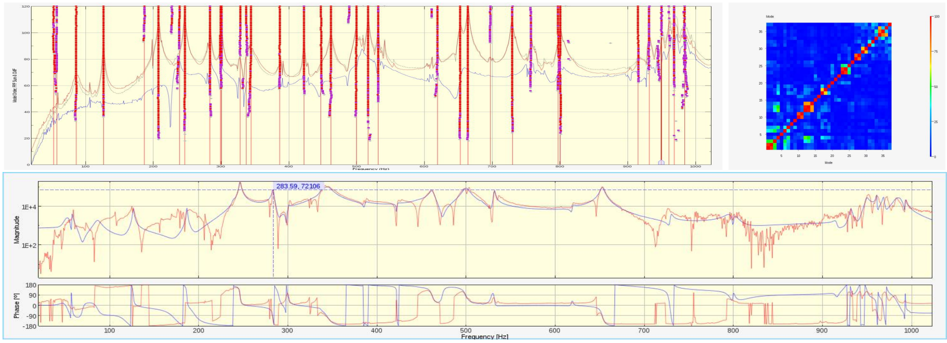

Figure 15. Stabilisation chart, AutoMAC matrix and FRF synthesis from EMA on ESPI dataset

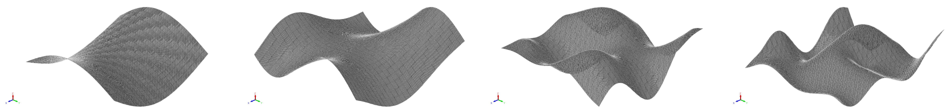

Figure 16. Modeshapes from EMA on ESPI dataset (126.2, 301.2, 724.8 and 982.9 Hz)

8.2 The modal model from DIC-based FRFs

Also DIC datasets were taken in their native spatial (11988 dofs) and frequency resolution (0.5 Hz), only restrained [18] to the common measured area among all the three optical gears. Some traces might be expected on the eigenshapes from the artefacts shown at lower frequencies.

While the AutoMAC matrix of Figure 13 put in evidence higher similarity among low frequency eigenshapes, again it did not confirm the much better continuity and quality (lower scattering), compared to that of SLDV, of the shapes in Figure 14; still, some traces of the artefacts could be noticed on the first and second eigenmode deployment. Many complex-valued pairs of double modes were identified. Also, the driving point FRF synthesised appeared better described by the modal base extracted, whereas the structural dynamics at higher frequencies in the range appeared less clear, starting from the stabilisation diagram, due to the minor sensitivity of native *receptance* FRF of DIC against *mobility* FRF of SLDV. The discrepancy in the eigenfrequencies was linked to the much higher excitation force during the DIC test, thus sensing a slightly softer dynamics.

8.3 The modal model from ESPI-based FRFs

The ESPI datasets were taken in their native spatial resolution (49042 dofs), only restrained [18] to the common measured area , but down-sampled in the frequency domain to a spectral distance of 0.78125 Hz (that of SLDV) by means of interpolation. Also, ESPI datasets were obtained with an old prototype instruments [6, 18] that, while surprisingly accurate in spatial domain, could be sometime disappointing on the frequency domain, especially at lower spectral lines, with potential repercussions on the quality of the modal base identification.

The stabilisation diagram of Figure 15 was enriched with more information at higher frequency than that from DIC, comparable with Figure 11. Also the eigenfrequencies were

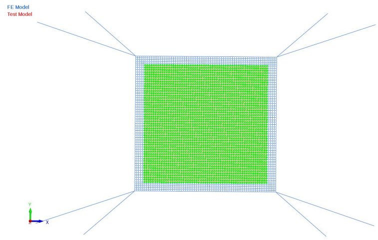

Figure 17. FE model grid (blue) and node point pairs (green) with test measurements

extremely close to those of SLDV datasets, confirming the linearity checks between the two experiments [6, 18]. Instead, the synthesis of the driving point FRF showed flows in the phase subdiagram, especially at lower frequency. Again, the AutoMAC did not put enough in evidence the quality of the shapes in Figure 16 in terms of continuity or smoothness of the fields, which had no artefacts nor distortions, and were so accurate to highlight the shakers' impedance head locations.

Complex-valued pairs of double modes were identified, even more than in DIC identification. The higher, and much more reliable, spatial sampling helped in the selection of the most physical shapes, leaving micro unevenness for the badly identified modes or pure numerical errors in the poles' search, as already noted in [14].

9. FE MODEL UPDATING FROM FULL FIELD MODAL BASE

In the industrial product refinement the model updating stage risks easily to be forgotten or strongly simplified for the costs, leaving an unpredictable and unreliable numerical model to forecast the behaviour of an unreal structure, even when the model is complex and with millions of degrees of freedom, albeit very expensive as computational cost. But even if the model updating is performed (anyway with a left discrepancy with reality), the best placement of lumped sensors is not completely determined: only the deep knowledge of the whole structural dynamics, matched with sensor typology, might suggest the best sensor placement for a specific quantity measurement. Problems like effective sensor placement, spatial averaging, mass burden and lumped measurements could affect the more conventional techniques, like accelerometers of strain gauge arrays. Further, multi-modal and multi-axes dynamics might be not adequately described by a limited number of sensors placed e.g. using brittle lacquer coatings or without an accurate dynamic analysis of the real sample. The high resolution mapping from full field dynamic measurements aimed at answering, as outlined below, if the right sensor was used in the best position, if that location could be optimal for any kind of sensor and in the whole frequency range of interest and if the sensors were enough to give the updating a reliable reference.

9.1 The FE model in brief

The numerical model of the test case of Figure 1 had to reproduce the thin aluminium plate described in [6, 18] and in Paragraph 4., the restraining wires at the plate corners, the influences of the two shakers and light restraints, as sketched in Figure 17. This FE model (an advancement compared to that in [14]) underlined that light asymmetry found in the dis-

Table 1. Best pairs of modeshapes from model and test SLDV, DIC and ESPI datasets

FEA	Hz	SLDV	Hz	MAC	FEA	Hz	DIC	Hz	MAC	FEA	Hz	ESPI	Hz	MAC
6	99.62	3	106.90	87.3	5	117.72	4	126.61	86.7	5	123.37	6	127.02	97.5
8	122.56	4	126.17	66.4	8	117.72	5	127.70	88.6	8	123.37	5	126.25	97.6
10	214.52	6	208.19	72.7	10	207.49	7	202.32	91.9	9	215.08	8	198.50	95.7
12	252.00	7	246.24	70.8	13	274.64	11	279.56	89.7	10	215.08	9	207.81	93.5
14	295.47	8	282.77	79.2	15	274.64	10	276.58	77.6	11	253.49	10	226.40	84.9
29	658.36	21	665.03	68.9	27	506.13	22	522.35	77.8	13	287.48	13	283.60	91.5

placement maps of the tests, showing nodal lines gathering close to the location of the shaker inputs, similarly as during the measurement campaign. Due to the limit of dynamic ESPI technology on very small displacements, which otherwise were masked by rigid body motion, the plate was not completely fixed, but was in a quasi-free-free condition, since the wires were used as a high-pass filter with threshold at 20Hz . The model was written by means of the script language of the FEMtools 3.8.1 software [39], which served also as solver and model updating driver.

9.2 FE model details

Thin shell isotropic elements modelled the aluminium plate of Paragraph 2.; the inner grid, in green colour on Figure 17, matched exactly that of the measurements, for an higher quality of all the FEM vs test comparisons, with SLDV geometry as reference. The impedance heads were modelled as mass-spring-damper lumped systems, attached to the ground and exactly at the same point of the plate as in the real set-up. Structural damping was added in the model.

At each corner of the real plate two different twisted wires were used to restrain the rigid body modes, therefore 8 potentially different spring elements (with structural damping) were added to the FE model. All the end points of the wires were coupled (to the plate or to the ground) by means of boundary conditions on their 3 displacement dofs. Eigenmodes were evaluated from 5 Hz up to 1250 Hz: a mixture of fairly rigid-body and elastic modes could be found in the band 5-90 Hz.

The attention was focused on the out-of-plane displacements only. The parameters of the updating were the density, the plate thickness and Young modulus, together with the stiffness properties of the 8 springs, for a total of 11 variables. Double modes could be considered and only modes above the MAC [23] value of 60% could be mated. Eigenshape distance on most active dofs was taken as minimizing target function: there resulted many responses to be used in the optimisation, depending on the adopted thresholds and test shape measurement quality. The standard Bayesian sensitivity [40] driven optimisation approach was adopted in FEMtools [39], but a non-optimal convergence to a clearly defined optimum was obtained.

9.3 Model updating exploiting full field modal bases

For the model updating stage were used three new EMA sets (from SLDV, DIC, ESPI), all restrained to the reference grid of the SLDV technology (57x51 nodes), due to the scattering seen in SLDV maps (see [18] and Paragraph 4.). It must be put in evidence that DIC and ESPI datasets were restrained to the SLDV geometry & frequency references *before* running the EMA procedure, thus were not the decimated version of the dataset previously shown in Figures 14 and 16, but completely new modal bases, identified with the same procedure. Any

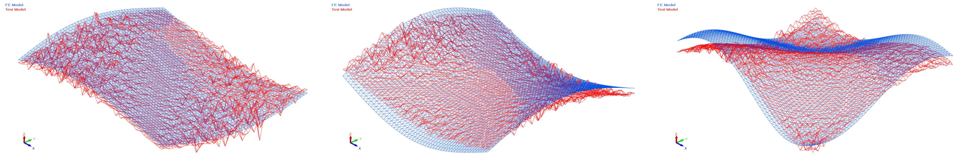

Figure 18. FEA vs TEST modeshape pairs from SLDV dataset
(MAC values at pairs 1: 87.3, 2: 66.4, 3: 72.7)

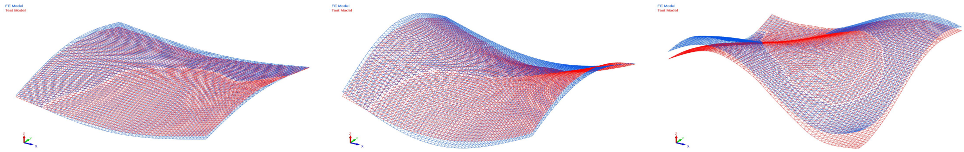

Figure 19. FEA vs TEST modeshape pairs from DIC dataset
(MAC values at pairs 1: 86.7, 2: 88.6, 4: 91.9)

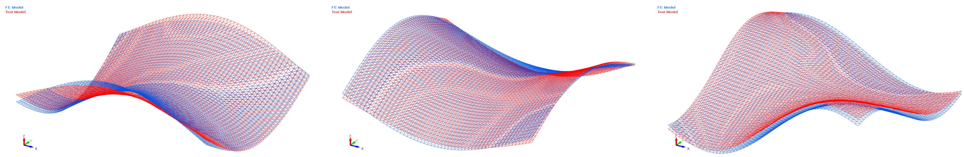

Figure 20. FEA vs TEST modeshape pairs from ESPI dataset
(MAC values at pairs 1: 97.5, 2: 97.6, 3: 95.7)

interpolation on SLDV data would have brought to the spreading of their uncertainty on the modeshapes, once extended to higher resolutions. Therefore the native full field technologies were here not completely exploited at their best as redundant sources, but, thanks to the higher consistency of FRF fields and resolution in space domain, were also able to deliver high quality reduced datasets.

Exactly the same FE model was used at the starting point of the 3 updating sequences. While already close to the measured test specimen, the model was updated by all the datasets without finding a clear convergence point, but only testing parameter values close to the starting ones: further work is needed on the improvement of the model optimisation.

9.3.1 SLDV vs FEM modal base comparison. The SLDV technology, here tested without extra smoothing on the data, proved to be the worst of the three non-contacting optical technologies, despite its reference technology position in the NVH instruments' market, as can be seen in Table 1, where the best mode pairs resulting from the model updating were proposed. In Figure 18 the eigenmodes of the FEA model against those of test were sketched. The mating modes showed the lowest MAC values of the whole comparison, probably as the result of the scattering on SLDV data before the EMA.

9.3.2 DIC vs FEM modal base comparison. In Figure 19 are shown the results of the model refinement by means of DIC dataset, sketching higher correlation from MAC values in Table 1 than that of SLDV, but for a reduced frequency range (here just the first three best matching pairs were presented, but it stopped at 647 Hz with MAC 0.601). Probably the artefacts of the lower frequency modes counter played for achieving the best correlation. It must be reminded that native full field datasets were interpolated on SLDV grid, but it might be surely of interest to extend the analysis to the advantage of increasing the dofs' number with native resolution, while maintaining the low noise scattering on eigenshapes seen from native full field technologies.

9.3.3 ESPI vs FEM modal base comparison. The matching of the model with ESPI modal base was remarkably better, here shown in Table 1 and Figures 20 just till the third shape, but extendible to 763 Hz with MAC 0.805, and waving values in between. It appeared that the high continuity of the ESPI shapes gave a strong contribution in refining the comparison with the numerical model. Beyond dofs' number effect, ESPI proved (e.g. [18, 21] and Paragraph 5.) to be the best of the challenged technologies to suggest an extension of the references' set for model updating, by means of consistent extra physical quantities, such as dynamic rotations & strains over the optically accessible surface: this will be another path on which to extend the researches.

10. CONCLUSIONS

This paper has briefly reported the main achievements in the activity of the TEFFMA project. In particular it highlighted the importance that full field measurements can have in advanced design procedures, underlining some potential benefits that may come from a widespread usage of Full Field FRFs and accurate spatial refinement. In the frame of a rigorous pointwise comparison, the growing full field measurements (SLDV, Hi-Speed DIC and dynamic ESPI) were able to match themselves, with promising quality on the same advanced experimental set-up. The pure full field measurement techniques (DIC & ESPI) showed to take advantage of the spatial resolution and consistency for a detailed evaluation of experimental *receptance* surfaces, together with the numerical derivation of advanced features, here rotations and strains, for complex design procedures, in particular showing the relevant advantage of consistent data fields when numerically processed.

This fundamental research activity has systematically extended to broad-band fully populated test spectra what proposed already in [8–10] showing a promising experiment-based procedure to assess the fatigue life on a component, by means of full field optical measurements obtained from different gears and approached with the same pointwise comparative procedure seen in [6, 18, 21]. The evaluation of detailed experimental *receptance* FRF maps was proposed as a promising approach to simulate fatigue life as function of the varying input spectra, excitation point and measurement technology, when measurement uncertainty is under control, but mainly overcoming any FE modelling.

Finally the quality of native full field technologies in sensing accurate displacements in broad frequency band structural dynamics has been brought to relevance, after the early steps [4] of the author. It appears now possible to run proficiently an Experimental Full Field Modal Analysis with increased spatial sampling thanks to the emerging full field optical techniques and augmented computing power, even with more accuracy and ease than that obtained in the past [5, 30, 31], when virtual datasets had to be managed to cope with the huge calculations of ESPI modal analysis [32], or with advanced reduction schemes [25].

The analyses made in these research streams have highlighted also potential weaknesses of today prototype gears: further refinements of all the three optical technologies will sure enhance the level of contact-less vibration measurements. Hi-Speed DIC and Dynamic ESPI have shown in this research, while not yet mature as the SLDV, to provide the awaited quality on the eigenshapes for driving a full modal identification and use proficiently the obtained modal base to make enhanced comparisons with numerical models, for all the applications that well assessed NVH procedures [23, 24] can investigate.

It is now possible to look at optical full field measurement techniques as more feasible means to systematically evaluate the distribution of awaited quantities (from the test side of general product enhancement), like *dynamic displacements*, *dynamic rotations* and *strains*. The path towards experimental Full Field NVH is paved with intriguing advancements.

Acknowledgements

This activity is part of the Project TEFFMA - Towards Experimental Full Field Modal Analysis, funded by the European Commission at the Technische Universitaet Wien, through the Marie Curie FP7-PEOPLE-IEF-2011 PIEF-GA-2011-298543 grant, for which the Research Executive Agency is greatly acknowledged. This work is intended to be part of the spreading of the results thereof. Vienna University of Technology, in the person of Prof. Wassermann and his staff, are kindly acknowledged for hosting the TEFFMA project of the author at the *Schwingungs- und Strukturanalyse* / Optical Vibration Measurement Laboratory. The workstation used to process the datasets was provided by the author on his own savings.

REFERENCES

[1] Rastogi, P. K., 1997. *Optical Measurement Techniques and Applications*. Artech House, Inc., Nordwood, MA 02062, U.S.A.

[2] Kreis, T., 2004. *Handbook of Holographic Interferometry*. Wiley-VCH, Berlin, Germany.

[3] Zanarini, A., 2005. "Dynamic behaviour carachterization of a brake disc by means of electronic speckle pattern interferometry measurements". In Proceedings of the IDETC/CIE ASME International Design Engineering Technical Conferences & Computers and Information in Engineering Conference, Long Beach, California, USA, September 24-28, ASME, pp. 273–280. Paper DETC2005-84630, doi:10.1115/DETC2005-84630.

[4] Zanarini, A., 2007. "Full field ESPI measurements on a plate: challenging experimental modal analysis". In Proceedings of the XXV IMAC, Orlando (FL) USA, Feb 19-22, SEM, pp. 1–11. Paper s34p04, `http://sem-proceedings.com/25i/sem.org-IMAC-XXV-s34p04-Full-Field-ESPI-Measurements-Plate-Challenging-Experimental-Modal-Analysis.pdf`.

[5] H. Van der Auweraer et al., 2001. "Industrial applications of pulsed-laser espi vibration analysis". In Proc. of the XIX IMAC, Kissimmee, FL, USA, SEM, pp. 490–496. `http://sem-proceedings.com/19i/sem.org-IMAC-XIX-191407-Industrial-Applications-Pulsed-laser-ESPI-Vibration-Analysis.pdf`.

[6] Zanarini, A., 2014. "On the estimation of frequency response functions, dynamic rotational degrees of freedom and strain maps from different full field optical techniques". In Proceedings of the ISMA2014 including USD2014 - International Conference on Noise and Vibration Engineering, Leuven, Belgium, September 15-17, KU Leuven, pp. 1177–1192. Dynamic testing: methods and instrumentation, paper ID676, `https://www.isma-isaac.be/past/conf/isma2014/proceedings/papers/isma2014_0676.pdf`.

[7] Zanarini, A., 2014. “Dynamic strain & stresses for enhanced reliability: from full field optical measurements to simulations”. In Proceedings of the ICAIM2014 International Conference on Applications for Image based Measurements, Leipzig, Germany, June 24-25, Dantecdynamics, pp. 1–18. ISBN 9783000453175, doi:10.13140/RG.2.1.4724.1045.

[8] Zanarini, A., 2008. “Fatigue life assessment by means of full field ESPI vibration measurements”. In Proceedings of the ISMA2008 Conference, September 15-17, Leuven (Belgium), P. Sas, ed., KUL, pp. 817–832. Condition monitoring, Paper 326, doi:10.13140/RG.2.1.3452.9365.

[9] Zanarini, A., 2008. “Full field ESPI vibration measurements to predict fatigue behaviour”. In Proceedings of the IMECE2008 ASME International Mechanical Engineering Congress and Exposition, October 31- November 6, Boston (MA) USA, ASME, pp. 165–174. Paper IMECE2008-68727, doi:10.1115/IMECE2008-68727.

[10] Zanarini, A., 2008. “ESPI measurements in structural dynamics: fatigue life assessment”. In Proceedings of the Dantec Dynamics 15th International Conference and User Meeting, Dantecdynamics GmbH, pp. 1–20. doi:10.13140/RG.2.1.3076.8724.

[11] Zanarini, A., 2009. “Full-field espi techniques in structural dynamics”. In Atti del convegno Seconda giornata di studio Ettore Funaioli,18 luglio 2008, Bologna, Italy, Quaderni di ricerca del DIEM, AMS Acta - Alm@DL Universitá di Bologna, pp. 31–56. See also URL `http://amsacta.cib.unibo.it/archive/00002552/`, doi:10.6092/unibo/amsacta/2552.

[12] Zanarini, A., 2011. “Full field optical measurements for advanced structural dynamics: first outcomes”. In Atti del convegno Quarta giornata di studio Ettore Funaioli,16 luglio 2010, Bologna, Italy, Quaderni di ricerca del DIEM, AMS Acta - Alm@DL Universitá di Bologna, pp. 17–31. See also URL `http://amsacta.cib.unibo.it/archive/00003043/`, doi:10.6092/unibo/amsacta/3043.

[13] Zanarini, A., 2011. “Dynamic strain & stresses for enhanced reliability: from full field optical measurements to simulations”. In Proceedings of the ICAIM2011 International Conference on Applications for Image based Measurements, Schloss Grosslaupheim (Ulm), Germany, March 22-23, Dantecdynamics, pp. 1–14. ISBN 9783000335914, doi:10.13140/RG.2.1.1316.2329.

[14] Zanarini, A., 2014. “On the role of spatial resolution in advanced vibration measurements for operational modal analysis and model updating”. In Proceedings of the ISMA2014 including USD2014 - International Conference on Noise and Vibration Engineering, Leuven, Belgium, September 15-17, KU Leuven, pp. 3397–3410. Operational modal analysis, paper ID678, `https://www.isma-isaac.be/past/conf/isma2014/proceedings/papers/isma2014_0678.pdf`.

[15] Zanarini, A., 2015. “Model updating from full field optical experimental datasets”. In Proceedings of the ICoEV2015 International Conference on Engineering Vibration, Ljubljana, Slovenia, September 7-10, Univ. Ljubljana & IFToMM, pp. 773–782. ID196.

[16] Liu, W., and Ewins, D., 1999. “The Importance Assessment of RDOF in FRF Coupling Analysis”. In Proceedings of the IMAC 17th Conference, Kissimmee, Florida, pp. 1481–1487. Society for Experimental Mechanics (SEM), `http://www3.imperial.ac.uk/pls/portallive/docs/1/49146.PDF`.

[17] Research network, 1998. QUATTRO Brite-Euram project no: BE 97-4184. Tech. rep., Eurpean Commision Research Framework Programs.

[18] Zanarini, A., 2015. “Comparative studies on full field FRFs estimation from competing optical instruments”. In Proceedings of the ICoEV2015 International Conference on Engineering Vibration, Ljubljana, Slovenia, September 7-10, Univ. Ljubljana & IFToMM, pp. 1559–1568. ID191.

[19] ESDU, 2006. “Spectral methods for the estimation of fatigue life 06011”. In *Estimation of fatigue life of structures subjected to random loading*, Vol. 9 of *Vibration and Acoustic Fatigue Series*. ESDU International Plc, London, November, pp. 1–56.

[20] Zanarini, A., 2015. “Full field experimental modelling in spectral approaches to fatigue predictions”. In Proceedings of the ICoEV2015 International Conference on Engineering Vibration, Ljubljana, Slovenia, September 7-10, Univ. Ljubljana & IFToMM, pp. 1579–1588. ID193.

[21] Zanarini, A., 2015. “Accurate FRFs estimation of derivative quantities from different full field measuring technologies”. In Proceedings of the ICoEV2015 International Conference on Engineering Vibration, Ljubljana, Slovenia, September 7-10, Univ. Ljubljana & IFToMM, pp. 1569–1578. ID192.

[22] Dirlik, T., 1985. “Application of computers in fatigue analysis”. PhD thesis, University of Warwick, January.

[23] Heylen, W., Lammens, S., and Sas, P., 1998. *Modal Analysis Theory and Testing*. Katholieke Universiteit Leuven, Leuven (Belgium). ISBN 90-73802-61-X.

[24] Ewins, D. J., 2000. *Modal Testing - theory, practice and application*, 2^{nd} ed. Research Studies Press Ltd., Baldock, Hertfordshire, England. ISBN 978-0-86380-218-8.

[25] Wang, W., Mottershead, J., Siebert, T., and Pipino, A., 2011. “Frequency response functions of shape features from full-field vibration measurements using digital image correlation”. *MSSP,* **28**, pp. 333–347. Elsevier Science Ltd, doi:10.1016/j.ymssp.2011.11.023.

[26] Maas, A. A. M., 1991. “Phase shifting speckle interferometry”. PhD thesis, Delft University Press.

[27] Press, W. H., Teukolsky, S. A., Vetterling, W. T., and Flannery, B. P., 1992. *Numerical Recipes in C: The Art of Scientific Computing*, 2^{nd} ed. Cambridge Univ. Press, England.

[28] Bendat, J., and Piersol, A., 2000. *Random data: analysis and measurement procedures*, 3^{rd} ed. John Wiley & Sons Inc.

[29] H. Van der Auweraer et al., 1999. “Structural modelling of car panels using holographic modal analysis”. In Proc. of the Noise and Vibration Conference, Traverse City (MI), USA, Vol. 3, pp. 1495–1506. SAE P-342, doi:10.4271/1999-01-1849.

[30] Van der Auweraer, H., Steinbichler, H., Haberstok, C., Freymann, R., and Storer, D., 2000. “Integration of pulsed-laser ESPI with spatial domain modal analysis: results from the SALOME project”. In Proc. of the 4th International Conference on Vibration Measurements by Laser Techniques: Advances and Applications, Vol. 4072, SPIE, pp. 313–322. doi:10.1117/12.386741.

[31] H. Van der Auweraer et al., 2002. “Application of stroboscopic and pulsed-espi to modal analysis problems”. *Measurement Science and Technology,* **13**(4), pp. 451–463. doi:10.1088/0957-0233/13/4/305.

[32] Haberstok, C., 2005. “Die Holographische Modalanalyse”. PhD thesis, Technischen Universitaet Muenchen, Germany.

[33] Lanza di Scalea, F., Hong, S. S., and Cloud, G. L., 1998. “Whole-field strain measurement in a pin-loaded plate by electronic speckle pattern interferometry and the finite element method”. *Experimental Mechanics,* **38**(1), pp. 55–60. SEM, doi:10.1007/BF02321268.

[34] Siebert, T., El-Ratal, W., Wegner, R., and Ettemeyer, A., 2002. “Combine simulation and experiment in automotive testing with ESPI measurement”. *Experimental Techniques*, May/June, pp. 42–47,. SEM, doi:10.1111/j.1747-1567.2002.tb00068.x.

[35] George, T. J., Seidt, J., Shen, M. H. H., Nicholas, T., and Cross, C. J., 2004. “Development of a novel vibration-based fatigue testing methodology”. *Int. J. Fatigue,* **26**(5), pp. 474–486. Elsevier Science Ltd, doi:10.1016/j.ijfatigue.2003.10.012.

[36] McDowell, D. L., 1996. “Multiaxial fatigue strength”. In *Fatigue and Fracture*, Vol. 19 of *ASM Handbook*. ASM International Handbook Committee, pp. 1–21.

[37] ESDU, 2006. “Fatigue damage and life under random loading 06009”. In *Estimation of fatigue life of structures subjected to random loading*, Vol. 9 of *Vibration and Acoustic Fatigue Series*. ESDU International Plc, London, May, pp. 1–41.

[38] ESDU, 2006. “Cycle counting methods for the estimation of fatigue life 06010”. In *Estimation of fatigue life of structures subjected to random loading*, Vol. 9 of *Vibration and Acoustic Fatigue Series*. ESDU International Plc, London, August, pp. 1–41.

[39] Dynamic Design Solutions, 2015. Femtoos 3.8.1 software. `http://www.femtools.com`.

[40] Mottershead, J., Link, M., and Friswell, M. I., 2011. “The sensitivity method in finite element model updating: A tutorial”. *Mechanical Systems and Signal Processing,* **25**(7), pp. 2275–2296. Elsevier Science Ltd, doi:10.1016/j.ymssp.2010.10.012.

ANALISI DI POSIZIONE DI UNA PIATTAFORMA DI GOUGH-STEWART MODIFICATA

Luca Luzi
Department of Industrial Engineering,
University of Bologna, Italy
E-mail: luca.luzi3@unibo.it

Nicola Sancisi
Department of Industrial Engineering,
University of Bologna, Italy
E-mail: nicola.sancisi@unibo.it

Vincenzo Parenti Castelli
Department of Industrial Engineering,
University of Bologna, Italy
E-mail: vincenzo.parenti@unibo.it

***Abstract**. In questo lavoro gli autori presentano una soluzione dell’analisi di posizione diretta di una piattaforma di Gough-Stewart modificata che, rispetto alla piattaforma classica, presenta alcuni vantaggi. La soluzione dell’analisi di posizione diretta del manipolatore è basata su una parametrizzazione che porta ad un sistema di quattro equazioni di chiusura.*

Keywords: *piattaforma di Gough-Stewart modificata, analisi di posizione diretta, sistema ridotto di equazioni.*

1. INTRODUZIONE

Diverse tipologie di piattaforma di Gough-Stewart (PGS) sono presenti in letteratura [1]. In questo lavoro viene analizzata un’architettura di PGS modificata, simile a quella proposta in [2]. Rispetto alla PGS standard, presenta alcune interessanti caratteristiche, ancora in fase di studio: ad esempio, analisi preliminari hanno mostrato che tale architettura presenta un ampio spazio di lavoro e una grande porzione di esso (contenente lo spazio effettivamente operativo) risulta libero da singolarità cinematiche.

In questo lavoro viene presentata una soluzione dell’analisi di posizione diretta (APD) della piattaforma. Le equazioni di chiusura del meccanismo sono determinate in base alla tecnica dell’apertura della catena cinematica, presentata per manipolatori spaziali paralleli in [3] e usata per risolvere la APD di diversi meccanismi. Diversamente dall’approccio classico che porta a definire un sistema di sei equazioni in sei incognite per la determinazione dei parametri di posa (ovvero posizione e orientamento) della piattaforma, viene mostrato che il problema può essere ridotto a un sistema di quattro equazioni in quattro incognite. Di seguito viene descritto brevemente il manipolatore e viene presentata la trattazione analitica della soluzione della APD.

2. PIATTAFORMA DI GOUGH-STEWART MODIFICATA

Il meccanismo (Fig. 1) è composto da una piattaforma mobile (1) (definita dai punti C_i, i=1,2,3, che definisco il piano σ), in grado di muoversi con sei gradi di libertà rispetto alla base (2) (definita dai punti $A_{i,j}$, i=1,2,3, j=1,2). Base e piattaforma sono connesse da tre catene cinematiche (Fig. 2), definite dai punti $A_{i,1}$, $A_{i,2}$, $B_{i,2}$, $B_{i,1}$, i=1,2,3. La piattaforma mobile è connessa ai membri superiori $B_{i,2}B_{i,1}$ delle catene cinematiche per mezzo di giunti cardanici centrati in C_i . I due assi del i-esimo giunto cardanico non devono essere paralleli alla normale al piano γ_i (definito come il piano che contiene i punti C_i, $A_{i,1}$, $A_{i,2}$), così da evitare ridondanza di vincolo. In ogni catena cinematica, i punti $B_{i,j}$ individuano le connessioni degli attuatori lineari con il membro superiore della catena cinematica per mezzo di coppie rotoidali mentre i punti $A_{i,j}$ individuano le connessioni degli attuatori con la base per mezzo di giunti sferici. In ogni catena cinematica gli assi delle coppie rotoidali sono paralleli (Fig. 2). Questa condizione fa sì che la i-esima catena cinematica giaccia nel piano γ_i per ogni configurazione del manipolatore.

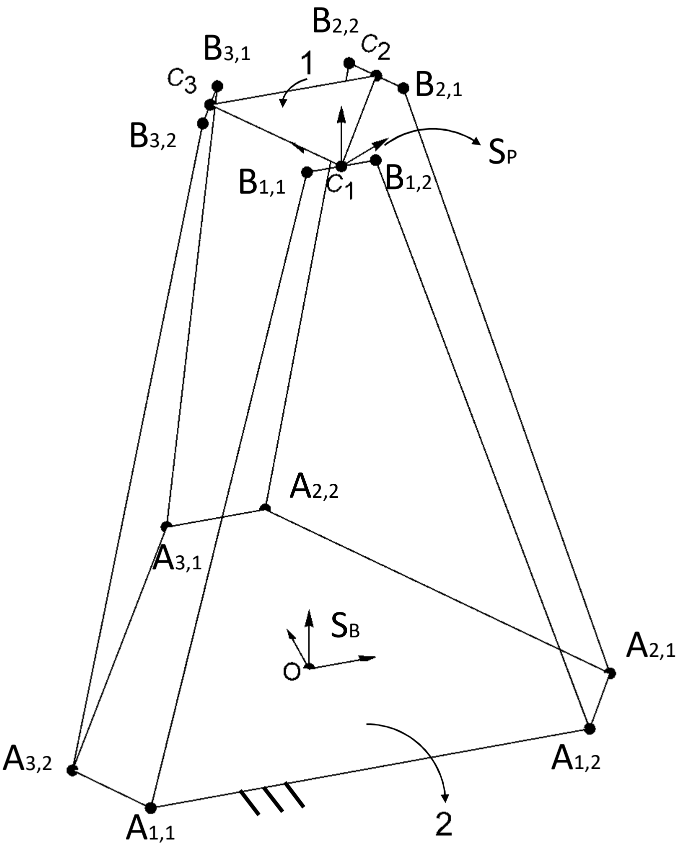

Figura 1. Rappresentazione schematica del manipolatore.

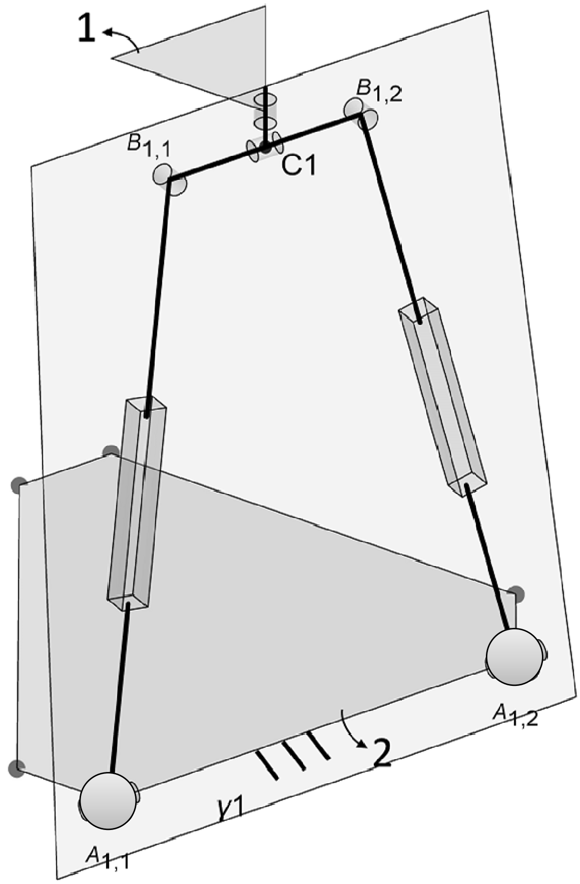

Figura 2. Rappresentazione dettagliata della prima catena cinematica.

3. ANALISI DI POSIZIONE DIRETTA

La APD consiste nel determinare la configurazione del manipolatore, assegnata la lunghezza degli attuatori. Per semplicità, i punti $A_{i,j}$ della base sono presi tutti sullo stesso piano, anche se la soluzione proposta della DPA rimane comunque valida per geometrie più generali. Siano definiti due sistemi di riferimento Cartesiani (Fig. 1). Il primo (S_B) è rigidamente connesso alla base: la sua origine coincide con il centroide della base, l'asse x è parallelo al vettore $\mathbf{A}_{1,1}\mathbf{A}_{1,2}$, l'asse z ortogonale al piano individuato dalla base e l'asse y di conseguenza. Il secondo sistema di riferimento (S_P) è rigidamente connesso alla piattaforma mobile: la sua origine coincide con il punto C_1, l'asse y è coincidente con la direzione $\mathbf{C}_1\mathbf{C}_3$, l'asse z è ortogonale al piano σ e l'asse x di conseguenza. La geometria del meccanismo è definita come segue: $\mathbf{a}_{i,j}$ è il vettore posizione del punto $A_{i,j}$ in S_B; $\mathbf{c}_i$ è il vettore posizione del punto C_i in S_P; $\mathbf{r}_i$ è il vettore che definisce il membro inferiore della i-esima catena cinematica e appartiene anche alla base, (cioè, $\mathbf{r}_i=\mathbf{A}_{i,2}\mathbf{A}_{i,1}$); $l_{i,j}$ è la lunghezza del j-esimo attuatore della i-esima catena cinematica (cioè, $l_{i,j}=\|\mathbf{A}_{i,j}\mathbf{B}_{i,j}\|$); **k** è il versore normale al piano σ (cioè, l'asse coincidente con l'asse z di S_P); $\mathbf{u}_i$ è il versore normale al piano γ_i; $\mathbf{t}_i$ è il versore che definisce la direzione del vettore $\mathbf{B}_{i,1}\mathbf{B}_{i,2}$ (i.e., $\mathbf{t}_i=\mathbf{B}_{i,1}\mathbf{B}_{i,2}/\|\mathbf{B}_{i,1}\mathbf{B}_{i,2}\|$), e l è la sua norma (i.e., $l=\|\mathbf{B}_{i,1}\mathbf{B}_{i,2}\|$).

La posizione dei punti C_1 and $B_{1,j}$ può essere descritta nel sistema di riferimento S_B con quattro parametri ψ_i (i=1,2,3,4) (Fig. 3): ψ_1 è l'angolo tra il vettore $\mathbf{r}_1$ e il vettore $\mathbf{A}_{1,1}\mathbf{B}_{1,1}$, ψ_2 è l'angolo tra il piano γ_1 e il piano della base, ψ_3 è l'angolo formato dai vettori **k** e $\mathbf{u}_1$, e ψ_4 è l'angolo tra il versore ottenuto come prodotto vettoriale tra **k** e $\mathbf{t}_1$ e l'asse y di S_P. In particolare, la posizione del punto C_1 può essere espressa come una funzione di ψ_1, ψ_2 e delle lunghezze $l_{1,1}$ and $l_{1,2}$ solamente, come sarà chiarito successivamente. Inoltre è facile notare che se gli attuatori sono bloccati la catena cinematica $A_{1,1}B_{1,1}B_{1,2}A_{1,2}$ è un quadrilatero articolato, e l'angolo θ (cioè, l'angolo tra il membro superiore e quello inferiore della catena cinematica) può essere espresso come funzione dell'angolo ψ_1 e delle lunghezze $l_{1,1}$ e $l_{1,2}$, secondo la nota relazione [4]:

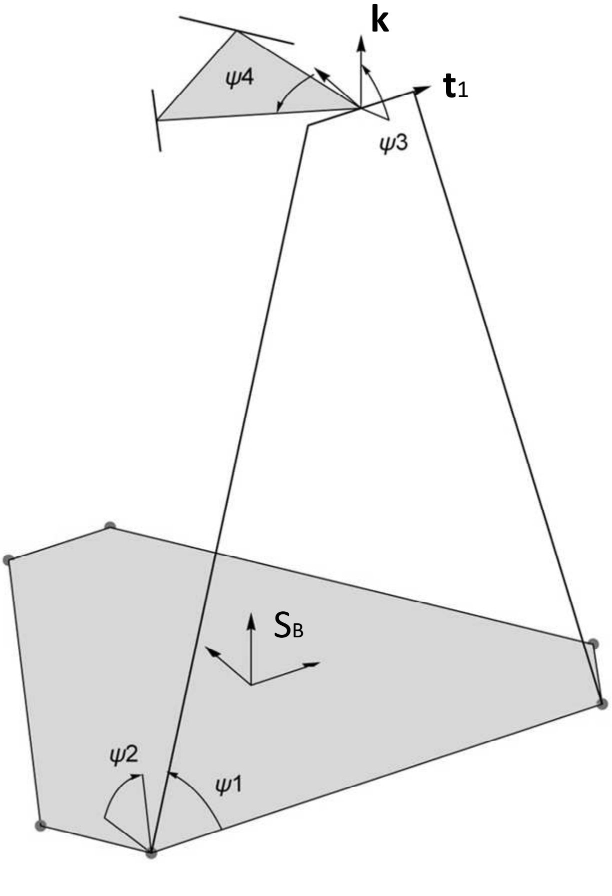

Figura 3. Rappresentazione dei quattro parametri utilizzati nella risoluzione della APD.

$$\theta = 2\tan^{-1}\left(\frac{-b-\sqrt{b^2-4ac}}{2a}\right) \tag{1}$$

dove

$$\begin{aligned} a &= -h_1 + (1+h_2)\cos(\psi_1) + h_4 \\ b &= -2\sin(\psi_1) \\ c &= h_1 - (1-h_2)\cos(\psi_1) + h_4 \end{aligned} \tag{2}$$

e

$$h_1 = \frac{r_1}{l_1}, \quad h_2 = \frac{r_1}{l}, \quad h_4 = \frac{-r_1^{\,2} - l_1^{\,2} - l^2 + l_2^{\,2}}{2\cdot l\cdot l_1} \tag{3}$$

Il vettore posizione del punto C_1 può essere quindi scritto come:

$$\mathbf{OC}_1 = \mathbf{a}_{1,1} + \mathbf{A}_{1,1}\mathbf{B}_{1,1} + \frac{\mathbf{B}_{1,1}\mathbf{B}_{1,2}}{2} \tag{4}$$

Il vettore $\mathbf{B}_{i,1}\mathbf{B}_{i,2}$, può essere espresso in S_B come:

$$^{B}(B_{1,1}B_{1,2}) = l\begin{pmatrix}\cos\theta \\ \sin\theta\cos\psi_2 \\ \sin\theta\sin\psi_2\end{pmatrix}, \quad ^{B}(A_{1,1}B_{1,1}) = l_{1,1}\begin{pmatrix}\cos\psi_1 \\ \sin\psi_1\cos\psi_2 \\ \sin\psi_1\sin\psi_2\end{pmatrix} \tag{5}$$

Il vettore posizione $\mathbf{OC}_i$ (i=2,3) può essere espresso come una funzione dei quattro parametri nel modo seguente:

$$^{B}(OC_i) = {}^{B}(OC_1) + {}^{B}\mathbf{R}_P\,{}^{P}c_i \quad i = 2,3 \tag{6}$$

dove

$$^{B}\mathbf{R}_P = \mathbf{R}_{\mathbf{r}_1}(\psi_2)\mathbf{R}_{\mathbf{u}_1}(\theta)\mathbf{R}_{\mathbf{t}_1}(\psi_3)\mathbf{R}_{\mathbf{k}}(\psi_4) \tag{7}$$

In (7), ogni $\boldsymbol{R}$ è una matrice ortonormale 3x3 che rappresenta una rotazione definita dall'angolo tra le parentesi, attorno all'asse indicato dal pedice.

Le coordinate dei punti $B_{i,j}$ (i=2,3; j=1,2) in S_B possono essere scritte come funzione degli stessi quattro parametri. In particolare, si fa notare che la direzione di $\mathbf{t}_i$ è ottenuta come l'intersezione tra i due piani σ and γ_i (Fig. 4). Infatti, il giunto centrato in C_i fa sì che al membro superiore della i-esima catena cinematica sia concessa una rotazione attorno all'asse **k**, e quindi il versore $\mathbf{t}_i$ giace nel piano σ. Inoltre, la direzione di $\mathbf{t}_i$ giace nel piano

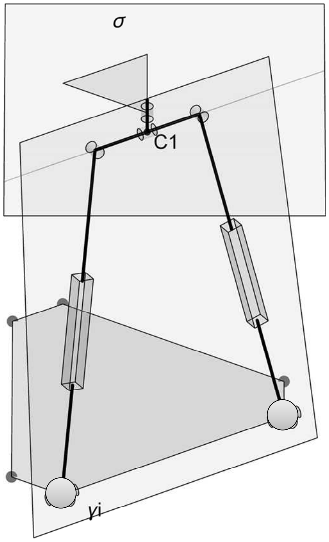

Figura 4. Definizione della retta che individua la direzione del membro superiore della catena cinematica.

γ_i, dal momento che il vettore $\mathbf{B}_{i,1}\mathbf{B}_{i,2}$ definisce il membro superiore della catena cinematica. Quindi, il versore $\mathbf{t}_i$ può essere determinato come il prodotto vettoriale tra $\mathbf{k}$ e $\mathbf{u}_i$:

$$\mathbf{t}_i = \frac{\mathbf{k} \times \mathbf{u}_i}{\left|\mathbf{k} \times \mathbf{u}_i\right|} \tag{8}$$

Per la seguente relazione:

$$\mathbf{u}_i = \frac{\mathbf{r}_i \times \mathbf{A}_{i,1}\mathbf{C}_i}{\left|\mathbf{r}_i \times \mathbf{A}_{i,1}\mathbf{C}_i\right|} \tag{9}$$

$\mathbf{t}_i$ può essere scritto senza aggiungere ulteriori variabili:

$$\mathbf{t}_i = \frac{\mathbf{k} \times (\mathbf{r}_i \times \mathbf{A}_{i,1}\mathbf{C}_i)}{\left|\mathbf{k} \times (\mathbf{r}_i \times \mathbf{A}_{i,1}\mathbf{C}_i)\right|} \tag{10}$$

dove

$$\mathbf{A}_{i,1}\mathbf{C}_i = \mathbf{OC}_i - \mathbf{a}_{i,1} \tag{11}$$

Il vettore posizione di $B_{i,j}$ in S_B può quindi essere espresso come:

$$\mathbf{OB}_{i,j} = \mathbf{a}_{i,j} + \mathbf{A}_{i,j}\mathbf{B}_{i,j} = \mathbf{OC}_i \pm l\frac{\mathbf{t}_i}{2} \tag{12}$$

dove tutte le quantità a destra sono funzioni dei quattro parametri introdotti. Ne segue, infine, che un sistema di quattro equazioni nelle quattro incognite ψ_n, n=1,…,4, può essere scritto come segue:

$$(\mathbf{A}_{i,j}\mathbf{B}_{i,j})^T(\mathbf{A}_{i,j}\mathbf{B}_{i,j}) = l_{i,j}^{\ 2} = (\mathbf{OC}_i \pm l\frac{\mathbf{t}_i}{2} - \mathbf{a}_{i,j})^T(\mathbf{OC}_i \pm l\frac{\mathbf{t}_i}{2} - \mathbf{a}_{i,j}) \tag{13}$$
$$i = 2,3; \quad j = 1,2;$$

Questo sistema rappresenta la soluzione della APD: permette infatti di ottenere i valori dei parametri ψ_n che descrivono la configurazione del meccanismo, quando sono date la geometria dello stesso e la lunghezza degli attuatori.

4. ESEMPI NUMERICI

Come esempio, in questo paragrafo viene presa in considerazione una specifica geometria del meccanismo e la sua posa viene determinata con la nuova soluzione della APD per tre casi rappresentativi della lunghezza degli attuatori. I punti $A_{i,j}$ giacciono su una circonferenza di diametro d_b=840mm; i vettori posizione di due punti $A_{i,j}$ consecutivi appartenenti a differenti catene cinematiche formano un angolo $\varphi=\pi/9$ (Fig. 5); i punti C_i della piattaforma mobile formano un triangolo equilatero inscritto in una circonferenza di diametro d_p=280mm; la lunghezza del membro superiore di ciascuna catena cinematica è l=100mm. Nel primo caso gli attuatori hanno tutti la stessa lunghezza (corrispondente alla posa iniziale della piattaforma); nel secondo caso, gli attuatori hanno la stessa lunghezza tre a tre (questo caso corrisponde ad una rotazione della piattaforma attorno all'asse z); nel terzo caso, gli attuatori hanno una lunghezza tale per cui la piattaforma è ruotata attorno all'asse y.

Tabella 1. Lunghezza degli attuatori e corrispondenti valori dei quattro parametri per tre pose della piattaforma.

$[l_{1,1}\ l_{1,2}\ l_{2,1}\ l_{2,2}\ l_{3,1}\ l_{3,2}]$	Ψ_1	Ψ_2	Ψ_3	Ψ_4
[958.6, 958.6, 958.6, 958.6, 958.6,958.6]	1.33736	1.43097	-1.43097	0.523599
[891.6, 847.8, 891.6, 847.8, 891.6,847.8]	1.21866	1.37925	-1.37925	1.183130
[973.3 969.8 1004.2 1002.9 939.5 941.6]	1.17517	1.43822	-1.47862	0.438011

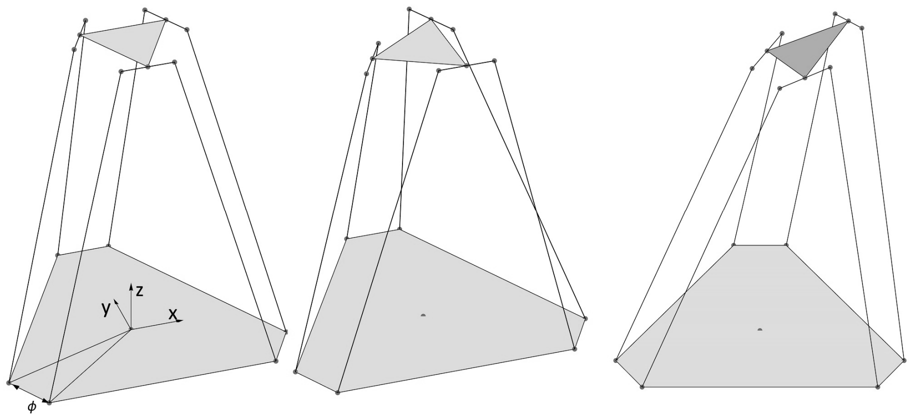

Figura 5. Tre configurazioni considerate negli esempi numerici.

5. CONCLUSIONI

In questo lavoro è stata presentata una soluzione della APD di una tipologia modificata della PGS standard: la piattaforma mobile è connessa alla base per mezzo di tre catene cinematica che si comportano come quadrilateri articolati quando gli attuatori sono bloccati. La nuova soluzione della APD si basa su una parametrizzazione che porta ad un sistema di quattro equazioni in quattro incognite e, quindi, riduce il sistema di sei equazioni in sei incognite che solitamente è proposto per questa tipologia di manipolatori per risolvere la APD. Questa parametrizzazione fa sì che la posa della piattaforma possa essere rappresentata a partire dalla configurazione di una singola catena cinematica, semplificando quindi la trattazione analitica e la comprensione dei risultati geometrici.

BIBLIOGRAFIA

[1] Bhaskar Dasgupta, T.S. Mruthyunjaya, 2000. "*The Stewart platform manipulator- a review*". Mechanism and Machine Theory, 35, 15-40.

[2] Haidi A.Akeel, 1996. Programmable positioner for the stress-free assembly of components, US005987726A.

[3] Innocenti C. and Parenti-Castelli, V, 1990. "*Direct position analysis of the Stewart platform mechanism*". Mechanism and Machine Theory, 25, 611–621.

[4] Hunt K.H, 1990. *Kinematic Geometry of Mechanisms*, 1*st* ed., Oxford Engineering Science Series. Oxford University Press, Chap. 6, pp. 191.

TRANSFER FUNCTION PARAMETER IDENTIFICATION IN THE FREQUENCY DOMAIN

Umberto Soverini
Department of Electrical, Electronic and Information Engineering,
University of Bologna, Italy
E-mail: umberto.soverini@unibo.it

Abstract. *This paper deals with the identification of Errors–in–Variables (EIV) models corrupted by additive and uncorrelated white noises when the noise–free input is an arbitrary signal, not necessarily periodic. In particular, the paper describes a frequency domain method, that resembles in many aspects the so–called Frisch Scheme approach, originally developed in the time domain. The method is applied to the identification of the dynamic parameters of simulated mechanical systems. The effectiveness of the proposed approach, even in presence of non linear model behavior, is verified by means of numerical simulations.*

Keywords: *System Identification, Errors–in–Variables Models, Mechanical Systems*

1. INTRODUCTION

This paper deals with the problem of identifying a linear dynamic system from input–output measurements affected by noise. Representations where errors or measurement noises are present on both inputs and outputs are usually called errors–in–variables (EIV) models. This class of models is present in several engineering applications and many solutions have been proposed with different approaches, see [1, 2] and the references therein.

Among them, frequency domain identification techniques are particular attractive [3]. As a matter of fact, the frequency domain approaches have some special features that are not easily implementable in the time domain. For example, filtering operations can be reduced to the selection of appropriate frequencies in a limited band of the signal spectrum [4].

In this work the EIV identification problem for SISO systems is addressed by using a frequency domain approach, when the noise-free input is an arbitrary sequence and the input–output noises are additive and uncorrelated white processes with unknown variances.

The proposed method can be considered as a frequency domain version of the so–called Frisch Scheme approach, originally developed in the time domain [5, 6]. In particular, the proposed solution can be viewed as the frequency domain counterpart of the procedure described in [7]. As a matter of fact, the method combines, in a frequency domain context, the characteristics of the Frisch scheme and the properties of the high order Yule-Walker (HOYW) equations.

This frequency domain approach was described for the first time in [8]. In this paper, the method is applied to mechanical systems, for the identification of their dynamic parameters. In this respect, this paper constitutes an extension of the results proposed [9]. Even if the identification method is suited assuming that the unknown model is linear and the uncertainties are due to additive measurements errors, in this paper it is shown that the method has equally good performances when the uncertainties are due to small non linearities in the model.

As in [9], the system is described by a parametric model that links the Discrete Fourier Transforms (DFT) of the input and output signals. According to the theoretic results described in [10], a polynomial term is added to the system equation in order to take into account the leakage and transient effects. Compared with other well–known Frequency Response Function (FRF) estimators [11] , the usage of this extended model makes it possible to deal with shorter data sequences and with arbitrary noise-free input signals, not necessarily periodic.

The organization of the paper is as follows. Section 2 defines the EIV identification problem in the frequency domain. In Section 3 the problem is reformulated as a Frisch Scheme problem. Section 4 describes a possible identification criterion, that can be directly formulated in the frequency domain. In particular, this criterion takes advantage of a set of equations similar to the HOYW equations. In Section 5 it is shown how the method can be applied to classical FRF identification methods, e.g. the H_1 method. Finally, in Section 6 the method is used for the identification of mechanical systems in presence of errors due to non linear model behaviors. The features of the proposed method are illustrated by means of a numerical simulation. A still open question is how the method performs when only a subset of the whole frequency range is used for the identification. This fact can be the subject of possible future investigation.

2. STATEMENT OF THE PROBLEM

Consider the linear time–invariant SISO system described by the linear difference equation

$$A(z^{-1})\,\hat{y}(t) = B(z^{-1})\,\hat{u}(t), \tag{1}$$

where $\hat{u}(t)$, $\hat{y}(t)$ are the noise–free input and output and $A(z^{-1})$ and $B(z^{-1})$ are polynomials in the backward shift operator z^{-1}

$$A(z^{-1}) = 1 + \alpha_1\, z^{-1} + \cdots + \alpha_n\, z^{-n} \tag{2}$$

$$B(z^{-1}) = \beta_0 + \beta_1\, z^{-1} + \cdots + \beta_n\, z^{-n}. \tag{3}$$

In the EIV environment the input and output measurements are assumed as corrupted by additive noise so that the available observations are

$$u(t) = \hat{u}(t) + \tilde{u}(t) \tag{4}$$

$$y(t) = \hat{y}(t) + \tilde{y}(t). \tag{5}$$

The following assumptions are made.

A1. The system (1) is asymptotically stable.

A2. $A(z^{-1})$ and $B(z^{-1})$ do not share any common factor.

A3. The order n of the system is assumed as *a priori* known.

A4. The noise–free input $\hat{u}(t)$ is a quasi–stationary bounded deterministic signal [12] and is persistently exciting of sufficiently high order.

A5. $\tilde{u}(t)$ and $\tilde{y}(t)$ are zero–mean ergodic white processes with unknown variances λ_u^* and λ_y^*, respectively. These processes are mutually uncorrelated and uncorrelated with the noise–free input $\hat{u}(t)$.

Remark 1. Assumptions A1–A4 are commonly imposed when dealing with general identification algorithms, not necessarily in an EIV context [12, 13]. Assumption A5 is common in the Frisch scheme context [5, 6] and as a basic assumption for analysing the EIV identification methods [1, 14]. For several EIV identification approaches, this assumption can be relaxed and correlated noises or coloured (output) noises can be considered [2].

Remark 2. The proposed method can be easily extended to the case when the polynomials $A(z^{-1})$ and $B(z^{-1})$ have different orders, n_a and n_b, respectively. However, for simplicity of exposition in this paper the two orders will be considered equal to n.

Let $\{u(t)\}_{t=0}^{(N-1)\Delta t}$ and $\{y(t)\}_{t=0}^{(N-1)\Delta t}$ be a set of input and output observations at N equidistant time instants t, $t + \Delta t$. In the following we will assume $\Delta t = 1$, without loss of generality. The corresponding DFTs are defined as

$$U(\omega_k) = \frac{1}{\sqrt{N}} \sum_{t=0}^{N-1} u(t)\,\mathrm{e}^{-j\omega_k t} \tag{6}$$

$$Y(\omega_k) = \frac{1}{\sqrt{N}} \sum_{t=0}^{N-1} y(t)\,\mathrm{e}^{-j\omega_k t}\ , \tag{7}$$

where $\omega_k = 2\pi k/N$ and $k = 0, \ldots, N-1$.

In the frequency domain, the problem under investigaion can be stated as follows.

Problem 1. Let $U(\omega_k)$, $Y(\omega_k)$ be a set of noisy measurements generated by an EIV system of type (1)–(5), under Assumptions A1–A5, where $\omega_k = 2\pi k/N$ and $k = 0, \ldots, N-1$. Estimate the system parameters $\alpha_i\ (i = 1, \ldots, n)$, $\beta_i\ (i = 0, \ldots, n)$ and the noise variances λ_u^*, λ_y^*.

3. FREQUENCY DOMAIN FRISCH SCHEME

The transfer function of (1) is represented as

$$G(\mathrm{e}^{-j\omega}) = \frac{B(\mathrm{e}^{-j\omega})}{A(\mathrm{e}^{-j\omega})}. \tag{8}$$

Similarly to equations (6)–(7), let $\hat{U}(\omega_k)$, $\hat{Y}(\omega_k)$ be the DFTs of the noise free signals $\hat{u}(t)$ and $\hat{y}(t)$ appearing in equation (1). It is a well–known fact [10] that for finite N, even in absence of noise, the ratio of $\hat{Y}(\omega_k)$ and $\hat{U}(\omega_k)$ is not equal to the true transfer function, i.e.

$$G(\mathrm{e}^{-j\omega_k}) \neq \frac{\hat{Y}(\omega_k)}{\hat{U}(\omega_k)}\ . \tag{9}$$

Rather, the DFTs $\hat{Y}(\omega_k)$ and $\hat{U}(\omega_k)$ exactly satisfy the following extended model that includes also a transient term

$$A(\mathrm{e}^{-j\omega_k})\,\hat{Y}(\omega_k) = B(\mathrm{e}^{-j\omega_k})\,\hat{U}(\omega_k) + T(\mathrm{e}^{-j\omega_k}), \tag{10}$$

where $T(z^{-1})$ is a polynomial of order $n-1$

$$T(z^{-1}) = \tau_0 + \tau_1\, z^{-1} + \cdots + \tau_{n-1}\, z^{-n+1} \tag{11}$$

that takes into account the effects of the initial and final conditions of the experiment.

By considering the whole number of frequencies, eq. (10) can be rewritten in a matrix form. For this purpose, introduce the parameter vectors

$$\theta_\alpha = [1\,\alpha_1 \ldots \alpha_n]^T \tag{12}$$

$$\theta_\beta = [\beta_0\,\beta_1 \ldots \beta_n]^T \tag{13}$$

$$\theta_\tau = [\tau_0 \ldots \tau_{n-1}]^T \tag{14}$$

and define the following vector Θ, with dimension

$$p = 3n + 2, \tag{15}$$

containing the whole set of parameters

$$\Theta = [\ \theta_\alpha^T\ \ -\theta_\beta^T\ \ -\theta_\tau^T\ ]^T. \tag{16}$$

In absence of noise, the parameter vector (16) can be recovered by means of the following procedure. Define the row vectors

$$Z_{n+1}(\omega_k) = [1\ \ \mathrm{e}^{-j\omega_k}\ \ \ldots\ \mathrm{e}^{-j(n-1)\omega_k}\ \ \mathrm{e}^{-jn\omega_k}\,] \tag{17}$$

$$Z_n(\omega_k) = [1\ \ \mathrm{e}^{-j\omega_k}\ \ \ldots\ \mathrm{e}^{-j(n-1)\omega_k}\,], \tag{18}$$

whose entries are constructed with multiple frequencies of ω_k, and construct the following matrices

$$\Pi = \begin{bmatrix} Z_{n+1}(\omega_0) \\ \vdots \\ Z_{n+1}(\omega_{N-1}) \end{bmatrix} \qquad \Psi = \begin{bmatrix} Z_n(\omega_0) \\ \vdots \\ Z_n(\omega_{N-1}) \end{bmatrix} \tag{19}$$

of dimension $N \times (n+1)$ and $N \times n$, respectively.

With the DFT samples $\hat{U}(\omega_k)$, $\hat{Y}(\omega_k)$ the following $N \times N$ diagonal matrices can be computed

$$\hat{V}_U^{diag} = \mathrm{diag}\,[\hat{U}(\omega_0),\, \hat{U}(\omega_1), \ldots, \hat{U}(\omega_{N-1})] \tag{20}$$

$$\hat{V}_Y^{diag} = \mathrm{diag}\,[\hat{Y}(\omega_0),\, \hat{Y}(\omega_1), \ldots, \hat{Y}(\omega_{N-1})] \tag{21}$$

and the following $N \times (n+1)$ matrices can be defined

$$\hat{\Phi}_A = \hat{V}_Y^{diag}\,\Pi \quad \hat{\Phi}_B = \hat{V}_U^{diag}\,\Pi \quad \hat{\Phi}_T = \Psi. \tag{22}$$

Thus, the $N \times p$ matrix can be constructed as follows

$$\hat{\Phi} = [\hat{\Phi}_A \,|\, \hat{\Phi}_B \,|\, \hat{\Phi}_T] \tag{23}$$

and eq. (10), for $k = 0, \ldots, N-1$, can be rewritten as

$$\hat{\Phi}\,\Theta = 0. \tag{24}$$

It then holds

$$\hat{\Sigma}\,\Theta = 0, \tag{25}$$

where $\hat{\Sigma}$ is the $p \times p$ matrix

$$\hat{\Sigma} = \frac{1}{N}(\hat{\Phi}^H \hat{\Phi}) \tag{26}$$

and $()^H$ denotes the transpose and conjugate operators.

Remark 3. Because of assumption A2, relation (10) cannot be satisfied by polynomials $A(z^{-1})$ and $B(z^{-1})$ with order lower than n. Therefore, the matrix $\hat{\Sigma}$ in (26) is positive semidefinite, with only one zero eigenvalue, i.e.

$$\hat{\Sigma} \geq 0 \qquad \dim\big(\ker \hat{\Sigma}\big) = 1. \tag{27}$$

In the presence of noise, the previous procedure can be modified as follows. With the noisy input–output DFT samples (6), (7) the $N \times N$ diagonal matrices can be defined as

$$V_U^{diag} = \mathrm{diag}\,[U(\omega_0),\, U(\omega_1), \ldots, U(\omega_{N-1})] \tag{28}$$

$$V_Y^{diag} = \mathrm{diag}\,[Y(\omega_0),\, Y(\omega_1), \ldots, Y(\omega_{N-1})]. \tag{29}$$

Thus, the following matrices can be computed

$$\Phi_A = V_Y^{diag}\,\Pi \quad \Phi_B = V_U^{diag}\,\Pi \quad \Phi_T = \Psi \tag{30}$$

and the $N \times p$ matrix

$$\Phi = [\Phi_A \,|\, \Phi_B \,|\, \Phi_T] \tag{31}$$

can be constructed. Because of assumptions A5, when $N \to \infty$, the following $p \times p$ positive definite matrix can be obtained

$$\Sigma = \lim_{N\to\infty} \frac{1}{N}(\Phi^H \Phi) = \hat{\Sigma} + \tilde{\Sigma}^*, \tag{32}$$

where

$$\tilde{\Sigma}^* = \begin{bmatrix} \lambda_y^*\, I_{n+1} & 0 & 0 \\ 0 & \lambda_u^*\, I_{n+1} & 0 \\ 0 & 0 & 0_n \end{bmatrix}. \tag{33}$$

From (25) and (32), the parameter vector Θ, defined in (16), can be obtained as the kernel of

$$\left(\Sigma - \tilde{\Sigma}^*\right)\Theta = 0, \tag{34}$$

where the first entry is normalized to 1.

Remark 4. Let us denote with $x(t)$ either $u(t)$ or $y(t)$. It can be observed that for $k = 0, \dots, \text{floor}\left(\frac{N-1}{2}\right)$

$$
\begin{aligned}
X(\omega_{N-1-k}) &= \frac{1}{\sqrt{N}} \sum_{t=0}^{N-1} x(t)\, \mathrm{e}^{-j\frac{N-1-k}{N}2\pi t} \\
&= \frac{1}{\sqrt{N}} \sum_{t=0}^{N-1} x(t)\, \mathrm{e}^{-j\frac{-(1+k)}{N}2\pi t} = X^*(\omega_{1+k}),
\end{aligned}
\tag{35}
$$

where X^* is the conjugate of X. Consequently, a redundant information has been used in the definition (32) of Σ. On the basis of this fact, the identification procedure that will be described in Section 4 can be set up by using only the first $M = \text{floor}\left(N/2\right)$ samples $U(\omega_k)$, $Y(\omega_k)$, $k = 0, \dots, \text{floor}\left(\frac{N-1}{2}\right)$, obtaining consistent estimates of the system parameters. However, simulation experiences have shown that the usage of the whole data set $U(\omega_k)$, $Y(\omega_k)$, $k = 0, \dots, N-1$ is to be preferred, in particular in case of short data length and when the Signal to Noise Ratio (SNR) is low.

Starting from knowledge of the noisy matrix Σ, the determination of the system parameter vector Θ and of the noise variances λ_u^*, λ_y^* can be seen as a Frisch Scheme problem [5, 6].

Consider the set of non–negative definite diagonal matrices of type

$$
\tilde{\Sigma} = \begin{bmatrix} \lambda_y I_{n+1} & 0 & 0 \\ 0 & \lambda_u I_{n+1} & 0 \\ 0 & 0 & 0_n \end{bmatrix}
\tag{36}
$$

such that

$$
\Sigma - \tilde{\Sigma} \geq 0 \qquad \det\left(\Sigma - \tilde{\Sigma}\right) = 0.
\tag{37}
$$

With the reasoning of [5], the following statements can be proved.

Theorem 1. The set of all matrices $\tilde{\Sigma}$ satisfying the conditions (37) defines the points $P = (\lambda_u, \lambda_y)$ of a convex curve $\mathcal{S}(\Sigma)$ belonging to the first quadrant of the noise space $\mathcal{R}^2$ whose concavity faces the origin. Every point $P = (\lambda_u, \lambda_y)$ on the curve can be associated with the noise matrix $\tilde{\Sigma}(P)$ and with the coefficient vector $\Theta(P)$ satisfying the relation

$$
\left(\Sigma - \tilde{\Sigma}(P)\right) \Theta(P) = 0.
\tag{38}
$$

In Figure 1 an example of $\mathcal{S}(\Sigma)$ is reported.

Theorem 2. Because of the relations (33) and (34), the point $P^* = (\lambda_u^*, \lambda_y^*)$, associated with the true variances of $\tilde{u}(t)$ and $\tilde{y}(t)$, belongs to $\mathcal{S}(\Sigma)$ and the corresponding coefficient vector $\Theta(P^*)$ is characterized (after a normalization of its first entry to 1) by the true system parameter vector, i.e. $\Theta(P^*) = \Theta$.

The next theorem describes a parametrization of the curve $\mathcal{S}(\Sigma)$ that makes it possible to associate a solution of (37) with every straight line departing from the origin and lying in the first quadrant. This parametrization plays an important role in the practical implementation of the identification algorithm [6].

Theorem 3. Let $\xi = (\xi_1, \xi_2)$ be a generic point of the first quadrant of $\mathcal{R}^2$ and r the straight line from the origin through ξ. Its intersection with $\mathcal{S}(\Sigma)$ is the point $P = (\lambda_u, \lambda_y)$ given by

$$
\lambda_u = \frac{\xi_1}{\lambda_M} \qquad \lambda_y = \frac{\xi_2}{\lambda_M}
\tag{39}
$$

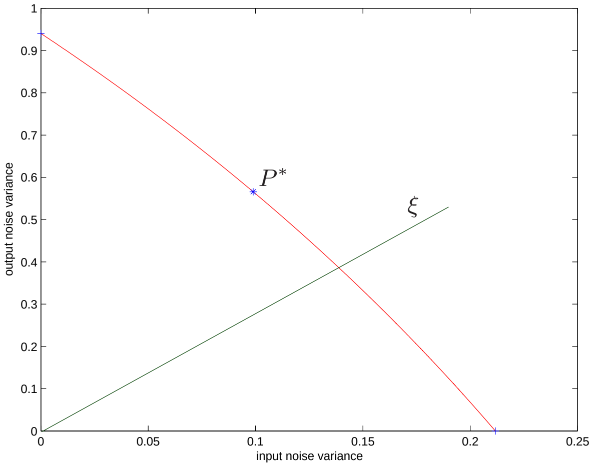

Figure 1. Typical shape of $\mathcal{S}(\Sigma)$.

where

$$\lambda_M = \max \operatorname{eig}\left(\Sigma^{-1}\tilde{\Sigma}_\xi\right) \tag{40}$$

$$\tilde{\Sigma}_\xi = \begin{bmatrix} \xi_2\, I_{n+1} & 0 & 0 \\ 0 & \xi_1\, I_{n+1} & 0 \\ 0 & 0 & 0_n \end{bmatrix}. \tag{41}$$

Remark 5. The described procedure allows the construction of the curve $\mathcal{S}(\Sigma)$ in the noise space (λ_u, λ_y) also when only a subset of the whole frequency range is used, the number of the selected frequencies being large enough. This subset must be chosen by the user on the basis of *a priori* knowledge of the frequency properties of the transfer function $G(\mathrm{e}^{-j\omega_k})$ and of the noise–free input $\hat{U}(\omega_k)$.

Remark 6. With reference to Remark 4, two choices are possible.

1. The identification makes use of $M = \text{floor}\left(N/2\right)$ samples $U(\omega_k)$, $Y(\omega_k)$, $k = 0, \ldots, \text{floor}\left(\frac{N-1}{2}\right)$.

   In this case, the frequency subset can be defined as $W_1 = [\omega_i,\, \omega_f]$, with $i \geq 0$ and $f \leq \text{floor}\left(\frac{N-1}{2}\right)$. The total number of frequencies used in the algorithm will be $L = f - i + 1$.

2. The identification is based of the whole data set $U(\omega_k)$, $Y(\omega_k)$, $k = 0, \ldots, N-1$.

   This choice is the one described in this paper and must be preferred in the case of short data length and low SNR conditions. Two distinct sets of frequencies must be jointly considered, the set $W_1 = [\omega_i,\, \omega_f]$, with $i \geq 0$ and $f \leq \text{floor}\left(\frac{N-1}{2}\right)$ and the set $W_2 = [\omega_{N-1-f},\, \omega_{N-1-i}]$. The total number of frequencies used in the algorithm will be $2L$. By considering a new matrix Φ with $2L$ rows, expressions (32)–(33) must be modified as follows

$$\Sigma = \frac{1}{2L}\big(\Phi^H\,\Phi\big) = \hat{\Sigma} + \tilde{\Sigma}^*, \tag{42}$$

where

$$\tilde{\Sigma}^* = \frac{N}{2L}\begin{bmatrix}\lambda_y^*\,I_{n+1} & 0 & 0\\ 0 & \lambda_u^*\,I_{n+1} & 0\\ 0 & 0 & 0_n\end{bmatrix}. \tag{43}$$

4. A CRITERION BASED ON HOYW–TYPE EQUATIONS

As asserted in Theorem 2, the determination of the point P^* on $\mathcal{S}(\Sigma)$ leads to the solution of Problem 1. For this purpose a search criterion must be introduced. Unfortunately, the theoretic properties of $\mathcal{S}(\Sigma)$ described so far do not allow to distinguish point P^* from the other points of the curve.

In this section we will describe a possible search criterion. This criterion is analogue to that reported in [7] with reference to time domain identification of EIV systems.

Select the integer $q \geq 3n+1$. Analogously to (17), consider the row vector

$$Z_{q+n+1}(\omega_k) = [1\ \mathrm{e}^{-j\omega_k}\ \ldots \mathrm{e}^{-j(q+n-1)\omega_k}\ \mathrm{e}^{-j(q+n)\omega_k}] \tag{44}$$

and extract from it the q–dimensional row vector

$$Z_q^h(\omega_k) = [\mathrm{e}^{-j(n+1)\omega_k}\ \ldots \mathrm{e}^{-j(q+n-1)\omega_k}\ \mathrm{e}^{-j(q+n)\omega_k}]. \tag{45}$$

Then, construct the following $N \times q$ matrix

$$\Pi^h = \begin{bmatrix} Z_q^h(\omega_0)\\ \vdots \\ Z_q^h(\omega_{N-1})\end{bmatrix} \tag{46}$$

and compute the $N \times q$ matrix

$$\hat{\Phi}^h = \hat{V}_U^{diag}\,\Pi^h. \tag{47}$$

Define now the $q \times p$ matrix

$$\hat{\Sigma}^h = \frac{1}{N}\big((\hat{\Phi}^h)^H\,\hat{\Phi}\big), \tag{48}$$

Because of (24) we have

$$\hat{\Sigma}^h\,\Theta = 0. \tag{49}$$

In an analogous way, we can compute the $N \times q$ matrix

$$\Phi^h = V_U^{diag}\,\Pi^h \tag{50}$$

and define the $q \times p$ matrix

$$\Sigma^h = \frac{1}{N}\big((\Phi^h)^H\,\Phi\big). \tag{51}$$

Because of assumptions A5, when $N \to \infty$, it results in

$$\Sigma^h = \hat{\Sigma}^h. \tag{52}$$

It is thus possible to write

$$\Sigma^h\,\Theta = 0. \tag{53}$$

Equation (53) constitutes a set of q equations, analogue to the time domain high order Yule–Walker equations, that does not involve the noise variances λ_u^*, λ_y^*. These equations could be directly used to obtain an estimate of the parameter vector Θ if $q \geq 3n+1$.

Remark 7. The value of the parameter q is a user choice. In general, this value can affect the quality of the estimates. However its influence is not straightforward to investigate. In the example of Section 6 the parameter q has been chosen at the minimal admissible value.

Thanks to equation (53) the search for P^* along $\mathcal{S}(\Sigma)$ can be performed by introducing the following cost function

$$J(P) = \Theta^T(P)(\Sigma^h)^H\,\Sigma^h\,\Theta(P) \tag{54}$$

which exhibits the following properties

i) $J(P) \geq 0$

ii) $J(P) = 0 \Leftrightarrow P = P^*$.

For a finite number of data, the minimum of $J(P)$ will not coincide with P^* and it will be denoted with P°.

On the basis of the previous considerations, it is thus possible to develop the following algorithm. The algorithm makes reference to the case of N data. As observed in Remark 4, if only $M = \text{floor}\big(N/2\big)$ data are considered, the algorithm must be modified in a straightforward fashion, by substituting N with M starting from step (2).

Algorithm 1.

1. Compute, on the basis of the available time domain data, the DFTs $U(\omega_k)$, $Y(\omega_k)$ with $\omega_k = 2\pi k/N$ ($k = 0, \ldots, N-1$).

2. Compute the matrices Φ_A, Φ_B and Φ_T as in (30) and construct the matrix Φ as in (31).

3. Compute, as in (32), the sample estimate of matrix

$$\Sigma = \frac{1}{N}(\Phi^H \Phi). \tag{55}$$

4. Select $q \geq 3n+1$ and construct the matrix Π^h as in (46), then compute Φ^h as in (50).

5. Compute, as in (51), the sample estimate of matrix

$$\Sigma^h = \frac{1}{N}\left((\Phi^h)^H\,\Phi\right). \tag{56}$$

6. Start from a generic point ξ (a generic direction) in the first quadrant of $\mathcal{R}^2$ and compute, by means of (39)–(41) the corresponding point $P = (\lambda_u, \lambda_y)$ on $\mathcal{S}(\Sigma)$.

7. Compute the estimates of $\hat{\Sigma}(P)$ and $\Theta(P)$ by means of the relations

$$\hat{\Sigma}(P) = \Sigma - \text{diag}\left[\,\lambda_y I_{n+1},\ \lambda_u\, I_{n+1},\ 0_n\,\right], \tag{57}$$

$$\hat{\Sigma}(P)\,\Theta(P) = 0. \tag{58}$$

8. Compute the value of the cost function $J(P)$ (54).

9. Search on the curve $\mathcal{S}(\Sigma)$ for the point P° associated with the minimum of $J(P)$.

Remark 8. The description of Algorithm 1 does not consider the filtering effects described in Remark 6.2. These effects can be easily taken into account by considering, instead of N, the $2L$ data belonging to W_1 and W_2, and by making reference to the relations (42) and (43). In an analogous way, for the M data case, straightforward modifications must be introduced when dealing with the filtering effects described in Remark 6.1.

5. APPLICATION TO CLASSICAL FRF IDENTIFICATION METHODS

In classical non–parametric FRF identification methods the noise level on the data is reduced by the averaging technique. Different estimators can be found in the literature, e.g. H_1, H_2 and H_v methods. However, in practice H_1 is the most often used FRF estimator since it is not affected by the noise on the output. For single input and single output measurements, the H_1 estimator is computed as follows. Using the notation introduced in Section 2 for noise–free data, the input and output sequences $\hat{u}(t)$ and $\hat{y}(t)$ are divided into N_b equal blocks. Denoting with N the number of the time samples $\hat{u}_b(t)$ and $\hat{y}_b(t)$ in the block b, the corresponding DFTs $\hat{U}_b(\omega_k)$ and $\hat{Y}_b(\omega_k)$ are computed according to the relations (6)–(7). Then, the cross–spectrum and the auto–spectrum are estimated by averaging on the N_b blocks

$$S_{UY}(\omega_k) = \frac{1}{N_b}\sum_{b=1}^{N_b} \hat{U}_b^H(\omega_k)\,\hat{Y}_b(\omega_k) \tag{59}$$

$$S_{UU}(\omega_k) = \frac{1}{N_b}\sum_{b=1}^{N_b} \hat{U}_b^H(\omega_k)\,\hat{U}_b(\omega_k). \tag{60}$$

Finally, the H_1 estimator is given by

$$H_1(\omega_k) = \frac{S_{UY}(\omega_k)}{S_{UU}(\omega_k)}. \tag{61}$$

In the rational case, the relation (61) yields an estimate of the transfer function defined in (8)

$$H_1(\omega_k) = G(\mathrm{e}^{-j\omega_k}) = \frac{B(\mathrm{e}^{-j\omega_k})}{A(\mathrm{e}^{-j\omega_k})}. \tag{62}$$

The H_1 estimator is asymptotically unbiased when the noise, white and uncorrelated with the input, is only present on the output. The contribution of the noise on the H_1 estimate will decrease proportionally with the square root of the N_b blocks averaged. The major drawback of the H_1 estimator is the trade–off between variance and bias. The variance, caused by the noise, decreases by increasing the amount of blocks. The bias is introduced by the leakage effects and it is inversely proportional to the square root of the amount of data samples within a block. For this reason, the H_1 estimator is successfully applicable only by using a window, e.g. a Hanning window, to reduce the leakage effects. In Section 3 we have shown that the errors introduced by the leakage phenomenon disappear by taking into account the transient polynomials as described in equation (10). This idea can be extended to the H_1 estimator, as follows [15].

Let us consider the equation (10), written for the DFTs $\hat{U}_b(\omega_k)$ and $\hat{Y}_b(\omega_k)$ of the generic block b

$$A(\mathrm{e}^{-j\omega_k})\,\hat{Y}_b(\omega_k) = B(\mathrm{e}^{-j\omega_k})\,\hat{U}_b(\omega_k) + T_b(\mathrm{e}^{-j\omega_k}), \tag{63}$$

where $T_b(z^{-1})$ is a polynomial of order $n-1$ that refers to the block b and takes into account the effects of the initial and final conditions. Multiply both sides of (63) for $\hat{U}_b^H(\omega_k)$ and averaging over the N_b blocks, we obtain the following relation

$$A(\mathrm{e}^{-j\omega_k})\,S_{UY}(\omega_k) = B(\mathrm{e}^{-j\omega_k})\,S_{UU}(\omega_k) + \frac{1}{N_b}\sum_{b=1}^{N_b} \hat{U}_b^H(\omega_k)\,T_b(\mathrm{e}^{-j\omega_k}). \tag{64}$$

In absence of noise on the data, for every ω_k ($k = 0, \ldots, N-1$), the equation (64) constitutes an exact relation between the cross–spectrum $S_{UY}(\omega_k)$ and the auto–spectrum $S_{UU}(\omega_k)$. Starting from this fact, the frequency identification method described in the previous Sections can be applied to equation (64) with straightforward modifications, in order to estimate the coefficients of the polynomials $A(\mathrm{e}^{-j\omega_k})$, $B(\mathrm{e}^{-j\omega_k})$.

6. STANDARD STRUCTURAL MODELING

A linear n Degrees Of Freedom (DOF) mechanical, lumped–parameter system is governed by the equation

$$M\,\ddot{q}(t) + C\,\dot{q}(t) + K\,q(t) = f(t), \tag{65}$$

$$\hat{y}(t) = H\,q(t), \tag{66}$$

where, as convention, a dot denotes the first derivative with respect to time (i.e. $\dot{x} = \frac{\mathrm{d}x}{\mathrm{d}t}$) and a double dot denotes the second derivative with respect to time (i.e. $\ddot{x} = \frac{\mathrm{d}^2x}{\mathrm{d}t^2}$).

Vector $q(t)$ represents the DOFs, $f(t)$ is the vector of the external forces and $\hat{y}(t)$ is the vector of the noise–free measurements obtained, in general, as a subset of $q(t)$.

The ($n \times n$) matrices M, K and C satisfy the following relations

$$M = M^T \quad M > 0\,, \qquad C = C^T \quad C \geq 0\,, \qquad K = K^T \quad K \geq 0 \tag{67}$$

and are associated with the kinetic, viscous and elastic system energy modeling, respectively.

The generalized force $f(t)$ acting on the system can be expressed as a linear function of a vector $\hat{u}(t)$, with dimension $m \leq n$, containing the only non–null input forces, measured in absence of noise. Thus, it results in

$$f(t) = L\,\hat{u}(t), \tag{68}$$

where L is a known matrix that describes the DOFs at which the input forces $\hat{u}(t)$ are applied. Without loss of generality, the matrix L can also contain the scaling factors that allow to integrate the equation (65)-(66) avoiding possible numerical ill conditioning problems, due to the fact that the measures of $|f(t)|$ and $|\hat{y}(t)|$ can differ for several order of magnitude.

If some nonlinear terms are present on the system, the model (65) can be extended as follows

$$M\,\ddot{q}(t) + C\,\dot{q}(t) + K\,q(t) = f(t) + G(q, \dot{q}), \tag{69}$$

where $G(\dot{q}, q)$ represents the nonlinear action that, in general, is a function of $q(t)$ and $\dot{q}(t)$.

The system (65)-(66) can also be represented in state space form. For example, defining $x = [\, q,\ \dot{q}\,]^T$, we obtain the $2n$ dimensional system

$$\dot{x}(t) = A\, x(t) + B\, \hat{u}(t) \tag{70}$$
$$\hat{y}(t) = H\, x(t), \tag{71}$$

where

$$A = \begin{bmatrix} 0 & I \\ -M^{-1} K & -M^{-1} C \end{bmatrix} \qquad B = \begin{bmatrix} 0 \\ M^{-1} L \end{bmatrix} = B_{_M} L \tag{72}$$

and $B_{_M} = [\, 0 \quad M^{-1}\,]^T$.

Since the data are usually collected in a digital form and the system identification procedure deals with discrete time models, the time discretization of model (70)–(72) is usually a necessary step. If a zero–order–hold discretization with sampling time T is considered, the equivalent discrete time model is given by

$$x(t+1) = A_d\, x(t) + B_d\, \hat{u}(t) \tag{73}$$
$$\hat{y}(t) = H_d\, x(t), \tag{74}$$

where

$$A_d = \mathrm{e}^{A\,T} \qquad B_d = \Big(\int_0^T \mathrm{e}^{A\tau} \mathrm{d}\tau\Big) B = \Big(\int_0^T \mathrm{e}^{A\tau} \mathrm{d}\tau\Big) B_{_M}\, L = B_{d_M}\, L \qquad H_d = H \tag{75}$$

and $B_{d_M} = \big(\int_0^T \mathrm{e}^{A\tau} \mathrm{d}\tau\big) B_{_M}$.

When a single input and a single output are considered, the discrete time system transfer function is given by

$$G(z) = H_d\, (zI - A_d)^{-1}\, B_d = \frac{H_d\, \mathrm{adj}(zI - A_d)\, B_d}{\det(zI - A_d)} = \frac{B(z)}{A(z)}, \tag{76}$$

where $\mathrm{adj}(A)$ denotes the adjoint matrix of A, i.e. the transpose of the matrix cofactors. The polynomials $A(z)$ and $B(z)$, in the forward shift operator z, have order $2n$ and $2n-1$ respectively. In other words, denoting with $\hat{u}(t)$ and $\hat{y}(t)$ the samples of the noise–free input and output, we obtain

$$\hat{y}(t) = \frac{B(z)}{A(z)}\, \hat{u}(t). \tag{77}$$

It can be observed that, when a single force $\hat{u}(t)$ acts on the single j–th DOF, the matrix L reduces to a column vector containing only one non–null element l in position j. Thus, it results in

$$B_d = B_{d_M}\, L = B'_d\, l, \tag{78}$$

where B'_d is the j–th column of matrix B_{d_M}. Then, the polynomial $B(z)$ can be written as

$$B(z) = H_d\, \mathrm{adj}(zI - A_d)\, B_d = H_d\, \mathrm{adj}(zI - A_d)\, B'_d\, l = B'(z)\, l \tag{79}$$

and equation (77) becomes

$$\hat{y}(t) = \frac{B'(z)}{A(z)}\, l\, \hat{u}(t). \tag{80}$$

Note that, rewriting (77) in the backward shift operator z^{-1}, we obtain the relation

$$A(z^{-1})\,\hat{y}(t) = B(z^{-1})\,\hat{u}(t) \tag{81}$$

that coincides with (1), except the order of the polynomials $A(z^{-1})$ and $B(z^{-1})$, that now are $2n$ and $2n-1$ respectively.

In order to avoid ill numerical conditioning problems, it is preferable to identify the polynomials $A(z^{-1})$ and $B'(z^{-1})$ appearing in (80), by scaling the input sequence $\hat{u}(t)$ with the factor l.

By introducing the DFTs $\hat{Y}(\omega_k)$ and $\hat{U}(\omega_k)$ of the time sequences $\hat{u}(t)$ and $\hat{y}(t)$, the frequency domain counterpart of relation (81) can be written as

$$A(\mathrm{e}^{-j\omega_k})\,\hat{Y}(\omega_k) = B'(\mathrm{e}^{-j\omega_k})\,l\,\hat{U}(\omega_k) + T(\mathrm{e}^{-j\omega_k}), \tag{82}$$

where $T(z^{-1})$ is a polynomial of order $2n-1$. Equation (82) is analogue to equation (10).

Similar considerations hold for the nonlinear model (69). The continuous time state space model is now

$$\dot{x}(t) = A\,x(t) + B\,\hat{u}(t) + F_{nl}(t) \tag{83}$$
$$y(t) = H\,x(t), \tag{84}$$

where the matrices A, B, and C have the same structure reported in (72) and the additional term $F_{nl}(t)$ can be considered as an additional force that takes into account the nonlinear effects. The structure of the vector $F_{nl}(t)$ is

$$F_{nl}(t) = \begin{bmatrix} 0 \\ M^{-1}\,G(q,\dot{q}) \end{bmatrix} = \begin{bmatrix} 0 \\ M^{-1} \end{bmatrix} G(q,\dot{q}) = B_{_M}\,G(q,\dot{q}). \tag{85}$$

Mapping the force $F_{nl}(t)$ on the output, the continuous time model (83)–(84) becomes

$$\dot{x}(t) = A\,x(t) + B\,\hat{u}(t) \tag{86}$$
$$y(t) = H\,x(t) + w_c(t), \tag{87}$$

where $w_c(t)$ can be considered an additive noise with expression

$$w_c(t) = H\,(sI - A)^{-1}\,F_{nl}(t) \tag{88}$$

and s is the derivative operator. The discrete time model equivalent to (86)–(87) is

$$x(t+1) = A_d\,x(t) + B_d\,\hat{u}(t) \tag{89}$$
$$y(t) = H_d\,x(t) + w(t), \tag{90}$$

where A_d, B_d and H_d have been defined in (75) and $w(t)$ is the discrete time version of $w_c(t)$, sampled with the sampling time T.

Model (89)–(90) has the following Errors–in–Variable representation

$$\hat{y}(t) = \frac{B(z)}{A(z)}\,\hat{u}(t) \tag{91}$$

$$y(t) = \hat{y}(t) + w(t), \tag{92}$$

where $A(z)$ and $B(z)$ have been defined in (76) and $w(t)$ is an additive noise correlated with the noise–free output $\hat{y}(t)$.

Rewriting (91)–(92) in the backward shift operator z^{-1}, we now obtain the relations

$$A(z^{-1})\,\hat{y}(t) = B(z^{-1})\,\hat{u}(t) \tag{93}$$
$$y(t) = \hat{y}(t) + w(t). \tag{94}$$

In the frequency domain, introducing the DFTs $\hat{Y}(\omega_k)$, $\hat{U}(\omega_k)$, $W(\omega_k)$ of the time sequences $\hat{u}(t)$, $\hat{y}(t)$, $w(t)$ the relations (93)–(94) can be expressed as

$$A(\mathrm{e}^{-j\omega_k})\,\hat{Y}(\omega_k) = B'(\mathrm{e}^{-j\omega_k})\,l\,\hat{U}(\omega_k) + T(\mathrm{e}^{-j\omega_k}) \tag{95}$$
$$Y(\omega_k) = \hat{Y}(\omega_k) + W(\omega_k), \tag{96}$$

where (95) coincides with (82).

Numerical Example. A mechanical system of type (69) is considered. The mass matrix M is

$$M = \mathrm{diag}[\,m_1 \;\; m_2 \;\; m_3\,], \tag{97}$$

where $m_1 = 1$, $m_2 = 2$ and $m_3 = 3$ (Kg).

The stiffness matrix K is

$$K = \begin{bmatrix} k_1 + k_2 & 0 & -k_2 \\ 0 & k_3 & -k_3 \\ -k_2 & -k_3 & k_2 + k_3 + k_4 \end{bmatrix}, \tag{98}$$

where $k_1 = 10^6$, $k_2 = 10^7$, $k_3 = 10^5$ and $k_4 = 10^3$ (N/m).

The damping matrix C is

$$C = \begin{bmatrix} c_1 & 0 & -c_1 \\ 0 & c_2 & -c_2 \\ -c_1 & -c_2 & c_1 + c_2 \end{bmatrix}, \tag{99}$$

where $c_1 = 10$, $c_2 = 100$ (Kg/s).

The external force $f(t)$ is applied to the 3–rd DOF. The FRF to be identified is the transfer function $G(j\omega) = \hat{Y}_3(j\omega)\,/\,F(j\omega)$ between the 3–rd DOF and $F(j\omega)$. The magnitude and the phase of $G(j\omega)$ are reported in Figure 2 (solid, red line).

A non linear action $F_{nl}(t)$ of type (85), representing a friction, is applied to the 2–nd DOF, with

$$G(q,\dot{q}) = \begin{bmatrix} 0 & -F_a\,\mathrm{sign}\,(\dot{q}_2) & 0 \end{bmatrix}^T \tag{100}$$

where the function

$$\mathrm{sign}\,(\alpha) = \begin{cases} 1 & : \;\alpha > 0 \\ 0 & : \;\alpha = 0 \\ -1 & : \;\alpha < 0 \end{cases}. \tag{101}$$

The system has been discretized with zero–order–hold reconstruction, at the sampling frequency $\mathrm{F}_s = 2000$ Hz, which is compatible with the frequency band of the system, as illustrated in Figure 1. The external force $F(j\omega)$, applied to the 3–rd mass, is a discrete–time

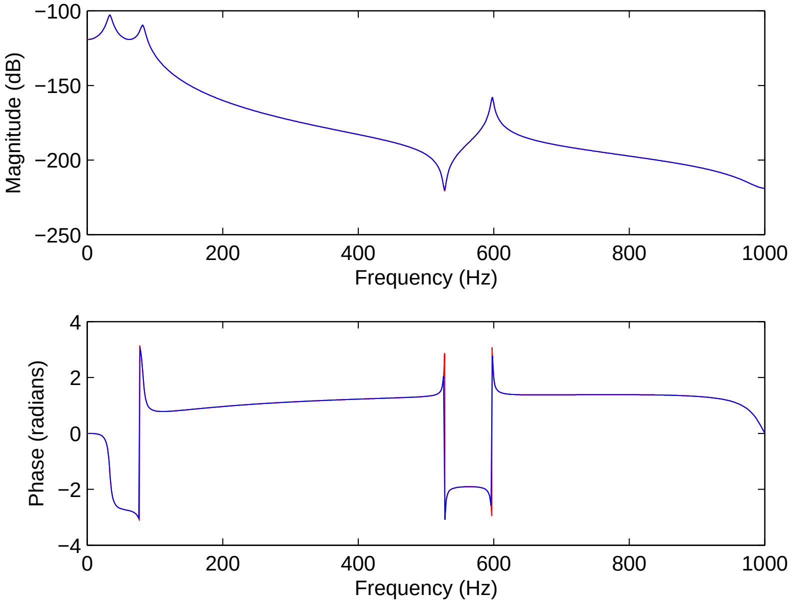

Figure 2. True TF: red (solid); Estimated TF: blue (dashed).

white noise process with length $N = 1000$ and maximal amplitude $F_0 = 1000$ N. Thus, the discrete–time system to be identified is

$$G(\mathrm{e}^{-j\omega_k}) = \frac{Y_3(\omega_k)}{F(\omega_k)} \tag{102}$$

$$Y_3(\omega_k) = \hat{Y}_3(\omega_k) + W(\omega_k), \tag{103}$$

where $\omega_k = 2\pi k/N$ and $W(\omega_k)$ is the DFT of $w(t)$, representing the additive effect of the non linear force $F_{nl}(t)$ on the measured output.

The rational transfer function (102) of order $2n$

$$G(\mathrm{e}^{-j\omega_k}) = \frac{B(\mathrm{e}^{-j\omega_k})}{A(\mathrm{e}^{-j\omega_k})} \tag{104}$$

has been identified by using the method described in Section 5, starting from the equation (64). For this purpose, a sequence of 4000 data has been considered by averaging $N_b = 4$ blocks of $N = 1000$ data each.

Figure 2 reports also the plots of the estimated magnitude and phase of $G(j\omega)$, discretized at the sampling time $\Delta t = 1/\mathrm{F}_s = 0.0005$ sec (dashed, blue line) when the non linear action is not present, i.e. $F_a = 0$. It can be observed that the true and the estimated plots coincide.

Once the system parameters have been determined, the poles of the transfer function $G(j\omega)$ can be easily estimated. Firstly, the poles p_i ($i = 1, \ldots, 2n$) of the identified discrete–time function $G(\mathrm{e}^{-j\omega_k})$ are estimated, by computing the roots of the polynomial $A(z^{-1})$.

Table 1. True and estimated values of the natural frequencies f_i and the damping ratios δ_i with $F_a/F_0 = 0.005$.

	f_1	f_2	f_3	δ_1	δ_2	δ_3
true	$33.5142\,\mathrm{Hz}$	$82.2063\,\mathrm{Hz}$	$597.7078\,\mathrm{Hz}$	0.0903	0.0366	0.0028
estimated	$33.2714\,\mathrm{Hz}$	$82.1415\,\mathrm{Hz}$	$597.5482\,\mathrm{Hz}$	0.1244	0.0362	0.0028

They are transformed into the continuous–time poles s_i by means of the relation

$$s_i = \log_e(p_i) \qquad i = 1, \ldots, 2n. \tag{105}$$

Then, the corresponding natural frequencies f_i and damping ratios δ_i are computed as

$$f_i = \frac{|\,p_i\,|}{2\pi} \qquad \delta_i = -\frac{\mathrm{Re}\,[p_i]}{|p_i|} \qquad i = 1, \ldots, n. \tag{106}$$

Tables 1 and 2 report the true values of f_i and δ_i, together with their estimates obtained with the proposed method when a non linear action with

$$F_a = 5\,N. \tag{107}$$

is applied to the system, corresponding to an entity of $F_a/F_0 = 0.005$ with respect to the external force $f(t)$. The results well illustrate the effectiveness of the proposed method even in presence of a moderate non linear action.

7. CONCLUSIONS

In this paper a frequency domain method has been proposed for the identification of EIV models with additive white noises. The method can be applied with general inputs, not necessarily periodic. The effectiveness of the proposed approach in presence of non linear model behavior has been verified by means of a numerical simulation.

Acknowledgements

The present study was supported by the Regione Emilia–Romagna, Progetto Tecnopolo POR FESR 2007-2013

REFERENCES

[1] Söderström, T., 2007. Errors–in–Variables methods in system identification. *Automatica*, **43**(6), pp. 939–958.

[2] T. Söderström, T., 2012. System identification for the errors–in–variables problem. *Transaction of the Institute of Measurement and Control*, **34**(7), pp. 780–792.

[3] Pintelon R. and Schoukens, J., 2012. *System identification: a frequency domain approach* (2nd ed.). NY: IEEE Press.

[4] McKelvey, T., 2002. Frequency domain identification methods. *Circuits Systems Signal Processing*, **21**(1), pp. 39–55.

[5] Beghelli, S., Guidorzi R. and Soverini, U., 1990. The Frisch scheme in dynamic system identification. *Automatica*, **26**(1), pp. 171–176.

[6] Guidorzi, R., Diversi R. and Soverini, U., 2008. The Frisch scheme in algebraic and dynamic identification problems. *Kybernetika*, **44**(5), pp. 585–616.

[7] Diversi, R., Guidorzi R. and Soverini, U., 2006. Yule–Walker equations in the Frisch scheme solution of errors–in–variables identification problems. In *Proc. of the 17th International Symposium on Mathematical Theory of Networks and Systems*, Kyoto, Japan, pp. 391–395.

[8] Soverini, U. and Söderström, T., 2015. Frequency domain EIV identification combining the Frisch Scheme and Yule–Walker equations. In *Proc. of the 14th European Control Conference*, Linz, Austria, pp. 2038–2043.

[9] Soverini U. and Catania, G., 2014. FRF parameter identification with arbitrary input sequence from noisy input-output measurements. In *Proc. of the 21–st MTNS*. Groningen, The Netherlands, pp. 551–556.

[10] Pintelon, R., Schoukens, J. and Vandersteen, G., 1997. Frequency domain system identification using arbitrary signals. *IEEE Transactions on Automatic Control*, **42**(12), pp. 1717–1720.

[11] Bendat, J.S. and Piersol, A.G., 2010. *Random Data: Analysis and Measurement Procedures*, John Wiley, NY.

[12] Ljung, L., 1999. *System identification–Theory for the user* (2nd ed.), Upper Saddle River, NJ, USA: Prentice–Hall.

[13] Söderström T. and Stoica, P., 1989. *System identification*, Hemel Hempstead: Prentice–Hall.

[14] Söderström T. and Soverini, U., 2017. Errors–in–variables identification using maximum likelihood estimation in the frequency domain. *Automatica*, **79**(5), pp. 131–143.

[15] Cauberghe, B, Guillaume, P. Verboven, P. Vanlanduit, S. and Parloo, E., 2004. Frequency response function–based parameter identification from short data sequences. *Mechanical Systems and Signal Processing*, **18**, pp. 1097–1116.

INDICE DEGLI AUTORI

In questo volume è raccolta la maggior parte delle memorie presentate in occasione della "Decima Giornata di Studio Ettore Funaioli", che si è svolta il 15 luglio 2016 presso la Scuola di Ingegneria e Architettura dell'Alma Mater Studiorum – Università di Bologna.
La Giornata è stata organizzata dagli ex allievi del Prof. Ettore Funaioli con la collaborazione del DIN – Dipartimento di Ingegneria Industriale e della Scuola di Ingegneria e Architettura dell'Alma Mater Studiorum – Università di Bologna, e con il patrocinio dell'Accademia delle Scienze dell'Istituto di Bologna e del GMA – Gruppo di Meccanica Applicata.

Questo volume è stato stampato con il contributo di G.D S.p.A.

ISBN 978-88-9385-037-7

AlmaDL
University of Bologna Digital Library

ISBN 978-88-9385-037-7